

FURTHER EXPLORATION OF OPTICAL/THERMAL INTERACTION EFFECTS ON HIGH-POWER
LASER SYSTEM PERFORMANCE AND OPTIMIZATION THROUGH MULTIPHYSICS SYSTEM-
LEVEL MODELING

A Dissertation submitted in partial fulfillment of the
requirements for the degree of
Doctor of Philosophy

by

NATHANIEL J. BUTT

M.S.M.E., Wright State University, 2018

B.S.M.E., Ohio Northern University, 2016

2022

Wright State University

Public Release Distribution Statement Page

This dissertation has been approved for public release Distribution Level A, Case # AFRL-2022-1527. The material was assigned clearance of CLEARED on 30 Mar 2022.

WRIGHT STATE UNIVERSITY
GRADUATE SCHOOL

4/29/2022

I HEREBY RECOMMEND THAT THE DISSERTATION PREPARED UNDER MY SUPERVISION BY Nathaniel J. Butt ENTITLED Further Exploration of Optical/Thermal Interaction Effects on High-Power Laser System Performance and Optimization Through Multiphysics System-Level Modeling BE ACCEPTED IN PARTIAL FULFILLMENT OF THE REQUIREMENTS FOR THE DEGREE OF Doctor of Philosophy.

Rory Roberts, Ph.D.
Dissertation Advisor

Ahsan Mian, Ph.D.
Program Director, Ph.D. in Engineering

Barry Milligan, Ph.D.
Dean of the Graduate School

Committee on Final Examination:

Rory Roberts, Ph.D.

Mitch Wolff, Ph.D.

George Huang, Ph.D.

Amir Farajian, Ph.D.

Soumya Patnaik, Ph.D.

Abstract:

Butt, Nathaniel J., Ph.D., Engineering Ph.D. Program, Department of Mechanical and Materials Engineering, Wright State University, 2022. Further Exploration of Optical/Thermal Interaction Effects on High-Power Laser System Performance and Optimization Through Multiphysics System-Level Modeling.

High-power laser systems (HPLS) have wide-ranging applications in many prominent areas. HPLS use laser diodes to pump fiber gain media. Understanding the functionality of both components is critical for achieving effective HPLS operation. System optical efficiency is a function of diode junction temperature. As junction temperature changes, the wavelength spectrum of the diode output shifts causing optical power losses in the fiber gain media. Optical/thermal interactions of the dynamically coupled laser diodes and fiber gain media are not fully understood. A system level modeling approach considering the interactions between optical performance and component temperature is necessary.

Four distinct models were created: Diode optical, diode thermal, fiber optical, and fiber thermal. Dynamically coupling these models together provided the capability to demonstrate how HPLS electro-to-optical efficiency changes when the laser diode pump spectrum shifts due to various levels of thermal management. Subsequent studies were done to determine which parameters across all four models had the most significant impact on laser performance from a designer's perspective. Next, a statistical surrogate model was created by varying these parameters to create a parameter space. Response variables of interest were then reduced to a single equation

as a function of these important parameters across the parameter space, allowing for quicker exploration of the potential design space. Lastly, laser time to steady state and laser efficiency were employed to determine when a specific diode cooling method should be used to achieve the highest laser efficiency.

Understanding the optical/thermal interactions of laser operation and exploring the impact of various thermal capabilities can provide better system design and optimization guidelines.

Bridging the gap between the optical and thermal aspects of laser operation in pursuit of such understanding has been made possible by the research herein.

Table of Contents:

1. History and Background:	1
The First Laser:	1
Technology Progresses:	2
Higher Power Applications and Fiber Lasers:	2
2. Problem Definition and Motivation:	6
3. Proposed Research Outcomes:	9
4. Fiber Laser Literature Review:	11
General State-of-the-Art:	11
Thermal Considerations:.....	15
Pump Diode Wavelength Shift:.....	18
Combining Optics:.....	20
Cladding Light Stripping:	21
5. HPLS Model Development/Explanation:	25
Laser Optical Model:	27
Fiber Optical Model – Rate Equations:	36
Fiber Optical Model – Heat Generation:.....	40
Diode Junction Temperature Estimation:	46
6. HPLS Model Functionality:	51
HPLS Performance – Simplified Fiber Model:	52
HPLS Performance – Full Fiber Model:	55
Fiber Rate Equation Comparison:	63
7. Diode and Fiber Thermal/Temperature Modeling:	72
8. Diode Thermal Model for Temperature Estimation:	74
Creating the Thermal Model:.....	76
Extension of the Thermal Model:	85
Diode Thermal Model Comparison:.....	89
9. Fiber Thermal Model for Temperature Estimation:	98

Creating the Thermal Model:.....	98
Analyzing Worst Case Scenario Fiber Temperature Profiles:	107
Fiber Temperature Comparison:.....	114
10. Laser and Thermal Performance Analysis:	121
Thermal Model Parameter Sweep Results:	125
11. Laser Diode Parameter Sensitivity Analysis:.....	141
12. Laser System Statistical Surrogate Modeling:.....	145
13. Laser Diode Cooling Methodologies:	163
14. Research Outcomes Achieved:	177
15. Conclusions and Discussion:	183
16. Possible Relevant Future Research Areas:.....	189
References:.....	191
Appendix A: Simplified Fiber Model Parameters and Equations	200
Appendix B: Full Fiber Model Parameter Values.....	205
Appendix C: Statistical Surrogate Model Data	207
Appendix D: Parameter values for Statistical Surrogate Model	218
Appendix E: Relevant Laser Physics/Component Overview	220
Laser Diodes – Structure and Operating Basics:	220
Laser Diodes – Optical Power Temperature Dependence:.....	226
Laser Diodes – Characteristic Temperatures:	231
Laser Diodes – Wavelength Shift Temperature Dependence:.....	245
Fiber Gain Media – Basics/Background:	253
Fiber Gain Media – LP Modes of Fibers:	258
Fiber Gain Media – Seeding a Fiber:	263

List of Figures:

Figure 1: Boeing YAL-1 Airborne Laser Testbed in flight ⁶	3
Figure 2: Helios LWS delployed on a navy ship ⁹	4
Figure 3: Optical train diagram of proposed HPLS model.....	26
Figure 4: Diagram of all coupled models for entire laser system	27
Figure 5: Diagram of laser optical model.....	27
Figure 6: Laser diode array diagram ³⁷	28
Figure 7: Laser diode module diagram ³⁷	29
Figure 8: Diagram of fiber optical model	37
Figure 9: Explanation of rate equations terms	42
Figure 10: Diagram of how right-hand side (RHS) quantities are interacting with the fiber core.....	43
Figure 11: Diagram of how right-hand side (RHS) quantities are interacting with the fiber core.....	43
Figure 12: Diagram of how right-hand side (RHS) quantities are interacting with the fiber core.....	45
Figure 13: Golden Bullet spectrum output at various current levels ⁷⁰	48
Figure 14: Mock temperature estimation profiles of the 5 diode bars (1, 2, 3, 4, 5) in a single (5x5) module throughout the activation pulse	50
Figure 15: Case 1 optical power output.....	53
Figure 16: Case 1 heat generation	53
Figure 17: Case 1 spectral power density curves.....	54
Figure 18: Optical power output of rate equation fiber model (a) and simplified model (b)	56
Figure 19: Heat output of rate equation fiber model (a) and simplified model from (b).....	57
Figure 20: Heat generation in a single active fiber	58
Figure 21: Optical performance of a single fiber	59
Figure 22: Diagram of three relevant active fiber efficiency values.....	61
Figure 23: Fiber heat deposition profiles at beginning (t = 5 sec) and end (t = 13 sec) of activation pulse.....	62
Figure 24: Pump and signal power levels [reprinted from Yu et al. ¹⁰⁰ , Fig. 7a]	65
Figure 25: Power plot of t = 5 sec in Figure 24 with fiber length 30 m.....	66
Figure 26: Sample fiber quantum defect profile [reprinted from Yu et al. ²⁰ , Fig. 1]	67
Figure 27: Linear heat deposition [reprinted from Mobini et al. ²⁹ , Fig. 3]	68
Figure 28: Heat deposition, three pumping schemes [reprinted from Abouricha et al. ¹⁰² , Fig. 4].....	69
Figure 29: Diagram of laser thermal model	74
Figure 30: Diagram for thermal model representation	75
Figure 31: Diagram of control volumes for thermal model analysis	76
Figure 32: Various heat transfer coefficient and mass flow rate relationships.....	86
Figure 33: Diagram of heat exchanger thermodynamic model ⁹⁸	90

Figure 34: Diagram of fin parameters and geometry ⁹⁸	92
Figure 35: Model Temperature Comparison Case 1, (a) is diode thermal model, (b) is WSU Cold Plate Model.....	95
Figure 36: Model Temperature Comparison Case 2, (a) is diode thermal model, (b) is WSU Cold Plate Model.....	95
Figure 37: Diagram of fiber thermal model.....	98
Figure 38: Fiber discretization diagram.....	101
Figure 39: Fiber temperature profiles at various points in time.....	108
Figure 40: Steady state fiber temperature profile.....	108
Figure 41: Max fiber temperature with natural convection.....	109
Figure 42: Max fiber temperature with forced convection, velocity of 1 m/s.....	111
Figure 43: Max fiber temperature with forced convection, velocity of 3 m/s.....	112
Figure 44: Max fiber temperature with forced convection, velocity of 5 m/s.....	113
Figure 45: Max fiber temperature with forced convection, velocity of 8 m/s.....	114
Figure 46: Fiber temperature profiles [reprinted from Li et al. ¹¹ , Fig. 2].....	116
Figure 47: Forward and backward fiber temperature profile [reprinted from Lv et al. ³⁵ , Fig. 5b].....	117
Figure 48: Fiber temperature profiles [reprinted from Abouricha et al. ¹⁰² , Fig. 5].....	118
Figure 49: Fiber temperature profile [reprinted from Wang et al. ¹³ , Fig. 2].....	119
Figure 50: Thermal model data explanation.....	124
Figure 51: Parameter sweep for average T_m steady state values.....	126
Figure 52: Parameter sweep for average T_f steady state values.....	127
Figure 53: Parameter sweep for range of T_m steady state values.....	128
Figure 54: Parameter sweep for range of T_f steady state values.....	129
Figure 55: Parameter sweep for time to steady state of T_m values.....	130
Figure 56: Parameter sweep for time to steady state of T_f values.....	131
Figure 57: Parameter sweep for range of time to steady state for T_m	132
Figure 58: Parameter sweep for range of time to steady state for T_f	133
Figure 59: Parameter sweep for overall E-O efficiency of diode array.....	134
Figure 60: Parameter sweep for overall O-O efficiency of the fiber.....	135
Figure 61: Parameter sweep for total optical energy out of laser with given pulse length.....	137
Figure 62: Parameter sweep for percent of maximum possible optical energy.....	138
Figure 63: Parameter sweep for <i>tratio</i> values.....	139
Figure 64: Interaction profiles for wavelength coefficient ($d\lambda/dT$), FWHM coefficient ($d\beta/dT$), T_0 and T_1 , showing the effects of each parameter on optical energy out ³⁸	142
Figure 65: JMP values for f_1 in Tm * surrogate model.....	150
Figure 66: JMP values for f_2 in Tm * surrogate model.....	151

Figure 67: JMP values for f_3 in tss surrogate model.....	153
Figure 68: Residuals for each response variable in surrogate models (source points)	158
Figure 69: Actual by predicted plots for each response variable in surrogate models (source points) ...	159
Figure 70: Two cooling methods, A and B	164
Figure 71: Efficiency plots at varying pulse lengths for cooling methods A and B (Case 1)	166
Figure 72: Efficiency plots at varying pulse lengths for cooling methods A and B (Case 2)	168
Figure 73: Average overall efficiency for Methods A and B (plots 1 and 2)	171
Figure 74: Average overall efficiency for Methods A and B (plots 3 and 4)	172
Figure 75: Average overall efficiency for Methods A and B (plots 5 and 6)	172
Figure 76: $tratio$ as a function of temperature delta	173
Figure 77: $tratio$ as a function of $\lambda shift$	174
Figure 78: Data plot for f_1 curve of Tm * equation.....	207
Figure 79: Data plot for f_2 curve of Tm * equation.....	207
Figure 80: Data plot for f_1 curve of Tf * equation.....	208
Figure 81: Data plot for f_2 curve of Tf * equation.....	209
Figure 82: Data plot for f_1 curve of tss equation.....	209
Figure 83: Data plot for f_2 curve of tss equation.....	210
Figure 84: Data plot for f_3 surface of tss equation	210
Figure 85: Data plot for f_1 curve of $overalleff$ equation.....	212
Figure 86: Data plot for f_2 curve of $overalleff$ equation.....	212
Figure 87: Data plot for f_3 curve of $overalleff$ equation.....	213
Figure 88: Data plot for f_4 curve of $overalleff$ equation.....	213
Figure 89: Data plot for f_5 surface of $overalleff$ equation.....	214
Figure 90: Data plot for f_6 surface of $overalleff$ equation.....	214
Figure 91: Data plot for f_7 surface of $overalleff$ equation.....	215
Figure 92: Data plot for f_8 surface of $overalleff$ equation.....	215
Figure 93: Data plot for f_9 surface of $overalleff$ equation.....	216
Figure 94: Data plot for f_{10} surface of $overalleff$ equation.....	216
Figure 95: Lasing wavelength for certain semiconductor materials in the active region ⁴⁶	221
Figure 96: Typical laser diode diagram showing materials/components for operation ⁴⁷	221
Figure 97: Explanation of laser diode operation using the Fabry-Perot Resonator ⁴⁶	222
Figure 98: Laser diode threshold current diagram ⁴⁸	223
Figure 99: Diagram Denoting the “Fast” and “Slow” Axis of Laser Diode Output ⁴⁶	224
Figure 100: Diagram of Gaussian Curve representing laser diode optical power output ³⁷	225
Figure 101: Generalized graph of optical output power vs. forward current showing the effects of junction temperature on threshold current and slope efficiency ⁴⁹	228

Figure 102: Experimental research showing the trend of increasing threshold current and decreasing slope efficiency due to increasing junction temperature (mW of optical power) ⁵⁰	229
Figure 103: Laser diode threshold current and slope efficiency experimental values ⁵⁰	232
Figure 104: Temperature dependence of L-I characteristic curves and relationship between threshold current density and operating temperature with $T_0 = 113K$ ⁵⁵	234
Figure 105: Temperature dependence of L-I characteristic curves and relationship between threshold current and operating temperature with $T_0 = 102K$ ⁵⁶	235
Figure 106: Relationship between threshold current and operating temperature with a varying number of quantum dot layers. The T_0 values for each sample were 51K for N = 5, 91K for N = 10, 116K for N = 15, and 148K for N= 20 dot layers ⁵⁷	236
Figure 107: Operating temperature versus the natural log of threshold current and lasing wavelength showing $T_0 = 101K$ and wavelength temperature coefficient $d\lambda/dT = 0.367 \text{ nm/K}$ ⁵⁸	237
Figure 108: Characteristic temperature T_0 for P-doped and undoped quantum dot lasers emitting in the $1.55 \mu\text{m}$ regime ⁵⁹	238
Figure 109: Graph showing invariant threshold current ($T_0 = \infty$) in the range of 278 to 348K ⁶⁰	239
Figure 110: Schematic of InGaAsP/InP MQW laser with tunnel layer ⁶¹	239
Figure 111: Laser characteristic temperature T_0 as a function of junction temperature comparing the performance of an InGaAsP laser diode with and without a tunnel barrier ⁶¹	240
Figure 112: L-I curves at various operating temperatures and operating temperature vs. threshold current density plots ⁶²	241
Figure 113: L-I curve at various operating temperatures, both characteristic temperature graphs, and T_0 variation with cavity length L ⁶³	242
Figure 114: Threshold current vs. operating temperature, slope of curve is $T_0 = 114K$ ⁶⁴	243
Figure 115: Threshold current vs. operating temperature for 2 n-doping levels ⁶⁵	244
Figure 116: Experimental results of characteristic temperature T_0 as a function of laser diode operating temperature ⁵³	245
Figure 117: Results showing average junction temperature as a function of forward current and the wavelength shift/spectral broadening due to higher junction temperatures from increased forward current levels ¹⁴	247
Figure 118: Wavelength shift due to higher junction temperatures from increased forward current in an 808 nm laser diode ⁶⁷	247
Figure 119: Laser diode output intensity changing with wavelength shift due to shifting heat sink temperature ⁶⁴	248
Figure 120: Spectral width changing with heat sink temperature, 0.28, 0.32, 0.37, and 0.43 nm for 10, 19, 28, and 37 °C, respectively ⁶⁴ . If FWHM is represented by β , then the slope of the line is $d\beta/dT = 0.0056 \text{ nm/K}$ ⁶⁴	249

Figure 121: Packaging of a high power semiconductor laser array showing laser output (“fast” divergence axis in vertical direction and “slow” divergence axis in the horizontal direction)⁷¹ 251

Figure 122: Laser bar “smile” showing a good spectrum vs. a bad spectrum⁷¹. A laser bar is operating optimally when the spectrums of all emitters are the same⁷¹ 251

Figure 123: Transverse temperature profile of quantum wells at steady state⁷² 252

Figure 124: Wavelength of steady state laser bar output for a particular operating current value and 60% of that value⁷² 253

Figure 125: Diagram of fiber geometry with core, inner cladding, and outer cladding. The refractive index profile (RIP) of each layer is given to show how its magnitude changes⁷³ 254

Figure 126: Illustration of relationship between focal length (f) and aperture diameter of lens (D), where F is the focal point (reprinted from Figure 2.4 in Motes et al. ³²). 255

Figure 127: Pump power is converted to signal power through an optical fiber by doping ions in the core, turns large NA pump light into small NA signal light⁷⁴ 256

Figure 128: Typical energy level diagram of Yb³⁺ ions in silica glass (a) and typical emission and absorption cross-sections in aluminosilicate (thicker lines) and phosphosilicate (thinner lines) fibers. The arrow represents the peak of the phosphosilicate emission/absorption⁷⁸. 258

Figure 129: Graphical solution showing V cutoff points for various LP modes. Parameters w and u come from the planar waveguide mode derivation of Maxwell’s equations and are defined such that $V^2=u^2+w^2$ (reprinted from Figure 2-14 in Motes et al. ³²). 260

Figure 130: Generic intensity profiles for guided LP_{l,m} modes of a fiber with V =11.4. The two colors indicate positive (red) and negative (blue) signs of the electric field⁷⁹ 261

List of Tables:

Table 1: Laser Diode Model Parameters ³⁸	30
Table 2: Characteristic temperature values from literature	35
Table 3: Wavelength and spectral width coefficient values from literature	36
Table 4: Variable definitions for rate equations	38
Table 5: Various parameter values for rate equation.....	40
Table 6: Thermal model parameters and definitions	81
Table 7: Thermal Model Comparison Parameter Values	94
Table 8: Fiber Thermal Model Parameters and Definitions.....	107
Table 9: Thermal parameter sweep values and definitions.....	123
Table 10: Sensitivity analysis high, low, and nominal parameter values ³⁸	141
Table 11: Individual Parameter Sensitivity Analysis ³⁸	143
Table 12: Parameter space definitions and ranges for Nu , $Pflux$, $d\lambda/dT$, and L	149
Table 13: Function coefficient values for Tm * surrogate model.....	151
Table 14: Percent error for all response variables from respective surrogate models.....	156
Table 15: Parameter values for test points.....	156
Table 16: Percent error for test points in all surrogate models	157
Table 17: Temperature delta, time to steady state, and efficiency data for cooling method comparison	170
Table 18: Temperature delta and $tratio$ cross point location value data	173
Table 19: Coefficients of fitted curves for Tm * equation.....	207
Table 20: Coefficients of fitted curves for Tf * equation.....	209
Table 21: Coefficients of fitted curves/surfaces for tss equation	211
Table 22: Coefficients of fitted curves/surfaces for $overalleff$ equation.....	217

1. History and Background:

Before explaining the details of the research described in this dissertation, some laser history and background is first pertinent. To understand current laser technology and its importance, consider the technological progression. Understanding the beginnings of laser technology and progression through the years will shed light on the present-day problems. Throughout the years, lasers have been applied in many different technological areas. Each application has certain problems and challenges designers must overcome. The history and background pertain specifically to the development of continuous wave (CW) lasers for high-power applications.

The First Laser:

In 1917, Albert Einstein suggested a process that, in theory, would make laser light possible. He called it stimulated emission¹. It is only mentioned briefly in his now famous article, but he proposed that electrons could be made to emit light at a particular wavelength. In 1960, Einstein's prediction was proven correct by Theodore Maiman who created the first working pulsed beam laser with pink ruby as the active medium^{2,3}. He built upon the theoretical work of Charles Townes and Arthur Schawlow. Interestingly, the article was published in Nature and was less than a single page in length. However, it is now considered the beginning of laser innovation. Laser is an acronym standing for Light Amplification by Stimulated Emission of Radiation. Laser light is different from normal light because it is monochromatic, coherent, and can be highly collimated. The light is of constant wavelength, phase, and can be focused in a very narrow beam yielding high intensity. Maiman was a physicist working for Hughes Research Laboratories at the time, and his invention sparked rapid innovation. By December of 1961, a little over one year later, a ruby laser created by American Optical was used for the first time in

a medical procedure⁴. Doctors used the laser to destroy a retinal tumor. Clearly, there were many potential applications yet to be explored. The race of laser innovation had begun.

Technology Progresses:

After Maiman's first laser demonstration, interest in lasers grew quickly. It seemed the new technology had unbounded potential. Researchers in many different areas began working to see how laser technology could benefit their particular area. In 1964, the Nd:YAG (neodymium-doped YAG) laser was developed by Bell Labs. It later found use in cosmetic applications like corrective surgery to repair vision in eyes⁴. In 1966, Charles Kao calculated that with pure enough glass, optical fibers had the potential to transmit light 5000 times further than state of the art fibers could at that time, paving the way for the eventual development of the fiber laser⁴. Researchers at Bell Labs created the first semiconductor laser to operate continuously at room temperature in 1971⁴. In 1982, the titanium sapphire laser developed by MIT Lincoln Laboratories achieved laser pulses in the picosecond to femtosecond ranges⁴. The ultrafast laser, as it is now called, has found application in a multitude of areas, like material processing, where short pulses with very high peak power are required. The same year, the compact disc (CD) was released and revolutionized the music industry⁴. Other laser applications are quite numerous, including measuring devices, printers, scanners, and even LED Christmas tree lights. The device that reads bar codes at the checkout counters in grocery stores is a laser. The multitude of both civilian and military applications is far too numerous to discuss in detail here. Lasers are everywhere and have become a product on which modern society very much relies.

Higher Power Applications and Fiber Lasers:

Many advances in laser technology seen on the civilian side of things have first been researched and tested for military applications. The heads-up display (HUD) has origins in the military and is

now used on the smart screens of cars. Laser guided ordinance has been heavily relied upon since its introduction during the Korean War era⁵. It is used in both air and ground-based vehicles.

One of the most interesting (though not the most practical) applications was the Boeing YAL-1 Airborne Laser Testbed. It was a megawatt class chemical oxygen iodine laser mounted in the nose of a Boeing 747-400 aircraft⁶. The purpose was to see if airborne lasers were viable given the technology of the time. The laser produced 1 kilowatt of optical power per every 55kg of mass. In 2007, the testbed proved it was possible to track and hit a target 10s of kilometers away while adjusting for atmospheric disruption to the beam.



Figure 1: Boeing YAL-1 Airborne Laser Testbed in flight⁶

However, the resources needed to outfit the aircraft and keep it running were astronomical, and it would have to be operated relatively close to the targets. Neither of these facts are desirable. With the continued advancements in laser technology, the idea of putting a laser on mobile vehicles has again gained significant traction. The AN-SEQ3 Laser Weapon System (LWS) is a 30-

kW solid state laser designed to be used on a navy ship in the marine theaters of operation⁷. It uses incoherent beam combining to focus the multiple beams in the same spot on a target. In tests, the high intensity beam was able to hit ground targets and even an unmanned drone at effective ranges of up to one mile. The navy is also researching and testing 60 and 150-kW laser systems, such as Helios, for ships^{8,9}.



Figure 2: Helios LWS deployed on a navy ship⁹

Helios is a step up from the 30 kW LWS. Lockheed Martin is also in the process of developing a concept they call the Tactical Airborne Laser Weapon System (TALWS)¹⁰. It is the same idea as was put forth in the Airborne Laser Project Boeing YAL-1, but the system is much smaller and podded for use on significantly smaller vehicles. Clearly, there exists great interest in laser system with optical power levels on the order of 10 and even 100 of kW.

Fiber lasers are a large part in these military applications, as they have characteristics that are very beneficial in many aspects of system performance. Fiber lasers use optical fibers as the gain media, which is pumped with light from a laser diode. Fiber lasers will be explained more in

pertinent areas of the document, but briefly, fiber gain media are used because of their high optical efficiency levels, relatively small mass and volume, and ease of cooling due to large surface areas¹¹⁻¹⁴. Technology advances have led to an increase in capabilities from 1 kW optical output power per fiber^{11,15,16} to 3-5 kW optical output power per fiber¹⁷⁻²⁴ in recent years.

Adequate thermal management for laser diodes and fibers, however, remains to be one of the limitations in high power laser system (HPLS) design^{14,25-27}. As is explained later in much greater detail, laser diodes and fibers have optimum operating conditions dependent on the system temperature. Hence, if the laser system is not adequately controlled from a thermal management perspective, system performance will change. Laser diodes and fibers both have dynamic efficiencies which are functions of system temperature. Knowing the interactions is of paramount importance to truly understand how HPLS are affected by improper thermal management, leading into the discussion of the motivations for this research.

2. Problem Definition and Motivation:

The main issue concerning HPLS design is thermal management. The desire to increase optical power out of the HPLS means an increase in heat generation, if the laser efficiency remains the same. A fiber-based HPLS contains 3 main components: Optical fiber gain media, laser diodes to pump the fiber gain media, and a combiner to put all the beams from each individual fiber together. Obtaining an accurate picture of how much heat is coming from each component is important. Furthermore, since laser diodes and fiber gain media efficiencies are temperature dependent, a useful laser system model needs to consider how the efficiencies change with temperature. The model must track how optical power changes as system temperature changes. Additionally, it must show a corresponding change in the total heat generated by the laser system. A model as such simulates the dynamic efficiency aspect of HPLS operation. The dynamic efficiency is important because of the potential for thermal runaway. An increase in system temperature yields a decrease in laser efficiency, meaning an increase in the heat generated. If the thermal management system (TMS) cannot compensate for this increased heat load, the temperature of the system will again increase leading to further decrease in laser efficiency. The downward spiral ends in a thermal runaway situation, where the laser efficiency has decreased so much that the amount of heat being produced is now detrimental to the laser system in the way of system components seeing significant degradation. For example, the laser diode life span has now been significantly decreased because of the exposure to higher than rated operating temperatures.

The HPLS model can then be coupled with TMS model to see how successful a certain TMS architecture is in controlling the laser system. In this way, the optical/thermal interaction is taken into account for a more accurate picture of what thermal management capacity is

necessary to achieve a certain level of performance for an HPLS. The model created for this research simulates how fiber absorption/emission degrades when laser diode output shifts due to improper thermal management. From this, different cooling methodologies can easily be tested to see which one provides the best HPLS performance against a certain metric. Some cooling methodologies might be driven by high heat transfer coefficient values, while others might be driven by large temperature differentials (i.e., very cold gas). Perhaps a thermal management system can only provide a certain amount of cooling. Is the HPLS performance acceptable? Such are the types of questions which can now be answered from this research. It has potential to assist in making high level design decisions in the optimization of HPLS performance and thermal management. As per the academic literature, very little consideration has been given to the optical/thermal interactions from such a perspective.

At this juncture, it is important to note laser physics is not a trivial topic. The research herein approaches the laser modeling problem from a heavily thermal perspective. The laser physics topics discussed are only presented to a deep enough level to understand their impact on the thermal aspect of laser operation. Laser physics contains some very complicated theories and mathematics, so it was necessary to determine what physics were necessary to include in order to create a laser model to answer the thermal questions. Some very complicated models exist for fiber laser beam development and propagation, but they provide little breakdown of what is happening on the thermal side. The model created for the research herein strives to bridge the gap between the optical side and the thermal side of HPLS operation, as understanding the interaction of both is necessary in designing and optimizing high power laser systems for particular applications. The research has potential to create a tool for making high-level design decisions in the optimization of HPLS performance balanced with thermal management

capabilities. It goes further in creating a methodology for modeling that can be extended to other laser-based systems like radar or lidar. Such systems have components similar to the high-power laser system presented herein, and the optical/thermal interactions will become more significant as the radar/lidar technology becomes smaller and more powerful. In this way, the research is broader and more applicable across a multitude of laser technologies.

3. Proposed Research Outcomes:

The overall goal of the research herein is to create a modeling tool to help make high level design decisions in the optimization of HPLS performance and thermal management from a more thermal perspective. There is certainly ample space in the literature for research in the topic of fiber laser optical/thermal interactions. The section here is put forth to outline the expectations of the research. There are several smaller steps along the road to the main goal that must be achieved in a specific order. They are milestones that need to be reached in terms of laser physics understanding, model development, and creating a methodology for representing and understanding the optical/thermal interactions in laser operation. The questions and novel outcomes to be answered and produced by this research are listed here, numbered for clarity.

1. It is known electro-to-optical (E-O) efficiency degrades if excess heat builds up in laser diodes. The question is: How significant is the efficiency degradation? If so, what fidelity of modeling the laser physics is necessary to capture said degradation?
2. Virtually no previous research exists in modeling the output of multiple laser diodes, as it is all done experimentally. The proposed research presents a methodology for stringing multiple laser diodes together in an array formation along with a thermal model to estimate laser diode temperatures, all through modeling and simulation.
3. In the proposed research, models of both the laser diode and fiber gain media will be coupled in a transient sense. Doing so will show how a change in laser diode output affects fiber gain media absorption/emission. Previous research shows laser diodes and fiber being coupled in steady state operation, but not in transient operation.

4. Fiber rate equations dictate how diode pump power is absorbed/emitted in the fiber, but they do not directly provide the heat generated inside the fiber. In the proposed research, a method is provided to dig deeper into the rate equations and understand this heat. The goal is to use the heat generation data to perform worst-case scenario analysis concerning fiber temperature and determine the thermal requirements for acceptable fiber operation. Little attention has been given to this area in previous research.
5. Are there any particular parameters, either in laser diodes/fiber gain media/thermal management, which have a more significant effect on optical power output than others?
6. These particular parameters could be used to understand laser performance response variables over a given parameter space and, in the process, eliminate the need constantly simulate the full physics laser models for every parameter combination. Such ability would greatly benefit laser system design decision making and optimization by providing insight into the effect of optical/thermal interactions on laser system performance and efficiency.
7. Are there cooling methodologies to achieve optimum laser performance? Perhaps fluid cooler than the laser diode reference temperature could be used so the diodes are on-design at steady state (moving to the reference temperature) instead of off-design (moving away from the reference temperature). Developing a metric to decide if one cooling methodology is better than another would be of great benefit.

The seven points above embody the essence and uniqueness of the proposed research herein. The problem and motivation for the research have now been fully presented and defined. The remainder of the dissertation is dedicated to answering the above questions and producing the above novel outcomes.

4. Fiber Laser Literature Review:

As with any topic of research, the first step is to see what already exists in the current literature.

The review presented here is very general with higher level topics and concepts in mind.

Literature reviews specific to laser diodes and fiber gain media, for the most part, are reserved for the respective sections of the dissertation. The goal here is to look at what kind of work has been done and see if anything similar to the model proposed in the problem definition and motivation section already exists.

The review consists of fiber lasers and thermal aspects related to them. Laser diodes, along with fiber gain media, are a part of fiber lasers. Literature more pertinent to laser diodes and fiber gain media in particular rather than fiber lasers as a whole have their own literature review in Appendix E.

General State-of-the-Art:

The optical power capabilities of fibers have been studied in depth, as increasing the amount of optical power out of a single fiber is a topic of great interest. Some of the research uses off-the-shelf fibers (from companies like Nufern), while others design and draw their own fibers. They consider mostly single mode fibers. Interestingly, most single mode fiber operation is actually created from multi-mode fibers. It is accomplished by coiling the multi-mode fibers at a specific bend diameter until the higher order modes are filtered out and only the fundamental LP₀₁ mode remains (see Appendix E for more explanation of the fundamental modes).

Beier et al.¹⁹ details a single mode, Yb-doped fiber laser capable of producing 3 kW of optical power with a signal wavelength of 1070 nm using diode pump light of 976 nm. The fiber had a core diameter of 24.5 μm and a cladding diameter of 450 μm with a length of 30 m. The signal

linewidth was reasonably narrow at 170 pm. The fiber had a slope efficiency of 90% with respect to absorbed pump power. The bend diameter used was 1 m. The fiber exhibited no signs of nonlinear optical effects (NLE), such as Stimulated Raman Scattering (SRS) or Stimulated Brillouin Scattering (SBS), or mode instabilities (MI) while producing 3 kW. Fiber operation can be SRS, SBS, and MI free if the core diameter, core numerical aperture (NA), and Yb doping concentration are optimized, as Beier et al.¹⁹ show in their research.

Beier et al.¹⁷ created 2 single mode fibers capable of 4.3 kW and 3.5 kW optical power output respectively. The signal linewidth was 7 nm and 180 pm respectively. The core diameter was 23 μm and the cladding diameter was 460 μm . Both fibers were operated without the presence of transverse mode instabilities (TMI). The 3.5 kW was seeded by 10 W of laser light at 1067 nm with a linewidth of 180 pm. The 4.3 kW fiber was seeded with a combination of lasers, one with a linewidth of 180 pm and one shifted by 300 pm, in order to increase the SBS threshold. This, in turn, caused an increase in linewidth to the much larger value of 7 nm. The 4.3 kW fiber is limited only by the pump power input and could theoretically handle larger pump power values with no adverse effects. The slope efficiencies were 90% for each fiber.

Yu et al.²⁰ were able to achieve fiber signal output of 3.1 kW with a 90% O-O efficiency (different from slope efficiency) and a linewidth of 45.5 pm. The fiber had an NA of 0.2 and a cladding radius of 200 μm . The fiber was pumped from both ends, yielding a peak heat load of 170 W/m along the fiber. A fiber's ability to handle this high heat load allows for future multi-kilowatt power scaling of such systems. References in this research indicate the authors used a fiber created, at least in part, by Nufern.

Shen et al.¹⁸ recorded 3.1 kW of continuous optical power out of a fiber. They were able to increase the SBS threshold and achieve single mode fiber operation. The fiber was seeded with light at 1064 nm and a linewidth of 181 pm at 14 W of optical power, and the 3.1 kW signal output linewidth was maintained at this value. The fiber was pumped with 976 nm diodes. The core diameter was 20 μm and the cladding diameter was 400 μm . They obtained an O-O efficiency of 85.6%

Lin et al.²¹ report a 3.7 kW single mode fiber laser with a full width half maximum (linewidth) of 0.30 nm. They studied various seed lasers to which best suppressed the SRS effect. They were also successful in suppressing mode instabilities (MI) by optimizing the active fiber's bend diameter. The seed laser was 80 W of 1064 nm laser light with a linewidth of 0.10 nm. The pump light coupled to the fiber was at 915 nm. They used a Nufern fiber with a core diameter of 25 μm and a cladding diameter of 400 μm . The highest O-O efficiency achieved was 76%.

Wang et al.²² detail a fiber laser capable of 6.85 kW optical power output. The fiber has a core diameter of 30 μm and a cladding diameter of 900 μm . They observed an O-O efficiency of 67.1%. The signal output was centered on 1079.79 nm with a linewidth of 1.89 nm. The pump light coupled to the fiber is around 10 kW at 976 nm. Due to the relatively large fiber core size and an NA of 0.059, at least 5 LP modes (LP₀₁, LP₀₂, LP₁₁, LP₂₁, and LP₃₁) are supported by the fiber. Hence, it is very likely an energy exchange between the fundamental LP₀₁ mode and all other higher order modes will occur and the beam quality will degrade to levels below that of a single mode fiber laser. Higher optical power levels do not necessarily mean a more effective laser if higher order modes are allowed to propagate.

Tao et al.²³ do a thorough job of presenting the mode instabilities inherent in high power fiber laser operation and suggest ways to minimize their negative effects. Along with being a research article, the work is also a review article and provides a good overview of the current fiber laser capabilities. In fact, the article makes mention of research by Fang et al.²⁴, in which they were able to create a single mode fiber capable of 5 kW optical power at a center wavelength of 1080 nm. The first fiber was 20 m long with a core diameter of 20 μm and a cladding diameter of 400 μm , manufactured by Nufern. They created a seed laser of 475 W at 1080 nm from the first fiber with 650 W of launched pump power at 976 nm. They then fed this output into a second fiber where the seed signal of 475 W was pumped with 5350 W of diode pump light at 976 nm. With an optical power level of 5010 W out of the second fiber, the O-O efficiency is around 83%. The coupling efficiency of this pump light into the second fiber is 98%. The second fiber was 23 m long with a core diameter of 30 μm and a cladding diameter of 600 μm . As of the publish date in 2017, no single mode fiber had output a larger optical power value. Based on the previous sources listed in this section, the research by Fang et al.²⁴ is still the highest published optical power level for a monolithic, near-diffraction-limited, single mode fiber.

Li et al.²⁸ look specifically at reducing the amount of SRS in a fiber output signal by way of the seed laser source's transmission fiber length. A longer fiber means a higher chance exists of significant SRS levels occurring. SRS severely decreases brightness out of the fiber and causes other various operational issues, all of which are detrimental to optimal fiber laser operation. Seed laser of different center wavelengths and linewidths all performed differently for the same active fiber length. Some suppressed SRS while others did not. The research shows how SRS is a serious concern when designing fiber lasers, as its onset causes serious optical problems. Since SRS is very difficult to model, work done by others¹⁷⁻²⁵ showing little to no SRS during fiber

operation is enough to say that if fibers have values for parameters within a certain range, SRS does not need to be modeled. Not having to account for SRS in the calculations makes simulating fiber laser power output much easier.

None of the research presented in the literature review considers the dynamic coupling of laser diode output and fiber gain media. The pump light launched into the fiber has a constant center wavelength and spectrum shape. They do not show how fiber O-O efficiency changes when the laser diode pump spectrum (center wavelength) changes.

Thermal Considerations:

Mobini et al.²⁹ observed how the pump-signal quantum defect is the dominant source of heat generation in kilowatt-level fiber lasers. They plot the linear heat density (W/m) along the fiber length for an input pump power of 3500 W, as they were able to find the amount of quantum defect using the rate equations coupled with the heat conduction equation. Temperature variation inside the entire fiber is quite small, but the difference between fiber temperature and ambient temperature can vary significantly. If the quantum efficiency is not high enough, too much heat will be generated and the fiber will need to be water cooled. However, with a high enough quantum efficiency and the typically large surface to volume ratios fiber exhibit, a Yb-doped fiber with a quantum efficiency of 92% may not need water cooling. Simple forced convection of air may be sufficient. In addition, there are other fiber design techniques and operating methods to consider so the heat can be more spread out and not so concentrated in the first half of the fiber. They give the acceptable temperature rise of a fiber to be 100°C. Motes et al.³² also gives 100°C as an acceptable temperature rise. For this range, fiber temperature does not affect its optical absorption/emission properties and quantum efficiency. They showed results where both air cooling and water cooling were sufficient to operate certain

fibers with 3500 W of input pump power given specific design variations to create more/less power loss from photodarkening and parasitic absorption.

Beier et al.³⁰ demonstrated the first *in situ* measurement of fiber core temperatures for various power levels all the way up to 1600 W of input pump power, with a maximum temperature change of 40°C at steady state operation. They also looked at the quantum defect by analyzing the thermal load values at various seed laser wavelengths, showing how if the seed laser was smaller (closer to the 976 nm input pump light), the quantum defect decreased. They were able to increase the TMI threshold given these shorter seed wavelengths. However, knowing the emission peak of the Yb spectrum at 1064 nm, any shift of the seed laser away from this value will yield lower power signal out of the fiber. Hence, fiber design really becomes a higher-level optimization problem, as just changing one value/parameter is not necessarily the most effective way to achieve the desired performance enhancement. Jauregui et al.³⁰ agree, stating the main conclusion from their work to be “the optimization of the active materials of fiber laser systems cannot be done [by] just trying to improve one particular parameter, but it has to follow a more holistic approach that focuses on improving the overall laser performance”.

Li et al.¹¹ used the 2-D heat conduction equations in cylindrical coordinates to model fiber temperature along the core at steady state operation. With a simulated pump power of 1000 W at 976 nm, they show about 2°C variation radially in the fiber and about 180°C variation longitudinally with a maximum fiber temperature of 480°C. Next, they created an experiment with a fiber pumped by 850 W of 976 nm light. The signal out of the fiber at steady state conditions was 621 W. They noted how optimizing the optical cavity parameters can help reduce the thermal effects to where they only needed air cooling to maintain proper fiber operation. For example, they created a fiber that allows heat to flow uninterrupted from the doped to the

undoped regions. The melting point of silica glass used in fiber core production is 1650°C ³². However, the cladding materials have lower melting points, and Li et al.¹¹ state “effective heat dissipation is important... with the aim of preventing damage to fiber end, interface, and coating”. They also found that a longer fiber used with a lower pump absorption coefficient showed a maximum temperature of 350°C (starting from room temperature). However, a longer fiber means more potential loss due to attenuation and scattering effects. They were able to create and operate a fiber in ambient air conditions, showing that while thermal effects in fibers need to be considered, future design innovation and optimization will almost certainly allow fibers to operate at the kW level with very little to no use of active cooling.

Shao et al.³³ looked at the temperature dependence of fiber operation and how the fiber length changes to achieve the same amount of optical power out for a given pump power. They found if the pump power is 3000 W, the fiber must be around 16 m long instead of 12 m to achieve the same amount of optical power out. The work shows how even at higher power levels, fiber operation remains uninhibited by temperature effects for a change of 150°C .

Newell et al.³⁴ studied the possible temperature dependence of ytterbium ion absorption and emission cross sections. Their plots show slightly better absorption peaks in the cross sections at cryogenic temperatures (77K) with a slightly decreasing trend up to 443K. Overall, they found temperature sensitive lasing occurs for smaller wavelength, where the changes in cross section absorption and emission are more significant. However, for wavelengths in the range of 1050 - 1080 nm, the lasing remains largely insensitive to temperature.

Lv et al.³⁵ presented a detailed analysis of a fiber from a thermal perspective using thermal resistance networks. They were able to create a thermal modeling using the rate equations to

find the heat generated in each discrete volume and then apply thermal resistance networks to calculate the fiber temperature. The analytical method used for fiber temperature prediction was proven accurate with their experiment, as the error between analytic and experimental values was within 8.8%. The pump power levels were only around 5 W, but their thermal modeling methodology could be directly applied to kilowatt level fiber lasers.

Pump Diode Wavelength Shift:

Albalawi et al.³⁶ studied how pump wavelength shift affects the signal power out of a fiber. While keeping pump power constant, they found a 10% penalty given a pump center wavelength shift of -13/+10 nm. Hence, to keep the optical power level out of the fiber constant, the pump power needs to increase appropriately. This is not always an option, as pushing pump diodes beyond their normal operating envelope can significantly decrease their lifetime and degrade their optical power output/quality. From their work, a tolerable wavelength shift can be determined based on how much fiber signal power loss is acceptable for a certain application. Their work was experimental, not computer modeled. To capture this work with a model, the pump power spectrum needs to be found and tracked. As the pump spectrum changes due to center wavelength shift, it must be dynamically integrated with a model of fiber laser physics to see exactly how the pump spectrum change affects the optical power absorption/emission in the fiber.

Butt et al.³⁷ also looked at pump diode wavelength shift, but from a modeling/simulation perspective instead of the experimental side. They studied how the center wavelength shift affects optical output of the fiber gain media using a simplified fiber model (no rate equations). The work focused on what happens when pump diodes are provided the same cooling capacity, but they are oriented in various array configurations (more diodes thermally in parallel vs. more

in series). The simulation showed how certain diode array configurations produce more fiber optical power than others when accounting for the pump wavelength shift, as certain configurations allow for better temperature control given identical cooling capacity.

Butt et al.³⁸ builds on their previous work³⁷ by studying laser diode performance in-depth. The junction temperature change in a laser diode is what causes the center wavelength shift. In addition, the full width half maximum (FWHM) of laser diode output also changes with junction temperature, as do the diode slope efficiency and threshold current. The slope efficiency and threshold current have a direct effect on the optical power out of the laser diode. A change in junction temperature changes the pump output spectrum shape and the amount of optical power contained in the spectrum. Fiber gain media is doped and seeded to absorb pump light at a specific wavelength. If diode temperature is not adequately controlled and pump center wavelength/spectrum shifts, the fiber can no longer operate at its design point. Hence, optical power out of the fiber will drop. Diode temperature control is paramount when it comes to successfully operating a high-power fiber laser. From Butt et al.³⁸, like in Albalawi et al.³⁶, a certain tolerance can be determined to decide what is and is not an acceptable amount of wavelength shift based on the optical power decrease out of the fiber due to said wavelength shift. This allows for a more accurate understanding of the thermal requirements necessary to keep the diode temperatures within the optimal range (whatever it may be) for achieving the desired level of optical power output. It all depends on how much optical power loss from optimal is acceptable.

The work by Butt et al.^{37,38} is part of the work presented in this dissertation. They were included briefly here to highlight the limited number of publications in the wider academic literature on

the topic of modeling HPLS from a more thermal perspective. They will be discussed in more detail when appropriate.

Combining Optics:

The literature review conducted shows combining optics are much more of a laser beam propagation topic. There has been significant work done in analyzing what methods of beam combining are best, but they are not pertinent to the discussion here. Just know the two types are coherent and incoherent beam combining. The thermal side of combining optics are quite separate from the laser physics. In terms of optical power, the combining optics are normally considered to have a constant efficiency of greater than 90% and are not significantly affected by temperature. Hence, for modeling purposes, the combining optics will be lumped together with a set constant efficiency value to determine the exiting optical power levels.

Stachowiak et al.⁸¹ achieved transmissions of 94.3% through the combining of five individual multimode fibers. Lei et al.⁸² attained a transmission of 98.5% from combining 7 Yb+ doped fibers, each outputting 2 kW for a total of ~14 kW of combined optical power. Yang et al.⁸³ provides an algorithm for modeling incoherent beam combining. Lei et al.⁸⁴ provides a review of the taper fused side pump combining method. Various research therein has accomplished a transmission through the combiner of ~96% efficiency. Sprangle et al.⁸⁵ provide a detailed explanation of the difference and advantages/disadvantages of incoherent combining vs. coherent combining, as well as an additional look at HPLS applications in the military. Bai et al.⁸⁶ describes a theoretical analysis of how the combining of individual fiber laser beams can significantly degrade the beam quality out of the combining optics. They include detailed explanations of how the irradiance is very important in effective beam combining. Chen et al.⁸⁷ calculates a possible combining efficiency of 94.6%. Their method is a novel way of using an

analytical model to investigate key parameters pertinent to enhancing the overall combining efficiency.

For the HPLS model in the research herein, three variables will be considered for the efficiency of the combining optics: Beam director, optical training mirrors, and aperture sharing element (η_{BD} , η_{MR} , and η_{ASE} respectively). The three parameters are multiplied together to give an overall efficiency value accounting for losses in the combining optics.

Cladding Light Stripping:

Getting rid of the excess pump light in the cladding at the end a fiber is very important, as the extra fluorescence needs to be taken away so it doesn't damage the area in which the fiber laser system is housed. The excess pump light is converted to heat by the cladding light stripper and needs to be removed. The literature review below provides insight into the amount of power that can be successfully stripped out of a single fiber, as this directly pertains to understanding all the heat generation in a fiber laser system.

Wetter et al.³⁹ demonstrated a cladding light stripper (CLS) capable of stripping 80 W of pump light without disrupting the signal light in the core. The stripper is a device put on the end of the fiber. It has varying NA values and, when coupled to the fiber properly, takes away the cladding light while leaving light in the core uninterrupted. It is a delicate process requiring precise manufacturing and installation pertaining to the stripping device. The inner temperature of the stripping device increased at a rate of 0.4°C per watt of heat dissipated.

Poozesh et al.⁴⁰ were able to get rid of 90 W of pump light, while keeping the stripping device temperature below 53°C through the use of a copper heat sink. The cooling system for the copper heat sink was set to flow water at a constant 20°C. The cladding pump light was removed

nearly uniformly. They used high refractive index materials to strip the light, as well as low/high refractive index polymers to recoat the fiber. The stripping device gets quite hot, as is expected, and thermal management is an important consideration.

Guo et al.⁴¹ used a cascaded light stripping technique to extract cladding light power levels of up to 150 W. They were able to achieve a maximum temperature in the stripper of 64°C, showing reasonable thermal control. Their method is simplistic in nature, and they anticipate the configuration will offer a practical solution for cladding light extraction for high power fiber laser applications.

Yan et al.⁴² created a stripper capable of removing over a kilowatt of cladding pump light. The stripper had 4 stages, gradually increasing the NA to the point where cladding light was removed and only the fiber core signal remained. This required four separate heat sinks. The 1.451 NA index stage of the stripper removes most of the cladding light (CLS B and C in Fig. 9 of Yan et al.⁴²). The heat sink temperatures did not go above 35°C. After the stripping, 1187 W of cladding pump light was reduced to just 2.6 W.

Zou et al.⁴³ fabricated a 150 mm long CLS for KW level operation. The device was able to strip up to 1.01 kW of pump light, with a temperature rise of just 0.05°C per watt of power stripped. The maximum temperature of the device was 78°C, and the stripped power density across the entire cladding light stripper was 7.165×10^6 W/m². They used a fan to provide forced cooling with ambient air at around 20°C. Unlike the work in Poozesh et al.⁴⁰, water cooling was not needed. Their work shows how continued research in CLS technology could lead to a design requiring little to no active thermal management.

Yan et al.⁴⁴ presented a CLS with 3 segments and tested based on several different coatings for each. Their results show a stripped pump light value of 438 W with a maximum temperature of 39.5°C. They provide an assumed heat transfer coefficient for the environmental conditions of 50 W/m² K, equating most likely to forced convection with ambient air. Using the heat conduction equation is useful in understanding the temperature distribution in the coating, and ultimately yields the thermal requirements to keep the CLS maximum temperature within a reasonable range.

There are many more research articles looking at experimental fiber laser operation. The ones listed here are the most well-known and acknowledged literature. The literature review contains many parameter values, from lasing wavelength to operating temperatures found through the use of applied heat conduction equations. Fiber specifications like the size of the core and cladding are given as well, and such parameters are very important to the fiber performance. Along with many others, these parameters are of great importance when it comes to modeling and simulating fiber laser performance. However, the literature is absent of what parameters are needed to accurately model laser output from a thermal perspective. The literature review contains many terms very specific to fiber gain media. The terms are further defined and explained in the fiber gain media section of this document. The fiber laser topic is very term-heavy, and it requires extensive specified knowledge to understand what is being said. Throughout the document, where appropriate, terms are defined and explained. Please view the fiber gain media section for a complete discussion of the concepts briefly presented in the above literature review. After an exhaustive search, practically no literature was found on modeling/simulation of fiber lasers, showing a gap does indeed exist in the literature when it comes to modeling/simulation of fiber laser performance and optical/thermal interactions.

Hence, the proposed research for this dissertation is well posed to bridge the aforementioned gap existing in current literature by way of studying high power fiber lasers from an optical/thermal interaction perspective in a modeling/simulation environment instead of an experimental environment.

5. HPLS Model Development/Explanation:

As per the review of laser physics (see Appendix E), the important laser components to be modeled have been investigated from a more thermal perspective. The next step is to create an HPLS model in Simulink with the three main laser components: laser diodes, fiber gain media, and combining optics. From a thermal perspective, four parameters of a laser diode, in addition to junction temperature are important: Center wavelength, FWHM, threshold current characteristic temperature, and slope efficiency characteristic temperature. Center wavelength and FWHM are used to define the output spectrum of the laser light, whereas the characteristic temperatures are used to find threshold current and slope efficiency, respectively, as functions of junction temperature. The optical power out of the laser diode as a function of junction temperature can then be calculated. As per the literature review, fiber efficiency is not temperature dependent until the fiber sees a rise of 100°C from the ambient temperature. Models for both laser diode temperature and fiber temperature estimation are created and presented later on. As for the combining optics, it is sufficient, modeling-wise, to assume a constant efficiency of combining components like beam directors and mirrors.

Figure 3 is a diagram of the optical train modeled. Laser light is generated in the diodes and then launched into the fibers. The pump light is absorbed and emitted in the fiber, and then fiber output is combined by the combining optics and leaves the system as a single beam containing a certain amount of optical power. Figure 3 will be explained more throughout the text.

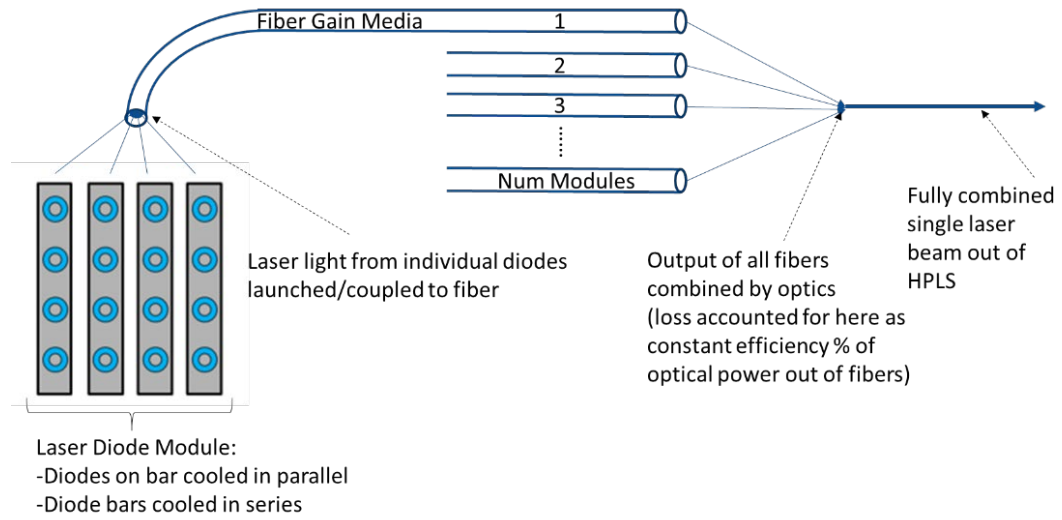


Figure 3: Optical train diagram of proposed HPLS model

In order to model the optical train from both an optical and thermal perspective, four models are needed: Diode Optical, Fiber Optical, Diode Thermal, and Fiber Thermal. A diagram is provided in Figure 4. Here, the heat sink temperature T_m is used as an estimation of the actual diode junction temperature T_j , as T_j is very challenging to calculate (see Appendix E for further explanation). Each model will now be discussed in detail.

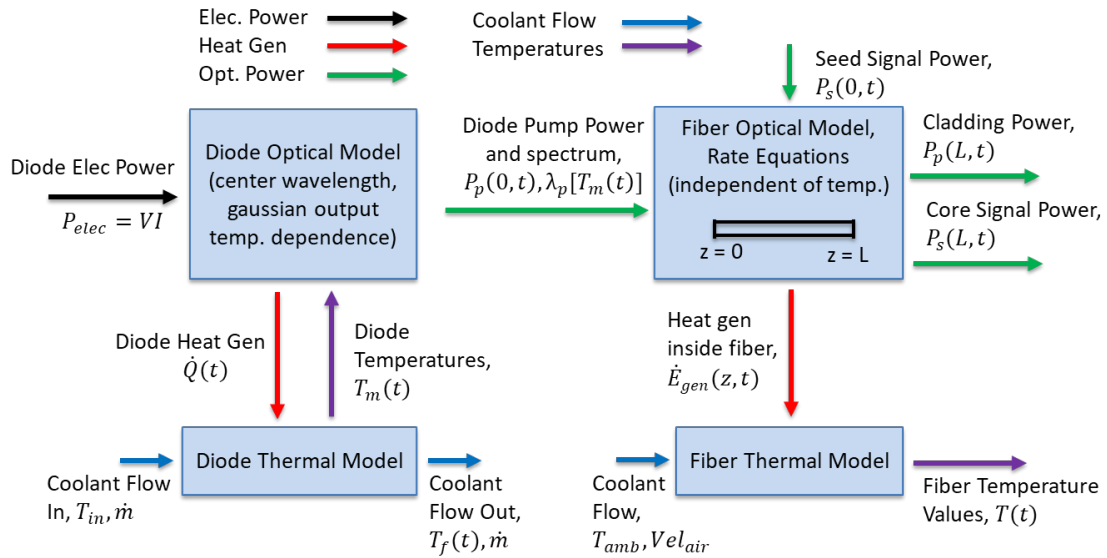


Figure 4: Diagram of all coupled models for entire laser system

Laser Optical Model:

The diode optical model is where pump light is produced. The model requires electrical power and diode temperatures as inputs and outputs diode pump power/spectrum data and diode heat generation. Note the heat generation term will be addressed in the diode thermal model section. A separate diagram is shown in Figure 5.

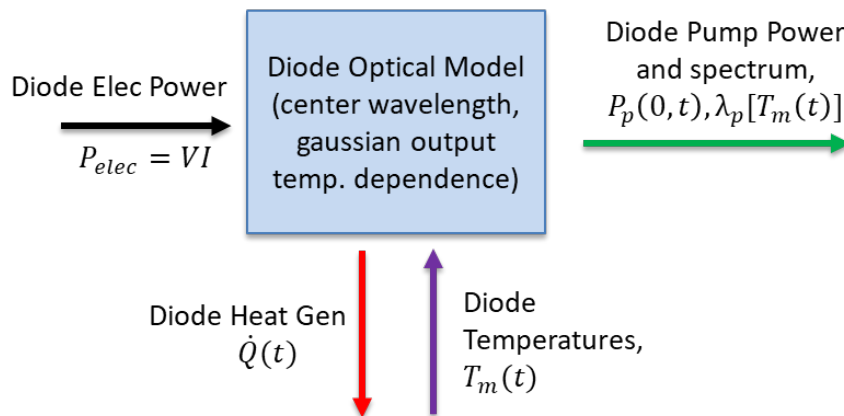


Figure 5: Diagram of laser optical model

Butt et al.^{37,38} looks at the details of the laser diode model and explains the model development.

Laser diodes are put in arrays, as shown in Figure 6.

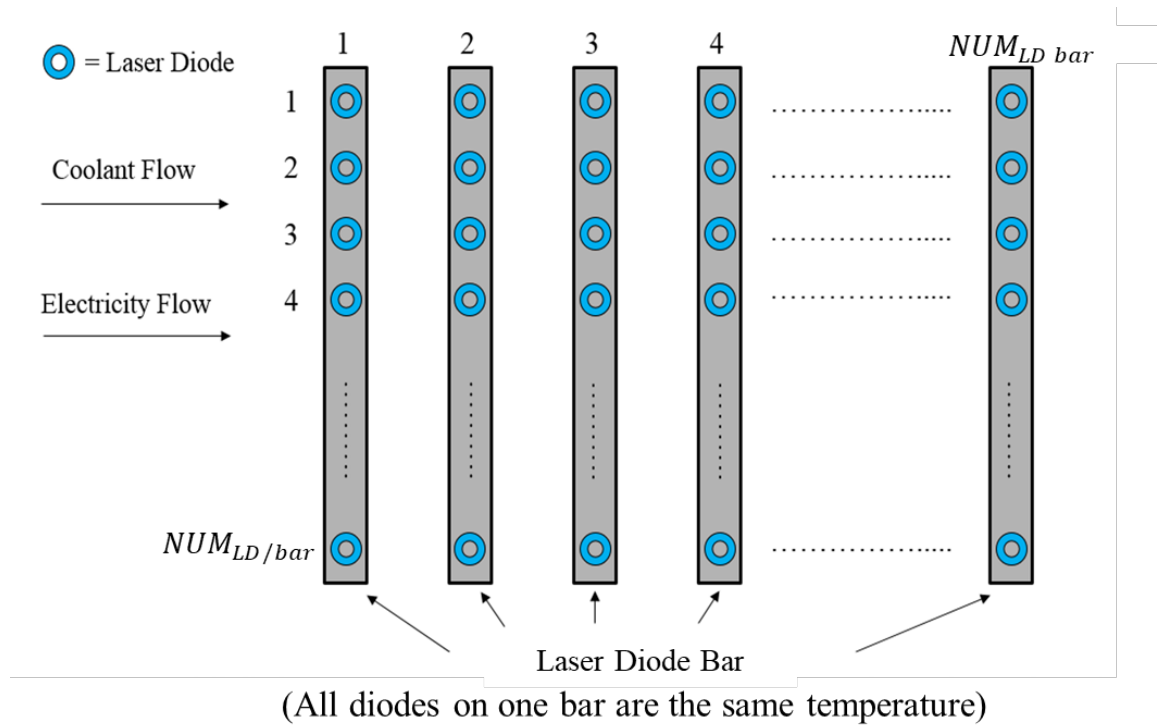


Figure 6: Laser diode array diagram³⁷

From a modeling/simulation point of view, the above representation is preferred because it is easier to keep track of parameters. Since the diode bars are cooled in parallel, all the diodes on a single bar are assumed to be the same temperature at any given time. A diode array contains a certain number of diodes in series and a certain number in parallel. For example, a 5 x 5 array contains 25 diodes. Hence, a single diode array has a certain optical power output. To reach the desired optical power level for the HPLS, just use the appropriate number of modules as shown in Figure 7.

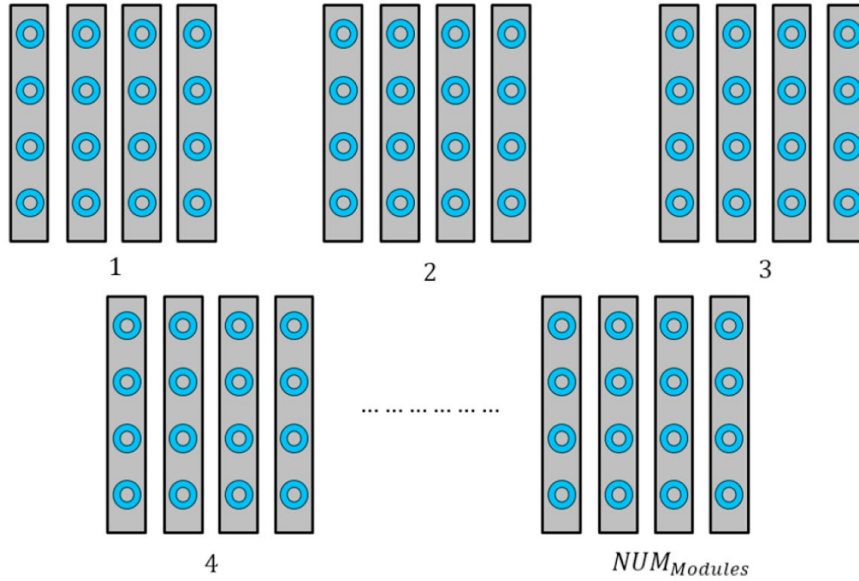


Figure 7: Laser diode module diagram³⁷

Appendix A shows reprinted data from Butt et al.³⁸ to explain the process used in the model to calculate laser diode output. The methodology and equations behind the model are presented and explained here.

Many parameters are needed to run the temperature dependent laser system model. They are provided in Appendix A and a few are listed here in Table 1.

Table 1: Laser Diode Model Parameters³⁸

Parameter – Definition
$T_{ref\ LD}$ – Reference Temperature for Laser Diode Characteristics (K)
$\lambda_{center\ LD\ nom}$ – Nominal Center Wavelength of Laser Diode Output at $T_{ref\ LD}$ (m)
$\lambda_{fwhm\ LD\ nom}$ – Nominal Full Width Half Maximum of Laser Diode Output (m)
$d\lambda/dT$ – Wavelength Temperature Coefficient for Laser Diode (m/K)
$d\beta/dT$ – Spectral Width Temperature Coefficient for Laser Diode (m/K)
$I_{th,ref}$ - Threshold Current Reference (A)
I_{max} – Max Current per Laser Diode (A)
V_{max} – Max voltage per Laser Diode (V)
$Power_{per\ LD,ref}$ – Reference optical power out per laser diode (W)
T_0 – Threshold Current Characteristic Temperature (K)
T_1 – Slope Efficiency Characteristic Temperature (K)
$NUM_{LD/bar}$ – Number of Laser Diodes per Bar (diodes thermally in parallel)
$NUM_{LD\ bars}$ – Number of Laser Diode Bars (diodes thermally in series)
$Power_{optical}$ – HPLS Design Optical Power from Laser Diodes (W)
$Power_{wall\ plug}$ – HPLS Wall Plug Power (W)

From these input parameters, all other needed values can be calculated. The equations that follow will define the process by which the model does calculations to find the laser diode efficiency.

There are more input variables that must be determined before the calculations start, and the

parameters from Table 1 are used to find these other input variables, shown in equations 1 through 8.

$\eta_{LD\ slope,ref}$ – Laser diode slope efficiency reference value (W/A)

$$\eta_{LD\ slope,ref} = \frac{Power_{per\ LD,ref}}{(I_{max}-I_{th,ref})} \quad (1)$$

I_{HPLS} – Current to Laser Diodes (Amps)

$$I_{HPLS} = I_{max} * NUM_{LD/bar} \quad (2)$$

V_{HPLS} – Voltage to Laser Diodes (Volts)

$$V_{HPLS} = \frac{Power_{wall\ plug}}{I_{HPLS}} \quad (3)$$

$V_{per\ LD}$ – Voltage per Laser Diode (Volts)

$$V_{per\ LD} = \frac{V_{HPLS}}{NUM_{LD\ bars}} \quad (4)$$

$Power_{per\ LD,elec}$ – Electrical Power per Laser Diode (W)

$$Power_{per\ LD,Elec} = V_{per\ LD} * I_{max} \quad (5)$$

$\eta_{LD,max}$ – Max Laser Diode Efficiency

$$\eta_{LD,max} = \frac{Power_{per\ LD,ref}}{Power_{per\ LD,Elec}} \quad (6)$$

$NUM_{Modules}$ – Number of laser diode modules in system

$$NUM_{Modules} = \frac{Power_{optical}}{Power_{per\ LD,ref} * NUM_{LD\ bars} * NUM_{LD/bar}} \quad (7)$$

NUM_{Diodes} – Total number of laser diodes in system

$$NUM_{Diodes} = NUM_{LD\ bars} * NUM_{LD/bar} * NUM_{Modules} \quad (8)$$

With all these variables defined and preliminary calculations solved, the model can now use these values to do the actual optical power production calculations. There is no power conditioning model here. The optical power out of each laser diode bar is first calculated. From this, the amount of heat generated from the laser diodes can be found. Next, the center wavelength and spectral width of each bar is calculated. Following this, the Gaussian Curve mathematics are used to represent the laser beams and find the Gaussian Curve spectrum profiles for one diode bar over a range of wavelength values. The Gaussian Curve profiles for each bar are then added together. The total optical power out of the laser diodes is the area under the curve of all the bar profiles added together. Equations 9 through 17 below outline this process. The equations are presented in order so the process of calculations can be easily followed.

The junction temperature dependent parameters for optical power are first calculated.

$I_{th}(T_j(x, t))$ – Threshold current based on junction temperature. The variable $T_j(x, t)$ is the laser diode junction temperatures. The variable x in all equations goes from 1 to $NUM_{LD\ bars}$ to represent all the bars.

$$I_{th}(T_j(x, t)) = I_{th,ref} e^{\left(\frac{T_j(x,t)-T_{ref}}{T_0}\right)} \quad (9)$$

$\eta_{slope}(T_j(x, t))$ – Slope efficiency based on junction temperature

$$\eta_{slope}(T_j(x, t)) = \eta_{LD\ slope,ref} e^{-\left(\frac{T_j(x,t)-T_{ref}}{T_1}\right)} \quad (10)$$

Now the optical power out of a single diode bar can be found.

$Power_{LD\ bar}(x, t)$ – Optical Output Power of the Laser Diode bars. Each value x is the power of $NUM_{LD/bar}$ diodes for each diode bar.

$$Power_{LD\ bar}(x, t) = \left[\eta_{slope}(T_j(x, t)) \left(I_{max} - I_{th}(T_j(x, t)) \right) \right] * NUM_{LD/bar} \quad (11)$$

$\lambda_{center\ LD}(x, t)$ – Center Wavelength of each bar. The variable $T_j(x, t)$ is the laser diode junction temperatures. The variable x goes from 1 to $NUM_{LD\ bars}$ to represent all the bars.

$$\lambda_{center\ LD}(x, t) = \lambda_{center\ LD\ nom} + \left((T_j(x, t) - T_{ref\ LD}) * d\lambda/dT \right) \quad (12)$$

$\lambda_{FWHM\ LD}(x, t)$ – Spectral width (FWHM) of each bar. $T_j(x, t)$ is the laser diode junction temperatures. The variable x goes from 1 to $NUM_{LD\ bars}$ to represent all the bars.

$$\lambda_{FWHM\ LD}(x, t) = \lambda_{FWHM\ LD\ nom} + \left((T_j(x, t) - T_{ref}) * d\beta/dT \right) \quad (13)$$

$C_{value\ LD}(x, t)$ – C Value for Laser Diode Gaussian Profile (spectral width).

$$C_{value\ LD}(x, t) = \frac{\lambda_{FWHM\ LD}(x, t)}{2\sqrt{2 \ln(2)}} \quad (14)$$

$A_{value\ LD}(x, t)$ – A Value for laser diode bar Gaussian profile (peak at center wavelength). The integral is the area under the Gaussian curve with a peak equal to 1. In considering laser diode optical power from a spectral power density perspective, the optical power out is synonymous with the area under the gaussian curve. The area (optical power) required under a curve with peak $A_{value\ LD}$ divided by the area (optical power) under a curve with a peak of 1 yields the peak $A_{value\ LD}$ required to achieve the area (optical power) required.

$$A_{value\ LD}(x, t) = \frac{Power_{LDbar}(x, t)}{\int_{\lambda_{center\ LD} - \lambda_{fwhm\ LD} * 10}^{\lambda_{center\ LD} + \lambda_{fwhm\ LD} * 10} \exp\left(\frac{-(\lambda - \lambda_{center\ LD}(x, t))^2}{2(c_{value\ LD}(x, t))^2}\right) d\lambda} \quad (15)$$

$Gaussian_{LD\ bar}(x, t)$ – Actual Gaussian Curve profiles for each diode on a single bar.

$$Gaussian_{LD\ bar}(x, t) = A_{value\ LD}(x, t) * \exp\left(\frac{-(\lambda - \lambda_{center\ LD}(x, t))^2}{2(c_{value\ LD}(x, t))^2}\right) \quad (16)$$

Here, λ ranges from 0 to 1500 nm (or whatever range is required) for each x. A Gaussian curve for each bar can be obtained and graphed. Each bar contains $NUM_{LD/bar}$ diodes. The Gaussian curve for one bar is this number of diode Gaussian curves added together, as the power used to find the Gaussian curve peak ($A_{value\ LD}$) for each bar is the combined power of all diodes on that one bar, again assuming the bar/junction is uniform in temperature.

$Gaussian_{all\ bars}(t)$ – Gaussian Curve for all Bar Profiles added together to form one curve. It is the output curves of all laser diodes added together to make a single curve. This value contains the spectrum/optical power launched into a single fiber.

$$Gaussian_{all\ bars}(t) = \sum_{x=1}^{NUM_{LD\ bars}} Gaussian_{LD\ bar}(x, t) \quad (17)$$

$Power_{optical\ LD}(t)$ – Total optical power out of all laser diodes, area under $Gaussian_{all\ bars}(t)$.

The main value of concern from the laser diode calculations is $Power_{optical\ LD}(t)$. This is the value, along with $Gaussian_{all\ bars}(t)$, that cascades into the next set of computations for the fiber gain media. All electrical power not converted to optical power by the laser diodes is

considered lost as heat. The optical power out of the laser diodes is the input optical power to the fiber gain media.

Table 2 shows a compilation of literature values for T_0 and T_1 of certain laser diode types with a particular nominal center wavelength output. Notice how the T_0 parameter has been studied and researched much more widely than the T_1 parameter.

Table 2: Characteristic temperature values from literature

Wavelength (nm)	Type	T0 (K)	T1(k)	Source
400	GaN	-360		[65]
400	GaN	129		[65]
500	InGaN	180		[54]
670	AlGaInP	114		[64]
700		<100		[46]
808		176	681	[50]
808		140		[46]
980		200		[46]
980	GaAs/InAs	101		[58]
1280	InGaAs	130		[62]
1300	InAs	∞		[60]
1310	InGaAs	95		[62]
1470	InGaAsP/InP	98		[61]
1470	InGaAsP/InP	126		[61]
1500	InAs/InGaAsP	235	205	[63]
1520	InAs	102		[56]
1529	InAs	113		[55]
1550	InAs	51		[57]
1550	InAs	91		[57]
1550	InAs	116		[57]
1550	InAs	148		[57]
1550	GaAs	210		[59]
1550	GaAs	52		[59]

Table 3 shows the $d\lambda/dT$ and $d\beta/dT$ values compiled together from several literature sources.

Notice how much more research has been done on the wavelength shift temperature coefficient than the spectral width shift temperature coefficient.

Table 3: Wavelength and spectral width coefficient values from literature

Wavelength (nm)	Type	$d\lambda/dT$ (nm/K)	$d\beta/dT$ (nm/K)	Source
670	AlGaInP	0.115	0.0056	[64]
808		0.25		[93]
808		0.27		[72]
808		0.28		[67]
930	GaAs	0.3	0.0884	[14]
980		0.32		[68]
980	GaAs/InAs	0.367		[58]
1300	GaInNAs	0.42		[69]

Using $d\lambda/dT$ to represent the wavelength temperature coefficient is the notation used throughout the laser community as seen in several references (see Kim et al.¹⁴, Fan et al.⁶⁷, Hu et al.⁶⁸, and Kondow et al.⁶⁹). The same goes for $d\beta/dT$. This concludes an explanation of the laser diode component model in the over-arching HPLS model. See Appendix E for further explanation of the fundamental physics behind laser diode operation and modeling laser diode output in the described manner.

Fiber Optical Model – Rate Equations:

The fiber optical model diagram is shown below in Figure 8. It requires diode pump power/spectrum data and seed signal power as inputs and outputs cladding pump power, core signal power, and heat generated inside the fiber.

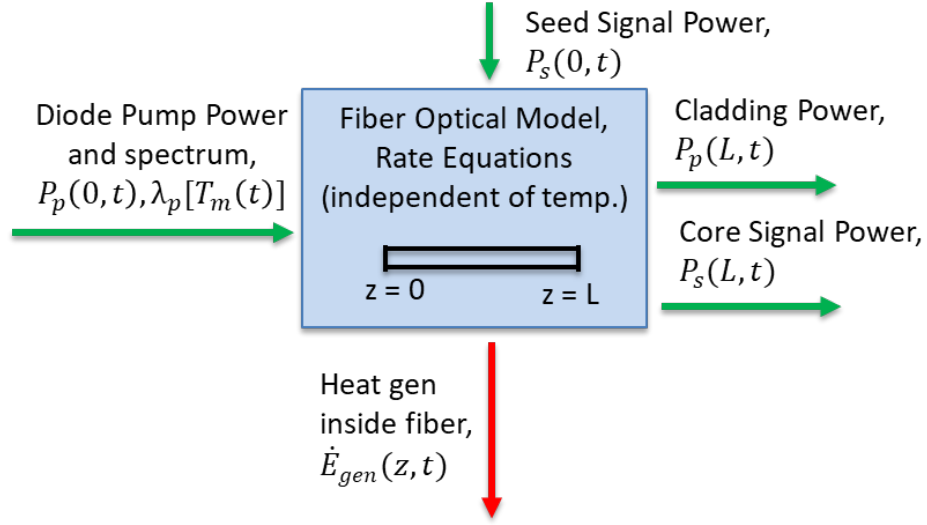


Figure 8: Diagram of fiber optical model

Optical power propagating through a fiber can be described by the rate equations, a system of four equations (shown in equations 18 through 21) calculating the upper-level population state, ground level population state, pump power in the fiber cladding, and signal power in the fiber core. The equations are 1st order PDEs and can be readily solved using a Runge-Kutta method. The rate equations have been well defined and used in several sources^{11,13,33,35,76,88-91}. Newer work by Yi et al.³⁵, Shao et al.³³, Li et al.¹¹, and Wang et al.¹³ all cite the rate equations defined in two research articles by Kelson et al.⁸⁸ and Kelson et al.⁸⁹. Kelson and Hardy cite Hardy et al.⁹⁰, Paschotta et al.⁷⁶, and Dignonnet⁹¹. Hence, the rate equations used have been peer reviewed many times as seen by tracing the citations, and they are well accepted.

$$\frac{N_1(z,t)}{N_{tot}} = \frac{[\sigma_{ap}\Gamma_p\lambda_p[T_j(x,t)]P_p(z,t)/(hcA_{core}) + \sigma_{as}\Gamma_s\lambda_sP_s(z,t)/(hcA_{core})]}{[(\sigma_{ap} + \sigma_{ep})\Gamma_p\lambda_p[T_j(x,t)]P_p(z,t)/(hcA_{core}) + (\sigma_{as} + \sigma_{es})\Gamma_s\lambda_sP_s(z,t)/(hcA_{core}) + (1/\tau)]} \quad (18)$$

$$N_{tot} = N_0(z, t) + N_1(z, t) \quad (19)$$

$$\frac{\partial P_p(z,t)}{\partial z} = \Gamma_p (\sigma_{ep}N_1(z, t) - \sigma_{ap}N_0(z, t)) P_p(z, t) - \alpha_p P_p(z, t) \quad (20)$$

$$\frac{\partial P_s(z,t)}{\partial z} = \Gamma_s(\sigma_{es}N_1(z,t) - \sigma_{as}N_0(z,t))P_s(z,t) - \alpha_s P_s(z,t) + 2\sigma_{es}N_1(z,t)\frac{hc^2}{\lambda_s^3}\Delta\lambda \quad (21)$$

In equations 18 through 21, there are many variables to understand. The complexity of the rate equations, however, is easily overcome through complete understanding of what each variable represents and what each term in the equations physically means. In equation 18, $\lambda_p[T_j(x,t)]$ is the value calculated in equation 17. It is the term coupling the laser diode and fiber physics models, showing how a change in diode junction temperature translates to a change in pump power center wavelength spectrum, which in turn changes the optical power calculations in the rate equations. Recall, T_j is interchangeable with T_m .

Table 4 provides definitions for all variables used in the rate equations. Each variable is defined in the context of fiber gain media.

Table 4: Variable definitions for rate equations

Parameter	Definition
L	Fiber length
z	Longitudinal position along the fiber (vector from 0 to fiber length L , discretized)
N_{tot}	Total population density of doping ions
$N_1(z,t)$	Upper-level population density (function of longitudinal location in fiber z)
$N_0(z,t)$	Lower-level population density (function of longitudinal location in fiber z)
$\lambda_p[T_j(x,t)]$	Pump wavelength spectrum (vector based on wavelength spectral power density of input pump spectrum)
$T_j(x,t)$	Diode temperature vector, used to calculate $\lambda_p[T_j(x,t)]$ as per equations 9 - 17
λ_s	Signal wavelength (vector based on desired signal wavelength range)
$\Delta\lambda$	Signal bandwidth
σ_{ap}	Pump absorption cross-section of doping ions based on λ_p
σ_{ep}	Pump emission cross-section of doping ions based on λ_p
σ_{as}	Signal absorption cross-section of doping ions based on λ_s
σ_{es}	Signal emission cross-section of doping ions based on λ_s

Γ_p	Fraction of pump power coupled to active core (pump power filling factor)
Γ_s	Fraction of signal power amplified in active core (signal power filling factor)
$P_p(z, t)$	Pump power remaining in cladding (function of longitudinal location in fiber z)
$P_s(z, t)$	Signal power absorbed into core (function of longitudinal location in fiber z)
α_p	Fiber attenuation coefficient for pump (cladding)
α_s	Fiber attenuation coefficient for signal (core)
τ	Spontaneous lifetime of doping ions at the upper level
A_{core}	Cross sectional area of fiber core, based on core radius r_{core}
A_{clad}	Cross sectional area of fiber cladding, based on cladding radius r_{clad}
h	Planck's constant (6.626e-34 J.s)
c	Light velocity in a vacuum (2.997e8 m/s)

Table 4 provides definitions for all variables used in the rate equations. Each variable is defined as clearly as possible in the context of fiber gain media. Some variables in Table 4 can be grouped together into new quantities to make equation 18 less complex. Pump photon energy and signal photon energy can be defined as

$$Ph_p = hc/\lambda_p[T_j(x, t)] \quad (22)$$

$$Ph_s = hc/\lambda_s \quad (23)$$

Hence, equation 18 becomes

$$\frac{N_1(z, t)}{N_{tot}} = \frac{[\sigma_{ap}\Gamma_p P_p(z, t)/(Ph_p A_{core}) + \sigma_{as}\Gamma_s P_s(z, t)/(Ph_s A_{core})]}{[(\sigma_{ap} + \sigma_{ep})\Gamma_p P_p(z, t)/(Ph_p A_{core}) + (\sigma_{as} + \sigma_{es})\Gamma_s P_s(z, t)/(Ph_s A_{core}) + (1/\tau)]} \quad (24)$$

The pump power filling factor Γ_p can be defined approximately by the ratio of the cross-sectional area of the core over the cross-sectional area of the cladding⁸⁸, as shown in equation 25.

$$\Gamma_p = A_{core}/A_{clad} \quad (25)$$

The core and cladding cross sectional areas are found from the core and cladding respective radii in equations 26 and 27.

$$A_{core} = \pi r_{core}^2 \quad (26)$$

$$A_{clad} = \pi r_{clad}^2 \quad (27)$$

All the variables in Table 4 are based on using Ytterbium (Yb) as the doping element for the fiber core. Typical values for some important parameters are given in Table 5. Parameter values can vary significantly, as most are determined during fiber fabrication and design.

Table 5: Various parameter values for rate equation

Parameter	Value(s)	Source(s)
L	30 m, 60m	[17], [11]
N_{tot}	4e25, 5.93e25, 1.02e26 m ⁻³	[88], [92], [92]
α_p	2e-3, 3e-5	[11], [88]
α_s	4e-4, 5e-5	[11], [88]
Γ_s	0.82, 0.85, 0.90	[11], [88], [28]
r_{core}	11.5, 16, 10, 10, 10 μm	[17], [11], [28], [18], [31]
r_{clad}	230, 300, 200, 200, 200 μm	[17], [11], [28], [18], [31]
τ	0.6e-3, 1e-3, 0.8e-3 sec	[11], [88], [28]

Fiber Optical Model – Heat Generation:

Fiber lasers generate heat from two main sources: quantum defect and unabsorbed cladding pump light, which needs to be stripped away. Unabsorbed cladding pump light does not deposit any heat in the fiber. Quantum defect is defined as the energy (or heat) lost from converting

pump photons to signal photons and can be estimated by the difference in the optical power levels going into and leaving the fiber. First, consider the definition of Stokes factor η_s , shown in equation 28 (eqn 5-7 in Motes et al.³²).

$$\eta_{stokes} = \frac{hc/\lambda_{s,nom}}{hc/\lambda_{p,nom}} = \frac{\lambda_{p,nom}}{\lambda_{s,nom}} \quad (28)$$

Here, $\lambda_{p,nom}$ and $\lambda_{s,nom}$ are the nominal wavelengths of pump and signal light respectively. The Stokes factor is the maximum possible fiber slope efficiency. Slope efficiency is the change in signal light emitted over the change in pump light absorbed. Since a Yb³⁺-doped fiber laser is typically pumped with a signal wavelength of 976 nm and has a signal wavelength of 1064 nm, it has a maximum possible slope efficiency (Stokes factor) of 91.7%. The actual slope efficiency of a fiber (different from the laser diode slope efficiency) at any point in time is given by equation 29, coming from Motes et al.³².

$$\eta_{slope}(t) = \frac{\Delta P_{s,out}}{\Delta P_{p,abs}} = \frac{P_s(L,t) - P_s(0,t)}{P_p(0,t) - P_p(L,t)} \quad (29)$$

Above, $P_s(L, t)$ is the signal power at the fiber exit, $P_s(0, t)$ is the signal power at the fiber entrance (from seed laser), $P_p(0, t)$ is the pump power in the cladding at the fiber entrance, and $P_p(L, t)$ is the pump power remaining in the cladding at the fiber exit. $P_p(L, t)$ is not usable optical power and needs to be stripped away. Hence, it becomes a loss as heat. The slope efficiency will never be larger than the Stokes factor. Next, the optical-to-optical (O-O) efficiency is the signal power out of the fiber over the total optical power into the fiber, as defined in equation 30. The slope efficiency and O-O efficiency are not the same, even though their names are sometimes used interchangeably in literature. Note that O-O efficiency will never be larger than fiber slope efficiency.

$$\eta_{opt}(t) = \frac{P_s(L,t)}{P_s(0,t)+P_p(0,t)} \quad (30)$$

The rate equations provide insight into the heat generation due to photon conversion in the fiber core. However, it is not straight forward and not clearly described in the previous research cited earlier^{11,13,33,35,76,88-91}. A deeper dive into the rate equations is required to understand this. To start, information in Figure 9 explains what each quantity in the rate equations physically means.

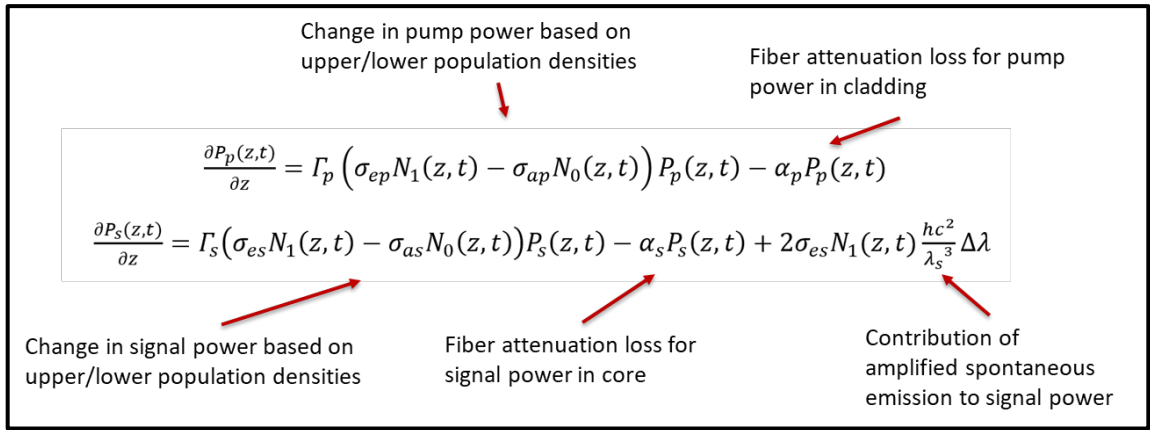


Figure 9: Explanation of rate equations terms

The change in pump/signal power is based on the upper and lower population densities of doping ions along the axial length of the fiber. Additionally, there are losses due to fiber attenuation in both the core (signal) and cladding (pump), in terms of power. The typical attenuation units of dB are not used as these terms are not measuring actual attenuation, but the power loss due to it. The right-hand side (RHS) of equations 20 and 21, called $RHS P_p$ and $RHS P_s$, represent the change in power as a function of fiber location z and time t . $RHS P_p$ is always negative. $RHS P_s$ is always positive. $RHS P_p$ is always larger in magnitude than $RHS P_s$. To understand what these terms actually represent, look at Figure 10.

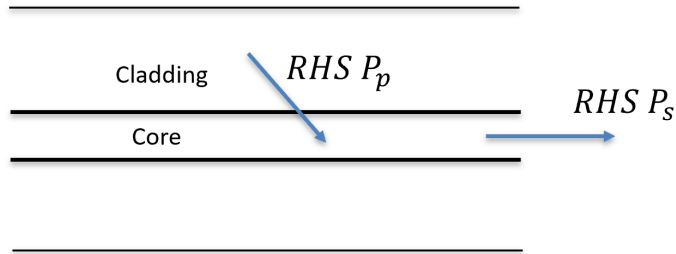


Figure 10: Diagram of how right-hand side (RHS) quantities are interacting with the fiber core

$RHS P_p$ is always negative because it signifies pump power leaving the cladding and moving into the core by photon conversion. $RHS P_s$ is always positive because it signifies an increase in signal power due to the converted pump power from $RHS P_p$. As an example, Figure 11 shows the $RHS P_p$ and $RHS P_s$ plots as a function of axial fiber location for an example steady state fiber of length 10.8 m being pumped by 5000 W of laser diode optical power with nominal output spectrum shape (perfect diode temperature control).

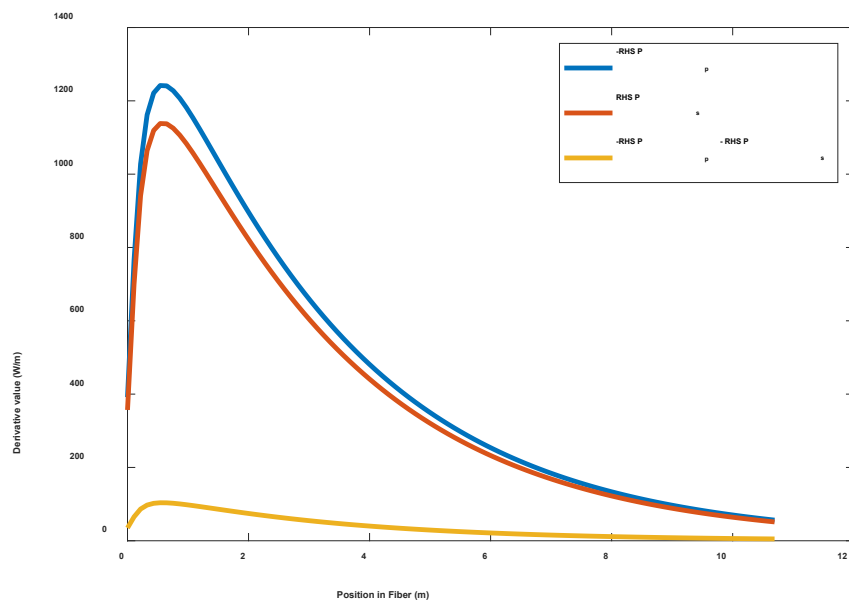


Figure 11: Diagram of how right-hand side (RHS) quantities are interacting with the fiber core

$RHS P_p$ is made negative here because it is originally leaving the cladding. The negative sign keeps with convention to show it entering the core, as per Figure 10. Taking the negative of $RHS P_p$ (blue line) and subtracting from it $RHS P_s$ (red line) will yield the difference between the two derivative quantities (yellow line). If this difference is not zero, it means the amount of pump power being converted to signal power is not equal. Since the negative of $RHS P_p$ is greater than $RHS P_s$, the discrepancy is positive. Call this quantity $\dot{E}_{gen}(z, t)$, defined as

$$\dot{E}_{gen}(z, t) = -RHS P_p - RHS P_s \quad (31)$$

Hence, $\dot{E}_{gen}(z, t)$ (the positive discrepancy between the two derivative quantities) can only be the heat generated inside the fiber at location z , as the rate equations presented here do not account for any other possible losses in the fiber. The profile shape is typical for an active fiber, as seen in research by Yu et al.²⁰. Figure 12 below shows the pump power P_p , signal power P_s , and amplified stimulated emission power (ASE) in the example fiber.

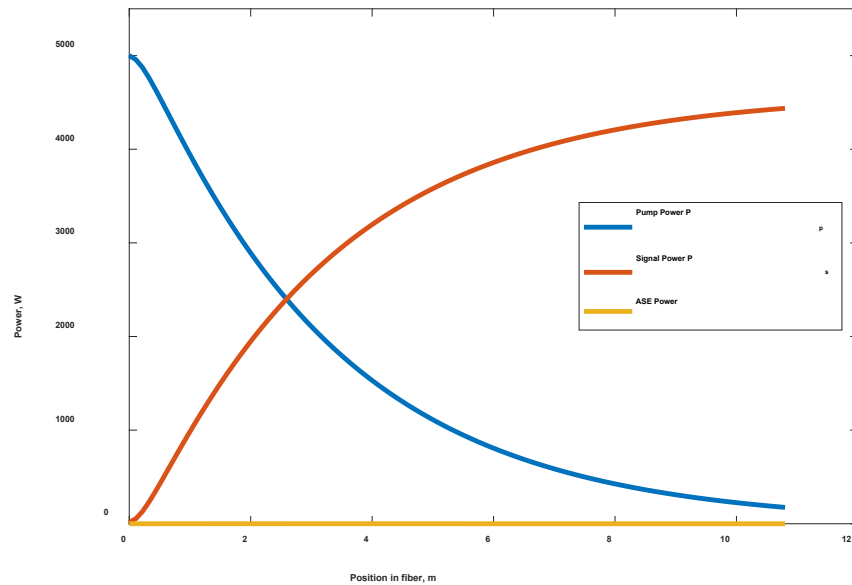


Figure 12: Diagram of how right-hand side (RHS) quantities are interacting with the fiber core

This plot shows how pump power decreases and signal power increases as a function of fiber position. ASE is important to track because it can be naturally produced when a fiber is pumped. It is an unwanted effect in lasers because it is incoherent and can negatively impact the fiber's ability to achieve maximum possible gain. For the realm of fiber operation considered in this research, ASE is not a factor and can be neglected. In the example of Figure 12, the max value of ASE power (yellow line) is 0.3 W. It does not pose a problem for fiber operation here.

In general, fiber lasers are easy to cool due to their large surface-area-to-volume ratio. For most situations, fibers operating even at the kilowatt level can be cooled just by flowing ambient air over them³². In addition, the beam quality and optical power output of a single mode fiber is mostly independent of gain media temperature (due to the core's support of only a single mode), so tracking fiber temperature is not a significant concern³². The fiber's O-O efficiency change is negligible when its temperature changes. It may just take a slightly longer fiber to

reach the same signal power level when accounting for temperature effects as per Fig. 6 in Shao et al.³³. Fiber gain media can operate at up to 100°C without degradation in optical power output³². Hence, fiber operation remains largely unaffected by temperature simply due to the nature of fiber geometry and materials. However, a thermal model for fiber temperature estimation will be presented later on in this research to show what is required to keep fiber temperatures from changing more than 100°C.

Diode Junction Temperature Estimation:

One thing remains: Obtaining an estimation of the laser diode junction temperature throughout laser activation. An academic and fundamental approach, presented here, is to simply create temperature profiles for the laser diode junction temperatures. The profiles can be created in such a way to show how the equations for laser physics/equations discussed here are properly implemented. The “mock” diode junction temperature profiles allow for study of the laser system without introducing the complexities of a thermal model. The diode thermal model created later for further investigation is presented in its own separate section.

In order to create the diode temperature profiles, lots of information can be gained from the laser diode manufacturer. The laser diode modeled in this research is the Northrop Grumman Golden Bullet. According to the spec sheet⁹³, it has nominal operating conditions when the heat sink temperature is kept at 298K (reference temperature). The nominal conditions include 200 Watts of optical power at 180 Amps, available nominal wavelengths of 790 to 980 nm, and wavelength shift ($d\lambda/dT$) of 0.25 nm/K. The operating temperature range is 258 to 368K. The Golden Bullet is considered to have a large optical power output for a single laser diode submodule, so it has attractive characteristics for use in high power applications.

Another reason the Golden Bullet was chosen is that experimental work has been done with it showing laser wavelength shift for a given thermal management system. Research by Schlenker⁷⁰ provides an experimental methodology of determining how effective a thermal control system is by observing the wavelength shift in an 808 nm Golden Bullet laser diode (tolerance of + or – 3 nm) at various points in time over a five second pulse. This was done for various levels of current provided to the diode. Other previous research^{37,38,45,49} shows the wavelength shift in a diode can be represented by the relation below.

$$\lambda_{center LD}(t) = \lambda_{center LD} + \left((T_j(t) - T_{ref}) * d\lambda/dT \right) \quad (32)$$

Here, $\lambda_{center LD}$ is the nominal center wavelength of the laser diode, T_{ref} is the reference temperature, and $d\lambda/dT$ is the wavelength temperature coefficient (nm/K). Also, $T_j(t)$ is the current junction temperature for the laser diode at time t and $\lambda_{center LD}(t)$ is the current center wavelength for the laser diode at time t based on the current junction temperature $T_j(t)$. See further explanation in Appendix E. Note how manufacturer spec sheet for the Golden Bullet specifies the reference temperature relative to the heat sink and not the diode itself, as diode junction temperature is very difficult to measure. Hence, the junction temperature T_j in equation 32 can be replaced with the heat sink temperature T_m . Junction temperature is constantly higher than heat sink temperature as per equation 76 in Appendix E and is assumed to change instantaneously with heat sink temperature for modeling/simulation purposes.

The research by Schlenker⁷⁰ does not investigate specific values for heat sink temperature. However, center wavelength values at various levels of current are provided. For current levels of 20, 60, and 100A, the center wavelengths of the diode output at five seconds were 803.6, 807.0, and 812.0 nm respectively. See Figure 13 below.

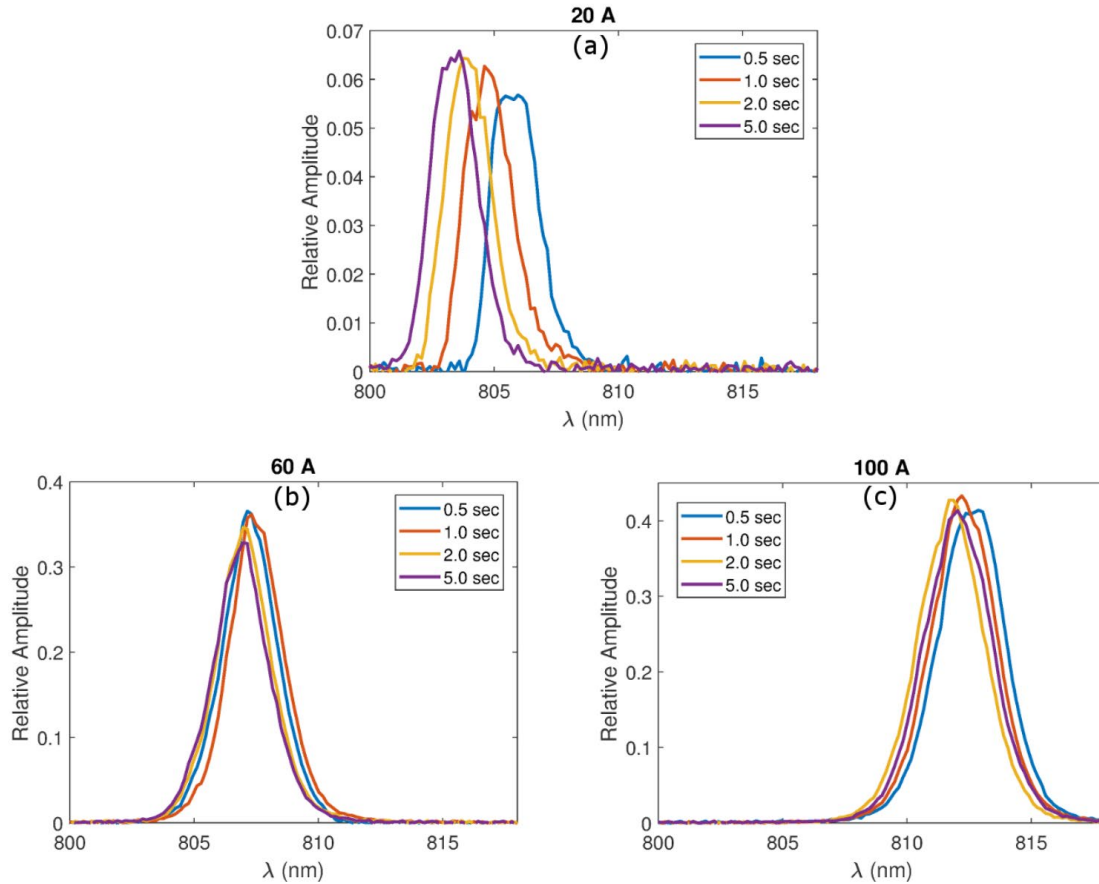


Figure 13: Golden Bullet spectrum output at various current levels⁷⁰

From the wavelength values at various levels of current, and plugging values from the spec sheet into equation 32, the heat sink temperatures for each level of current can be calculated. They are 278, 294, and 314K respectively. Bringing together Schlenker's research and the wavelength shift relation from equation 32 in such a manner provides a solid foundation on which to model the laser diode for use in this research, as now the mock temperature profiles can be based on the performance of an actual Golden Bullet laser diode. It is now known how much wavelength shift arises from a given temperature change not just based on the manufacturer spec sheet but from independent experimentation as well. Time to steady state is strictly dependent on the thermal management system controlling heat sink temperature. In Schlenker's work⁷⁰, the 100A

case seeing a heat sink temperature of 314K could be increased to the nominal 180A. The heat sink temperature could still be 314K if a more effective thermal management system was used. Hence, when creating the mock temperature profiles to represent heat sink temperature for testing the coupled laser diode and fiber models, the main thing to capture is the diode temperatures and not the time to steady state. The mock diode temperature profiles need to start at the heat sink reference temperature.

The mock temperature profiles are defined as follows. The diode array modeled will be 5 x 5, so five temperature profiles are needed to represent the five diode bars in series. The mock diode temperature profiles are given in Figure 14 for the entirety of the activation pulse to be used in the simulation. For the first 5 seconds, the diode bar temperatures are set to 298K. For the next 8 seconds, the bar temperature profiles come from the following formulations.

$$T_1 = 314 + \frac{(298 - 314)}{e^{1/2(t-5)}}$$

$$T_2 = 314.5 + \frac{(298 - 314.5)}{e^{1/2(t-5)}}$$

$$T_3 = 315 + \frac{(298 - 315)}{e^{1/2(t-5)}}$$

$$T_4 = 315.5 + \frac{(298 - 315.5)}{e^{1/2(t-5)}}$$

$$T_5 = 316 + \frac{(298 - 316)}{e^{1/2(t-5)}}$$

The equations here come from the response of typical 1st order dynamic systems. They simulate the temperature of the diodes rising to a certain value in a certain amount of time. From 13

seconds onward the, temperature profiles are set to 298K. Notice how the five temperatures average ~314K by the end of the activation pulse.

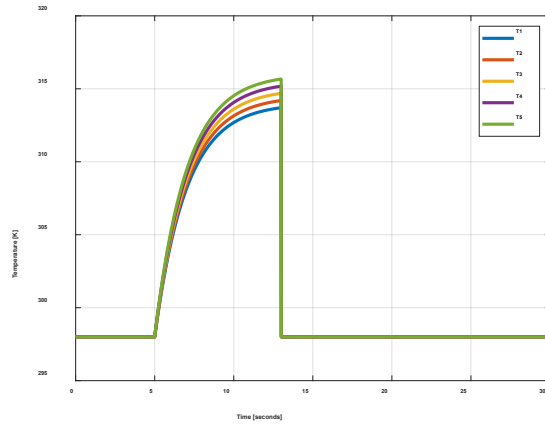


Figure 14: Mock temperature estimation profiles of the 5 diode bars (1, 2, 3, 4, 5) in a single (5x5) module throughout the activation pulse

6. HPLS Model Functionality:

In order to make certain the model is functioning properly and giving expected results, various test simulations were conducted to show performance results. Both the simplified fiber model proposed by Butt et al.³⁷ and the full fiber model with the rate equations are studied to show the differences between the two models. The main difference between the simplified model and the full fiber model is the simplified model had the maximum fiber optical-to-optical (O-O) efficiency as an input (see Appendix A). For the results here, the maximum fiber optical-to-optical efficiency was set to 80%. Additionally, it did not use the rate equations. The full fiber model actually calculates the maximum fiber optical-to-optical efficiency through the use of the rate equations. The mock diode temperature profiles (Figure 14) are used to simulate the changing junction temperatures and their effect on laser optical power output. They are based the same Golden Bullet laser diode used in research by Schlenker⁷⁰. For now, this is appropriate modeling to confirm proper laser operation. A set laser activation profile is used for all the simulations to maintain consistency for comparison. The design optical power for the simulation is 75 kW. The simulation models a laser diode based on the Golden Bullet by Northrop Grumman, as noted in Butt et al.³⁸. Values for some parameters including central wavelength, spectral width, threshold current, $d\lambda/dT$, and optical power at optimum operating conditions are taken from the Golden Bullet information sheet. Values for T_0 and T_1 are estimated from work by Bacchin et al.⁵⁰. Values for $d\beta/dT$ are taken from various sources^{93, 14}. The combining optics efficiency is set to a combined 84% for the beam director, mirrors, and aperture sharing element.

HPLS Performance – Simplified Fiber Model:

In the results shown here, the fiber model used is a simplified concept proposed by Butt et al.³⁷ and used again in Butt et al.³⁸. An explanation of the simplified model, along with parameter values for this simulation, is listed in Appendix A. The simulation consists of one case, Case 1, which runs the HPLS model with all four junction temperature dependent parameters included ($d\lambda/dT$, $d\beta/dT$, T_0 , T_1). Plots of the Gaussian output intensity curve for each bar of a single laser diode module are provided to show how including junction temperature dependence effects the shaping of the power output spectrum.

A (5x5) laser diode array configuration is used, with 5 diode bars and 5 diodes per bar (see Figure 6) for 25 diodes per module with a total of 15 modules (see Figure 7). The total simulation time is 30 seconds. The laser is activated for 8 seconds starting at 5 seconds into the simulation.

Figure 15 shows the optical power out of the laser diodes (solid line), fiber gain media (dashed line), and the overall power out of the HPLS including combining optics losses (dotted line) for Case 1. Notice how the power levels change throughout the activation pulse due to inclusion of the four junction temperature dependent diode parameters. Figure 16 shows the heat out of the laser diodes (solid line), fiber gain media (dashed line), and combining optics (dotted line) for Case 1. Notice how the heat generated in the diodes and fiber increase throughout the activation pulse due to inclusion of all four junction temperature dependent parameters. The change in optical power throughout the pulse is due to the diode junction temperatures changing. When they change, the amount of power absorbed in the gain media changes too, as is expected.

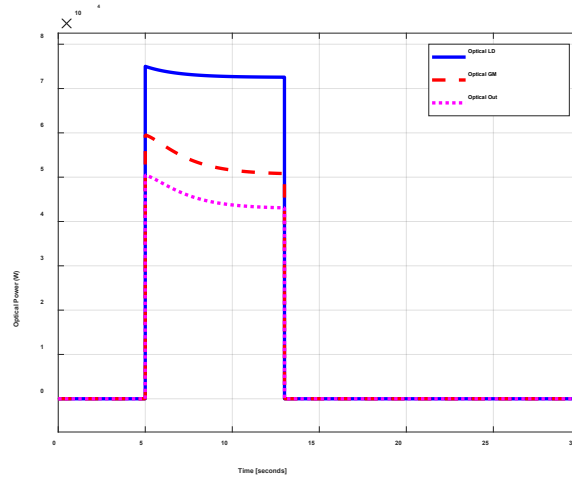


Figure 15: Case 1 optical power output

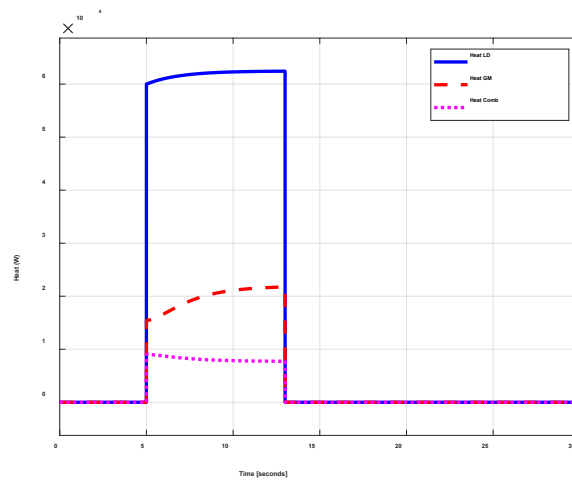


Figure 16: Case 1 heat generation

In addition to optical power, spectral power density is an important laser performance metric describing the focus, or intensity, of a laser light. Laser light focused into the smallest possible bandwidth wavelength is advantageous for some applications. The spectral power density is determined from representing the laser light output of each laser diode as a Gaussian curve, where the area under the curve equals the optical power contained in the laser beam. A larger

peak spectral power density means more power is concentrated along the desired signal bandwidth (wavelength). Spectral power density plots of the five laser diode bars on a single module are shown for Case 1 in Figure 17.

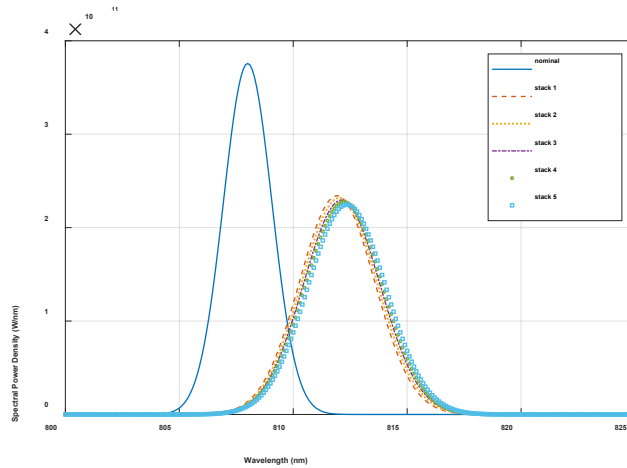


Figure 17: Case 1 spectral power density curves

In Figure 17, the nominal curve shows the output spectrum if the laser diode bar is operating at its prescribed reference temperature. The other curves show the output spectrum for the five diode stacks (bars) of a single module at the end of the activation pulse, showing how the spectrums shift and change shape from the nominal position and shape based on the mock junction temperature estimation profiles. Note how the spectrum center wavelengths shift to around 812 nm from the nominal 808 nm. This replicates the experimental data taken from research by Schlenker⁷⁰, but spectral power density is used instead of relative amplitude to display how the peak is actually changing as the center wavelength moves from the nominal on-design 808 nm to the off-design 812 nm. The change in diode temperature from 298K to 314K yields a wavelength shift from 808 nm to 812 nm in laser diode output. The diode spectrum shift here in Figure 17 is comparable to the provided experimental data⁷⁰ (see Figure 13).

The spectrums in Case 1 look quite different compared to the nominal. Not only are their peaks smaller than the nominal, but the full width half maximums of the curves have changed as well. The area under each curve is also less when compared to the nominal curve, showing the optical power levels are dropping. The spectrums are now more spread out over a larger wavelength range, meaning the laser light intensity is now considerably degraded. This aspect of which temperature dependent parameters ($d\lambda/dT$, $d\beta/dT$, T_0 , T_1) are most significant to overall laser system performance will be considered later on.

HPLS Performance – Full Fiber Model:

For this set of simulations, the rate equations were used in the fiber model in place of the simplified fiber model. Parameter values for this simulation set are listed in Appendix B. As in the previous simulations, the HPLS model simulation is 30 seconds long. The HPLS is activated for 8 seconds starting at 5 seconds into the simulation. The design optical power for the simulation is again 75 kW, so there are 15 laser diode modules with 25 diodes on each module at 200 W nominal optical power per diode. The simulation models a Golden Bullet by Northrop Grumman⁹³, except it uses a center wavelength of 976 nm.

Figure 18 shows the total optical power out of all laser diodes (solid line), all fibers (dashed line), and the combiner (dotted line) with the new fiber model (a) and the simplified model from Figure 15 (b). The combiner represents the optical out of all the fibers after they have been put through the beam combining optics (represented simply by a constant efficiency loss), and this value is the optical power out of the HPLS. The full fiber model with the rate equations gives a better overall fiber efficiency versus the simplified fiber model. The max O-O efficiency for the full fiber model is 87%, compared to 80% for the maximum O-O efficiency for the simplified fiber model. Even if the max O-O efficiencies were the same, there would still be a larger decrease in

the simplified fiber model O-O efficiency for the given diode temperature profile. In (a), the optical power out of the fiber drops from 65,250W down to 58,000W, a change of 7,250W. In (b), the optical power out of the fiber drops from 60,000W down to 50,700W, a change of 9,300W. A simple percent error analysis for the change in power of each model shows 28.3%. This is significant. Hence, the simplified model is inaccurate when it comes to the amount of heat generated during fiber operation, showing higher fidelity modeling of the fiber is beneficial and the rate equations should be considered when modeling. The mock temperature estimation values throughout the entire pulse corresponding to Figure 18 are the same as before (see Figure 14).

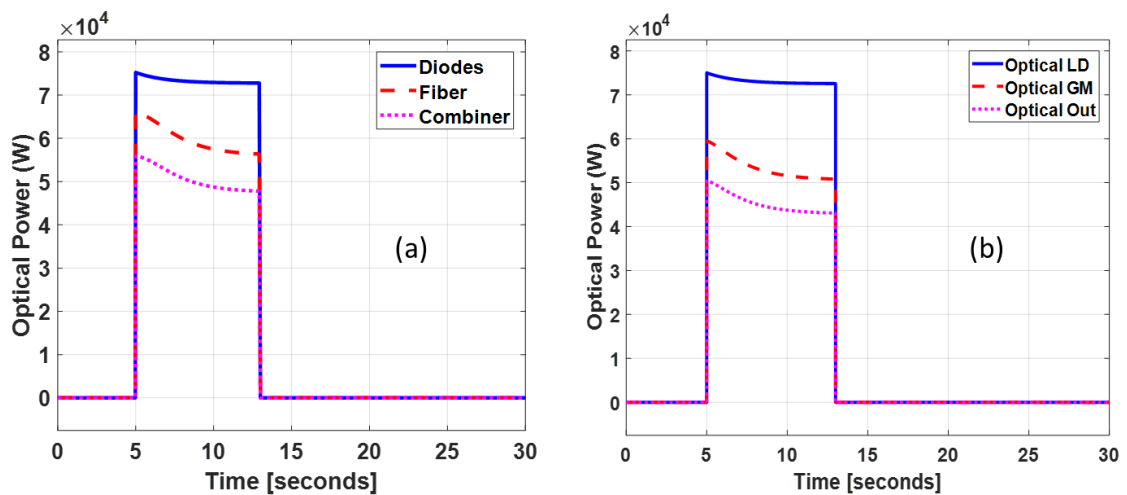


Figure 18: Optical power output of rate equation fiber model (a) and simplified model (b)

Figure 19 shows the total heat generation in all laser diodes (solid line), all fibers (dashed line), and the combining optics (dotted line) with the new fiber model (a) and the simplified model from Figure 16 (b). In comparison, the new fiber model with the rate equations generates less heat versus the simplified fiber model. Fiber heat generation is due to the laser diode output power/spectrum dependence on junction temperature.

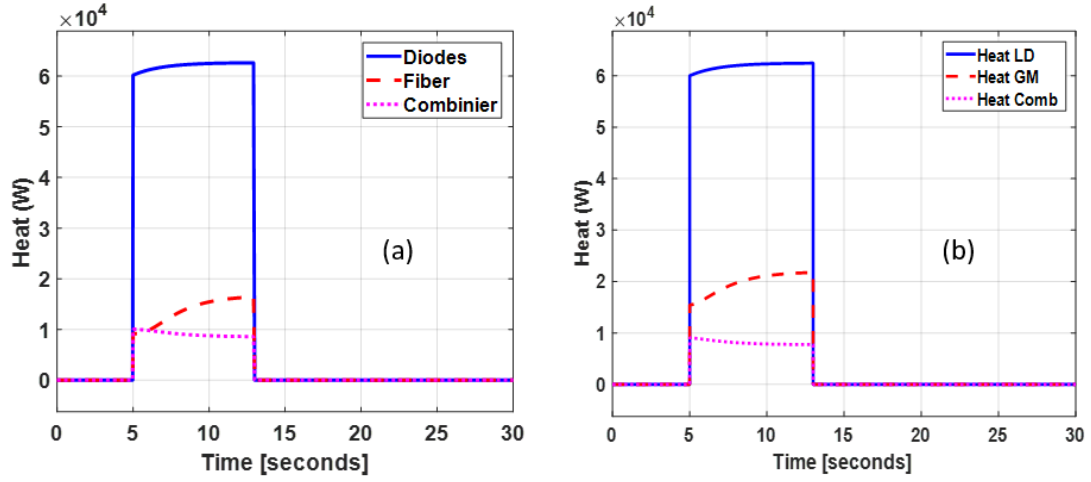


Figure 19: Heat output of rate equation fiber model (a) and simplified model from (b)

The results in Figure 18 and Figure 19 show high fidelity multiphysics models of laser diodes and fibers being dynamically coupled together. The results directly show how a change in laser diode junction temperature cascades down the optical train affecting the absorption and emission of laser light within an active fiber. Figure 20 displays the $\dot{E}_{diss}(t)$ (solid line) and $P_p(L, t)$ (dashed line) in a single active fiber throughout the activation pulse. The diagram shows how the amount of heat dissipated in the fiber and amount to be stripped away are a function of diode junction temperature. The term $\dot{E}_{diss}(t)$ is the sum of $\dot{E}_{gen}(z, t)$ in equation 31 for all points z . $P_p(L, t)$ is significantly less than $\dot{E}_{diss}(t)$ when junction temperature is well controlled. However, as junction temperature deviates from the reference temperature, $P_p(L, t)$ starts to increase and eventually surpasses $\dot{E}_{diss}(t)$ given enough deviation.

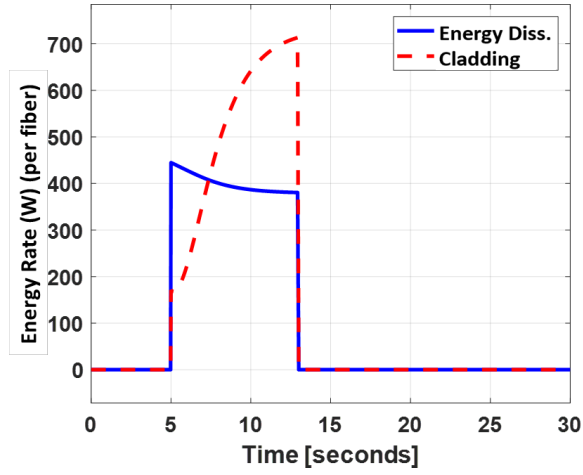


Figure 20: Heat generation in a single active fiber

Now, look at the optical performance of a single fiber at three different points during the activation pulse (Figure 21).

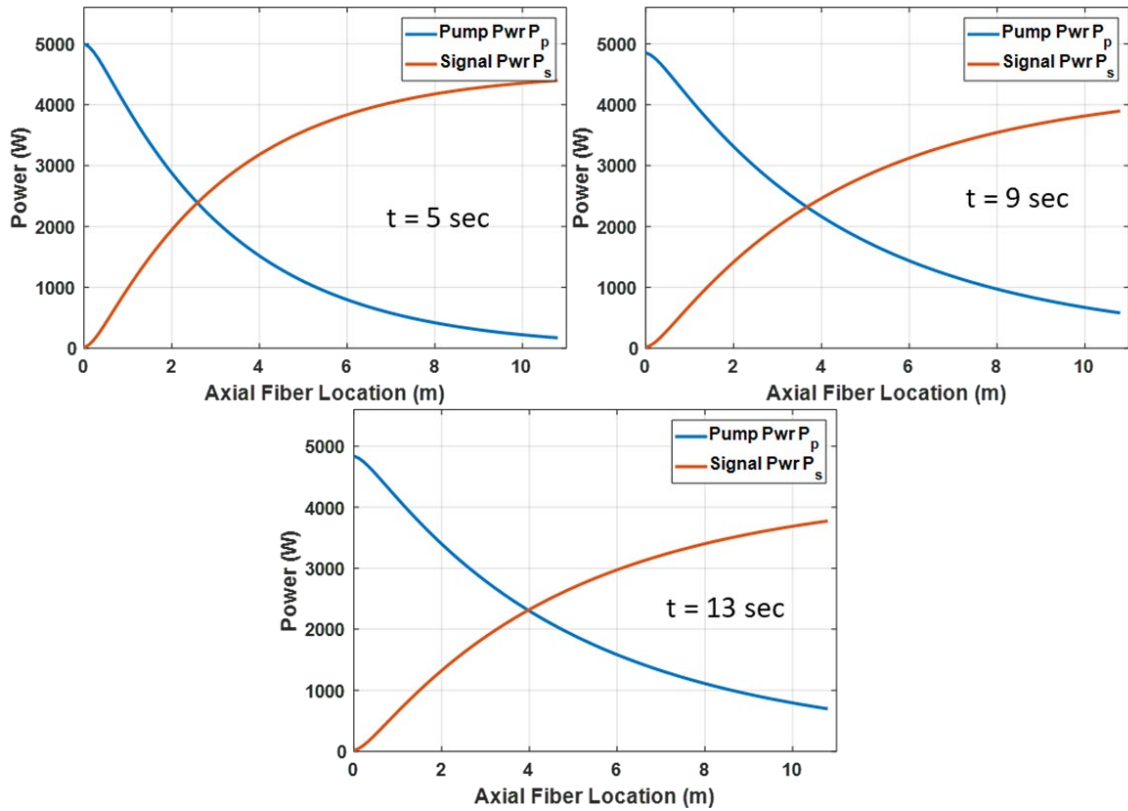


Figure 21: Optical performance of a single fiber

The pump and signal power are shown as a function of axial fiber location at times of 5, 9, and 13 seconds. Notice how the curves change with time due to the diode temperature increasing and moving away from the laser diode reference temperature. A larger diode temperature shift leads to less pump power being converted to signal power over the given fiber length, leaving more pump power left over in the cladding at the fiber exit, as seen in Figure 20. From Figure 21, the slope efficiency of the fiber (different from diode slope efficiency) can be found by the relation below (reprinted from Motes et al.³²)

$$\eta_{slope} = \frac{P_s(L, t) - P_s(0, t)}{P_p(0, t) - P_p(L, t)}$$

The slope efficiency found from Figure 21 at 5 seconds is 90.7%. This is when the diodes are at their optimum temperature and produce the desired wavelength of 976 nm. At times of 9 and 13 seconds, the slope efficiencies increase to 91.2 and 94.1. The increase in slope efficiency can be deceiving, for it shows an increase as the diode pump spectrum wavelength changes. However, it does not mean the fiber is more efficient overall. In fact, the opposite is true. In reality, the efficiency based solely on the optical power launched into the fiber η_{opt} is more useful and is considered next.

Figure 22 provides the η_{opt} , $loss_{clad}$, and $loss_{\dot{E}}$ for a single fiber throughout the activation pulse. These efficiency quantities are defined below.

$$\eta_{opt} = \frac{P_s(L, t)}{P_s(0, t) + P_p(0, t)}$$

$$loss_{clad} = \frac{P_p(L, t)}{P_s(0, t) + P_p(0, t)}$$

$$loss_{\dot{E}} = \frac{\dot{E}_{diss}(t)}{P_s(0, t) + P_p(0, t)}$$

The efficiency quantities are defined by the amount of pump or signal power at the fiber entrance or exit. The power quantities come from the data in Figure 21 at each point in time.

The data shows an η_{opt} , also known as the O-O efficiency, (blue line) of 87% at the pulse start, which is reasonable when compared to previous research values for O-O efficiency (see fiber literature review). By the pulse end, O-O efficiency (η_{opt}) has dropped to 78%. The parameter $loss_{\dot{E}}$ (purple dot line) is also decreasing throughout the pulse. This is expected, as a drop in O-O efficiency means less heat generation in the fiber. The unabsorbed pump power remaining in the cladding increases because less pump power is being converted to signal power, so more

pump power remains at the fiber exit that needs to be stripped away, as seen by the red dashed line $loss_{clad}$. Cladding light strippers (CLS) have been well-researched and can strip away optical power values up to 1184 W from a single fiber (see literature review).

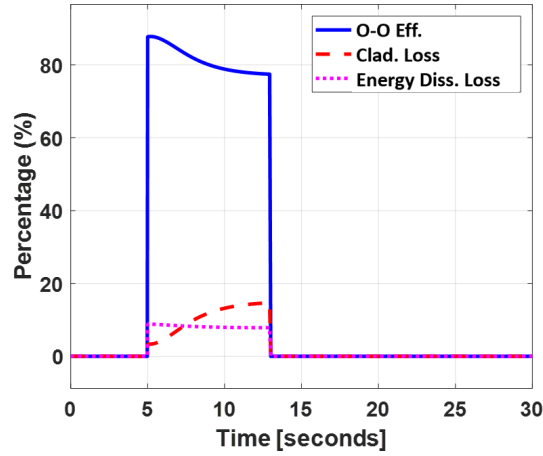


Figure 22: Diagram of three relevant active fiber efficiency values

The total heat generated inside the fiber is important. It is also helpful to know exactly how much heat is being deposited in what part of the fiber. Using the energy balance analysis of every single fiber segment (see Figure 10 and equation 31), the heat generated as a function of segment number can be plotted. This is $\dot{E}_{gen}(z, t)$. The total heat generated in the fiber as a function of time can be found by adding up the elements of $\dot{E}_{gen}(z, t)$ while multiplying according by the fiber length. Figure 23 shows the heat dissipation profiles of $\dot{E}_{gen}(z, t)$ in W/m along the axial length of single fiber at the beginning (solid line) and end (dashed line) of the activation pulse. The fiber is divided into 100 segments for a length of 0.108 m per segment. Multiply the y-axis value by 0.108 to get actual heat dissipated in that particular fiber segment. Adding all 100 y-axis values together for the solid and dashed lines in Figure 23 equals the value of the solid line of Figure 20 at 5 seconds and 13 seconds respectively.

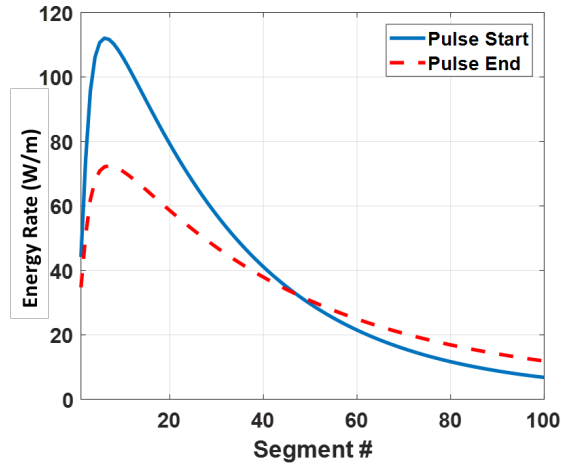


Figure 23: Fiber heat deposition profiles at beginning (t = 5 sec) and end (t = 13 sec) of activation pulse

The heat deposition profiles show less heat is being deposited from the pulse beginning to end.

This confirms \dot{E}_{diss} is decreasing throughout the pulse, which is observed from the data in

Figure 20. The results show most heat is deposited within the first third of the fiber length. The profile shape is typical for an active fiber, as seen in research by Yu et al.²⁰.

Since the rate equations are solved with a 4th order Runge-Kutta algorithm, the fiber discretization must be such that the algorithm converges to an accurate answer. Through a convergence study, it was found 60 segments met the convergence criterion ε given in the equation below, where k denotes the iteration number.

$$\varepsilon = \left| \frac{P_p^k(L) - P_p^{k-1}(L)}{P_p^k(L)} \right| \leq 0.01$$

Increasing iteration numbers correspond to an increasing number of segments where k = 0 has 25 fiber segments and k = 75 has 100 fiber segments. The convergence study was conducted without the diode temperature dependence. Diode junction temperatures were held constant

so the input to the rate equations was always constant, making for a more accurate convergence study. Since computation resources were sufficient, the number of fiber segments in the model was increased to 100 to ensure algorithm accuracy.

Fiber Rate Equation Comparison:

The fiber performance of the coupled laser diode-fiber model is compared to previous research to confirm proper rate equation implementation. Previous work on simulating fiber performance with the rate equations is considered along with experimental fiber performance results to confirm the rate equations, as implemented here, match both simulation and experimental results. The main challenge in comparing work done by the rate equations is each simulation or experimental setup uses different values for parameters in the rate equations (i.e., doping ion type and concentration, absorption/emission cross sections, filling factors, attenuation coefficients, fiber/core radii, and fiber length). The wavelength and power level of pump light launched into the fiber vary, along with the signal wavelength of light coming out of the fiber. Most simulation work on the rate equations has, up to this point, considered laser diode pump powers on the order of 10 to 1000W launched into a fiber, whereas the experimental work shows up to 5000W of pump light being launched into a fiber. Very little attention has been paid to the simulation of coupled laser diode/fiber operation in the literature thus far. This means the effect of a dynamic laser diode spectrum due to insufficient diode temperature control on fiber emission absorption remains largely unstudied. Hence, directly comparing the performance of the coupled laser diode-fiber model presented here to previous work is very challenging, if not unrealistic. Lastly, fiber performance is mainly characterized in the literature at steady state, which means the pump spectrum and power launched into the fiber is constant with respect to time. As such, the fiber efficiency value to compare with will be

taken $t = 5$ seconds on Figure 22 (blue line). That optical-to-optical (O-O) fiber efficiency value at optimal diode pump spectrum conditions is 87%. There will also be comparisons back to the data in Figures 21 and 23 when appropriate.

Experimental work by Beier et al.¹⁷ achieved an output power of 4.3 kW from a single Yb³⁺ doped fiber with a slope efficiency of 90%. In Figure 21, the coupled laser diode-fiber model achieves a slope efficiency of 90.7% with an output power of 4.35 kW at the time of 5 seconds. Beier et al.¹⁷ do not list the O-O efficiency of their fiber. The research focused on studying the power levels at which the onset of transverse mode instabilities (TMI) or stimulated Raman scattering (SRS) start to occur. Beier et al.¹⁷ use a fiber with core and cladding radii of 23/460 μm . The coupled laser diode-fiber model uses core and cladding radii of 20/400 μm . Beier et al.¹⁷ make no mention of wanting light to propagate in a specific mode.

Experimental work by Fang et al.²⁴ launched 5 kW of 976 nm pump light into a Yb³⁺ doped fiber and reported an output power of 4.4 kW, yielding an O-O efficiency of 88%. The coupled laser diode-fiber model has an O-O efficiency of 87%. Since the pump power and wavelength launched into the fiber from the work by Fang et al.²⁴ matches very well with the model presented here, it lends good confidence to the proper implementation of the rate equations. Furthermore, since the coupled laser diode-fiber model uses a reference value for 5 kW of pump power launched into the fiber, the work by Fang et al.²⁴ allows for a direct comparison of fiber performance through actual optical power levels, not just efficiency values. Additionally, fibers in the work by Fang et al.²⁴ used a core and cladding radius of 20/400 μm . This is identical to core and cladding radii used in the model presented here. Fang et al.²⁴ make no mention in their research about being concerned with a certain mode of light propagating inside the fiber.

Experimental and simulation research by Yu et al.¹⁰⁰ provides another basis for comparison. On the experimental side, they created a single mode (LP₀₁) Yb³⁺ doped fiber emitting at 1080 nm with a maximum output power of 3.15 kW and an O-O efficiency of 75.1%. It has a significantly lower O-O efficiency value than that of the coupled laser diode-fiber model (87%). However, Yu et al.¹⁰⁰ performed a simulation of rate equations with launched pump power levels of 4 kW, on the same order of magnitude as the 5 kW for the model presented here. Additionally, the rate equations they used were the forward pumping scheme version of the rate equations presented by Kelson et al.⁸⁹. The forward pumping scheme version of these equations (equations 18 through 21) were used in the model presented here. Hence, the data from the rate equation simulation by Yu et al.¹⁰⁰ can be used as a good comparison because the rate equation formulations for the forward pumping scheme are identical, minus the Raman gain terms. Since no Raman gain shows up in the results presented by Yu et al.¹⁰⁰, the comparison is still valid. The pump and signal power as a function of time for the simulation by Yu et al.¹⁰⁰ is provided in Figure 24.

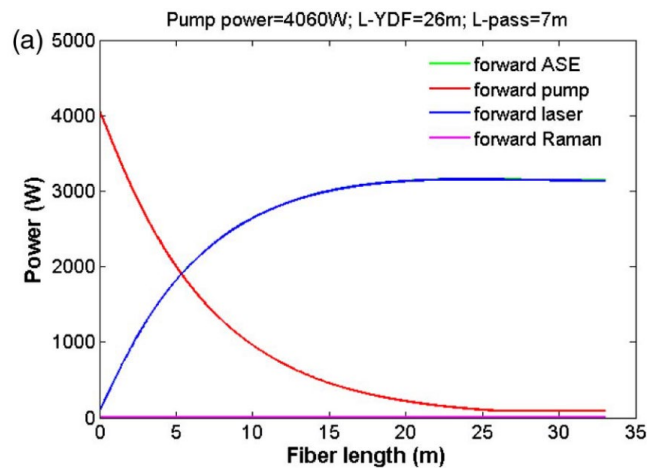


Figure 24: Pump and signal power levels [reprinted from Yu et al.¹⁰⁰, Fig. 7a]

Figures 24 and 21 differ in that the fiber lengths are not the same. The plot for $t = 5$ seconds in Figure 21 is provided again in Figure 25 below. However, in this new simulation, the fiber length was changed to 30 m for a better comparison with Figure 24.

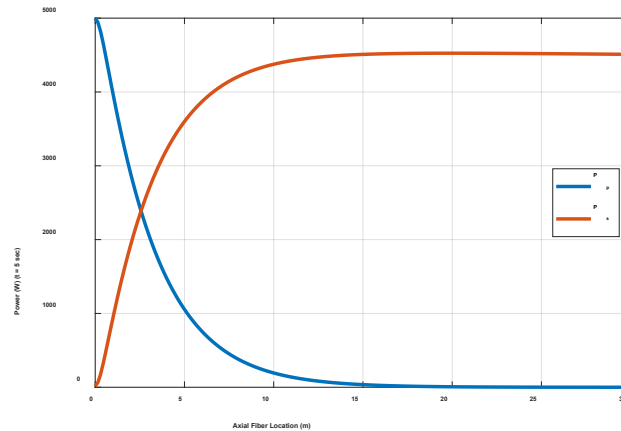


Figure 25: Power plot of $t = 5$ sec in Figure 24 with fiber length 30 m

Comparing Figures 24 and 25, the curves share significant similarities. Pump power decreases and signal power increases along the fiber length. Both Figures show a fiber length at which the signal power is at a maximum. This means there is an optimum fiber length for achieving maximum possible signal power. In Figure 24, that value is 25 m. In Figure 25, that value is 20 m. The differences can be attributed to different value parameter values used when solving the rate equations. Yu et al.¹⁰⁰ used a fiber core radius of $20 \mu\text{m}$. They also chose to use a seed power of 100 W, much larger than the 15 W used in the coupled laser diode-fiber model (Figure 25). Also, they used a signal wavelength of 1080 nm versus the 1064 nm in Figure 25. A different signal wavelength means different absorption/emission cross section values, which will yield a different rate of photon conversion leading to different rates of pump/signal power loss/generation. 1064 nm is generally known to provide better absorption and emission, so this helps to explain why the pump and signal power in Figure 24 do not change at the same rate

with respect to fiber location as in Figure 25. Otherwise, they do not specify values of other parameters in the rate equations, like power filling factors or pump/signal attenuation coefficients. Figure 24 and 25 show same trends in pump power decreasing and signal (laser) power increasing as a function of fiber length. Figure 24 is the best comparison in all the literature review to prove proper implementation of the rate equations for the model created here.

Yu et al.²⁰ present a Yb³⁺ doped fiber with a maximum output of 3.1 kW and an O-O efficiency of 90%, compared to the 87% for the model presented here. This experimental data shows the simulation of the rate equations for the coupled laser diode-fiber model provide a reasonable O-O efficiency value. Although it is not studied in-depth, Yu et al.²⁰ briefly discuss the heat generated due to quantum defect (photon conversion) inside a fiber. They provide a graphic shown in Figure 26.

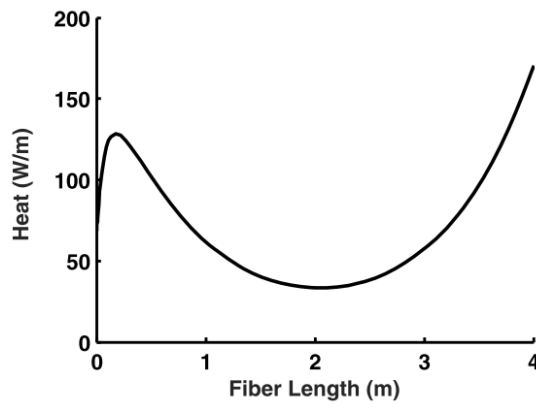


Figure 26: Sample fiber quantum defect profile [reprinted from Yu et al.²⁰, Fig. 1]

The pumping scheme in Figure 26 is bi-directional (fiber is pumped with diode light from both ends). The pumping scheme used in the coupled laser diode-fiber model is forward, meaning pump light is launched into one end and travels from left to right along the fiber length. Looking

at Figure 23, which again uses the forward pumping scheme, they look very similar. In Figure 23, the units on the y-axis are also W/m. Moving from left to right in Figure 23, the curve goes up and then drops off in the first part of the fiber, trailing off towards the end. This is expected, as most of the photon conversion occurs in the first third of the fiber. If the pumping scheme shown in Figure 26 was forward (instead of bi-directional), it would show the same trend.

Yu et al.²⁰ do not explicitly state where Figure 26 comes from. An extensive literature search on all their cited sources reveals Figure 26 did not come from any of the cited sources. Admittedly, some of the citations from Yu et al.²⁰ were not detailed enough to look up, so it is difficult to actually know where the figure came from. Regardless, the heat deposition profile in Figure 26 is accepted among the wider fiber laser community as a typical profile shape¹⁰¹.

Mobini et al.²⁹ use the rate equations to calculate the heat deposition in a fiber as a function of axial fiber location, as seen in Figure 27.

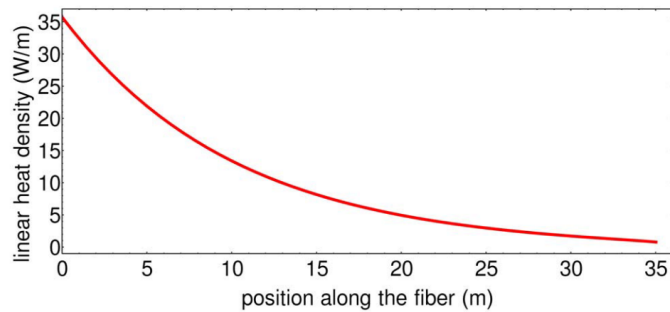


Figure 27: Linear heat deposition [reprinted from Mobini et al.²⁹, Fig. 3]

They use a launched pump power of 3.5 kW, a pump wavelength of 976 nm, and a signal wavelength of 1067 nm. The values seen here are smaller than in Figure 23, due to different parameter values used in the rate equations. Another difference is the curve in Figure 27 has its highest value at $z = 0$ where the pump light is injected. Further away from the fiber entrance,

the heat density drops the same as occurs in Figure 23 because most photon conversion takes place in the first third of the fiber.

Abouricha et al.¹⁰² considered the heat deposition in a fiber for forward, backward, and bi-directional pumpig schemes. Their data is provided in Figure 28.

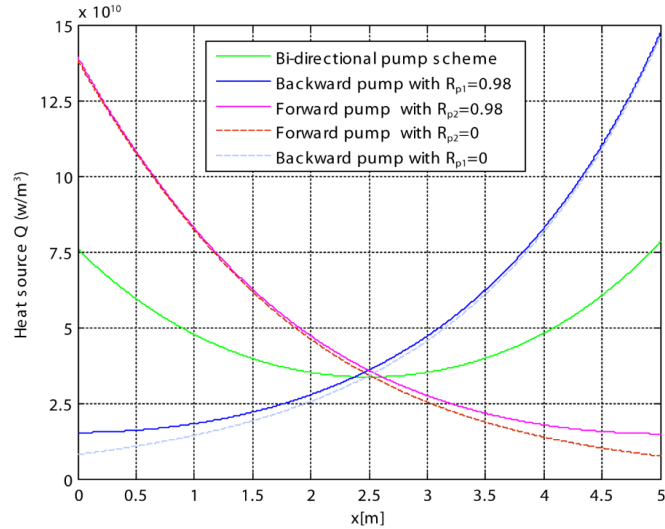


Figure 28: Heat deposition, three pumping schemes [reprinted from Abouricha et al.¹⁰², Fig. 4]

The data differs from Figure 23 in several ways. First, parameter values for solving the rate equations are different, notably the total population density of doping ions ($1.6e26$ in Figure 28 data versus $7.9e25$ in Figure 23 data). Second, the unit on the y-axis is W/m^3 versus W/m . Third, the amount of pump power launched into the fiber is an order of magnitude smaller than in Figure 23 (hundreds instead of thousands of Watts). However, looking at the forward pumping scheme with $R_{p02} = 0$, a similar trend emerges. More heat deposition coincides with the known area of higher photon conversion rates. Further along the fiber, heat deposition rates decrease significantly as less photon conversion occurs.

In Figure 23, the heat deposition is plotted at both the beginning and end of the pulse. At the beginning, laser diodes are operating at their reference temperature and providing pump light at the nominal center wavelength. At the end, laser diodes are operating at off-design conditions with the center wavelength now shifted due to diode temperature change. The literature review revealed no previous work in which a dynamic pump wavelength was considered in a solution to the rate equations, so the dynamic aspect of the coupled laser diode-fiber model created here cannot be directly compared to previous work.

Providing and comparing to some previous research shows the challenge of trying to verify the coupled laser diode/fiber model created here for this research. The previous research, while absolutely valid, is also very disjointed and at times disorganized. The authors, in general, do their own thing without significant quantitative verification. At times, they fail to provide values for parameters used in their solutions to the rate equations, making reproduction of the research results impossible. The various authors look at fiber lasers with different launched pump power, seed power, pump/signal wavelength, power filling factors, and attenuation coefficients, thereby making comparisons very difficult. For comparisons and verification against this previous work, looking at the previous work and comparing efficiencies and general trends in the rate equation solutions is the best that can be expected. Quantitative verification of results is unrealistic given the current publications on fiber laser research. A standard by which to present results and provide data for quantitative comparison would benefit the fiber laser research community greatly. It would be very helpful to see all parameter values used in the rate equations clearly laid out in a table. Some previous work has done this but others have not. In some previous work, the values are buried in the article text making them more difficult to find. Moreover, some previous work fails to list all the parameter values used, making

replication of the work impossible. Additionally, the variable symbols used to represent the rate equation parameters are not entirely consistent throughout the larger body of research. While this is technically acceptable, it makes understanding the rate equations significantly more challenging. Such a standard to present the rate equations and their many parameters would help promote further understanding and more possible application of the rate equations by the wider scientific community.

7. Diode and Fiber Thermal/Temperature Modeling:

Since the HPLS model with temperature dependent efficiency aspects has been created, the next step is to consider the thermal modeling. Coupling models capable of simulating both the laser and thermal aspects will help with understanding optical/thermal interaction from a high-level design decision perspective. Thermal management is an important consideration for HPLS design, as improper thermal management causes a significant decrease in E-O efficiency and can lead to catastrophic failure of system components. To further investigate the optical/thermal interactions, a diode thermal model has been created to estimate the diode junction temperatures in place of the mock temperature profiles from Figure 14.

The optical power of any laser system comes from a pump source. For an HPLS, the pump source is normally laser diodes. Recall in Figure 3 the optical train of the fiber laser model and how optical power cascades through the various components. Laser diodes are arranged in modules. The output from all the diodes in a module is combined and sent to a single optical fiber for amplification. There are as many modules as needed to achieve the design optical power out of the HPLS. Previous work by Butt et al.^{37,38} shows when laser diode temperature is not tightly controlled, the optical wavelength spectrum of the output power shifts. The shift causes a drastic decrease in the pump light absorption taking place in the optical fiber, leading to a decrease in E-O efficiency. The decrease in efficiency is mainly seen in the fiber gain media, as the pump light not absorbed exits the fiber without being converted to signal light. The current state-of-the-art in terms of the maximum optical power that can be launched into a single fiber is 5 kW²⁴. At optical power levels of 5 kW per fiber, the pump light not absorbed in the fiber exits the other end and can cause external damage if not disposed of effectively. This heat, however, is not deposited in the fiber and does not contribute to the rise in fiber

temperature during operation. Hence, laser diode temperature control is key to achieving the best performing HPLS. Additionally, fiber temperature must be kept within a certain range. Thermal models of both the diode and the fiber have been created to assist in the research. The next few sections describe the models in detail.

8. Diode Thermal Model for Temperature Estimation:

The diode thermal model diagram is shown below in Figure 29. It requires diode heat generation and cooling flow as inputs and outputs diode temperatures and cooling flow out data.

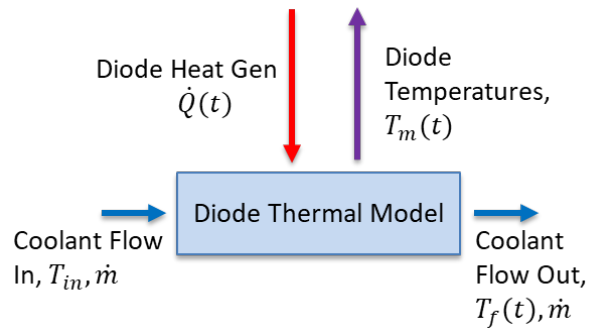


Figure 29: Diagram of laser thermal model

The goal is to create a thermal model for calculating the laser diode temperature estimations based on some set of thermal management parameters, including cooling flow properties, thermal mass material, and other pertinent variables. This will allow for detailed study of the optical/thermal interactions when coupled with the laser physics models. Being able to perform parameter sweeps around important thermal and optical parameters is the basis for designing the systems to operate as desired.

The approach to build the thermal model uses the basic building blocks of heat transfer and fluid flow coupled together through a thermal circuit analogy for a representation of the system.

To start, consider Figure 30.

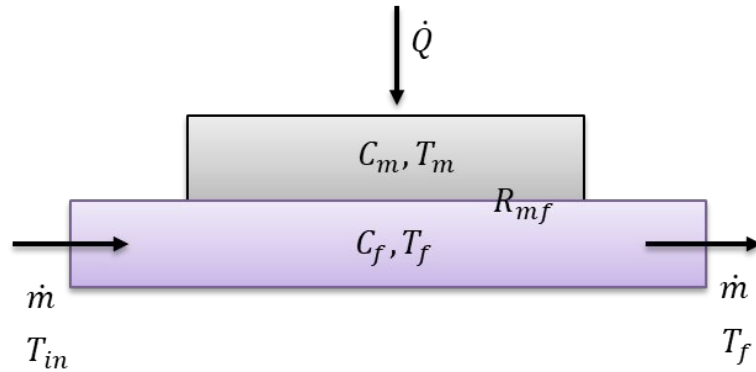


Figure 30: Diagram for thermal model representation

There are two separate control volumes to consider: The heat sink material (grey color) and the fluid (purple color). The temperature of the material is the heat sink temperature, which is the laser diode temperature estimation. Laser diode manufacturers design their diodes to operate at the reference point when the heat sink the diodes are attached to is at a certain temperature. For example, Lockheed Martin’s Golden Bullet requires a heat sink temperature of 15°C for the diode to operate at its reference point⁹³. As described earlier, finding the actual laser diode junction temperatures T_j is very challenging due to all the different layers of various materials within the semi-conductor. Hence, this “material” is the heat sink on which the laser diode is mounted, and the heat sink temperature T_m is used in place of T_j . Heat generated in the diode flows from the diode into the heat sink material (grey), which is represented by \dot{Q} . This value depends on when the laser diode is activated and is also dependent on the temperature of the heat sink T_m . The heat sink has certain material properties (density, specific heat etc.) based on the type of material (metal, polymer etc.). The heat sink also has a certain capacitance C_m based on its volume, with a temperature of T_m . The fluid (purple) is provided at a certain flowrate \dot{m} and a temperature T_{in} . The fluid flows through a certain volume of space inside of a mock heat exchanger. The fluid has certain properties (density, specific heat etc.) based on the type of

fluid. With a certain volume of fluid in the mock heat exchanger and the control volume V_f set accordingly, the fluid provides a certain capacitance C_f . The fluid leaves the control volume at a temperature T_f . The resistance between the material and the fluid is represented by R_{mf} , which is based on the effective surface area through which heat transfer occurs and the heat transfer coefficient at that particular location. The fluid capacitance C_f and the resistance R_{mf} are functions of the mock heat exchanger geometry, heat transfer coefficient h and \dot{m} .

Creating the Thermal Model:

The two states to solve for are T_f and T_m , and can be done through an energy balance analysis for each component: The heat sink (grey) and the fluid (purple). The red lines depict the control volumes of each component, shown in Figure 31.

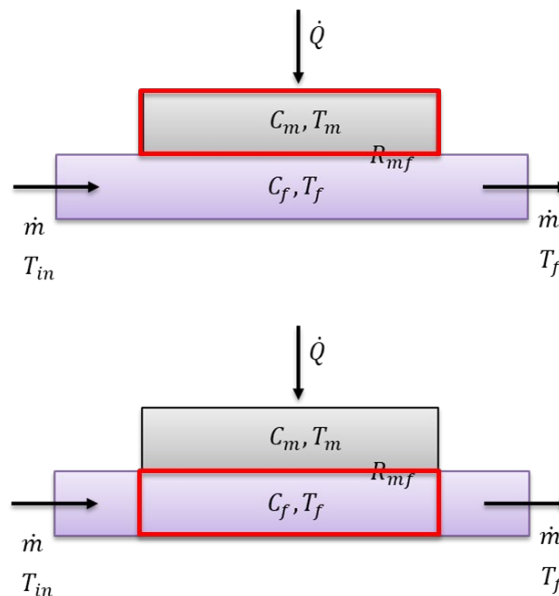


Figure 31: Diagram of control volumes for thermal model analysis

Before deriving equations, consider the assumptions pertinent to the problem. For the heat sink, the goal is to have a geometry such that lumped system analysis can be applied. In other

words, the Biot Number should be less than 0.1 so the material temperatures of the heat sink remain within 5% of each other at any given time. Additionally, the heat sink material properties (specific heat, density etc.) are constant with respect to the heat sink temperature. This is a reasonable assumption for a certain temperature range, meaning the capacitance C_m is independent of the heat sink temperature T_m . For the fluid, assume sufficient mixing inside the mock heat exchanger such that the temperature of fluid both close to and far away from walls/surfaces is the same temperature. All fluid changes temperature together as bulk aggregate. This is more accurate when the heat exchanger capacitance C_f is smaller. Also, the fluid properties (specific heat, density etc.) are assumed constant with temperature, meaning the capacitance C_f is independent of fluid temperature T_f . The fluid assumptions here are leading towards the mock heat exchanger being of the microchannel type. Microchannel heat exchangers provide very high heat transfer coefficients on the order of $10,000 \text{ W/m}^2 \text{ K}^{37}$. They also have smaller internal volumes, which yield small capacitances. The small internal volume supports the assumption of sufficient mixing for fluid temperatures to be the same close to/far away from walls and surfaces. For this model, the heat transfer coefficient h is defined by the Gnielinski Nusselt Number correlations without requiring the actual dimensions or type of heat exchanger. Keeping the model general allows for simpler calculations and generalization of heat transfer performance across various types of microchannel heat exchangers, as designers might choose different heat exchangers in a real system.

To develop a mathematical model for this system, start with the basic energy equation in word form and then variable form.

$$Heat_{in} = Heat_{out} + Heat_{stored}$$

$$\dot{E}_{in} = \dot{E}_{out} + \frac{d\dot{E}}{dt}$$

From this, both the material and the fluid can be analyzed with the various forms of heat and their interaction with the control volume. Considering the heat sink (grey), the “heat in” comes from the diode \dot{Q} . The “heat out” is from the material to the fluid by way of convective heat transfer. The “heat stored” is due to the capacitance of the heat sink. Development of the equation for the heat sink is shown below.

$$\dot{Q} = \frac{T_m - T_f}{R_{mf}} + \frac{d}{dt}(C_m T_m)$$

From the assumption of material property independence from temperature, C_m can come outside of the derivative without loss of generality.

$$\dot{Q} = \frac{T_m - T_f}{R_{mf}} + C_m \frac{dT_m}{dt}$$

This can be rearranged to yield

$$\frac{dT_m}{dt} = \frac{\dot{Q}}{C_m} - \frac{T_m - T_f}{C_m R_{mf}}$$

The same can be done for the fluid. Start with

$$\dot{E}_{in} = \dot{E}_{out} + \frac{d\dot{E}}{dt}$$

Considering the fluid (purple), the “heat in” comes from convective heat transfer between the heat sink and the fluid, along with the coolant flow in. The “heat out” is from the coolant flow out. The “heat stored” is due to the capacitance of the fluid. Development of the equation for the fluid is shown below.

$$\frac{T_m - T_f}{R_{mf}} + \dot{m}c_{p,f}T_{in} = \dot{m}c_{p,f}T_f + \frac{d}{dt}(C_f T_f)$$

From the assumption of fluid property independence from temperature, C_f can come outside of the derivative without loss of generality.

$$\frac{T_m - T_f}{R_{mf}} + \dot{m}c_{p,f}T_{in} = \dot{m}c_{p,f}T_f + C_f \frac{dT_f}{dt}$$

This can be rearranged to yield

$$\frac{dT_f}{dt} = \frac{\dot{m}c_{p,f}(T_{in} - T_f)}{C_f} + \frac{T_m - T_f}{C_f R_{mf}}$$

Additionally, the equations for contact thermal resistance R_{mf} and capacitances C_m , C_f are shown below.

$$R_{mf} = \frac{1}{A_s h}$$

$$C_m = c_{p,m} \rho_m V_m$$

$$C_f = c_{p,f} \rho_f V_f$$

In reality, \dot{Q} is not constant, as it is a function of T_m going back to how laser diode efficiency is temperature dependent based on the laser diode optical power given in equation 75. Hence, the ODEs are non-linear and are most easily solved numerically. The optical power equation is reprinted below.

$$P_{Opt} = \eta_{ref} e^{-\left(\frac{T_m - T_{ref}}{T_1}\right)} \left(I_{op} - I_{ref} e^{\left(\frac{T_m - T_{ref}}{T_0}\right)} \right)$$

The heat generated by the laser diodes \dot{Q} is then calculated using the electrical power provided to the diodes.

$$\dot{Q} = P_{Elec} - P_{Opt}$$

Here, it is clear how \dot{Q} is a function of T_m . Remember, the heat sink temperature is the temperature laser diode manufacturers specify to be controlled. They do not specify the actual junction temperature T_j . If the laser diode reference temperature is 298K, that refers to the heat sink temperature required for nominal diode operation (nominal light wavelength and optical power). The actual junction temperature is higher than the heat sink due to the diode thermal resistance. In using the heat sink temperature T_m , the diode thermal resistance does not need to be considered as the diode has a much faster thermal response than the heat sink. Essentially, the junction temperature tracks with the heat sink temperature. It is just higher than the heat sink temperature by a value of the resistance multiplied by the heat generated (refer to equation 76).

The equations needed for the diode thermal model are shown together below.

$$\frac{dT_m}{dt} = \frac{\dot{Q}}{C_m} - \frac{T_m - T_f}{C_m R_{mf}} \quad (33)$$

$$\frac{dT_f}{dt} = \frac{\dot{m} c_{p,f} (T_{in} - T_f)}{C_f} + \frac{T_m - T_f}{C_f R_{mf}} \quad (34)$$

$$\dot{Q} = P_{Elec} - \eta_{ref} e^{-\left(\frac{T_m - T_{ref}}{T_1}\right)} \left(I_{op} - I_{ref} e^{\left(\frac{T_m - T_{ref}}{T_0}\right)} \right) \quad (35)$$

Equations 33 and 34 are two coupled ODEs with two state variables, so the equations can be solved simultaneously for T_m and T_f . The thermal model parameters and definitions are listed in Table 6 for reference.

Table 6: Thermal model parameters and definitions

Parameter	Definition
A_s	Surface area through which heat transfer occurs (m ²)
h	Heat transfer coefficient (W/m ² K)
$c_{p,m}$	Heat sink material specific heat (J/kg K)
ρ_m	Heat sink material density (kg/m ³)
V_m	Heat sink material volume (m ³)
k_m	Heat sink thermal conductivity (W/m K)
$c_{p,f}$	Fluid specific heat (J/kg K)
ρ_f	Fluid density (kg/m ³)
V_f	Fluid volume inside HX (m ³)
T_{in}	Fluid temperature into HX (K)
\dot{m}	Mass flow rate (kg/sec)
\dot{Q}	Heat generated in diodes (W)
P_{Elec}	Electrical power to diodes on a single bar (W)
η_{ref}	Diode slope efficiency (W/A)
I_{op}	Current sent to diodes on a single bar (A)
I_{ref}	Threshold Current (A)
T_{ref}	Laser diode reference temperature (K)
T_0	Threshold current characteristic temperature
T_1	Slope efficiency characteristic temperature

Next, define the capacitances and the relationship between mass flow rate and heat transfer coefficient.

Remember the assumptions stated earlier. The heat sink material can be anything, as long as the chosen material has properties that can be considered independent of temperature in the appropriate range. Similarly, the type of fluid used must have properties that can be considered independent of temperature in the appropriate range. To meet these requirements, the fluid

must be single phase liquid. If the fluid is a gas or two-phase, the above analysis and equations are not valid. Additionally, to meet the assumption of lumped capacitance, the Biot Number should be less than 0.1 so the material temperatures of the heat sink remain within 5% of each other at any given time.

To show this process, an example of how to choose a design that meets the Biot requirements is provided here. First, choose the heat sink material and type of fluid. Consider copper for the heat sink material and water for the working fluid. Consider the Biot number of the copper heat sink to determine its characteristic length.

$$Bi = \frac{hL_c}{k} < 0.1$$

$$L_c < \frac{0.1k}{h}$$

The maximum value for the heat transfer coefficient h needs to be considered as well. Since microchannel heat exchangers can produce heat transfer coefficients on the order of 10,000 $W/m^2 K$, set h arbitrarily to be 40,000 $W/m^2 K$. The thermal conductivity for copper is 401 $W/m K$. Hence,

$$L_c < \frac{0.1(401)}{40000} \rightarrow L_c < 0.0010025$$

Now, the geometrical requirements for the heat sink can be calculated. Using the characteristic length L_c , the heat sink material volume V_m and the surface area through which heat transfer occurs A_s can each be determined when the other is known. For example,

$$L_c = \frac{V_m}{A_s} = \frac{1e^{-5} m^3}{0.01 m^2} = 0.001$$

$$V_m = A * l_{thick}$$

Here, A is the area required by the laser diodes to simulate proper mounting on the heat sink. The heat sink thickness l_{thick} is used to find the volume of the heat sink material. At this high of a value for heat transfer coefficient, the geometry requirements to meet the Biot Number limitation are very strict. V_m is determined from the area required to mount the laser diodes. More diodes on a bar means the area of the heat sink needs to increase. Consequently, the thickness of the heat sink must decrease to meet the Biot Number limitation. The process described here applies to any heat sink material, not just copper. The provided process needs to be performed for a certain type of heat sink material and required heat sink thickness or area. It is an iterative process.

Based on the Biot Number analysis, the heat sink material volume is known. The next step is to calculate the heat sink material capacitance, as shown below. Both the specific heat capacity and density of copper are known and assumed independent of temperature, as stated previously.

$$C_m = c_{p,m} \rho_m V_m$$

$$C_m = 385 * 8954 * 1e^{-5} = 34.473 J/K$$

This is the process of finding the characteristic length (thickness) and the subsequent capacitance. Meeting the requirements means lumped capacitance applies and the heat sink material be considered a single temperature at any point in time.

A smaller fluid capacitance, as per the assumptions, means it is more accurate to assume the temperature of the fluid within the heat exchanger changes temperature in bulk and the fluid temperature close to/far away from walls are equal. Since the working fluid is water, the fluid

properties like specific heat capacity and density are assumed independent of temperature, the fluid capacitance can be found by

$$C_f = c_{p,f} \rho_f V_f$$

Notice here, since the specific heat capacity and the density are constant, the only variable that can cause a change in the fluid capacitance is the internal heat exchanger volume V_f . At this point, consider C_f to not have a set value. In the analysis to come, it will change based on a varying value of V_f .

Now, further consider the heat transfer coefficient h . The Nusselt correlation to find h can differ based on the geometry of the heat exchanger used. Since no specific geometry has been defined for this research, any Nusselt correlation can technically be considered. In order to achieve the high heat transfer coefficients required for laser diodes of this optical power level, the Gnielinski Correlations for internal flow have been implemented to simulate a microchannel heat exchanger. They are shown in the equations below, along with other pertinent variable definitions, taken from Cengel et al.⁹⁵.

$$Nu = \frac{(f/8)(Re - 1000)Pr}{1 + 12.7(f/8)^{0.5}(Pr^{2/3} - 1)}$$

Here, the Reynold's Number is defined as

$$Re = \frac{\rho_f V_{avg} D_h}{\mu}$$

$$V_{avg} = \frac{\dot{m}}{\rho_f A_c}$$

Notice the use of hydraulic diameter D_h . The average velocity V_{avg} is found by knowing the cross-sectional flow area of the internal flow A_c . The Prandtl Number is defined as

$$Pr = \frac{\mu c_{p,f}}{k}$$

Finally, the heat transfer coefficient can be found by

$$h = \frac{Nu k}{D_h}$$

Additionally, the friction factor f , required for the calculations, is defined by the Haaland Equation shown below.

$$\frac{1}{\sqrt{f}} = -1.8 \log \left[\frac{6.9}{Re} + \left(\frac{\varepsilon/D_h}{3.7} \right)^{1.11} \right]$$

Here, ε is the equivalent roughness of the material surface adjacent to the flow. For simplicity, the values for D_h , A_c and ε are kept constant at 0.00134 m, 2.2e-5 m², and 5e-6 m. As mentioned earlier, all other values for fluid properties are constant with fluid temperature, taken at 20°C.

Again, the Nusselt Number correlation used here attempts to model a micro channel type heat exchanger, as this type is capable of the high heat transfer coefficients (on the order of 10,000 W/m² K) required for laser diodes of this optical power level. Any Nusselt correlations could be substituted here and should be substituted appropriately when needed.

Extension of the Thermal Model:

Currently, only a single diode bar/node is considered in the diode thermal model. In order to represent an entire diode array, the thermal model capabilities must be extended to include

multiple diode bars. The thermal model must calculate diode temperature estimations and fluid temperatures at multiple nodes, not just a single node. Going back to equations 33 and 34 along with Figure 31, each node has two state variables (T_m and T_f) with two governing ODEs created from analyzing the two control volumes for both the heat sink material and the fluid using an energy balance approach. Now, refer to Figure 32 shown below.

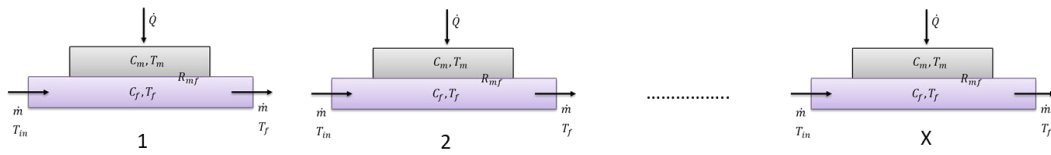


Figure 32: Various heat transfer coefficient and mass flow rate relationships

At node 1 in Figure 32, the fluid temperature coming in is from some source (T_{in1} , a boundary condition which is known/provided). The temperature of the fluid out of node 1 is T_{f1} . If these nodes are put together, and the fluid flow moves from left to right in Figure 32, the fluid in temperature at node 2 T_{in2} is equal to T_{f1} . The same goes for node 3: T_{in3} is equal to T_{f2} . Things continue in this fashion until the last node. The last node is x, which is equal to the value of the number of diode bars $NUM_{LD\ bars}$ from earlier laser diode model development. Hence, multiple diodes bars (nodes) can be represented in a quasi-one-dimensional lumped capacitance model with individual \dot{Q} at each node dependent on the value of T_m at that particular node. Lumped capacitance is valid for the heat sink temperature T_m at every node, but the value of T_m at each node can differ due to the increase in fluid temperature from the previous node. It is assumed there is no conduction considered between the heat sink materials of each node. Heat transfer only occurs through the heat sink material into the fluid at each node.

For modeling a configuration as shown in Figure 32, the number of state variables to solve for increases by two for every additional node. The total number of state variables to solve for is $2 * NUM_{LD\ bars}$. The coefficient matrix for equations 33 and 34 will change as well when more nodes are considered.

Consider a thermal model with $NUM_{LD\ bars}$ equal to 2. This means the model will have four state variables and four ODEs to solve simultaneously with two separate equations for \dot{Q} at each node based on the T_m value at each node. The ODEs for this condition are shown below. The first node equations are the same as equations 33, 34, and 35. They can be manipulated to a more standard form as follows, adding to them the notation to represent variables at each node now since there is more than one node.

$$\frac{dT_{m1}}{dt} = -\frac{1}{C_m R_{mf}} T_{m1} + \frac{1}{C_m R_{mf}} T_{f1} + \frac{\dot{Q}_1}{C_m}$$

$$\frac{dT_{f1}}{dt} = \frac{1}{C_f R_{mf}} T_{m1} - \left(\frac{\dot{m} c_{p,f} R_{mf} + 1}{C_f R_{mf}} \right) T_{f1} + \frac{\dot{m} c_{p,f} T_{in1}}{C_f}$$

$$\dot{Q}_1 = P_{Elec} - \eta_{ref} e^{-\left(\frac{T_{m1} - T_{ref}}{T_1}\right)} \left(I_{op} - I_{ref} e^{\left(\frac{T_{m1} - T_{ref}}{T_0}\right)} \right)$$

The equations for the second node are shown below. Remember, as stated before, the value for T_{in2} is equal to T_{f1} as per Figure 32. So, the equations end up looking like this.

$$\frac{dT_{m2}}{dt} = -\frac{1}{C_m R_{mf}} T_{m2} + \frac{1}{C_m R_{mf}} T_{f2} + \frac{\dot{Q}_2}{C_m}$$

$$\frac{dT_{f2}}{dt} = \frac{1}{C_f R_{mf}} T_{m2} - \left(\frac{\dot{m} c_{p,f} R_{mf} + 1}{C_f R_{mf}} \right) T_{f2} + \frac{\dot{m} c_{p,f} T_{f1}}{C_f}$$

$$\dot{Q}_2 = P_{Elec} - \eta_{ref} e^{-\left(\frac{T_{m2}-T_{ref}}{T_1}\right)} \left(I_{op} - I_{ref} e^{\left(\frac{T_{m2}-T_{ref}}{T_0}\right)} \right)$$

The substitution of T_{in2} equaling T_{f1} shows how the state variables for the current node are dependent on that of the previous node. The system of equations can be built in this way for as many diode bars as exist, and they can all be solved numerically. At each node, the value for \dot{Q} can be different, and this model, as it is formulated, captures the possible difference in \dot{Q} between nodes due to the variation in T_m between nodes. This can be put together more concisely in matrix form, shown below.

$$\bar{T}' = A\bar{T} + \bar{g}$$

$$A = \begin{bmatrix} a & b & 0 & 0 \\ d & e & 0 & 0 \\ 0 & 0 & a & b \\ 0 & j & d & e \end{bmatrix}, \quad \bar{g} = \begin{bmatrix} u_1 \\ i \\ u_2 \\ o \end{bmatrix}, \quad \bar{T} = \begin{bmatrix} T_{m1} \\ T_{f1} \\ T_{m2} \\ T_{f2} \end{bmatrix}$$

$$a = -\frac{1}{C_m R_{mf}}, \quad b = \frac{1}{C_m R_{mf}}, \quad u_x = \frac{\dot{Q}_x}{C_m}$$

$$d = \frac{1}{C_f R_{mf}}, \quad e = -\left(\frac{\dot{m}c_{p,f}R_{mf} + 1}{C_f R_{mf}}\right), \quad i = \frac{\dot{m}c_{p,f}T_{in1}}{C_f}, \quad j = \frac{\dot{m}c_{p,f}}{C_f}$$

Here, u_x represents the generic forcing function term for a node x based on the \dot{Q} associated with that node x and x going from 1 to the number of nodes. In the example here, x = 2 for two nodes. Next, an example with 5 nodes is presented in order to show the patterns that occurs in both the coefficient matrix A and the forcing vector g. In matrix form, this becomes

$$\bar{T}' = A\bar{T} + \bar{g}$$

$$\mathbf{A} = \begin{bmatrix} a & b & 0 & 0 & 0 & 0 & 0 & 0 & 0 & 0 \\ d & e & 0 & 0 & 0 & 0 & 0 & 0 & 0 & 0 \\ 0 & 0 & a & b & 0 & 0 & 0 & 0 & 0 & 0 \\ 0 & j & d & e & 0 & 0 & 0 & 0 & 0 & 0 \\ 0 & 0 & 0 & 0 & a & b & 0 & 0 & 0 & 0 \\ 0 & 0 & 0 & j & d & e & 0 & 0 & 0 & 0 \\ 0 & 0 & 0 & 0 & 0 & 0 & a & b & 0 & 0 \\ 0 & 0 & 0 & 0 & 0 & j & d & e & 0 & 0 \\ 0 & 0 & 0 & 0 & 0 & 0 & 0 & 0 & a & b \\ 0 & 0 & 0 & 0 & 0 & 0 & 0 & j & d & e \end{bmatrix}, \quad \bar{\mathbf{g}} = \begin{bmatrix} u_1 \\ i \\ u_2 \\ o \\ u_3 \\ 0 \\ u_4 \\ 0 \\ u_5 \\ 0 \end{bmatrix}, \quad \bar{\mathbf{T}} = \begin{bmatrix} T_{m1} \\ T_{f1} \\ T_{m2} \\ T_{f2} \\ T_{m3} \\ T_{f3} \\ T_{m4} \\ T_{f4} \\ T_{m5} \\ T_{f5} \\ 0 \end{bmatrix}$$

Notice the trend that occurs in the coefficient matrix A

$$\mathbf{A} = \begin{bmatrix} a & b & 0 & 0 & 0 & 0 & 0 & 0 & 0 & 0 \\ d & e & 0 & 0 & 0 & 0 & 0 & 0 & 0 & 0 \\ 0 & 0 & a & b & 0 & 0 & 0 & 0 & 0 & 0 \\ 0 & j & d & e & 0 & 0 & 0 & 0 & 0 & 0 \\ 0 & 0 & 0 & 0 & a & b & 0 & 0 & 0 & 0 \\ 0 & 0 & 0 & j & d & e & 0 & 0 & 0 & 0 \\ 0 & 0 & 0 & 0 & 0 & 0 & a & b & 0 & 0 \\ 0 & 0 & 0 & 0 & 0 & j & d & e & 0 & 0 \\ 0 & 0 & 0 & 0 & 0 & 0 & 0 & 0 & a & b \\ 0 & 0 & 0 & 0 & 0 & 0 & 0 & j & d & e \end{bmatrix}, \quad \bar{\mathbf{g}} = \begin{bmatrix} u_1 \\ i \\ u_2 \\ o \\ u_3 \\ 0 \\ u_4 \\ 0 \\ u_5 \\ 0 \end{bmatrix}, \quad \bar{\mathbf{T}} = \begin{bmatrix} T_{m1} \\ T_{f1} \\ T_{m2} \\ T_{f2} \\ T_{m3} \\ T_{f3} \\ T_{m4} \\ T_{f4} \\ T_{m5} \\ T_{f5} \\ 0 \end{bmatrix}$$

In general, coefficient matrix A can be considered sparse except along the diagonal where after the first two rows, the same pattern repeats along the diagonal (shown in the red circles). The j term in the coefficient matrix A shows how the state variables at the current node are dependent on data from the previous node. The system of coupled ODEs can still be easily solved by numerical methods.

Diode Thermal Model Comparison:

Work done by Eastbourn⁹⁶ and Roberts et al.^{97,98,99} use a more detailed heat exchanger model for heat transfer performance analysis, similar to the diode thermal model created for this research. The heat exchanger model used by Eastbourn⁹⁶ and Roberts et al.^{97,98,99} was validated against experimental data. It models an offset strip fin heat exchanger capable of representing a

microchannel heat exchanger when hydraulic diameter becomes small enough. It uses the Gnielinski Correlations for heat transfer, same as the diode thermal model created here. Hence, it provides a possible means of verifying correct implementation of the Gnielinski Correlations in the diode thermal model.

The heat exchanger is modeled after an offset strip-fin, counterflow compact heat exchanger. It is created from a collection of thermodynamic, geometric, and heat transfer models. It is implemented as a one-dimensional model, discretized along the flow direction as shown in Figure 33 below.

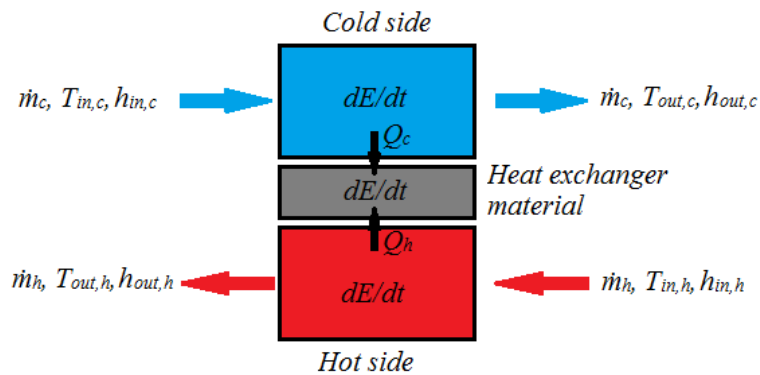


Figure 33: Diagram of heat exchanger thermodynamic model⁹⁸

The thermodynamic system shows a single node in the flow wise direction. The entire heat exchanger uses multiple nodes discretized along the axial flow direction using a finite difference approximation. It contains two working fluids (cold and hot) with a heat exchanger mass separating the two. Energy and mass conservation balance equations for the working fluids and the heat exchanger material account for the heat transfer of the system. One-dimensional flow behaviors and incompressible flow are assumed. The energy balance equations are reprinted from equations 18 to 21 in Roberts et al.⁹⁹ and briefly explained.

$$m_{HX}c_{v,HX} \frac{dT_{HX}}{dt} = \dot{Q}_{cold} + \dot{Q}_{hot}$$

$$m_{hot}c_{v,hot} \frac{dT_{hot}}{dt} = \dot{Q}_{hot} + \dot{m}_{hot}h_{hot,in} - \dot{m}_{hot}h_{hot,out}$$

$$m_{cold}c_{v,cold} \frac{dT_{cold}}{dt} = \dot{Q}_{cold} + \dot{m}_{cold}h_{cold,in} - \dot{m}_{cold}h_{cold,out}$$

$$\dot{Q}_i = h_i A_{HX} (T_{fluid} - T_{HX})$$

The heat exchanger material block computes an energy balance using equation 18 and relays the heat exchanger temperature to the fluid stream blocks. The heat exchanger material is mass that stores or supplies thermal energy depending on the transients. Equations 19 and 20 provide the energy balance for calculation of the temperatures of each flow stream. The heat flows into and out of the heat exchanger mass, Q , are calculated using equation 21. \dot{Q}_i represents either the hot or cold side (\dot{Q}_{hot} or \dot{Q}_{cold}) and T_{fluid} is either the hot or cold side temperatures (T_{hot} or T_{cold}). h_i is the heat transfer coefficient on the hot or cold side at each node. h_{hot} is the hot side specific enthalpy in or out, and h_{cold} is the cold side specific enthalpy in or out. m hot or cold is the mass of fluid in that node on the hot or cold side. c_v is the specific heat capacity of constant volume at the hot or cold side. A_{HX} is the area through which heat transfer occurs. The equations are the same for multiple nodes. The output of one node cascades to the input of the next node. Solving these equations at every time step in the simulations, along with the finite difference approach for multiple nodes, yields a heat exchanger model capable of transient and steady state analysis. For this model, all fluid properties are a function of hot or cold side temperature.

The Gnielinski Correlations are applied in order to get a more accurate estimation for the heat transfer coefficient. They are listed in Roberts et al.⁹⁹. Additionally, since the model attempts to

simulate an offset strip fin heat exchanger, the hydraulic diameter used for Reynold’s Number calculations is specifically defined. The parameters that make up the hydraulic diameter as shown in Figure 34 below.

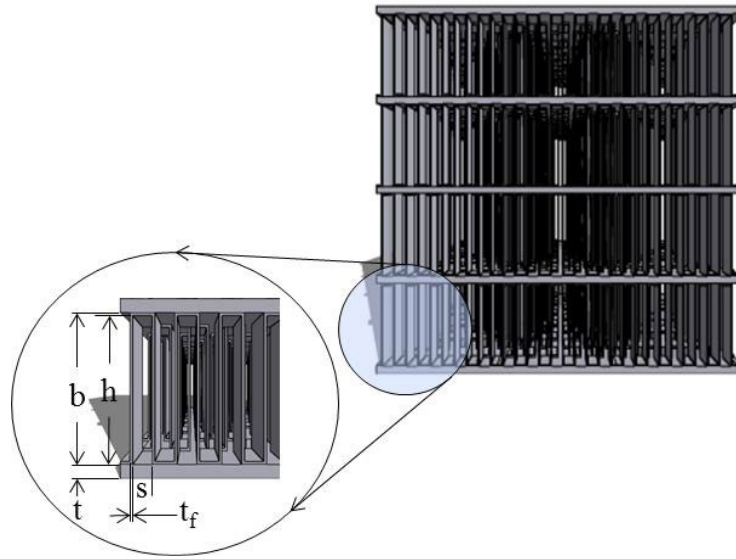


Figure 34: Diagram of fin parameters and geometry⁹⁸

The hydraulic diameter is given as

$$D_h = \frac{4shl}{2(sl + hl + t_f h) + t_f s}$$

Here, s is fin spacing, h is fin height, b is fin channel size, t is fin channel separation material thickness, t_f is fin thickness, and l is fin length along the channel (in/out of paper when referencing Figure 34). The parameter b is used in another section of the model for proper heat exchanger sizing. Refer to Roberts et al.^{97,98,99} for more information.

For comparison with the diode thermal model, the heat exchanger used by Roberts et al.^{97,98,99} (from now on referred to as the WSU model) has been studied in-depth. The WSU model can also be adapted for use as a cold plate to which a heat load is applied. Simply take away the hot

equation and replace it with a heat load value (Figure 33). Now, \dot{Q}_{hot} is the only value needed for the hot side. This \dot{Q}_{hot} is now going to represent the heat generated from the laser diodes. Since the WSU model is specific to a type of heat exchanger and the diode thermal model is not, there must be reconciliation between the models to make their geometry similar. The diode thermal model has no specific geometry, except for hydraulic diameter and the area through which heat transfer occurs. The WSU cold plate model also has hydraulic diameter and area through which heat transfer occurs. If the hydraulic diameter and area through which heat transfer occurs are set to identical values in both the diode thermal model and the WSU cold plate model, the performance between the two models can be compared. It will take some trial and error to reconcile the appropriate values for fin parameters (Figure 34) to achieve the same hydraulic diameter and area through which heat transfer occurs, but doing so will allow a comparison between the diode thermal model and the WSU cold plate model. Reynold's Numbers need to be matched through identical values for mass flow rate and flow velocity. Additionally, the friction factors will need to be matched as well, since the Gnielinski Correlations required friction factor. Such a comparison will help confirm and verify the Gnielinski Correlations have been implemented correctly in the diode thermal model, as well as confirm how well the diode thermal model operates compared to experimental data.

Table 7 shows the parameters values for each model for two cases. Case 1 has worse diode temperature control (lower mass flow rate) and Case 2 has better diode temperature control (higher mass flow rate). The Reynold's Number, Nusselt Number, and heat transfer coefficient are calculated by each model. Hydraulic diameter and surface area through which heat transfer occurs are the same for each model.

Table 7: Thermal Model Comparison Parameter Values

Case	Model	Re	Nu	D _h (m)	A _{Hx} (m ²)	h (W/m ² K)
1	WSU Cold Plate	9000	73	1.34e-3	0.002	32000
	Diode Thermal	9200	76	1.34e-3	0.002	32600
2	WSU Cold Plate	13600	108	1.34e-3	0.002	47200
	Diode Thermal	14000	109	1.34e-3	0.002	48400

The diode physics model is easily coupled to the WSU cold plate model, incorporating the increase in diode heat generation as laser diode temperature moves away from the reference temperature. The heat generation term \dot{Q}_{hot} comes directly from the laser diode physics model. The temperature curves of the two cases are shown and compared. The temperature profiles for Case 1 are provided in Figure 35. They show the node temperatures as a function of time. The laser is activated at 5 seconds. Recall, the temperatures shown here are the heat sink temperatures, which are analogous to diode temperatures. Both models have five nodes, and the surface area given in Table 7 is the surface area for each node. Since there are five nodes, the models predict five heat sink temperatures, one for each node.

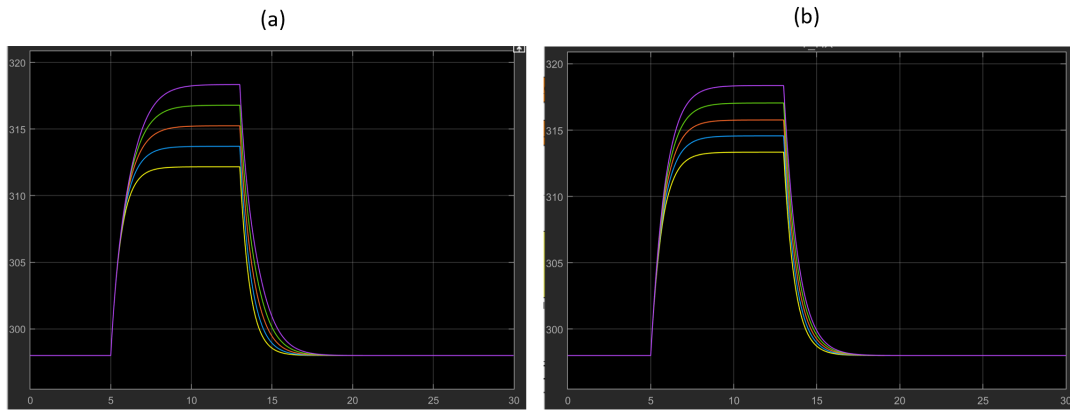


Figure 35: Model Temperature Comparison Case 1, (a) is diode thermal model, (b) is WSU Cold Plate Model

The temperature profiles for Case 2 are provided in Figure 36.

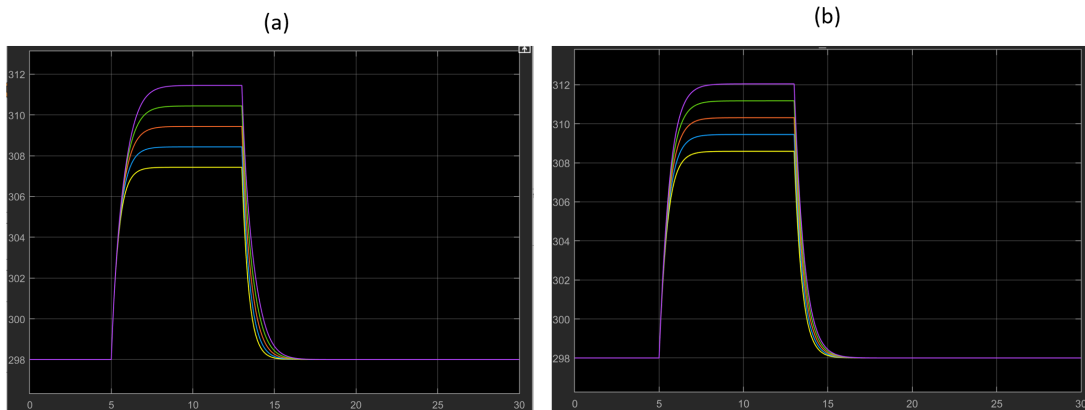


Figure 36: Model Temperature Comparison Case 2, (a) is diode thermal model, (b) is WSU Cold Plate Model

In Case 1 (Figure 35), the diode thermal model has a larger range between the first and last node temperatures than does the WSU cold plate model. Overall, the temperatures of the diode thermal model are smaller than the WSU cold plate model, but not by much. The percent error

between the nodes of each model (from nodes 1 to 5) are less than 1%. Hence, for very similar thermal capability shown in the Table 7 parameters, both models exhibit very similar temperature profiles. The WSU cold plate model does reach steady state slightly faster than the diode thermal model. Another thing of note is the WSU cold plate calculates fluid properties at every time step as a function of fluid temperature, which is an additional reason as to the slight temperature discrepancy. In the diode thermal model, fluid properties are constant with temperature.

In Case 2 (Figure 36), things are quite similar. Higher Nusselt Numbers do provide better temperature control in Case 2 than in Case 1. A maximum temperature of around 317K in Case 1 versus 312K in Case 2. The diode thermal model again has a larger range between the first and last node temperatures than does the WSU cold plate model. Overall, the temperatures of the diode thermal model are smaller than the WSU cold plate model, but not by much. The percent error between the nodes of each model (from nodes 1 to 5) are less than 1%. Hence, for very similar thermal capability shown in the Table 7 parameters, both models exhibit very similar temperature profiles. Again, the WSU cold plate model does reach steady state slightly faster than the diode thermal model.

The high similarity between the temperatures predicted by each model lends confidence to the diode thermal model and that the Gnielinski Correlations have indeed been properly implemented. Neglecting the specific heat exchanger geometry and using just the hydraulic diameter and heat exchanger surface area, as done in the diode thermal model, is useful from a higher-level system design decision making perspective. However, in reality, the complex geometry in actual heat exchangers plays a critical role in their heat transfer characteristics. The WSU cold plate model had to be specifically configured to get matching hydraulic diameters

through manipulating the size of the fins. The simplified diode thermal model cannot currently incorporate the complex geometries, so understanding this particular limitation is key.

However, keeping it general makes it more useful. As the comparison has shown, the diode thermal model correctly implements the Gnielinski Correlations. Another thing to keep in mind is how the heat transfer correlations can often be off by as much 25%. Hence, the comparison further verifies the diode thermal model performance as acceptable given the assumptions therein.

9. Fiber Thermal Model for Temperature Estimation:

The fiber thermal model diagram is shown below in Figure 37. It requires heat generation inside the fiber and cooling flow as inputs and outputs fiber temperature.

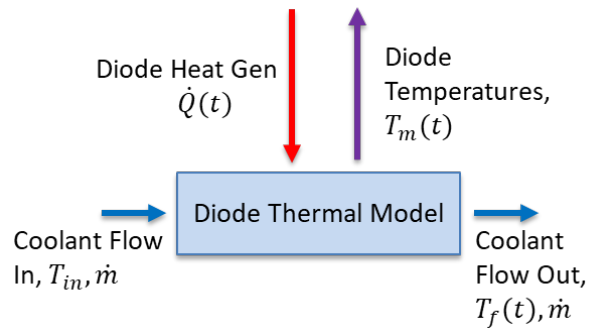


Figure 37: Diagram of fiber thermal model

In addition to the diodes, fiber temperature during laser operation is important to capture. This section explains the creation of the thermal model and the ramifications of what happens when the fiber is or is not properly cooled. Additionally, it mentions how cooling under various heat transfer conditions can affect the duty cycle of fiber operation.

Creating the Thermal Model:

Knowing the maximum fiber temperature as function of time is critical to fiber operation. As cited previously, a typical fiber with a silica glass core and polymer cladding can see a change in temperature from ambient of 100K before the optical-to-optical (O-O) efficiency starts to significantly degrade. Up to a change in temperature of 100K, no discernable change in (O-O) efficiency typically occurs³². A fiber can be thought of a long, flexible cylinder with a length much longer than its diameter. A polymer cladding is added on the outside of the fiber core. There is normally an inner and outer cladding. The cladding helps to direct the pump light into the core

where it can be absorbed and emitted as signal power. Outside the cladding, there is a polymer coating which is very thick compared to the actual fiber. The thermal conductivity of this coating is much larger than that of silica glass, as much as 20-30 times higher. Including this coating, the entire diameter can be as much as 4 mm³². Even with this coating, the fiber is still quite flexible and can be coiled to take up less space.

In order to make a thermal model of the fiber, consider the fiber to be a long, uncoiled cylinder. Since a normal fiber has a polymer coating that draws heat away from the core with a larger thermal conductivity, the worst-case scenario for a thermal model would assume the entire fiber (core, cladding, and coating) was all made of silica glass. The lower thermal conductivity of silica glass would mean the thermal model will estimate a higher fiber temperature than really exists. In this way, the thermal model is applied to the research here such that it is the worst-case fiber temperature. If the fiber coating is modeled, which has much larger thermal conductivity, the actual temperature would be less than the model predicts. As stated earlier, the state of the art for the highest levels of optical power launched into a fiber while maintaining the LP₀₁ mode is 5000W as per Fang et al.²⁴. This shall be the max value considered in the analysis, as a value lower than this will yield a smaller/slower temperature increase in the fiber. Additionally, the 5000W of pump light is considered to be at the optimum wavelength and spectrum as well, meaning the fiber will be operating at maximum optical-to-optical (O-O) efficiency. Hence, the heat generation in the fiber will be at its largest.

In order for simplicity and ease of calculation, the fiber is thermally modeled using the 1D heat conduction equation shown below. This is appropriate as the temperature in the fiber varies with both location in the axial (z) direction and time (t).

$$\alpha \frac{\partial^2 T}{\partial z^2} = \frac{\partial T}{\partial t}$$

Here, α is the thermal diffusivity. However, this assumes an insulated rod, which does not allow for the inclusion of convective heat transfer on the outer fiber surface. Hence, the actual governing partial differential equation required is more complicated than the classical heat conduction PDE. The fiber can be modeled as a long rod or cylinder with constant cross-sectional area, internal heat generation as a function of axial fiber position, insulated boundary conditions at the fiber ends, convective heat transfer boundary conditions along the lateral fiber surface, and constant material properties. The PDE representing these listed specifications is a variant of the transient heat conduction equation with a lateral convection boundary condition and internal energy generation. It is shown below.

$$\frac{\partial^2 T}{\partial z^2} - \frac{hP}{Ak} (T_\infty - T) + \frac{\dot{e}(z,t)}{k} = \frac{\rho c_p}{k} \frac{\partial T}{\partial t} \quad (36)$$

Here, T is fiber temperature, z is axial location in fiber, A is fiber cross-sectional area, P is the fiber perimeter, h is heat transfer coefficient as function of the fiber temperature (which can vary with time and fiber location), k is fiber thermal conductivity, and $\dot{e}(z, t)$ is the heat generated per unit volume inside the fiber. Density, specific heat, and thermal conductivity of fiber material are constant with fiber position z . The above PDE is not trivial to solve, so a numerical method must be applied.

First, consider the diagram of fiber discretization below in Figure 38.

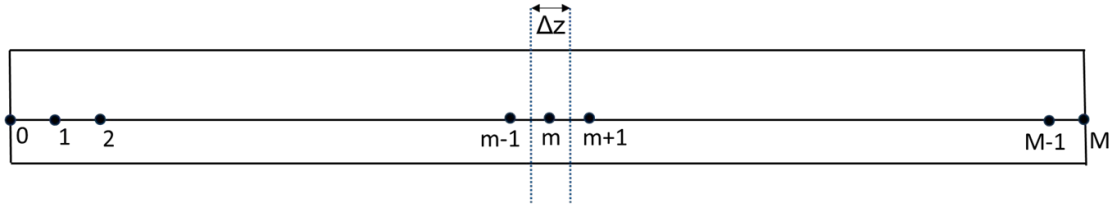


Figure 38: Fiber discretization diagram

The entrance of the fiber (where pump light is launched in) is located at node 0. The end of the fiber where signal light comes out is located at node M. The fiber is discretized into sections each with a length of Δz . The overall fiber has length L. Around each node is considered a control volume.

Develop the 1D heat equation from the more general energy equation.

$$Energy_{in} + Energy_{gen} = Energy_{out} + Energy_{stored}$$

In rate form, this becomes

$$\dot{E}_{in} + \dot{E}_{gen} = \dot{E}_{out} + \frac{dE}{dt}$$

From here, switch for heat terms represented by Q. Look at the sum of heat into and out of an internal control volume. Each internal control volume has conduction to the left and right of it along with convection from the surface area of that control volume. The energy equation then becomes

$$\sum_{all\ sides} (\dot{Q}) + \dot{E}_{gen} = \frac{dE}{dt}$$

$$E = m_{cv}c_pT = \rho V_{cv}c_pT$$

Here, the mass of the fiber segment is calculated from the density and the volume of fiber material in that control volume V_{cv} . Since fibers can handle a change of 100K without loss of (O-O) efficiency, fiber properties can be considered constant with temperature. Therefore, ρ and c_p can come out of the derivative, yielding

$$\sum_{all\ sides} (\dot{Q}) + \dot{E}_{gen,elm} = \rho V_{cv} c_p \frac{dT}{dt}$$

The right hand side of this equation is the change in energy of the fiber material in the control volume. $\dot{E}_{gen,elm}$ is the heat generated inside the fiber control volume. This term is already calculated from the fiber rate equations, so it is known. The sum of Q term is the heat into/out of the control volume due to conduction from the left/right and convection on the fiber surface.

Disregarding the first and last nodes (O and M nodes in below in Figure 38), all other nodes are internal. Using an explicit method for solving the ODE, an equation for the internal nodes can be developed in both space (z) and time. Note, T_m here represents the temperature at a particular node within the fiber. It does not mean the same as it does in the previous section with the laser diode thermal model.

$$\sum_{all\ sides} (\dot{Q}_m^i) + \dot{E}_{gen,m}^i = \rho V_{cv} c_p \left(\frac{T_m^{i+1} - T_m^i}{dt} \right)$$

The letter i represents the current time step, and the letter m represents the current spacial location (see Figure 38). Next, the conduction and convection that make up the sum of Q term need to be defined.

$$\dot{Q}_m^i = \dot{Q}_{m,cond,left}^i + \dot{Q}_{m,cond,right}^i + \dot{Q}_{m,conv}^i$$

$$\dot{Q}_{m,cond,left}^i = \frac{kA(T_{m-1}^i - T_m^i)}{\Delta z}$$

$$\dot{Q}_{m,cond,right}^i = \frac{kA(T_{m+1}^i - T_m^i)}{\Delta z}$$

$$\dot{Q}_{m,conv}^i = h_m^i A_s (T_\infty - T_m^i)$$

$$V_{cv} = A\Delta z$$

Here, k is the thermal conductivity of silica glass, A is the cross-sectional area of the fiber. A_s is the surface area of the fiber control volume for convection to occur through. T_∞ is the ambient temperature of the fluid around the fiber, and h is the heat transfer coefficient (dependent on the fiber temperature at the particular control volume). The heat transfer coefficient h will be different at different locations axially along the fiber (z direction). The variables are further defined below.

$$A = \pi \left(\frac{D}{4}\right)^2$$

$$A_s = \pi D\Delta z$$

Additionally, the energy generation term is defined as follows.

$$\dot{E}_{gen,m}^i = \dot{e}_m^i A\Delta z$$

Here, D is the entire fiber diameter, including fiber core, cladding, and coating. The energy generation rate per volume \dot{e}_m^i is actually calculated by the fiber rate equations and fiber gain media heat generation modeled developed and presented earlier in this document and comes from the $\dot{E}_{gen}(z, t)$, referring back to Figure 10. So, this data must be calculated separately and then it can be used in the fiber thermal model.

Putting all this together yields the final form of the explicit formulation of the 1D heat equation for the internal nodes of fiber thermal modeling.

$$\frac{kA(T_{m-1}^i - T_m^i)}{\Delta z} + \frac{kA(T_{m+1}^i - T_m^i)}{\Delta z} + h_m^i A_s (T_\infty - T_m^i) + \dot{e}_m^i A \Delta z = \rho A \Delta z c_p \left(\frac{T_m^{i+1} - T_m^i}{\Delta t} \right)$$

For the end nodes, 0 and M, two more equations are needed. They are slightly different to account for the half control volume used at the ends instead of the full control volume.

Additionally, the area of the fiber ends is not included in the surface area through which convection occurs. The equation for node 0 is shown below.

$$\frac{kA(T_1^i - T_0^i)}{\Delta z/2} + \frac{h_0^i A_s (T_\infty - T_0^i)}{2} + \frac{\dot{e}_0^i A \Delta z}{2} = \frac{\rho A \Delta z c_p}{2} \left(\frac{T_0^{i+1} - T_0^i}{\Delta t} \right)$$

The equation for node M is shown below.

$$\frac{kA(T_{M-1}^i - T_M^i)}{\Delta z/2} + \frac{h_M^i A_s (T_\infty - T_M^i)}{2} + \frac{\dot{e}_M^i A \Delta z}{2} = \frac{\rho A \Delta z c_p}{2} \left(\frac{T_M^{i+1} - T_M^i}{\Delta t} \right)$$

As a note, the temperatures of all nodes are initialized to the ambient temperature. Also, the Δt term is identical to what was used to solve the rate equations. This is necessary so the energy generation terms are accounted for in the correct time steps. The Δz term is such that the explicit formulation produces a stable, convergent solution. Incidentally, the Δz term used in the fiber heat generation discretized equations is appropriate for use here in the fiber temperature explicit formulation as well. The values for Δz in both equations can be the same. This is fortunate as it is necessary for the energy generation terms to be accounted for at the correct time steps and spacial location.

The next task is to calculate the heat transfer coefficient for each node. Remember, it is based on the temperature of that node. Hence, it will change with both location and time as well. Two cases of convection are considered: External natural and forced convection.

For natural convection, the properties of the fluid around the fiber are of importance. The properties should be found at the film temperature, defined as

$$T_{film,m}^i = \frac{(T_m^i + T_\infty)}{2}$$

Then, use T_{film} to find the temperature dependent parameters like thermal conductivity, kinematic viscosity, thermal expansion coefficient (assuming a gas), and Prandtl Number. For natural convection on a horizontally oriented cylinder, the Rayleigh Number and Nusselt Number correlations are defined as shown below⁹⁵. The characteristic length required here is the fiber diameter D .

$$Ra_{D,m}^i = \frac{g\beta(T_m^i - T_\infty)D^3Pr}{\nu^2}$$

$$Nu_{u,m}^i = \left(0.6 + \frac{0.387 * Ra_{D,m}^{(1/6)}}{\left(1 + (0.559Pr)^{9/16} \right)^{8/27}} \right)^2$$

Here, g is acceleration of gravity, β is the thermal expansion coefficient, Pr is Prandtl Number, and ν is kinematic viscosity. From this, h_m can be found from

$$h_m^i = \frac{k}{D} Nu_{u,m}^i$$

For forced convection, the properties of the fluid around the fiber are just as important. The properties should be found at the film temperature, defined as

$$T_{film,m}^i = \frac{(T_m^i + T_\infty)}{2}$$

Additionally, for forced convection, the Reynolds Number is important.

$$Re = \frac{vD}{\nu}$$

Here, v is the fluid velocity and, as before, ν is the kinematic viscosity and D is the fiber diameter. The relationship for Nusselt number in forced convection for a cylinder in cross flow are functions of Reynolds Number and Prandtl Number as shown below⁹⁵. The empirical relations are different depending on the Reynolds Number.

For Re between 40 and 3999,

$$Nu = 0.683Re^{0.466}Pr^{(1/3)}$$

For Re between 4000 and 39999,

$$Nu = 0.193Re^{0.618}Pr^{(1/3)}$$

For Re between 40000 and 400000,

$$Nu = 0.027Re^{0.805}Pr^{(1/3)}$$

Both Reynold's and Nusselt Numbers here are found at every spacial location for every timestep, as the fluid properties change with fiber temperature. Then, the heat transfer coefficient can again be found by

$$h_m = \frac{k}{D} Nu$$

Since the film temperature changes as the fiber temperature changes, h_m changes as well.

Hence, a value for h_m has to be found at every spacial location for every timestep when solving the discretized 1D heat equation in order to get an accurate solution. The fiber temperature calculations are computationally time consuming in comparison to the diode thermal model.

Analyzing Worst Case Scenario Fiber Temperature Profiles:

The discretized 1D heat equation is easily solved by the explicit formulation. The equation yields a temperature profile of the entire fiber at each time step. As stated earlier, the 5000W of pump light entering the fiber is considered to be at the optimum wavelength and spectrum as well, meaning the fiber will be operating at maximum optical-to-optical (O-O) efficiency. In turn, the heat generation in the fiber will be at its largest. This is the worst-case scenario.

The fiber thermal model parameters, values, and definitions are listed in Table 8 for reference.

Table 8: Fiber Thermal Model Parameters and Definitions

Parameter	Value	Definition
D	0.004	Entire fiber diameter (m)
L	10.8	Fiber length (m)
ρ	2200	Silica glass density (kg/m^3)
k	1.38	Silica glass thermal conductivity (W/m K)
c_p	749	Silica glass specific heat (J/kg K)
T_∞	298	Ambient temperature (K)
T_{init}	298	Initial fiber temperature (K) (same as T_∞)

Using these parameters, the 1d heat equation explicit formulation can be solved to yield the fiber temperature profiles. Figure 39 shows fiber temperature profiles over an 8 second laser activation period occurring at 5 seconds into simulation time. At 13 seconds, the laser turns off.

Notice how $t = 16.6$ sec is smaller than $t = 13.1$ sec, as heat generation is no longer occurring because the laser is off.

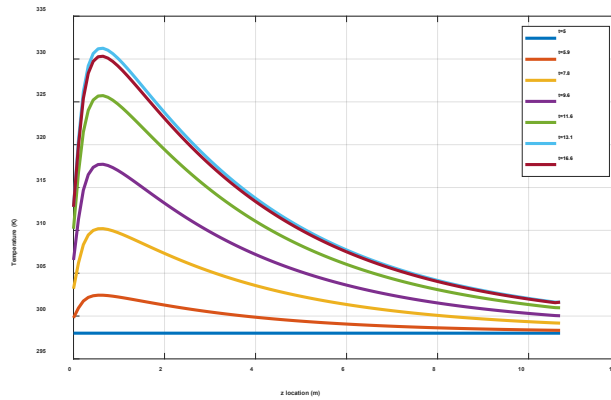


Figure 39: Fiber temperature profiles at various points in time

Natural convection is used in the temperature profile data of Figure 39. Next, consider Figure 40.

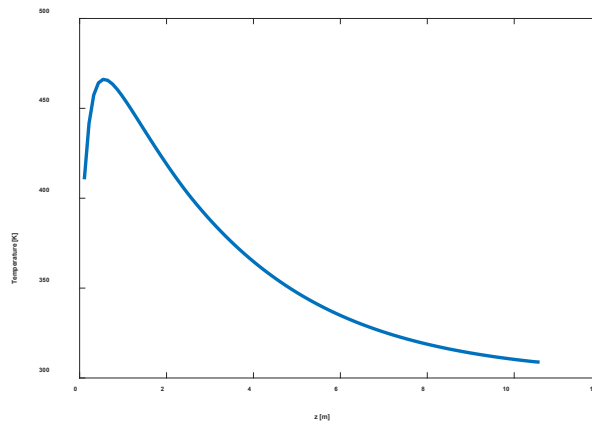


Figure 40: Steady state fiber temperature profile

Here, the fiber temperature profile is taken at steady state conditions using natural convection, meaning the temperature profile is no longer changing with time. This would eventually be reached if the data in Figure 39 was plotted with continuous laser activation. The main take

away here is to note the following. On each profile, a maximum temperature exists. Since the only stipulation on fiber temperature is that the maximum temperature never change by more than 100K, the maximum temperature in the fiber as a function of time is the important data point. Hence, at each time step, keep track of the maximum temperature in the fiber. This way, the data can be simplified for presentation. For example, in Figure 39, there is a maximum temperature of each profile shown. They can be plotted as a function of time. This process is used next to show fiber performance over a range of convection conditions and how the type of convection affects the fiber's duty cycle.

First, consider the natural convection condition. Figure 41 shows the maximum fiber temperature as a function of time for natural convection

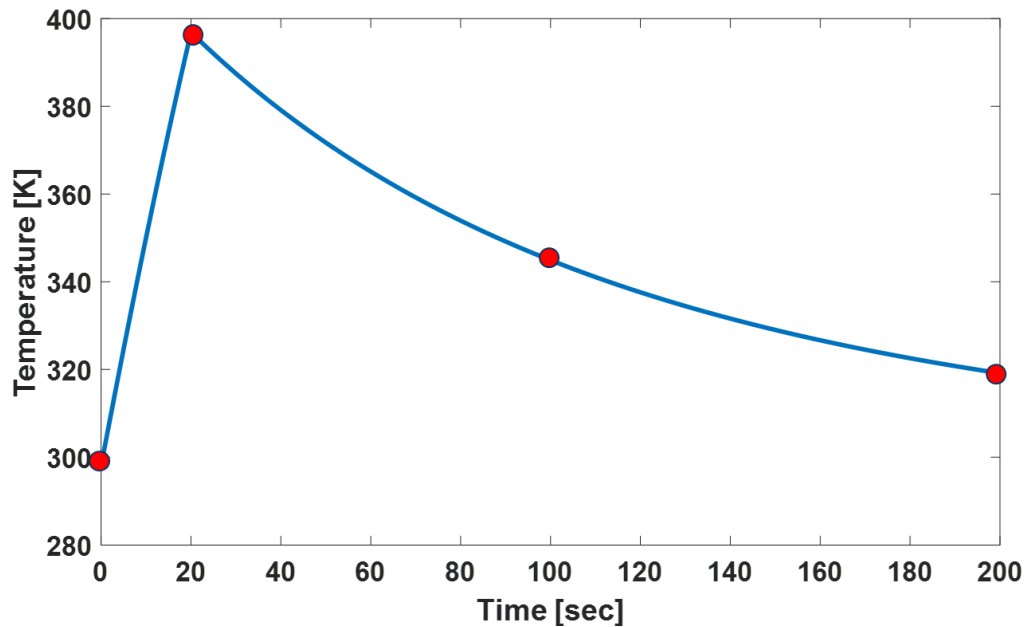


Figure 41: Max fiber temperature with natural convection

The max fiber temperature is within a change of 100K for about 20 seconds. After 20 seconds, the laser turns off and the fiber temperature starts to decrease due to natural convection. At

180 seconds after laser shut off, the max fiber temperature is down to around 320K, not yet back to ambient temperature of 298K. This is characteristic of natural convection, as it is not the most effective way to cool an object. Looking further into the data from Figure 41, the idea of fiber duty cycle can be considered. Duty cycle, as it applies here, is the percent of time the laser can be activated where fiber temperature remains within bounds (delta of 100K). For example, a 40% duty cycle means the laser can be active 40% of the time while remaining within the prescribed temperature bounds with the given thermal management capability. Looking at Figure 41, data shows the fiber temperature increases at a rate of 100K/20 seconds, or 5K per second. At 100 seconds, the max fiber temperature is down to 350K. At 5K per second, it would take almost 10 seconds for the max fiber temperature to increase back to 398K (max temperature allowed). Hence, after the initial activation from 0 to 20 seconds, the fiber could be activated once every 90 seconds for 10 seconds at a time. The duty cycle is $10/90 = 11\%$. The duty cycle needs to be considered in this manner based on the required activation pulse time, as a shorter pulse time means less recovery time required. In other words, the laser can activate more often, just with a shorter activation pulse. It all depends on what the specific laser application requires. Next, the duty cycle for various levels of forced convection is studied.

For forced convection, look at what happens to the max fiber temperature when fluid velocity over the fiber increases. The fluid used in the analysis here is air. Figure 42 shows the maximum fiber temperature as a function of time for forced convection with an air velocity of 1 m/s

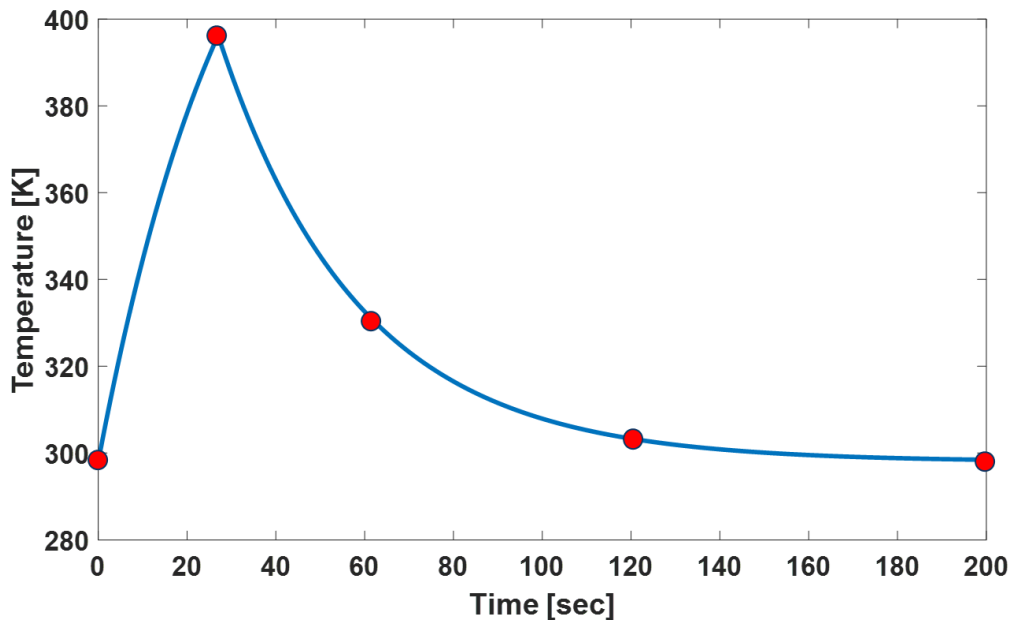


Figure 42: Max fiber temperature with forced convection, velocity of 1 m/s

In Figure 42, the initial rise in max fiber temperature is very similar to that in Figure 41. The max fiber temperature is within a change of 100K for about 25 seconds. However, when the laser is shut off, the fiber temperature cools much faster. At 60 seconds, the fiber temperature is already down to 330K, and back down to 298K by 200 Seconds. Looking at duty cycle in the same manner and observing performance after the initial rise in temperature, the average temperature rise is $100\text{K}/25$ seconds or 4K per second. For the fiber temperature to get from the peak to 330K, it takes 35 seconds. At this point, the laser can then be activated again for 17 seconds to stay within the temperature bounds. The total time for this fall and rise is $35 + 17 = 62$. Hence, the duty cycle for this case of forced convection is $17/62 = 27\%$. Again, the required laser activation time can vary according to the specific laser application. A shorter pulse time means less recovery time.

Figure 43 shows the maximum fiber temperature as a function of time for forced convection with an air velocity of 3 m/s.

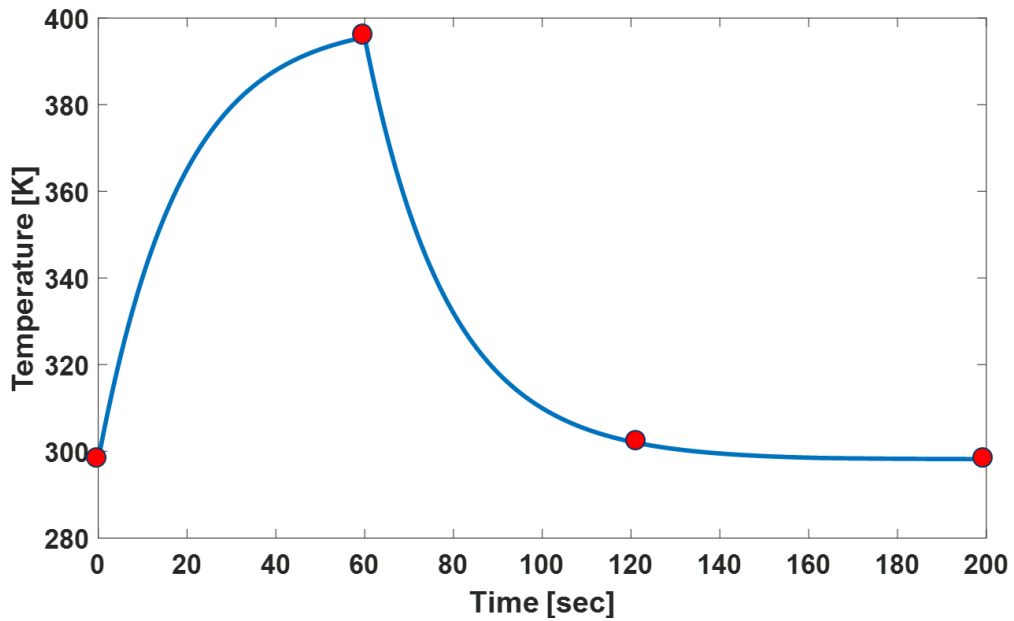


Figure 43: Max fiber temperature with forced convection, velocity of 3 m/s

Here, the max fiber temperature doesn't increase as fast. Now, it takes 60 seconds for the fiber to reach the max temperature limit, and another 60 seconds to drop back down to close to ambient temperature. Hence, the duty cycle here has now increased to $60/120 = 50\%$. This value could be even large if shorter laser activation times were acceptable for the particular application. As expected, an increase in convection is leading to better control of the max fiber temperature. The next plots increase the air velocity even further to confirm this trend.

Figure 44 shows the maximum fiber temperature as a function of time for forced convection with an air velocity of 5 m/s.

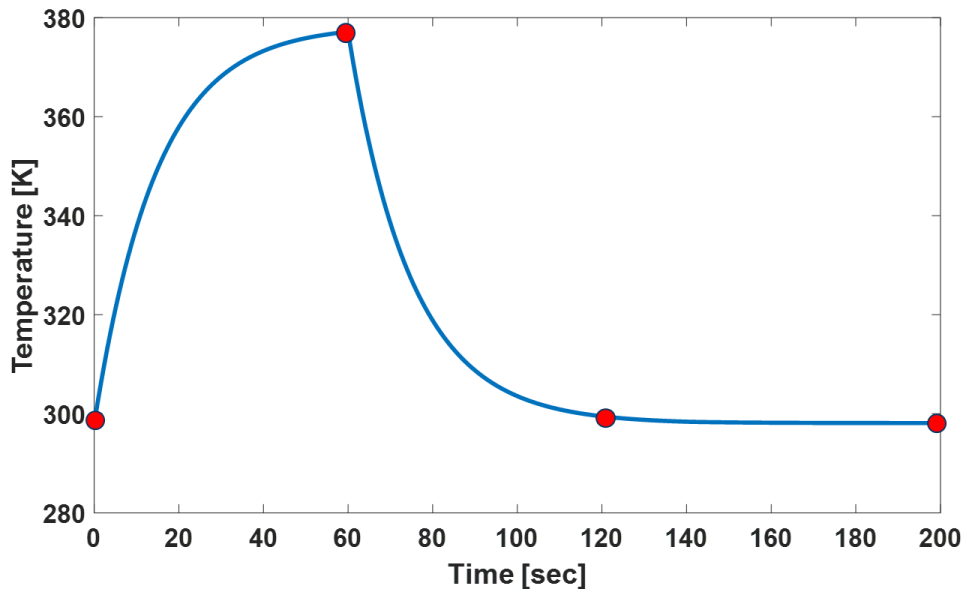


Figure 44: Max fiber temperature with forced convection, velocity of 5 m/s

Here, it is observed that even if the laser was activated for an infinite amount of time, the max fiber temperature would level off before it reached the maximum allowable delta of 100K. This means the convection cooling is such that the fiber can operate for as long as desired and the duty cycle is 100%. At this point, with convective cooling, the fiber temperature is no longer the limiting factor in the amount of time the laser can operate. The limiting factor now is how long the diodes can be properly cooled for. Each laser component has its own duty cycle. If all the respective duty cycles can be 100%, the laser can be operated whenever commanded for as long as commanded. Just to confirm the trend, Figure 45 shows the maximum fiber temperature as a function of time for forced convection with an air velocity of 8 m/s.

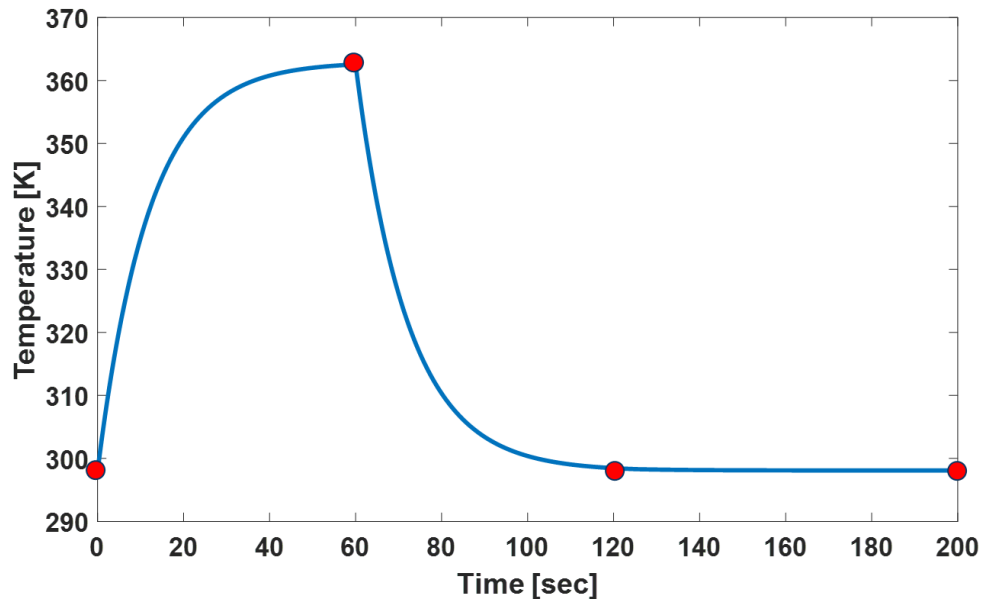


Figure 45: Max fiber temperature with forced convection, velocity of 8 m/s

The max fiber temperature plot here are very similar to Figure 44, except instead of reaching a steady state value of around 380K, the max fiber temperature now reaches a steady state value of around 360K. Clearly, a higher air velocity is giving diminishing returns at this point. The duty cycle of the fiber is again 100%, just as in the case with an air velocity of 5 m/s. It seems 8 m/s is overkill. Hence, there exists a sweet spot, in terms of air velocity, where the fiber duty cycle is 100% but energy is not wasted in providing more convective cooling than is required.

Fiber Temperature Comparison:

The discretized 1D heat equation for solving the fiber temperature here is a simplified approach when compared to previous research, mainly because the previous research has already covered the topic in-depth from the perspective of 2D heat equation (radially and axially along a fiber). The main difference between the previous work and this current research is previous work was done at steady state. The research here (Figure 39) shows fiber temperature profiles

in their transient period of operation. Figure 40 shows the temperature profile at steady state. Additionally, looking at the maximum fiber temperature as a function of time allows for further insight into understanding the thermal requirements to keep the fiber within a certain temperature limit along with the operational duty cycle stemming from a given level of cooling provided to the fiber. Previous research does not compare varying levels of convection to show how fiber temperature reacts to better thermal management. Previous research also does not explicitly state the relations used for finding the heat transfer coefficient. In general, they pick a value and keep that value constant. The fiber thermal modeling developed earlier in this chapter differs from previous work as it lists the Nusselt correlation used (natural or forced convection over a long cylinder) and also recalculates the heat transfer coefficient at every timestep for every fiber segment based on the changing temperature of said fiber segment.

Li et al.¹¹ modeled the steady state temperature profile of a 20 m Yb^{3+} fiber at various levels of launched pump power up to 1000W. They used the 2D heat equation in its cylindrical form with a convection boundary condition on the lateral fiber surface, coupled with the rate equations for finding the heat generation term. They do not list a value for the heat transfer coefficient in temperature calculations, but the temperature profiles are reminiscent of natural convection. Figure 46 shows their temperature profiles.

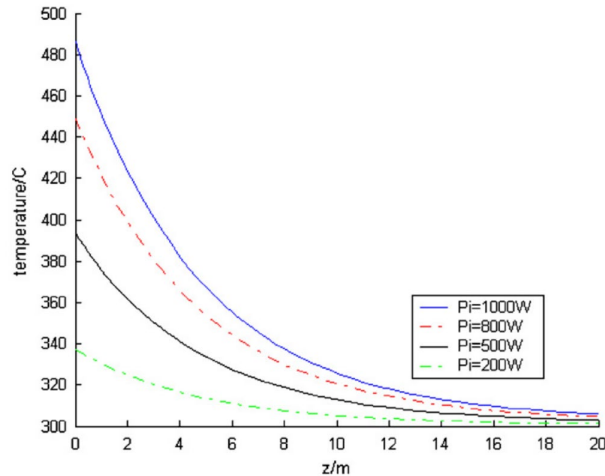


Figure 46: Fiber temperature profiles [reprinted from Li et al.¹¹, Fig. 2]

A higher launched pump power leads to more photon conversion meaning higher temperatures seen in the fiber. In their work, Li et al.¹¹ make note of how the temperature in the radial direction of the fiber varies less than 2°C at the highest power level of 1000 W. The most significant temperature varying occurs axially along the fiber. They note how the maximum temperature of over 480°C means active cooling of the fiber is a necessity. The temperature profiles data in Figure 39 and Figure 40 have a launched pump power of 5000 W, significantly higher than the work by Li et al.¹¹, and yet Figure 40 shows a lower maximum steady state temperature of 152°C versus the 480°C. The reason for the discrepancy here is that Li et al.¹¹ do not model relatively thick polymer coating, giving them a much higher heat generation per unit volume than seen in the data from Figure 40. In general, the trend of fiber temperature being largest where the pump light is being launched match between Figures 40 and 46.

Lv et al.³⁵ calculated temperature profiles of a Yb³⁺ fiber using both the forward and backward pumping schemes of the rate equations. The fiber is 2 m long, much shorter than most other research. Figure 47 shows their temperature profiles.

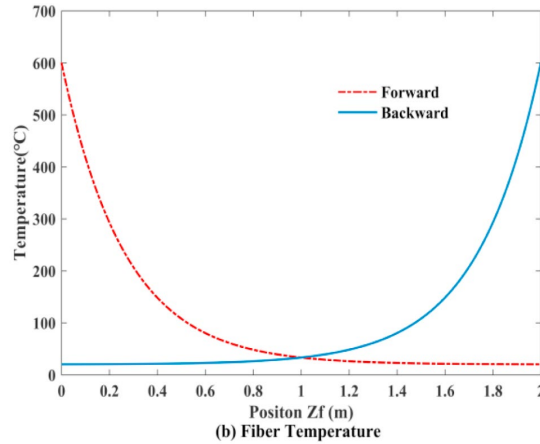


Figure 47: Forward and backward fiber temperature profile [reprinted from Lv et al.³⁵, Fig. 5b]

The launched pump power is 31 W. The pump power filling factor Γ_p is set to 0.25, two orders of magnitude larger than used in the data of Figure 40. This is why the simulated temperatures are so high in such a short fiber. A larger Γ_p means more pump power can be converted in a much shorter distance, generating more heat in a smaller section of fiber. They used a heat transfer coefficient of 3.178 W/m² K. Again, looking at the temperature profiles, it is likely natural convection was modeled. In their work, Lv et al.³⁵ make note of the large temperatures seen in the fiber at steady state and state how the temperature has gone well beyond the safe work scope. They recommend using effective cooling measures for higher pump power levels, and such a recommendation is further evidence that they did not use any type of forced convection when simulating the fiber temperature.

Abouricha et al.¹⁰² simulated the steady state temperature of a Yb³⁺ doped fiber with a length of 5 m. They used the rate equations to find the heat generation and the 2D heat equation in cylindrical coordinates to find the fiber temperature distribution for forward, backward, and bi-directional pumping schemes. They launched 174 W of pump power into the fiber. They model natural convection in air for cooling the fiber, as evidenced by their use of the Grashof Number

and other telling formulations. The values for parameters used in the rate equations are very similar to that used in the fiber thermal modeling developed earlier in this chapter (similar core/cladding radii, pump/signal power filling factors, doping ion density etc.). Only the launched pump power differs significantly, as 174 W is much less than the 5000 W used in the fiber thermal modeling developed earlier in this chapter. The steady state fiber temperature profiles from Abouricha et al.¹⁰² are provided in Figure 48.

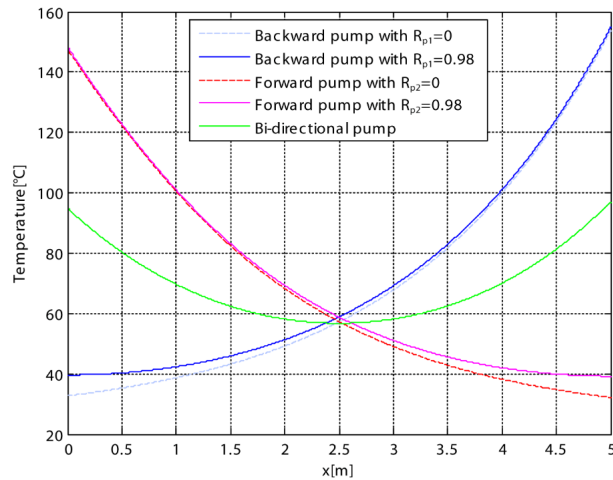


Figure 48: Fiber temperature profiles [reprinted from Abouricha et al.¹⁰², Fig. 5]

Notice again, the same general trend as seen in other previous research appears. For the forward pumping scheme with $R_{p2} = 0$, the highest temperatures are seen near the entrance where pump light is launched. Most photon conversion, as stated before, takes place in this region. Abouricha et al.¹⁰² acknowledge that more active cooling is required to lower fiber temperature to an acceptable value for effective operation and reduction of thermal stresses on the fiber for increased fiber operational lifetime.

Yet another previous work on fiber temperature, Wang et al.¹³, looks at the fiber temperature profiles of a 20 m long Yb^{3+} doped fiber under a bi-directional pumping scheme and

uniform/nonuniform pump absorption coefficients. The fiber thermal modeling developed earlier in this chapter only uses uniform pump absorption coefficients, so only those results from Wang et al.¹³ are presented and discussed. Additionally, the pump power launched into the fiber was 500 W from each end. Wang et al.¹³ were very specific about the thermal management they used for their fiber setup. The fiber was attached to a heat sink. They used natural convection as evidenced by the Grashof Number. Additionally, they selected the required level of natural convection to keep the heat sink at a constant temperature of 300K. The steady state fiber temperature profile from Wang et al.¹³ is provided in Figure 49.

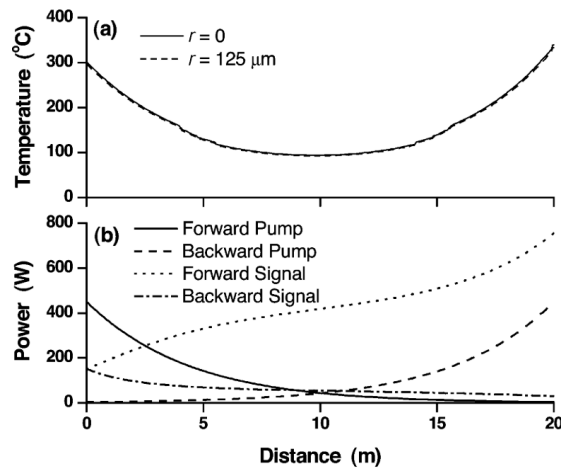


Figure 49: Fiber temperature profile [reprinted from Wang et al.¹³, Fig. 2]

Since the fiber is pumped bi-directionally, there is a temperature rise at each end due to photon conversion taking place. Again, a similar trend emerges in that the the temperature decreases furhter away from where pump light is launched. Although it is not mentioned, the simulated fiber temperature profiles are very high and more active cooling is required to reduce thermal effects on fiber efficiency and performance.

The previous work presented here does not consider thermal management techniques to keep fiber temperature within reason. They simply state that more active cooling is required. They also do not consider the polymer coating of a fiber, which works very well to pull away heat and help maintain reasonable fiber temperatures³². In this way, the fiber thermal modeling developed earlier in this chapter is more robust as it shows how the maximum fiber temperature can be controlled with various level of thermal management. Hence, it can be better understood what level of thermal management is required to achieve a certain maximum temperature in a fiber at steady state while also understanding the system level requirements to provide such cooling capacity to the fiber. Until now, thermal management of the fiber has been largely ignored from such a perspective.

10. Laser and Thermal Performance Analysis:

Presently, a comprehensive model of an HPLS has been created including a representation of fiber laser performance through laser physics along with a set of simplified thermal equations for estimating the laser diode temperatures. Doing so has yielded a multiphysics model capable of capturing what happens to HPLS performance when laser diode temperatures are not properly controlled. The section here uses the newly created model capability to see exactly how diode temperature variation affects HPLS performance.

Time to steady state is an important concept in system analysis. Commonly, the time to steady state is defined as the time it takes for some parameter to reach 99% of its steady state value. In terms of the laser, optical power out reaches steady state when the diode temperatures reach steady state. Hence, the time to steady state for the laser can be found by looking at the time it takes for the final diode bar in the diode array to reach steady state. Recall that the diode temperature estimations are the heat sink temperatures calculated from the diode thermal model. When the final diode bar temperature reaches steady state, the laser output is at steady state. Temperature data from the diode thermal model can easily be used to find this time to steady state. Additionally, the laser is set to activate for a specific amount of time, called the activation time. This activation time, or pulse length, is determined from the particular application. It can vary based on the type of laser and what the laser is being used for. The pulse time and the time to steady state can be combined to create the following parameter.

$$t_{ratio} = \frac{t_{ss}}{t_{pulse}}$$

Here, t_{ss} is the time to steady state of the final heat sink temperature from the diode thermal model and t_{pulse} is the pulse time for the laser. This parameter is useful in determining what

percentage of the pulse time the laser is in transient operation. A lower value of t_{ratio} means the laser is in transient operation for a smaller percentage of the pulse. Driving this value smaller is a sign of better laser thermal management.

Another sign of better laser thermal management is the actual heat sink temperature control. A smaller change in heat sink temperature from reference temperature means more optical energy out of the laser over a certain period of time.

In coupling the laser and thermal models, this information and much more can be gathered for a certain range of input parameters. First, the major parameters in the thermal model are varied to determine some rules for what parameter values produce certain laser performance. These parameters are listed below in Table 9.

Table 9: Thermal parameter sweep values and definitions

Parameter	Value	Definition
A_s	0.001, 0.005, 0.01	Surface through which heat transfer occurs (m ²)
$c_{p,m}$	385	Heat sink material specific heat (J/kg K)
ρ_m	8954	Heat sink material density (kg/m ³)
V_m	1e-5	Heat sink material volume (m ³)
C_m	34.47	Heat sink capacitance (J/K)
k_m	401	Heat sink thermal conductivity (W/m K)
$c_{p,f}$	4184	Fluid specific heat (J/kg K)
ρ_f	1000	Fluid density (kg/m ³)
V_f	2.3e-5, 1.67e-5, 9.65e-6	Fluid volume inside HX (m ³)
C_f	100,70,40	Fluid capacitance (J/K)
C_{ratio}	0.3447, 0.4596, 0.8618	Capacitance ratio
T_{in}	298	Fluid temperature in (K)
\dot{m}	0.05, 0.1, 0.2	Mass flow rate (kg/sec)
P_{Elec}	1800	Electrical power to diodes on a single bar (W)
η_{ref}	1.212	Diode slope efficiency (W/A)
I_{op}	180	Current sent to diodes on a single bar (A)
I_{ref}	15	Threshold Current (A)
T_{ref}	298	Laser diode reference temperature (K)
T_0	180	Threshold current characteristic temperature
T_1	680	Slope efficiency characteristic temperature

Other pertinent parameter values for the laser diode and fiber models are given in Appendix B.

Only one diode array is being simulated in the parameter sweep here. Since diode arrays are cooled in parallel, the thermal performance of each diode array is thermally identical. They can simply be added together for larger laser sizes if desired. Additionally, the fiber is assumed to be a perfect fiber as long the temperature is kept within the limit by appropriate convection cooling. Imperfections in the fiber will only serve to decrease overall laser efficiency. The fiber is very much a laser physics topic and further exploration of it does not serve the purpose and goal of the research presented herein. An entire dissertation could be done on the fiber itself. The

parameters to be varied are each given three possible values. All combinations of these values will be considered in the parameter sweep.

In order to perform the parameter sweep, a design of experiments (DOE) was set up to run the model simulations with every combination of the parameters to be varied: A_s , \dot{m} , and C_{ratio} .

The DOE is 3x3x3, so 27 individual simulations are required. The goal of the DOE is to see trends and observe what values of the parameters yield the best laser performance, then create comes rules of guidance based on these trends.

The DOE simulates a single 5x5 diode array (refer to Figure 6 for a reminder on diode array notation). A sample of diode temperature data is given in Figure 50 how and where values are found based on data from the models.

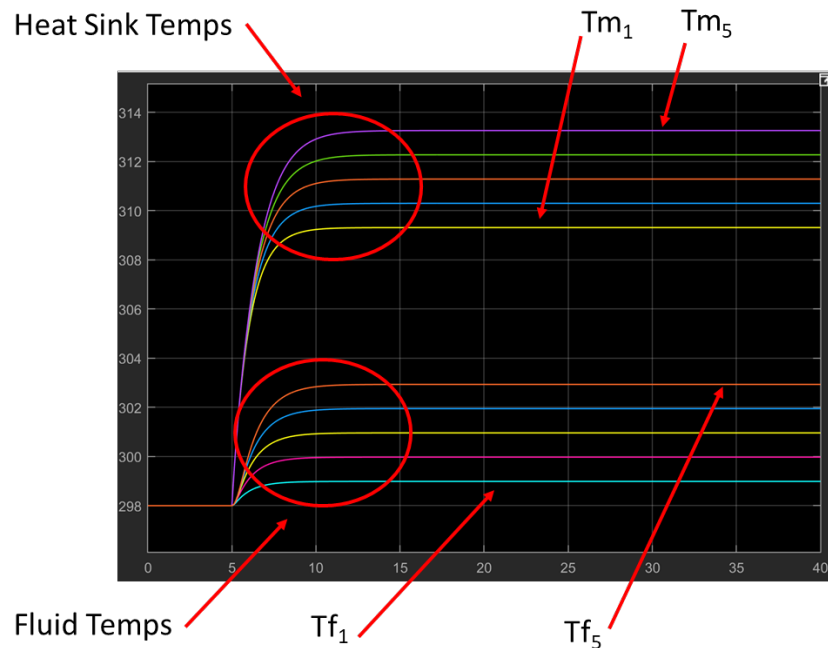


Figure 50: Thermal model data explanation

The sample data is from a 5x5 laser diode array. It gives the 5 values of T_m and T_f as solved for by the thermal model ODEs. For simplicity, the parameters sweep DOE records the average value of T_m and T_f . The range of the T_m and T_f values can be found as well. A smaller range means the laser diode output is more focused around the same center wavelength. This, coupled with T_m values that are closer to the reference temperature, make for a more efficient HPLS because the laser light from the diodes is more likely to be absorbed properly in the fiber. The time to steady state for T_m and T_f can also be found from the thermal model data. When the final heat sink temperature (in this example T_{m5}) reaches steady state, this location in time can be used to find the time to steady state. The same can be performed for T_f . The range of time to steady is also considered here. The earlier nodes in the thermal model come to steady state faster than the later nodes. Hence, the range of time to steady state is a measure of how much longer it takes the final node to reach steady state when compared to the first node. For the parameter sweep data presented here, this means the range is $T_{m5} - T_{m1}$. The same goes for T_f .

Thermal Model Parameter Sweep Results:

The DOE parameters sweep simulations are performed to observe trends and determine what values of the parameters A_s , \dot{m} , and C_{ratio} yield the most change in laser performance over the parameter space. Then, the most significant of the three parameters affecting laser operation can be determined.

The parameter sweep data plots for the laser performance analysis are displayed and discussed here. The laser pulse used in the simulation is 25 seconds long. This time is sufficient to allow

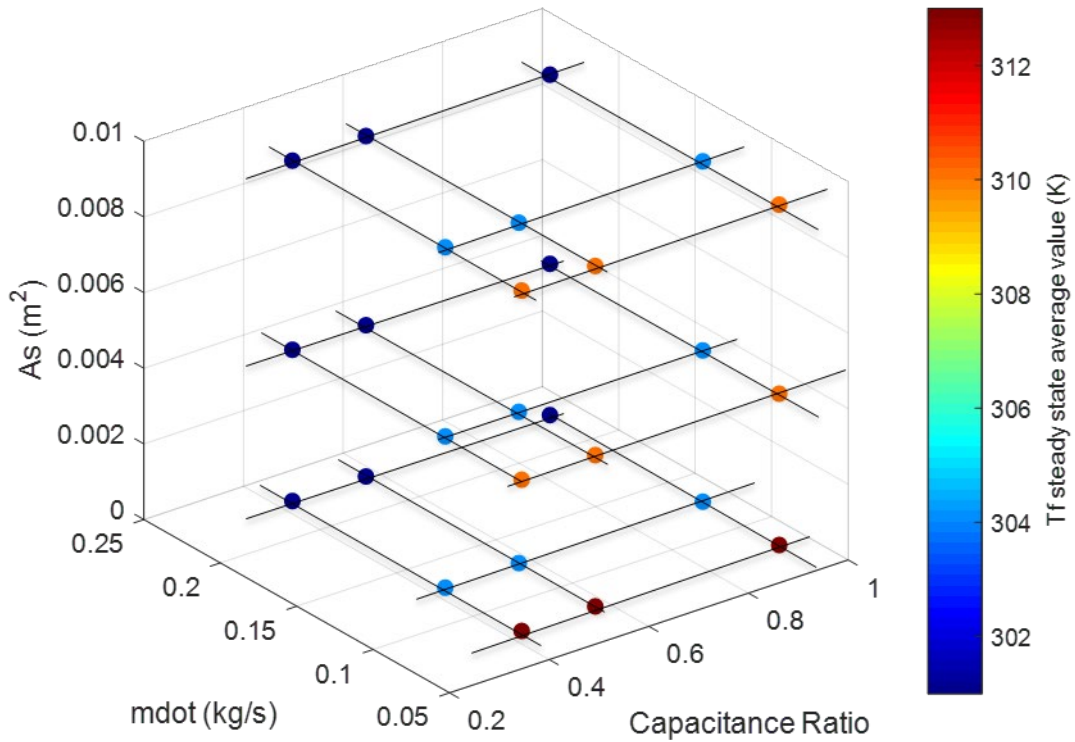


Figure 52: Parameter sweep for average T_f steady state values

The average temperature is found by taking the average of the steady state temperature values of all the nodes in the thermal model. For both plots here, C_{ratio} has no effect on the steady state temperature value. As per the ODEs developed for the thermal model, this is expected. A larger A_s and \dot{m} give a smaller average steady state temperature. This makes sense because these two parameters are used in the contact resistance term. When they are larger, it makes the contact resistance smaller which means better heat transfer occurs. Figure 53 contains the range of T_m steady state values for each combination of parameters.

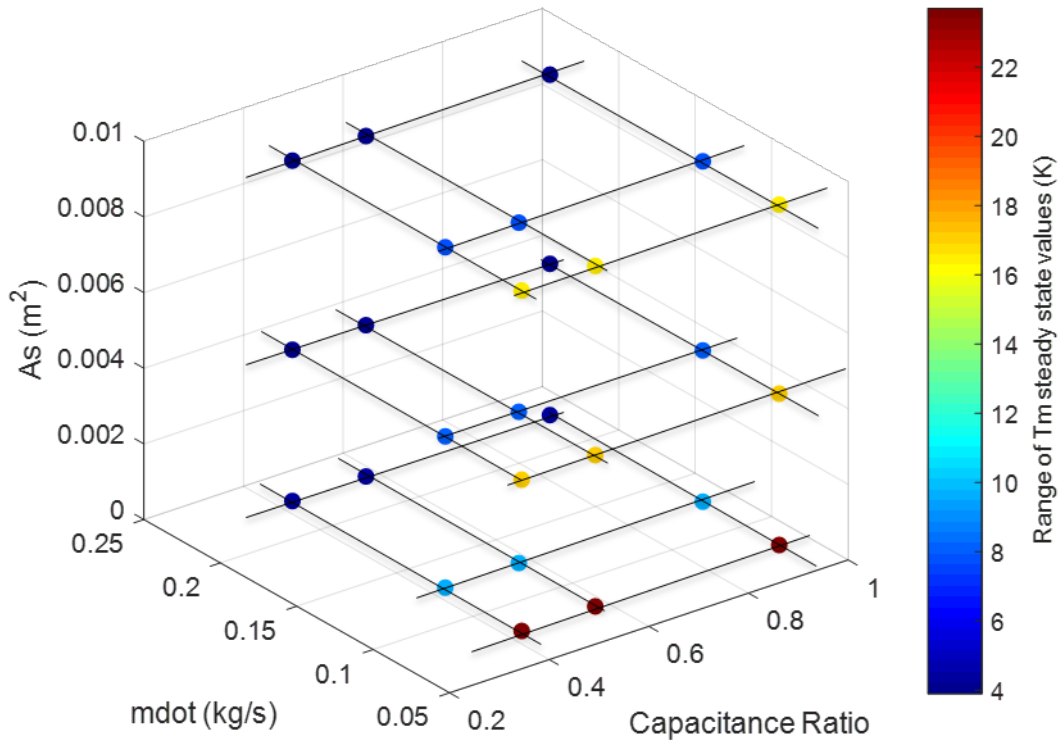


Figure 53: Parameter sweep for range of T_m steady state values

Figure 54 contains the range of T_f steady state values for each combination of parameters.

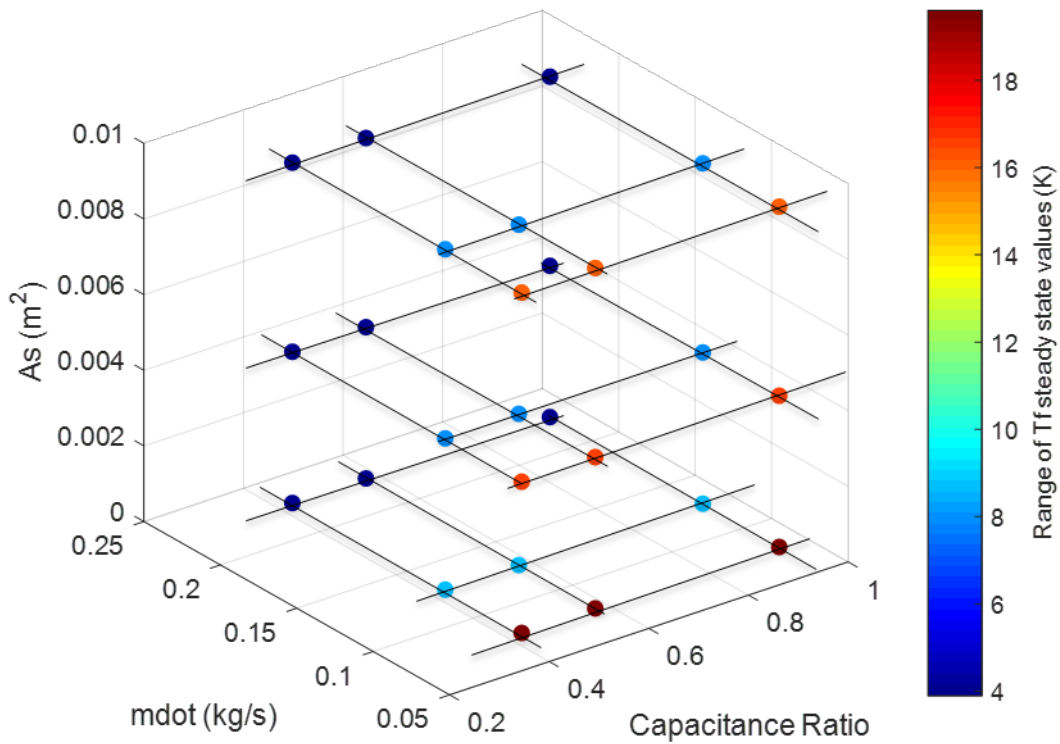


Figure 54: Parameter sweep for range of T_f steady state values

The range is the difference between the temperature values at the first and last node in the thermal model. The range of temperatures for both the heat sink and the fluid is dependent on the A_s and \dot{m} values. Smaller values for temperature range mean a tighter temperature control is achieved. The main observation here is better heat transfer in terms of the contact resistance means the temperatures at each node are closer together. Diodes operating at similar temperatures have a similar output spectrum and center wavelength. Figure 55 contains the time to steady state of T_m for each combination of parameters.

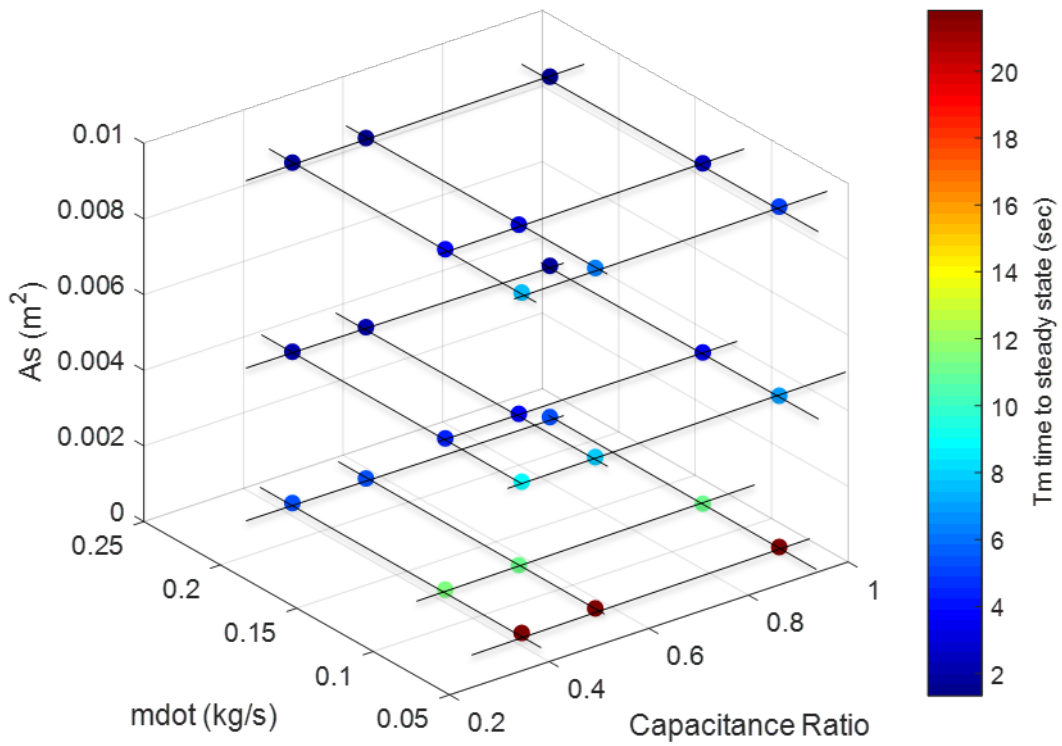


Figure 55: Parameter sweep for time to steady state of T_m values

Figure 56 contains the time to steady state of T_f for each combination of parameters.

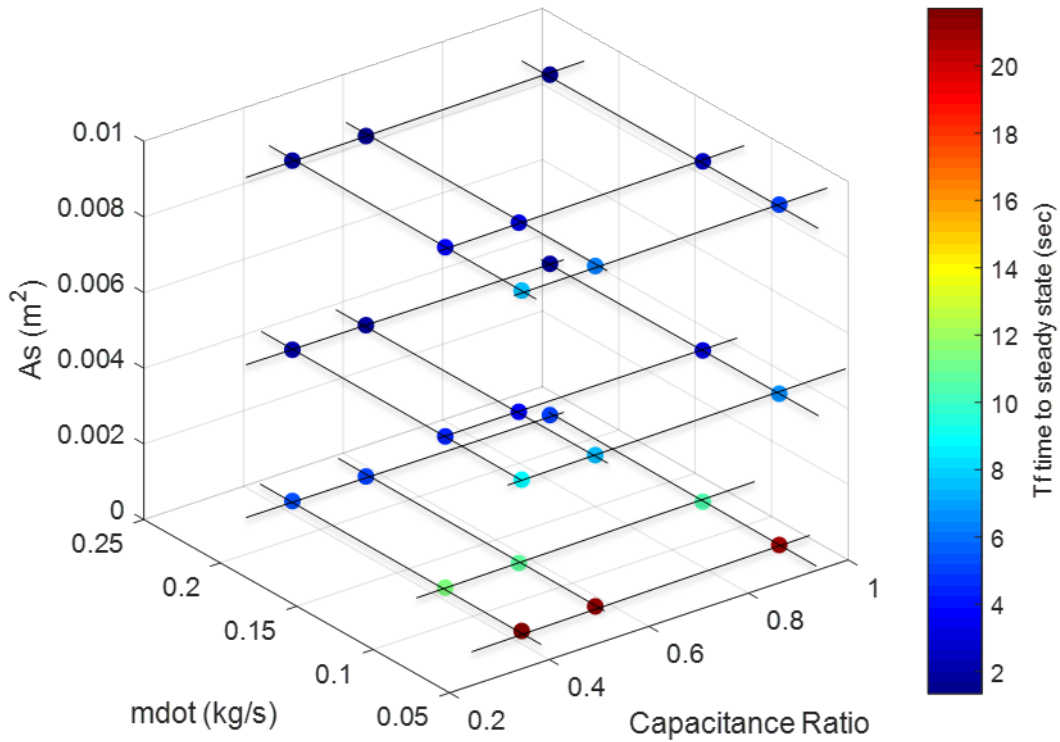


Figure 56: Parameter sweep for time to steady state of T_f values

Here, the times to steady values are from the final thermal node, meaning the laser is considered to be at steady state when the final node temperatures reach steady state. In this parameter sweep, this is the 5th node, as the diode array has 5 diode bars in series. Again, larger A_s and \dot{m} values yield a smaller time to steady state. Notice how the time to steady state is also slightly affected by the C_{ratio} , especially at the lower mass flow rate of 0.05 kg/s. This is from the capacitance delay. A smaller C_{ratio} yields a larger time to steady state. This is because the fluid capacitance is larger than the heat sink capacitance, so the heat sink temperature rise time is limited to the slower rise time of the fluid. Figure 57 contains the range of time to steady state for T_m .

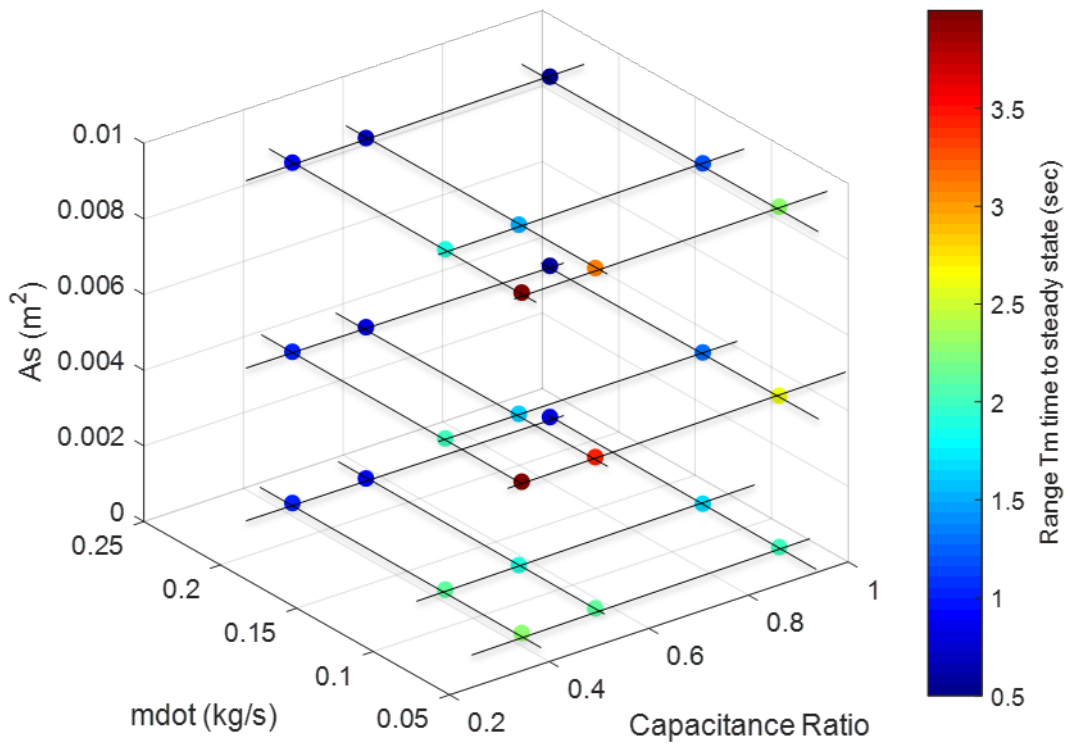


Figure 57: Parameter sweep for range of time to steady state for T_m

Figure 58 contains the range of time to steady state for T_f .

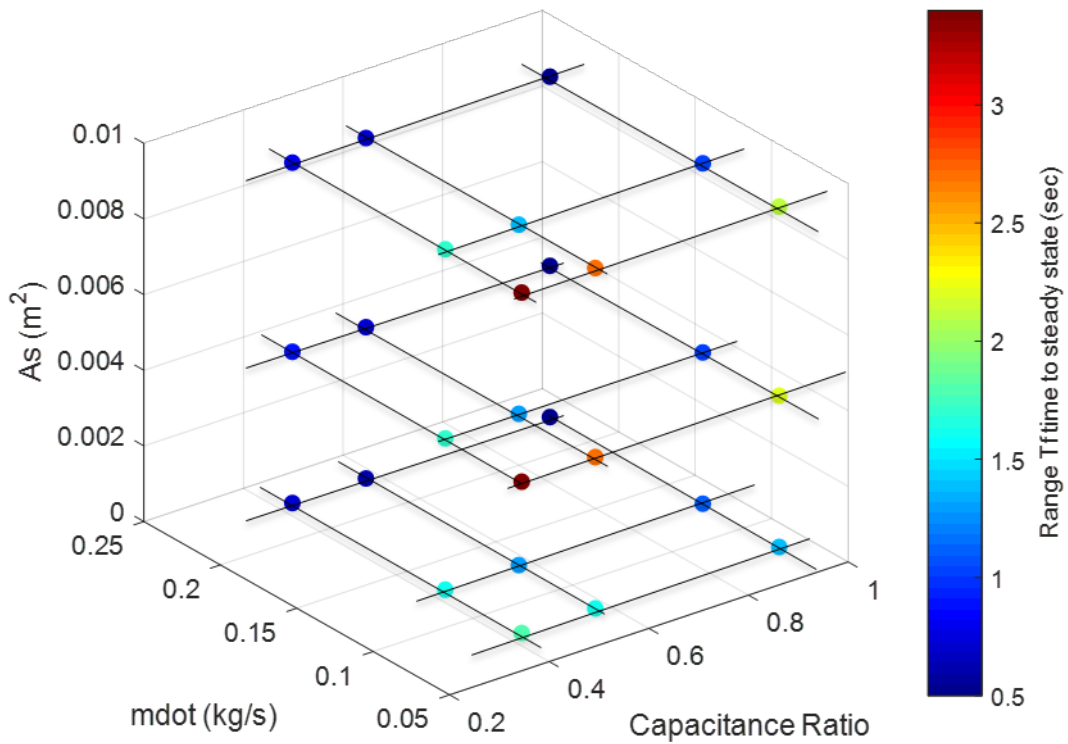


Figure 58: Parameter sweep for range of time to steady state for T_f

The range of time to steady state is the time between when the first node reaches steady state and when the last node reaches steady state. Larger A_s and \dot{m} values yield a smaller range. This is where the capacitance delay really comes into play. Notice how the range of time to steady state changes with C_{ratio} . As C_{ratio} gets closer to one, the range gets smaller. The larger fluid capacitances mean temperatures take longer to reach steady state. Hence, this observation makes sense in the way C_{ratio} is defined. Also, for a small value of \dot{m} , an increasing value of A_s yields an increase in the range. Notice also how the range is increasing as surface area increases. This goes back to how the contact resistance terms and the other terms with \dot{m} affects the ODE solutions. At larger values of \dot{m} , the A_s has less of an effect on the range of time to steady state.

Next, efficiency data for the laser diode and fiber are presented. The efficiency value shown is the steady state efficiency. Figure 59 contains the overall electro-optical (E-O) efficiency of the laser diode array.

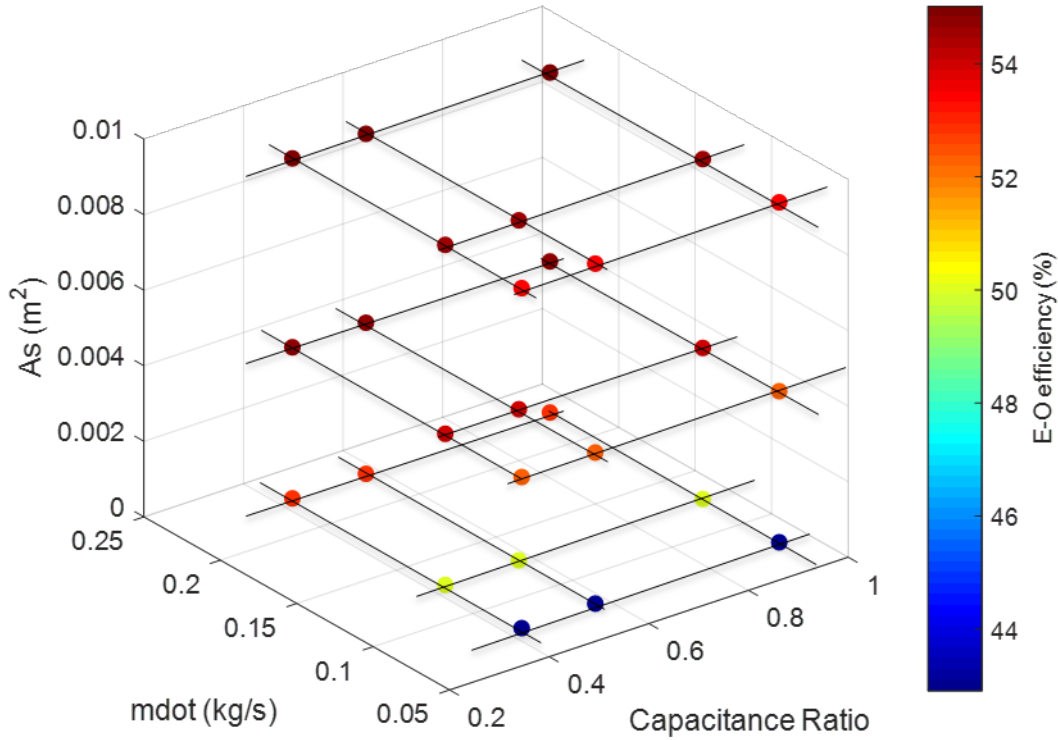


Figure 59: Parameter sweep for overall E-O efficiency of diode array

The overall E-O efficiency of the diode is the efficiency at steady state operation. The maximum overall diode array E-O efficiency is 55%. Again, larger A_s and \dot{m} values yield a higher E-O efficiency because such values yield better heat transfer characteristics in terms of the contact resistance. The lowest value of the E-O efficiency is around 43%, a change of 12% through the parameter space. Figure 60 contains the overall optical-optical (O-O) efficiency of the fiber.

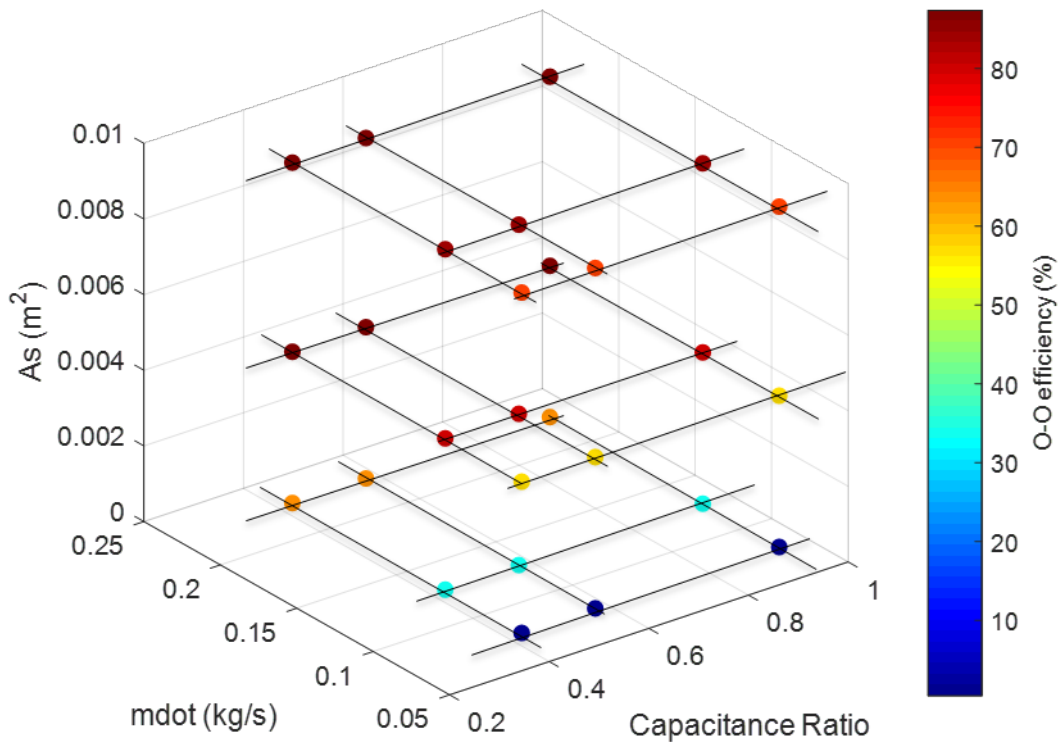


Figure 60: Parameter sweep for overall O-O efficiency of the fiber

The overall O-O efficiency of the fiber is the efficiency at steady state operation. The maximum overall fiber O-O efficiency is 87%. Larger A_s and \dot{m} values yield a higher O-O efficiency because such values yield better diode temperature control. The lowest value of the O-O efficiency is less than 1%. That is an 86% change, significantly larger than the change in E-O efficiency for the same heat sink temperatures. For the fiber, this means the pump light is not being absorbed by and converted in the core. The pump light is simply passing through the fiber and exiting the other side in the cladding. This shows the importance of capturing the center wavelength shift in laser diode output as a function of temperature. It's not just the optical power drop out of the diodes that causes a drop in optical power out of the system. A 12% decrease in diode E-O efficiency actually correlates to an 86% decrease in fiber O-O efficiency due not only to diode

power output decrease, but to center wavelength shift as well. This is a clear indication of why diode temperature control is important. It not only affects the diode performance, but even more significantly affects the fiber performance. The parameter sweep data is evidence of the correlation.

Looking at the E-O efficiency of the diode and the O-O efficiency of the fiber is important, but it doesn't tell the entire story. The data contained in these plots and the other previous parameter sweep data plots are independent of the length of the laser activation pulse. The next three plots are key to tying together the time response and the laser performance. Figure 61 contains the total optical energy out of the fiber over the given laser activation pulse, as a function of the various combinations on thermal parameters. Optical energy output over a given pulse length is an important performance metric.

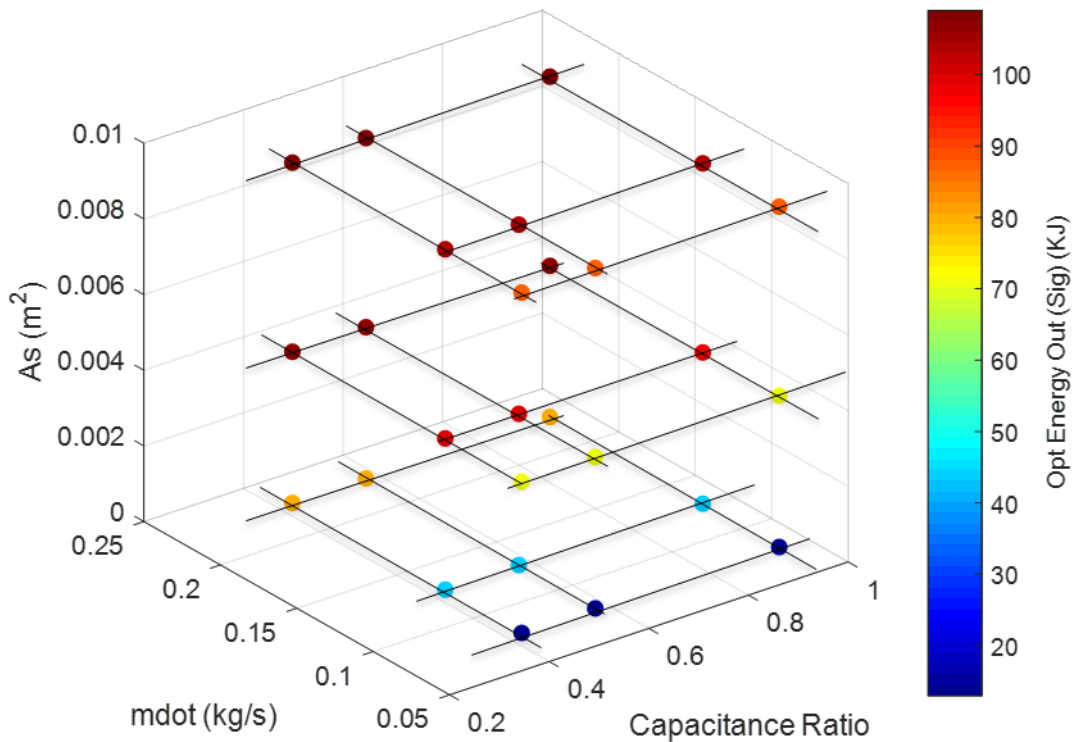


Figure 61: Parameter sweep for total optical energy out of laser with given pulse length

Here, the highest optical energy values are obtained when the A_s and \dot{m} parameters are larger, which really affects performance by way of a smaller contact resistance R_{mf} . Again, laser activation pulse length considered here is 25 seconds. With a different activation pulse length, a different amount of optical energy would be produced by the laser. A longer pulse means more optical energy can be produced during that pulse, with opposite being true for a shorter pulse. Now, consider a situation where diode temperatures are perfectly controlled and maintained at the optimal reference temperature of 298K. For this case, the maximum optical energy out of the laser over the given 25 second pulse is 109,535 J. Then, using the data from Figure 61, a percent of maximum possible optical energy is created to show how well the laser is performing

compared to what it is capable of when diode temperatures are perfectly controlled. This data is shown in Figure 62.

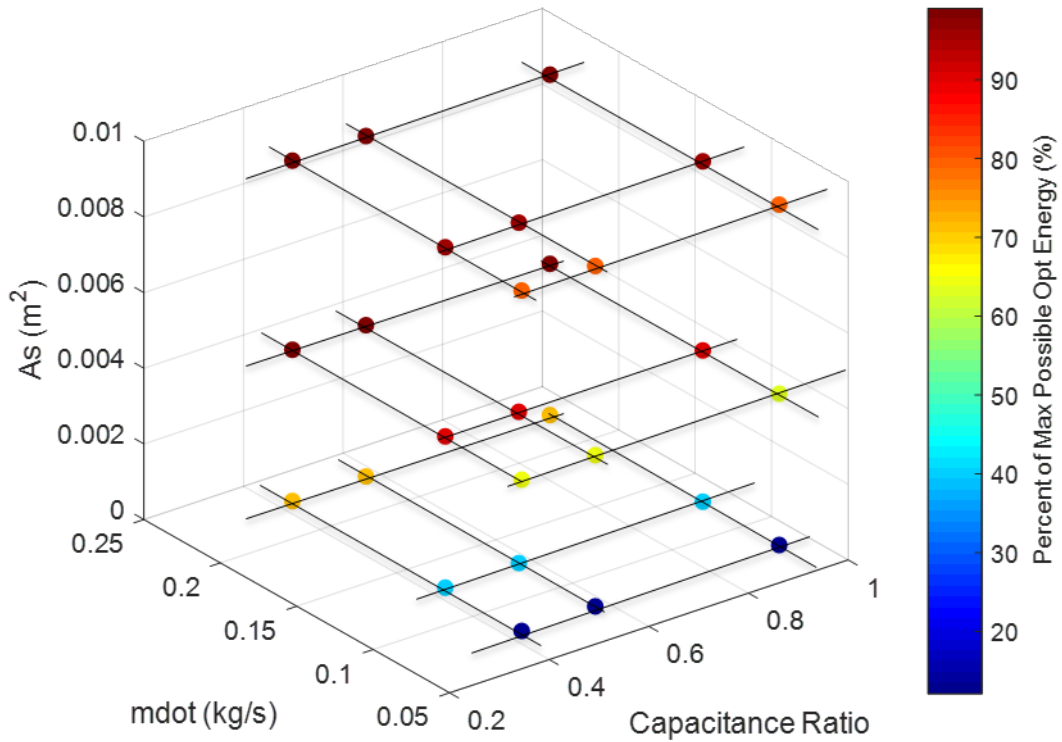


Figure 62: Parameter sweep for percent of maximum possible optical energy

Better thermal control is achieved at higher mass flow rates and surface areas. Those correspond to a higher percentage of maximum possible optical energy. Next, consider the t_{ratio} parameter defined earlier. This is a measure of the percentage of the laser activation pulse during which the laser is in transient operation. The data is shown in Figure 63.

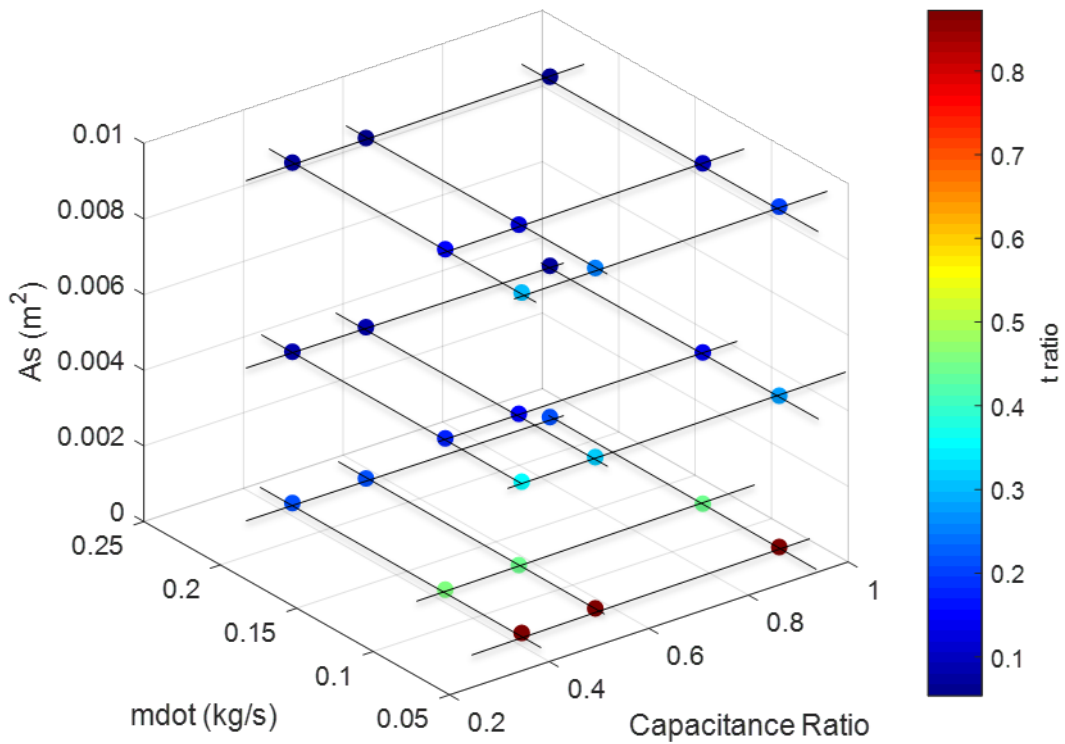


Figure 63: Parameter sweep for t_{ratio} values

The t_{ratio} value can yield valuable insight into laser diode durability. Without going into too much detail (as laser diode durability is not a focus of this research), the amount of time a laser diode spends in transient operation compared to its total operation time affects its lifetime. When laser diodes operate, they experience thermal stresses. This cyclic stress occurs with every pulse. A smaller temperature change (better temperature control) along with a smaller percentage of time spent in transient operation work together for a longer diode lifetime. The time to failure of a laser diode by various modes can be predicted by an empirical Arrhenius equation. Instead of needing experimental data, the data shown in the parameter sweep here directly provides average diode operating temperature predictions and the percentage of time

spent in transient operation. Data from the parameter sweep can be used to calculate values for direct use in an Arrhenius equation if desired.

The parameter sweep provides insight into the most significant thermal parameters affecting laser operation. The two most significant thermal parameters are the area through which heat transfer occurs A_s and the mass flow rate \dot{m} (which extends more generally to Nusselt Number N_u). The capacitance of the diode material and the fluid will vary based on the particular heat exchanger being considered. However, the capacitance only affects the time to steady state, not the steady state temperature. Additionally, it makes sense from a design perspective to keep the capacitances constant, as they are more inherent to the design and not as easy to change. The surface area through which heat transfer occurs A_s is relatively easy to change with different heat exchanger designs (i.e., finned heat exchangers versus shell/tube). Varying A_s can be accomplished in a way that changes the capacitance of the aggregate heat exchanger material very little. If the capacitance values are constant, A_s and N_u are the most significant parameters on the diode thermal side.

11. Laser Diode Parameter Sensitivity Analysis:

A sensitivity analysis is performed on the pertinent laser diode parameters to demonstrate how they affect laser performance. This is considered in a slightly different manner from the parameter sweep performed. The pertinent laser diode parameters are measures of how sensitive a laser diode is to a given temperature change, so the sensitivity analysis here is based around a constant parameter thermal model. The goal is to find out which laser diode parameters are most significant pertaining to laser performance.

The sensitivity analysis provided shows how laser performance changes with the junction temperature dependent parameters ($d\lambda/dT$, $d\beta/dT$, T_0 , T_1). It shows how the optical energy out of the HPLS over an entire pulse (area under the optical power curve) changes when the four parameters are varied by $\pm 25\%$ of their nominal values. The interaction plot also shows how certain parameters affect optical energy more than others. The parameter values used are shown in Table 10.

Table 10: Sensitivity analysis high, low, and nominal parameter values³⁸

Parameter	+25%	Nominal	-25%
$d\lambda/dT$ (nm/K)	0.3125	0.25	0.1785
$d\beta/dT$ (nm/K)	0.1105	.0884	0.0663
T_0 (K)	225	180	135
T_1 (K)	850	680	510

The number of simulations required to capture all the possibilities in Table 10 is given by $3^4 = 81$ total runs for 81 data points of optical energy. Pertinent statistical parameters about the optical energy data are found as follows. Mean: 360.316 kJ. Max: 376.859 kJ. Min: 342.406 kJ. Range: 34.453 kJ. For a $\pm 25\%$ change in the four parameters (Table 10), the optical energy out changes

by +4.6% and -5.0% from the nominal 360.316 kJ. The results provide adequate assurance as to reasonable uncertainty while using the extremes of possible parameter values. Between the four parameters, it is also interesting to look at which ones are most significant in terms of their effect on optical energy out. An interaction plot of the optical energy data is provided in Figure 64.

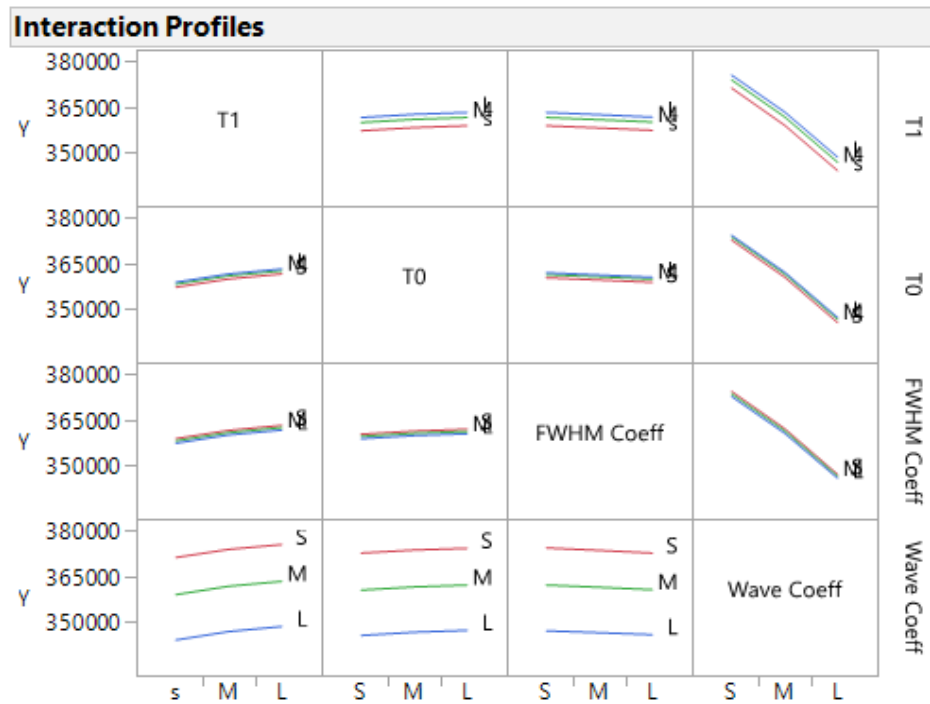


Figure 64: Interaction profiles for wavelength coefficient ($d\lambda/dT$), FWHM coefficient ($d\beta/dT$), T_0 and T_1 , showing the effects of each parameter on optical energy out³⁸

From the interaction plot, $d\lambda/dT$ parameter has the most significant effect on optical energy. Notice the bottom row of graphs showing $d\lambda/dT$ compared to other parameters. The three levels of $d\lambda/dT$ values are given as the three lines on each graph. S, M, and L means -25%, nominal, and +25% values respectively. The curves are relatively far apart, showing a significant effect of $d\lambda/dT$ on optical energy. The next most significant parameter, as seen in Figure 64, is

T_1 . Notice the top row of graphs showing T_1 compared to other parameters. The graphs show a smaller distinction between the S, M, and L levels of T_1 , meaning a smaller effect exists of T_1 on the optical energy. $d\beta/dT$ and T_0 have the least significant effect on optical energy, as per Figure 64. Since no lines in the interaction plot cross or change slope significantly, it can be assumed there are no major interactions between the parameters.

Next, looking at the sensitivity of each parameter individually shows what a 25% variation does to the overall optical output. The data is provided in Table 11. For each run, the parameter values changed are noted. All other parameter values are at the nominal conditions from Table 10.

Table 11: Individual Parameter Sensitivity Analysis³⁸

Parameter	Value	Energy (kJ)	% of Nominal Energy
$d\lambda/dT$ (nm/K)	0.3125	346.90	-4.1
	0.25 (nom)	361.76	--
	0.1785	375.35	+3.8
$d\beta/dT$ (nm/K)	0.1105	360.98	-0.2
	0.0884 (nom)	361.76	--
	0.0663	362.48	+0.2
T_0 (K)	225	362.36	-0.2
	180 (nom)	361.76	--
	135	360.73	+0.3
T_1 (K)	850	363.38	-0.4
	680 (nom)	361.76	--
	510	359.04	+0.7

A 25% change in parameter $d\lambda/dT$ yields a range of optical energy from -4.1% to +3.8% of the nominal optical energy value, $d\beta/dT$ yields -0.2 to +0.2%, T_0 yields -0.2 to +0.3%, and T_1 yields -0.4 to +0.7%. Again, in terms of optical energy, $d\lambda/dT$ is the most significant parameter.

However, in looking at Figure 17, $d\lambda/dT$ and the other three parameters shape the power spectrum curves significantly. All four parameters together change the power spectrum curves

in ways that negatively affect not only the optical energy out, but the spectral power density as well. The amount of optical power contained within a certain signal bandwidth is important in most laser applications, as stated earlier. The extremely focused laser light in a very small wavelength range is what makes a laser effective. All the energy needs to be focused around a single wavelength. As the junction temperature increases and the power spectrum curves get smaller peaks (significantly lower spectral power density) and become wider, less optical power is focused in a certain signal bandwidth wavelength range and the laser becomes much less effective, as the optical power is no longer focused. In most laser applications, the decrease in spectral power density and spectral broadening due to junction temperature change is a bigger concern than the decrease in optical power level (area under the curve). A high level of optical power doesn't mean much if the laser light is not focused along the required signal bandwidth. All four parameters may need to be considered in HPLS modeling depending on the particular laser application required. Overall, values for $d\lambda/dT$, $d\beta/dT$ should be smaller and values for T_0 , T_1 should be larger to create a laser diode with less sensitivity to temperature change. As per the parameter sensitivity analysis shown here, $d\lambda/dT$ is the most significant parameter on the diode physics side.

12. Laser System Statistical Surrogate Modeling:

In research presented thus far, the various laser physics and thermal models have been developed and discussed. When simulated in a coupled manner, the models provide a more complete picture of laser system performance as it relates to optical/thermal interaction than previous research. However, the models are large, complex, and time consuming when used in running simulations. For a given parameter space, it would be highly beneficial to have a surrogate model that can predict various response variables of interest using the most important parameters from the diode physics, fiber physics, and diode thermal models. There are many parameters across all the models that are going to be chosen by the system designer and/or set to required values for the particular laser application (i.e., nominal pump diode center wavelength, required fiber signal wavelength, and heat exchanger parameters like hydraulic diameter etc.).

As a designer, some parameters for a system design are determined ahead of time. Hence, the designer is somewhat limited in terms of the changes they can make to a system. For example, in a laser system, a specific fiber might be chosen for use. Therefore, the fiber cannot be changed. The doping concentration and pump/signal filling factors cannot be changed. The only thing a designer could change, in this situation, is perhaps the length of the fiber. The current section strives to look at laser system design and optimization from a designer's perspective, a practical and applicatory point of view as opposed to a purely theoretical and academic point of view. The research presented thus far has looked at the diode/fiber optical and thermal aspects. In these three areas, from a designer's perspective, there are several parameters that could be changed and adjusted to show laser performance over the parameter space. Realistically, any parameters could be chosen to explore a parameter space. The ones investigated here are

chosen to be from a designer's perspective. Four system parameters are considered: A_s and N_u from the diode thermal model, $d\lambda/dT$ from the diode optical model, and fiber length L from the fiber optical model. The surface area through which heat transfer occurs A_s could be more meaningful if coupled with a power value so it becomes a flux of some kind. The power value used should be constant so the parameter is constant with temperature change. Electrical power provided to the diode bar is a good candidate. Form the parameter as shown below.

$$P_{flux} = \frac{P_{elec}}{A_s}$$

The new parameter P_{flux} is a ratio of the electrical power provided to one diode bar over the area through which the heat generated from that diode bar can move. Recall, A_s is the value of surface area through which heat transfer occurs for one diode bar (one node of the diode thermal model). Multiple diode bars cooled in series requires multiple nodes to be modeled.

The total surface area for the diode array is $A_s * Num_{LD bars}$.

Now, the four parameters across all the models are N_u , P_{flux} , $d\lambda/dT$, and L . The goal is to find a way to predict the values of meaningful response variables (like diode temperature, time to steady state, efficiencies etc.) in a much simpler way while minimizing the error between the predicted values of the surrogate fiber laser model and the actual values of the full fiber laser model. All variables except the four parameters are held to a constant value. In reality, any parameters could be considered, not just four. More parameters simply make the parameter space larger and more difficult to represent through the use of a surrogate model.

The laser optical and thermal models created for this research are complicated. Finding the best surrogate modeling approach is challenging. The process began with no intimate knowledge of what regressions might capture the physics in the parameter space, as the interaction between

the diode and fiber physics models is nonlinear. The regression to best capture the physics could be exponential, logarithmic, quadratic, or a higher order power series. Another question is how to do this for not just one input parameter, but a number of input parameters. Accounting for the interactions between the four most significant parameters (if any exist) is important. At first, simple regression modeling of different forms was used to create a surrogate model. It yielded large errors between the surrogate model predictions and the full physics model actual values for the response variables of interest. The problem required a different approach. The model may be so nonlinear that a sufficiently accurate surrogate model may not be possible.

The next approach to try is a statistical surrogate model, taking things beyond just a regression equation to finding the statistical data on the parameters space from the full physics model. Such values include the average, standard deviation, minimum, maximum, and range. Statistical software is integral for doing such an analysis where there might be thousands of data points within a parameter space.

The software JMP was used to create the statistical surrogate model. JMP allows the user to import simulation data and perform various statistical analysis and modeling. Four response variables were considered: Dimensionless average diode temperature T_m^* , dimensionless average fluid temperature out T_f^* , time for diodes to reach steady state t_{ss} , and overall laser efficiency $overall_{eff}$. $overall_{eff}$ is found from the optical power out of the fiber over the electrical power supplied to the diodes. These four are most meaningful to the current research. The values for all other model parameters used in creating the source data for the statistical modeling are given in Appendix D. Any number of response variables could be considered, depending on what data is relevant. JMP statistical models can be created by the user, and various levels of parameter interaction can be included. More interactions mean a more

complicated statistical model, but it captures more variation. Balancing this will give the simplest statistical model that captures enough variation to sufficiently minimize the percent error between the surrogate model values and the full physics model values.

For data sets of a certain size, JMP provides equations for each parameter and parameter interaction. These equations tell the contribution of each parameter or parameter interaction to the variation of the response variable value from the response variable's average value. When the data set is larger than a certain size, JMP simply provides the contribution at each parameter value. The data sets used for this research are above that certain size, so it will require finding equations of best fit for the contribution of each parameter to the variation of the response variable from its average. This will be further explained when appropriate.

The equations for response variables, whether they are given by equations or created from data to be curve fitted, always contain the average value of the response variable across the data set. Then, the individual functions that represent the contribution to the variation from average are added as necessary, including parameters and parameter interaction. Consider the equation generic equation below.

$$var(1,2,3) = \mu + f(1) + f(2) + f(3) + f(1,2) + f(1,3) + f(2,3)$$

Here, some response variable var is a function of parameters 1, 2, and 3. μ is the statistical average value of var . The various functions in var represent the contribution to the variation of var with a certain value of the parameters. For example, $f(1)$ represents the contribution to the variation of var due to the value of parameter 1. Additionally, $f(1,2)$ represents the contribution to the variation of var due to the value of the interaction of parameters 1 and 2. In order to minimize percent error between the surrogate model and the full model, not all terms

may be used. The interactions may not be significant. Shown are interactions up to degree 2. It is possible that higher degree interactions may be significant. Going through the statistical analysis and adding terms until a desired percent error is reached becomes possible through the use of software like JMP. Next, the concept of this generic formulation is applied to the particular statistical model developed based on the parameter space of N_u , P_{flux} , $d\lambda/dT$, and L . Table 12 contains the range of the four parameters for the statistical surrogate model.

Table 12: Parameter space definitions and ranges for N_u , P_{flux} , $d\lambda/dT$, and L

Parameter	Lower	Upper	Sample Points	Total Points
P flux (kW/m ²)	180	900	180, 214, 264, 346, 500, 900	6 ⁴ = 1296
Nu	146	335	146, 185, 223, 261, 298, 335	
Wave Coeff. (nm/K)	0.05	0.25	0.05, 0.09, 0.13, 0.17, 0.21, 0.25	
Fiber L (m)	5	17	5, 7.4, 9.8, 12.2, 14.6, 17	

In this parameter space, there are 1296 points for each possible combination of parameter values. The response variable values at each of these points can be compared with the full physics model data for percent error analysis.

Consider the first of the four response variables T_m^* . It is defined as

$$T_m^*(N_U, P_{flux}) = \mu_{T_m^*} + f1(N_U) + f2(P_{flux}) \quad (37)$$

From the statistical analysis, $\mu_{T_m^*}$ is 1.0388. The $f1$ and $f2$ functions here are defined by curve fitting data provided by JMP. Figure 65 shows the points provided by JMP for $f1$.

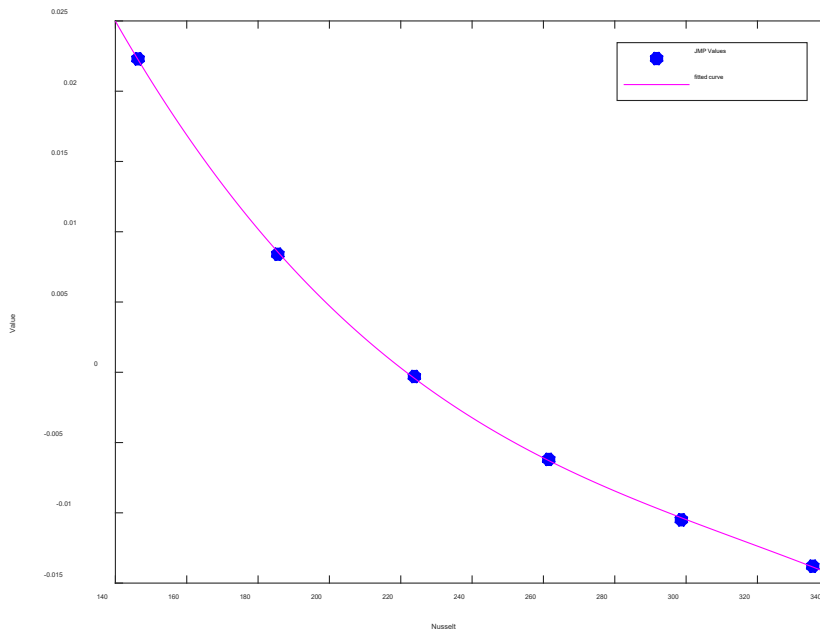


Figure 65: JMP values for $f1$ in T_m^* surrogate model

As N_U changes, $f1$ changes by the fitted curve shown here. The fitted curve is third order, defined as

$$f1(N_U) = p_1 N_u^3 + p_2 N_u^2 + p_3 N_u + p_4$$

The coefficients p are given in Table 13. The same is shown for $f2$ in Figure 66.

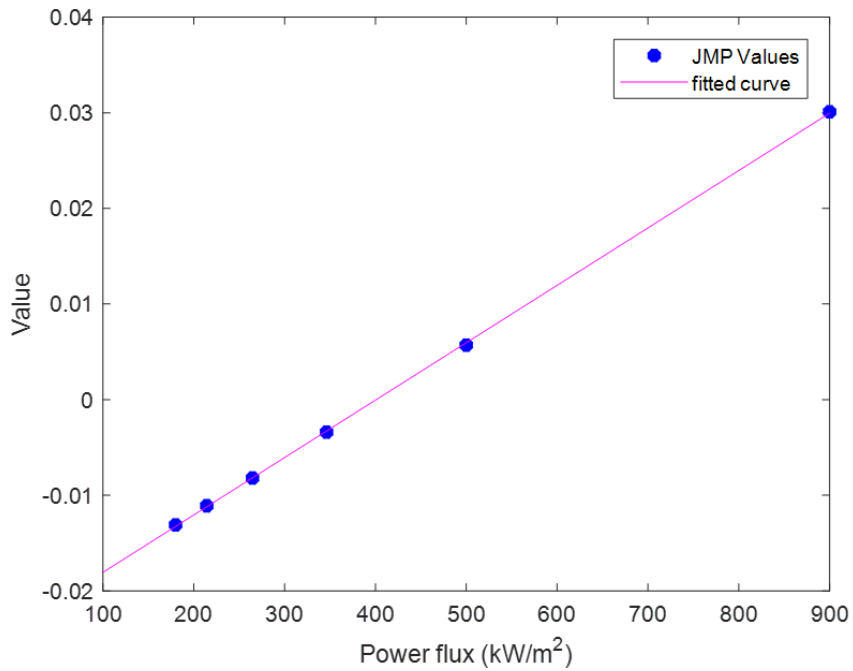


Figure 66: JMP values for f_2 in T_m^* surrogate model

As P_{flux} changes, f_2 changes by the fitted curve shown here. The fitted curve is first order, defined as

$$f_2(P_{flux}) = p_1 P_{flux} + p_2$$

The coefficients p are given in Table 13.

Table 13: Function coefficient values for T_m^* surrogate model

Function	f1 (Nu)	f2 (Pflux)
p1	-3.77873660267427E-09	6.00290163459493E-05
p2	3.57816198745859E-06	-2.40630914247324E-02
p3	-1.22317111829595E-03	
p4	1.36462544571765E-01	

Using the statistical surrogate model as described in equation 37, the average percent error of all 1296 points when compared to the full physics model is 0.30%. The maximum percent error

of all points is 1.58%. Such low percent errors show a reasonably accurate surrogate model to predict T_m^* .

Consider the second of the four response variables T_f^* . It is defined as

$$T_f^*(N_U, P_{flux}) = \mu_{T_f^*} + f1(N_U) + f2(P_{flux}) \quad (38)$$

From the statistical analysis, $\mu_{T_m^*}$ is 1.0156. The $f1$ and $f2$ functions here are defined by curve fitting data provided by JMP. In equation 38, $f1$ and $f2$ functions are defined as

$$f1(N_U) = p_1 N_u^3 + p_2 N_u^2 + p_3 N_u + p_4$$

$$f2(P_{flux}) = p_1 P_{flux} + p_2$$

The plots of $f1$ and $f2$ functions in equation 38, along with the coefficients p , are listed in Appendix C. Using the statistical surrogate model as described in equation 38, the average percent error of all 1296 points when compared to the full physics model is 0.01%. The maximum percent error of all points is 0.04%. Such low percent errors show a reasonably accurate surrogate model to predict T_f^* .

Consider the third of the four response variables t_{ss} . It is defined as

$$t_{ss}(N_U, P_{flux}) = \mu_{t_{ss}} + f1(N_U) + f2(P_{flux}) + f3(N_U, P_{flux}) \quad (39)$$

From the statistical analysis, $\mu_{t_{ss}}$ is 1.5678. The functions here are defined by curve fitting data provided by JMP. In equation 39, $f1$ through $f3$ functions are defined as

$$f1(N_U) = p_1 N_u^3 + p_2 N_u^2 + p_3 N_u + p_4$$

$$f2(P_{flux}) = p_1 P_{flux} + p_2$$

$$\begin{aligned}
f3(N_u, P_{flux}) = & p_1 + p_2 N_u + p_3 P_{flux} + p_4 N_u^2 + p_5 N_u P_{flux} + p_6 P_{flux}^2 + p_7 N_u^3 \\
& + p_8 N_u^2 P_{flux} + p_9 N_u P_{flux}^2 + p_{10} P_{flux}^3 + p_{11} N_u^4 + p_{12} N_u^3 P_{flux} \\
& + p_{13} N_u^2 P_{flux}^2 + p_{14} N_u P_{flux}^3 + p_{15} P_{flux}^4 + p_{16} N_u^5 + p_{17} N_u^4 P_{flux} \\
& + p_{18} N_u^3 P_{flux}^2 + p_{19} N_u^2 P_{flux}^3 + p_{20} N_u P_{flux}^4
\end{aligned}$$

The plots of $f1$ and $f2$ functions in equation 39, along with the coefficients p , are listed in Appendix C. Notice the interaction term $f3$ is now included. $f1$ and $f2$ are lines in one dimension, whereas $f3$ is a surface in two dimensions. The surface of $f3$ is defined by curve fitting data provided by JMP, 5th order in N_u and 4th order in P_{flux} . The surface is shown in Figure 67. The blue dots are JMP data.

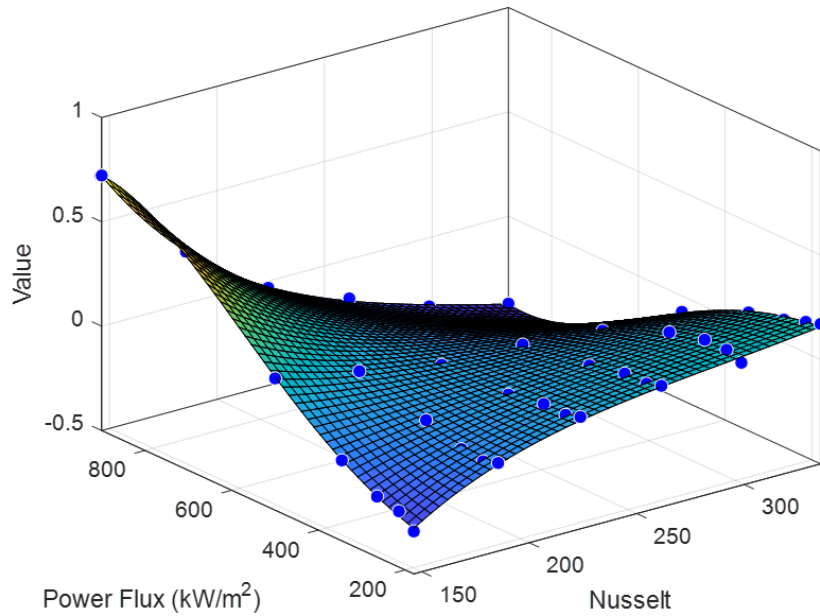


Figure 67: JMP values for $f3$ in t_{ss} surrogate model

The coefficients p for $f3$ are listed in Appendix C. Using the statistical surrogate model as described in equation 38, the average percent error of all 1296 points when compared to the full

physics model is 2.18%. The maximum percent error of all points is 9.68%. The percent errors show a reasonably accurate surrogate model to predict t_{ss} .

The T_m^* and T_f^* surrogate models each require 6 coefficients p . For comparison, the t_{ss} surrogate model has 26 coefficients. The $overall_{eff}$ surrogate model has even more coefficients. Higher order curve fits for the JMP data, especially on the interaction functions, leads to more terms which require more coefficients.

Consider the last response variables $overall_{eff}$. It is defined as

$$\begin{aligned} overall_{eff}(N_U, P_{flux}, \Delta\lambda/\Delta T, L) = & \mu_{overall_{eff}} + f1(N_U) + f2(P_{flux}) + f3(\Delta\lambda/\Delta T) + \\ & f4(L) + f5(N_U, P_{flux}) + f6(\Delta\lambda/\Delta T, P_{flux}) + f7(L, P_{flux}) + f8(\Delta\lambda/\Delta T, N_U) + f9(L, N_U) + \\ & f10(L, \Delta\lambda/\Delta T) \end{aligned} \quad (40)$$

It is a function of all four parameters. From the statistical analysis, $\mu_{overall_{eff}}$ is 44.536. The functions here are defined by curve fitting data provided by JMP. In equation 40, $f1$ through $f10$ functions are defined as

$$f1(N_U) = p_1 N_u^3 + p_2 N_u^2 + p_3 N_u + p_4$$

$$f2(P_{flux}) = p_1 P_{flux}^3 + p_2 P_{flux}^2 + p_3 P_{flux} + p_4$$

$$f3(\Delta\lambda/\Delta T) = p_1 (\Delta\lambda/\Delta T)^3 + p_2 (\Delta\lambda/\Delta T)^2 + p_3 \Delta\lambda/\Delta T + p_4$$

$$f4(L) = p_1 L^3 + p_2 L^2 + p_3 L + p_4$$

$$\begin{aligned} f5(N_U, P_{flux}) = & p_1 + p_2 N_U + p_3 P_{flux} + p_4 N_u^2 + p_5 N_U P_{flux} + p_6 P_{flux}^2 + p_7 N_u^3 \\ & + p_8 N_u^2 P_{flux} + p_9 N_U P_{flux}^2 + p_{10} P_{flux}^3 \end{aligned}$$

$$f6(\Delta\lambda/\Delta T, P_{flux})$$

$$= p_1 + p_2 \Delta\lambda/\Delta T + p_3 P_{flux} + p_4 (\Delta\lambda/\Delta T)^2 + p_5 \Delta\lambda/\Delta T P_{flux} + p_6 P_{flux}^2 \\ + p_7 (\Delta\lambda/\Delta T)^3 + p_8 (\Delta\lambda/\Delta T)^2 P_{flux} + p_9 \Delta\lambda/\Delta T P_{flux}^2 + p_{10} P_{flux}^3$$

$$f7(L, P_{flux}) = p_1 + p_2 L + p_3 P_{flux} + p_4 L^2 + p_5 L P_{flux} + p_6 P_{flux}^2 + p_7 L^3 + p_8 L^2 P_{flux} \\ + p_9 L P_{flux}^2 + p_{10} P_{flux}^3 + p_{11} L^4 + p_{12} L^3 P_{flux} + p_{13} L^2 P_{flux}^2 + p_{14} L P_{flux}^3 \\ + p_{15} P_{flux}^4$$

$$f8(\Delta\lambda/\Delta T, N_u) = p_1 + p_2 \Delta\lambda/\Delta T + p_3 N_u + p_4 (\Delta\lambda/\Delta T)^2 + p_5 \Delta\lambda/\Delta T N_u + p_6 N_u^2 \\ + p_7 (\Delta\lambda/\Delta T)^3 + p_8 (\Delta\lambda/\Delta T)^2 N_u + p_9 \Delta\lambda/\Delta T N_u^2 + p_{10} N_u^3 + p_{11} (\Delta\lambda/\Delta T)^4 \\ + p_{12} (\Delta\lambda/\Delta T)^3 N_u + p_{13} (\Delta\lambda/\Delta T)^2 N_u^2 + p_{14} \Delta\lambda/\Delta T N_u^3 + p_{15} N_u^4$$

$$f9(L, N_u) = p_1 + p_2 L + p_3 N_u + p_4 L^2 + p_5 L N_u + p_6 N_u^2 + p_7 L^3 + p_8 L^2 N_u + p_9 L N_u^2 + p_{10} N_u^3 \\ + p_{11} L^4 + p_{12} L^3 N_u + p_{13} L^2 N_u^2 + p_{14} L N_u^3 + p_{15} N_u^4$$

$$f10(L, \Delta\lambda/\Delta T) = p_1 + p_2 L + p_3 \Delta\lambda/\Delta T + p_4 L^2 + p_5 L \Delta\lambda/\Delta T + p_6 (\Delta\lambda/\Delta T)^2 + p_7 L^3 \\ + p_8 L^2 \Delta\lambda/\Delta T + p_9 L (\Delta\lambda/\Delta T)^2 + p_{10} (\Delta\lambda/\Delta T)^3 + p_{11} L^4 + p_{12} L^3 \Delta\lambda/\Delta T \\ + p_{13} L^2 (\Delta\lambda/\Delta T)^2 + p_{14} L (\Delta\lambda/\Delta T)^3 + p_{15} (\Delta\lambda/\Delta T)^4$$

The plots of $f1$ through $f10$ functions in equation 40, along with the coefficients p , are listed in Appendix C. Note how $f1$ through $f4$ are third order, one dimensional curve fits. $f5$ is a two-dimensional surface fit using 3rd order in N_U and 3rd order in P_{flux} . $f6$ is a two-dimensional surface fit using 3rd order in $\Delta\lambda/\Delta T$ and 3rd order in P_{flux} . $f7$ through $f10$ are two-dimensional surface fits using 4th order in all respective parameters. Using the statistical surrogate model as described in equation 40, the average percent error of all 1296 points when compared to the full

physics model is 1.40%. The maximum percent error of all points is 13.43%. The percent errors show a reasonably accurate surrogate model to predict $overall_{eff}$.

All the various functions that make up equation 40 have a total of 96 coefficients. Like terms could be combined, but that would not significantly reduce the number of coefficients and would actually make organization and implementation of these complex surrogate models more challenging.

The percent error for all response variables are summarized in Table 14.

Table 14: Percent error for all response variables from respective surrogate models

Response Variable	Max error % Source Points	Mean error % Source Points
Overall Eff. (%)	13.43	1.40
Tm* avg	1.58	0.30
Tf* avg	0.04	0.01
time to SS (sec)	9.68	2.18

The data is a source points comparison using the points described in Table 12. In order to confirm the surrogate model accuracy, pick several test points for each parameter that are in between source points. This will tell how good the curve fits are that define each individual function in the response variable equation. The parameter values for these test points are given in Table 15.

Table 15: Parameter values for test points

Parameter	Test Points	Total Points
P flux (kW/m ²)	240, 600, 720	3 ⁴ = 81
Nu	157, 232, 315	
Wave Coeff. (nm/K)	0.07, 0.10, 0.22	
Fiber L (m)	6, 10, 13	

The percent error from the source points can be compared with the test points. The percent error data for the test points is shown in Table 16.

Table 16: Percent error for test points in all surrogate models

Response Variable	Max error % Test Points	Mean error % Test Points
Overall Eff. (%)	6.77	1.64
Tm* avg	0.76	0.34
Tf* avg	0.02	0.01
time to SS (sec)	7.62	3.28

In comparing the test point percent errors with the source point percent errors, the test points show lower maximum percent errors for all response variables. This gives confidence that the curve fits of JMP data are sufficiently accurate within the set parameter ranges. If parameter values are outside of the prescribed ranges, the surrogate model predictions are not guaranteed to be accurate as the surrogate model would be extrapolating in such an instance.

In addition to percent error, the residuals for the source points of each response variable are important to consider. They give a better visual of how the predicted values relate to the actual values and can show for what predicted values the difference is smallest. Percent error is not capable of such insight. The residual data from JMP is provided in Figure 68.

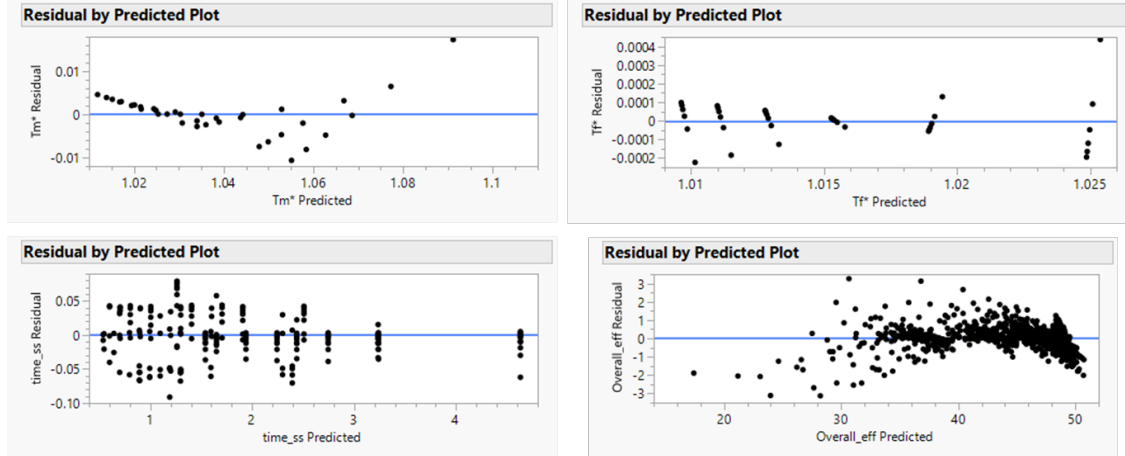


Figure 68: Residuals for each response variable in surrogate models (source points)

As an example, for $overall_{eff}$, the residual is generally lower when the predicted values are larger. Residual values are more scattered when the predicted value is lower. Of the 1296 source points, most are located at larger predicted values (notice the concentration of dots on the right half of the plot). It looks like there are fewer data points for all response variables except $overall_{eff}$. They are dependent only on two parameters, whereas $overall_{eff}$ depends on all four parameters. Hence, parameter combinations repeat themselves throughout the parameter sweep.

Other statistical measures exist as well. Figure 69 shows the actual by predicted plots for the surrogate models of each response variable.

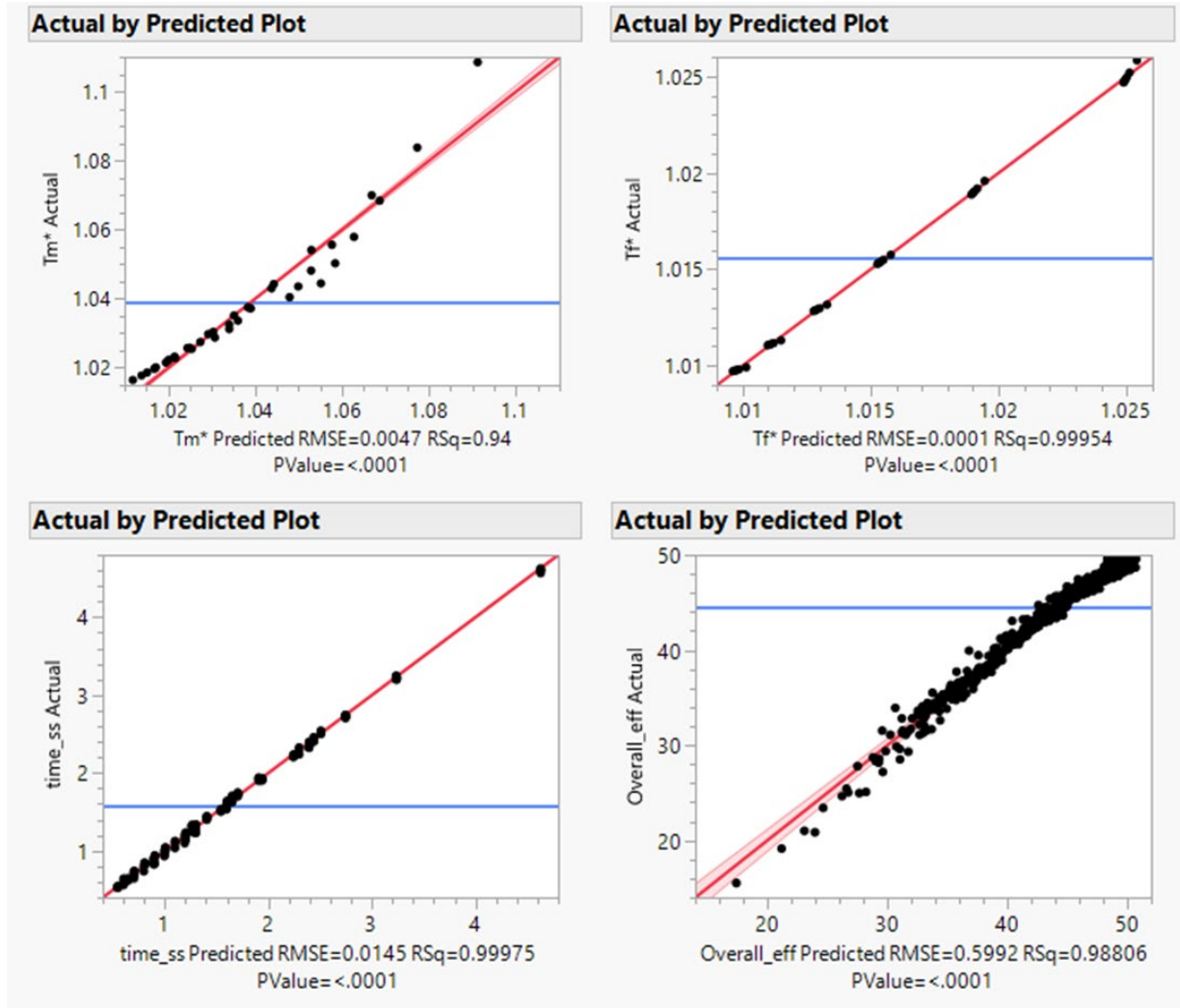


Figure 69: Actual by predicted plots for each response variable in surrogate models (source points)

The R^2 values are provided and they are quite high, which is a good sign. However, they alone cannot guarantee adequate correctness of the model. Correctness and accuracy can be confirmed through using the R^2 value along with the percent error analysis. The statistical significance P value is also listed. In using JMP for the purpose of creating surrogate model for a specified parameter space, the P value doesn't mean much. There is no hypothesis being made with the goal accepting or rejecting a corresponding null hypothesis. Since the full physics model

is determinant (meaning it produces the same result every time for a given set of parameters), there is no meaningful variation to capture in typical sense of a statistical analysis. Rather, the JMP statistical solution to the parameters space is used to create the surrogate model for said parameter space. The statistical solution is only valid with the R^2 and percent error accuracy within the given parameter ranges. Outside those ranges, the surrogate model accuracy is not guaranteed. In the end, the percent error of the surrogate model versus the full physics model tells whether or not it is useful for a particular application. Only a designer can make such a decision as to what percent error is acceptable. Some applications may require lower percent errors, so low that the statistical approach may no longer be sufficient. The solution methodology described here could be used for any other response variables of interest to laser operation, in any prescribed range. The response variables considered here were chosen based on their relevance to this particular research area.

The statistical surrogate model presented has the capability to take complex laser and thermal physics models and simplified them down so each response variable of interest can be represented by a single equation. The single equation is a function of up to four parameters deemed to be the most important from diode physics side, diode thermal side, and fiber physics side. Even with the large number of coefficients in the equations, it provides a way to explore a parameter space with ease. All the data could be exported to a software as basic as Microsoft Excel for design decision making about a given parameter space. An intimate understanding of the most significant parameters and the effect of such understanding on the laser optical/thermal interactions has not, until now, been presented with such coherence and cohesion. Additionally, there has not been presented, until now, a way to bring together all the various laser and thermal physics, along with their most significant parameters, in a way to truly

conceptualize what happens to laser performance when thermal demands are not adequately met. The parameter space forms the basis for more effective system design, as designers now have an exact knowledge of the thermal capability required for a laser system to performance at a specified efficiency.

The surrogate model concept is the bridge to obtaining knowledge about the optical thermal interaction of a laser system within a specified parameter space for further use in higher-level system designing and decision making. Now, for a set of thermal parameters, a designer can quickly see the laser performance and decide if that performance is good enough as per some metric. The metric would differ for each individual application. Perhaps a decrease of efficiency by 10% from maximum is acceptable. The designer can then quickly see which combination of thermal parameters would give that performance. It also allows for the designer to do trade studies.

For example, if the wavelength temperature coefficient $d\lambda/dT$ is made smaller, this means the diode can perhaps see a larger temperature change while producing an identical pump spectrum and optical power level. Now, diode thermal control doesn't need to be as rigorous. Of course, laser diode manufacturing would need innovative technology to do this. The laser diode manufacturers could perhaps look into semiconductor materials that have lower coefficients of thermal expansion, or materials that can deal with higher temperatures.

On the other hand, perhaps laser diode technology is what it is. If diode technology innovations prove more difficult or are not an option, the designer can then focus their attention on the thermal side of things. They can focus on what technologies are available to provide the required thermal capabilities, namely better values for N_u and P_{flux} . It allows them to see how well a specific heat exchanger performs and whether or not that heat exchanger performance is

adequate in terms of diode temperature control. If it is not, they can look at ways to make the heat exchanger more effective. However, they may be limited by size and weight restrictions, as well as heat exchanger technology. The focus then goes back to the entire system. The designer now at least has the tools to decide what laser operation is required and if it is possible to reach that level of operation, given the known system limitations. The statistical surrogate model methodology provides both previously unavailable exploratory capability and design decision making capability pertaining to high power laser systems.

13. Laser Diode Cooling Methodologies:

The surrogate model approach can be used to find any response variable of interest, not just the four described earlier. Certain response variables can be used to analyze any aspect of laser operation. Here, it is shown how knowing overall laser system efficiency for various diode temperatures and times to steady state can be used to determine the best cooling methodology for achieving the highest possible average laser efficiency over an activation pulse with a given thermal capability.

The coolant flow provided to the laser dictates laser performance. Coolant flow rate and flow temperature are key, since the diode thermal model created are only valid for single phase flow.

The time to steady state is an important metric for laser operation. Lasers operate best when they spend the majority of operation time at steady state conditions (pump spectrum is not changing). For a given pulse length, it is best if the laser spends the majority of that pulse in steady state operation. The t_{ratio} value used earlier is again relevant.

$$t_{ratio} = \frac{t_{ss}}{t_{pulse}}$$

The typical profile of laser diode temperature change during a pulse has been shown previously. The temperature starts at a value, normally equal to the cooling fluid inlet temperature, and increases to some steady state value higher than the fluid temperature. The laser diodes should operate at their reference temperature for maximum efficiency. Hence, two possibilities can be considered:

- Laser off-design conditions at steady state, starts at on-design conditions. Diode reference temperature is the same as coolant fluid inlet temperature. (Method A)

- Laser on-design conditions at steady state (precooling), starts at off-design conditions. Coolant fluid temperature is lower than diode reference temp by required amount (diode warms up to its reference temperature). Alternatively, fluid inlet temperature could be the same, and diode with an appropriately higher reference temperature could be used. (Method B)

Figure 70 shows the temperature plots of what Method A and B would look like.

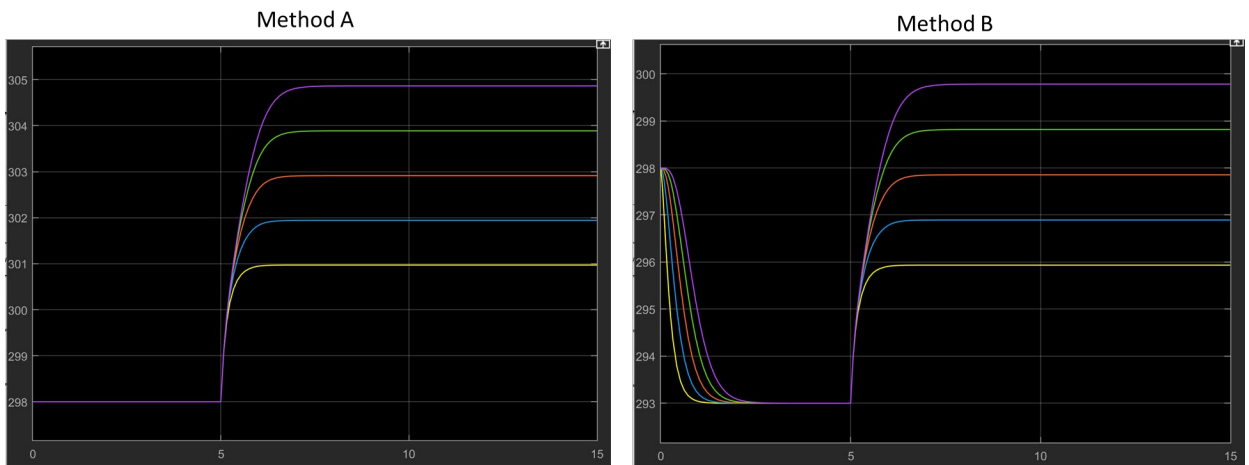


Figure 70: Two cooling methods, A and B

Notice how In Method A, the diode temperatures start at the diode reference temperature (298K) and increased from there when the laser is activated. In Method B, the diode temperature cool from initial temperature condition to the lower fluid in temperature and then warm up to the diode reference temperature, plus or minus some delta based on the range of laser diode temperatures. A certain change in temperature always exists between the diode and the fluid. The goal is to understand how laser performance over a pulse can change depending on where the diode temperatures end up at steady state compared to the diode reference

temperature. Recall, the laser operates at highest efficiency when the laser diode temperatures are kept as close to the diode reference temperature as possible.

The two possibilities, Methods A and B, will both be considered in two separate cases:

1. Adequate diode thermal control (smaller time to steady state, smaller temperature changes)
2. Inadequate diode thermal control (larger time to steady state, larger temperature changes)

The time to steady state t_{ss} and a varying pulse length t_{pulse} will be used to study when a certain cooling methodology can yield better steady state efficiencies for a certain level of diode thermal control. Overall efficiency plotted with increasing pulse length can be used to visualize the effectiveness of the cooling methodologies. The difference between Case 1 and Case 2 for achieving better/worse thermal control is to simply increase or decrease the mass flow rate of cooling fluid.

First, consider Case 1. The thermal capability represented here yields a delta between the laser diode temperatures and coolant fluid of 5K, which is considered very good thermal control. It yields a time to steady state of 2 seconds. For Method A, coolant flow is provided at 298K. For Method B, coolant flow is provided at 293K. Look at the efficiency plots for each cooling methodology (A and B) for varying pulse times from 2 seconds up to 20 seconds, shown in Figure 71.

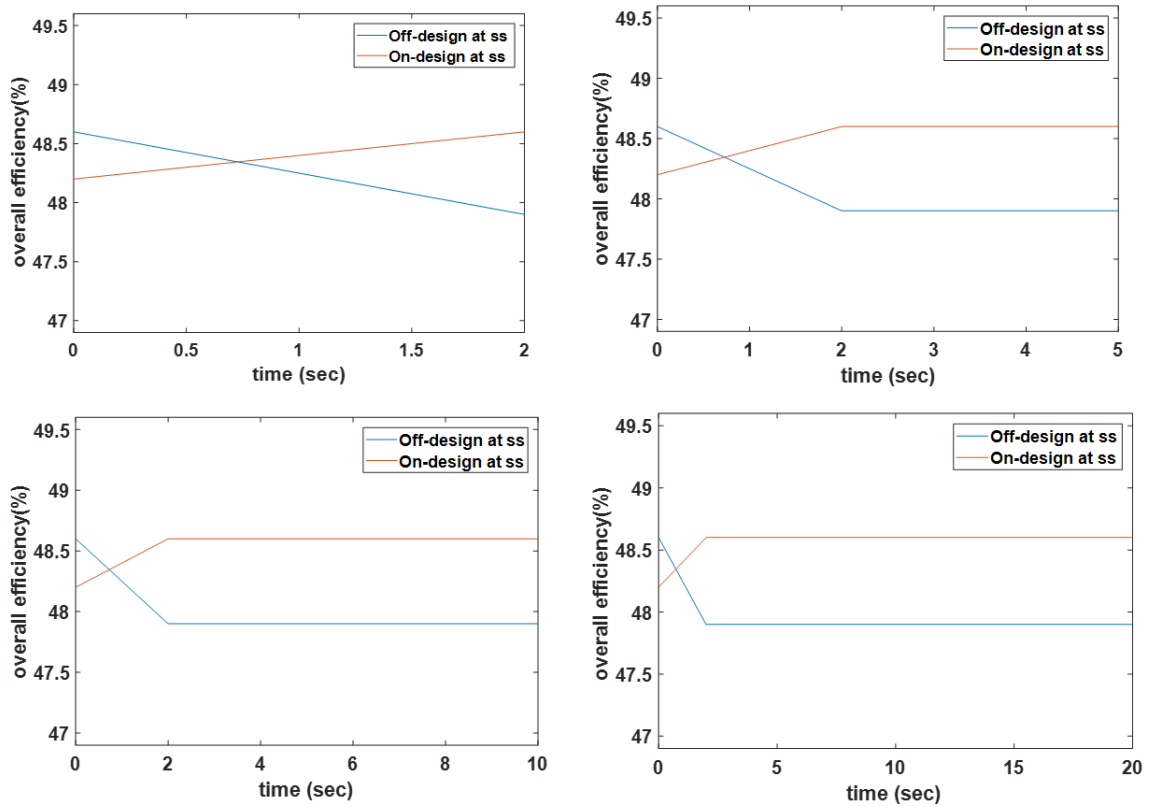


Figure 71: Efficiency plots at varying pulse lengths for cooling methods A and B (Case 1)

The overall efficiency values are known at time of 0 seconds and at the steady state time of 2 seconds. As pulse length increases, the laser operating time at steady state increases, meaning a decrease in t_{ratio} . Case 1, with its good thermal control, shows very little difference between methods A and B. The overall efficiency for each method only differs by half a percent. Here, method A and B give very similar results for overall efficiency, although Method B appears to give slightly higher overall efficiency. Half a percent different would be considered very small for most laser applications.

During the transient period from 0 to 2 seconds, the laser efficiency is changing and represented linearly. This is an approximation to easily represent laser efficiency change during the transient

period. The actual overall efficiency curves during the transient period are more curved in a convex shape towards the magnitude at which they settle out. The shape more follows the laser diode temperature profiles. Since the approach here is for high level design decision making, the already small difference between the linear representation and actual efficiency curve becomes insignificant.

Next, consider Case 2. The thermal capability represented here yields a delta between the laser diode temperatures and coolant fluid of 23K, which is considered poor thermal control. It yields a time to steady state of 4.6 seconds. For Method A, coolant flow is provided at 298K. For Method B, coolant flow is provided at 275K. Look at the efficiency plots for each cooling methodology (A and B) for varying pulse times from 4.6 seconds up to 20 seconds, shown in Figure 72.

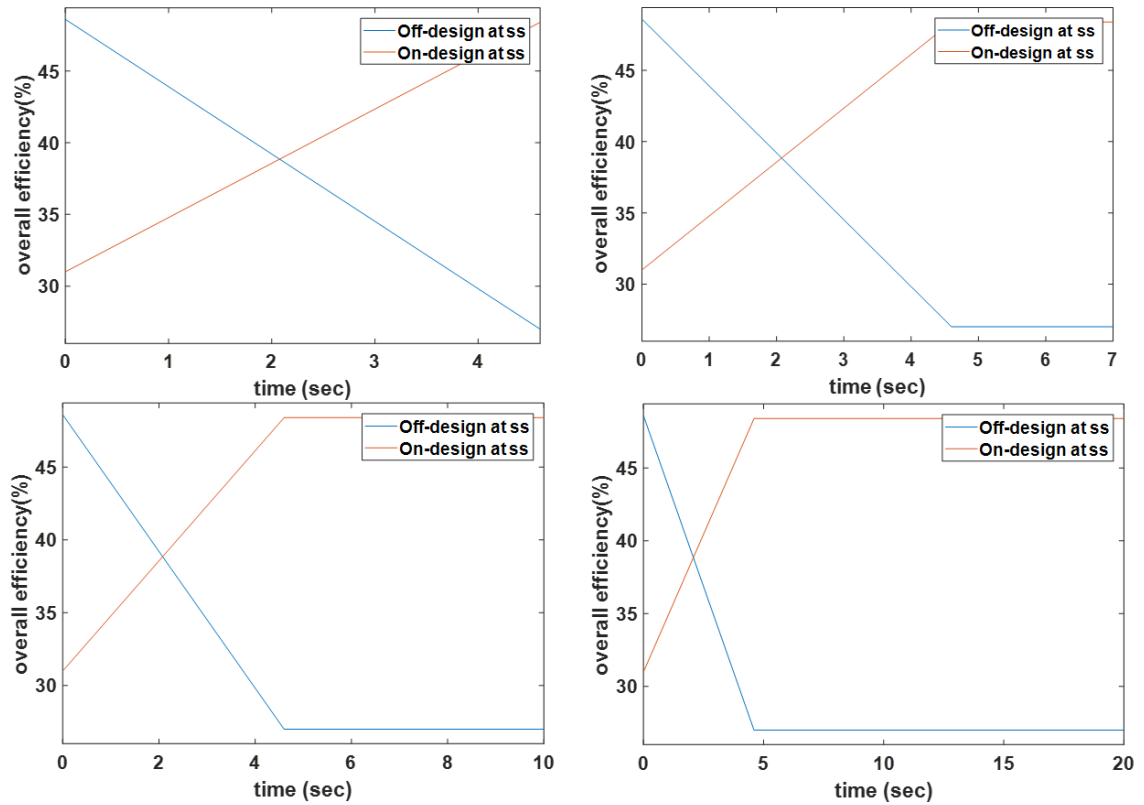


Figure 72: Efficiency plots at varying pulse lengths for cooling methods A and B (Case 2)

The overall efficiency values are known at time of 0 seconds and at the steady state time of 4.6 seconds. As pulse length increases, the laser operating time at steady state increases, meaning a decrease in t_{ratio} . Case 2, with its now poor thermal control, shows significant difference between methods A and B. The overall efficiency for each method differs by over 20%. Here, method A and B give very different results for overall efficiency, and Method B appears to give much higher overall efficiency.

There is a big difference in performance when thermal control is good versus when it is bad. When the temperature delta between the diodes and cooling fluid increases, there is a larger difference between the effectiveness of cooling methods A and B. Hence, it is ideal to operate laser diodes with the smallest possible temperature delta between the diodes and the fluid.

Tentatively, it can be stated Method B is most effective given a sufficient pulse length. However, at this point there is no definite way to find out at what specific pulse length does Method B become the most effective. Additionally, requiring coolant flow at 275K is quite cold for most thermal management systems. For example, water can only be so cold when used as a coolant before it freezes and become unusable. However, instead of changing the coolant fluid temperature, the diode reference could be increased by the appropriate amount so that if coolant fluid temperature is kept the same (298K), the diode reference temperature could be matched to the known temperature rise the diodes will see. For example, if the temperature delta is 23K, the diode reference temperature could be pulse change set to 321K instead of 298K, thus eliminating the need to provide coolant fluid at a lower temperature. However, this would require a new laser diode to be used which has this specific required reference temperature. The diode materials would need to be capable of operating at higher temperatures, which provides some motivation for more research into better laser diode manufacturing processes and material technologies. Instead of better thermal control, a more thermally forgiving laser diode could solve the problem.

There is not just one way to think about optimizing the laser performance from a thermal perspective. If flow regimes other than single phase are an option, the same thing (delta temperature between diodes and fluid plus the relationship with diode reference temperature) will need to be considered in addition to how the new flow regimes behave. It requires thoughtfulness in terms of system design.

The next thing is to develop a metric to show under what circumstances a certain cooling methodology is better for achieving the best possible laser performance. The t_{ratio} parameter will be useful for such an analysis. The approach here uses the average overall laser efficiency

across the entire pulse length from both the transient and steady state sections. It will provide a single overall efficiency value at each given t_{ratio} for Methods A and B. There is a certain value for t_{ratio} where the respective curves for Methods A and B will cross each other. The set of curves will be plotted at increasing values of temperature delta between the laser diodes and the cooling fluid. First, Table 17 provides the temperature delta and corresponding time to steady state for each plot.

Table 17: Temperature delta, time to steady state, and efficiency data for cooling method comparison

Plot #	Delta T (K)	t_{ss} (sec)	Eff @ t = 0 (A)	Eff @ t = t_{ss} (A)	Eff @ t = 0 (B)	Eff @ t = t_{ss} (B)
1	5	2	48.6	47.9	48.2	48.6
2	10	2.7	48.6	46	46.1	48.6
3	13	3.4	48.6	44.1	43.6	48.5
4	19	4.3	48.6	38.5	36.6	48.5
5	24	5.9	48.6	33.7	32.1	48.4
6	33	6.2	48.6	27	31	48.4

To find the average efficiency over a given pulse using the data in Table 17, a pulse length needs to be chosen. Then, in varying the pulse length, the average efficiency for various values of t_{ratio} can be calculated. For example, to find the average efficiency over a pulse if the pulse length is 5 seconds for plot 1 in Table 17, find the average of the efficiency from $t = 0$ to $t = t_{ss}$. This is the average efficiency of the transient section. The average efficiency of the steady state section is the efficiency at t_{ss} . The transeint section of 2/5 of the total pulse time, and the steady state section is 3/5 of the total pulse time. The efficiencies of each section are weighed according to pulse length. Look at equation 41 below. Here, η is used to represent efficiency.

$$\eta_{avg} = \eta_{tran} \frac{t_{ss}}{t_{pulse}} + \eta_{steady} \frac{t_{pulse} - t_{ss}}{t_{pulse}} \quad (41)$$

$$\eta_{tran} = \frac{\eta_{@t=0} + \eta_{@t=t_{ss}}}{2}$$

η_{avg} is then plotted for varying values of pulse length, giving at average efficiency over the entire pulse as a function of t_{ratio} .

Figure 73 shows the average overall efficiency over an increasing pulse length as a function of t_{ratio} for plots 1 and 2.

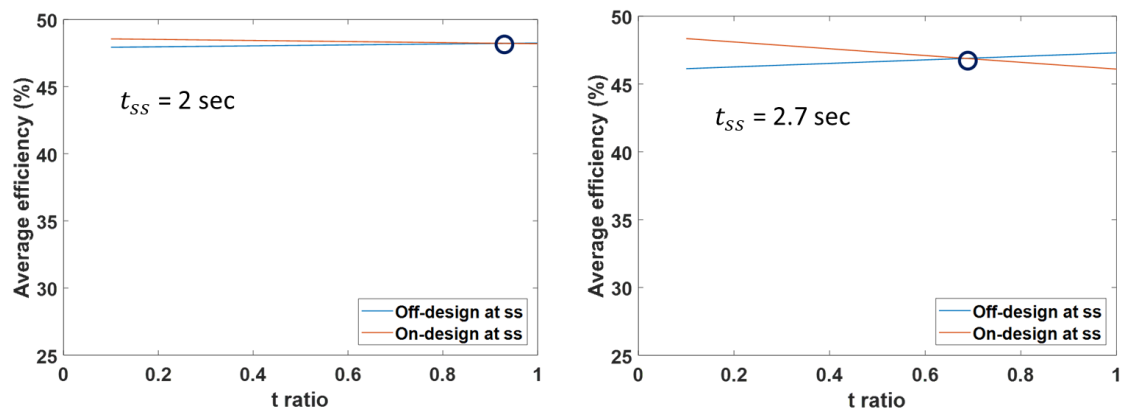


Figure 73: Average overall efficiency for Methods A and B (plots 1 and 2)

The black circle on each plot is the point at which the efficiency lines cross each other. For a t_{ratio} greater than the point of crossing, Method A provides the best efficiency. For a t_{ratio} less than the point of crossing, Method B provides the best efficiency. Notice how slight the difference is between both methods in plot 1. Method B is only slightly better, even at small t_{ratio} values. A smaller temperature delta means there is less difference between the efficiency of each method. Figures 74 and 75 show the average overall efficiency over an increasing pulse length as a function of t_{ratio} for plots 3,4 and plots 5,6 respectively.

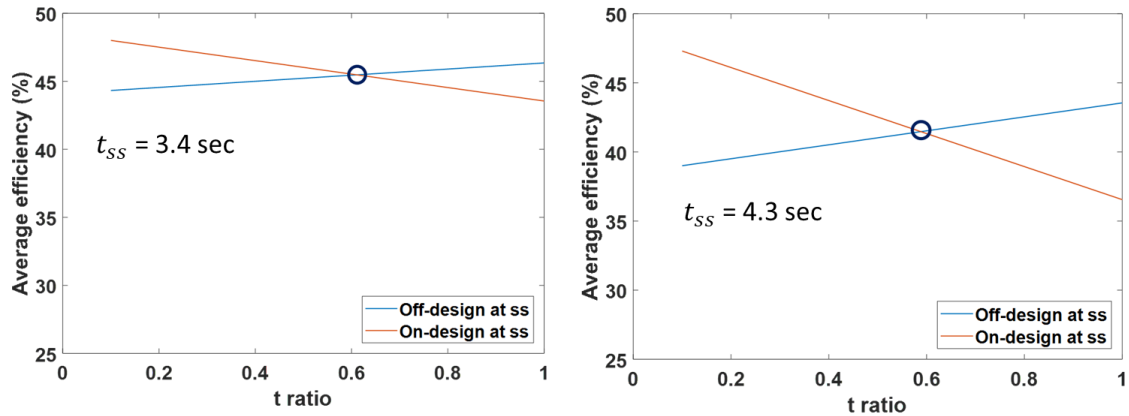


Figure 74: Average overall efficiency for Methods A and B (plots 3 and 4)

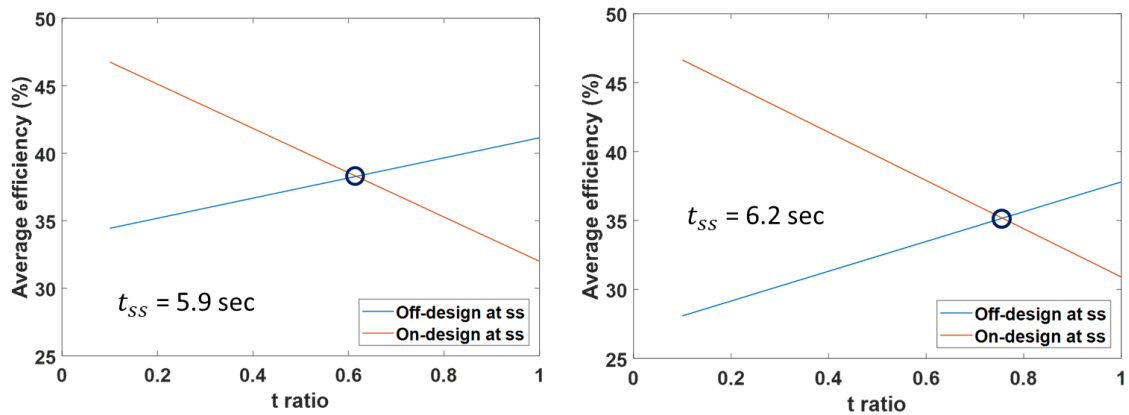


Figure 75: Average overall efficiency for Methods A and B (plots 5 and 6)

The plots not only show the location where the efficiency lines cross, but they also show just how drastically the efficiency curve steepness changes with a decrease in t_{ratio} as the temperature delta increases. For a t_{ratio} greater than the point of crossing, Method A provides the best efficiency. For a t_{ratio} less than the point of crossing, Method B provides the best efficiency. However, as temperature delta increases, it is clear that a smaller t_{ratio} (and therefore larger pulse length) must be obtained in order to achieve the shown efficiencies for

Method B. Table 18 provides the temperature delta and corresponding t_{ratio} cross point location value.

Table 18: Temperature delta and t_{ratio} cross point location value data

Delta T (K)	t_{ratio} at cross point
5	0.93
10	0.69
13	0.61
19	0.59
24	0.62
33	0.76

Plotting data in Table 18 yields the graph in Figure 76.

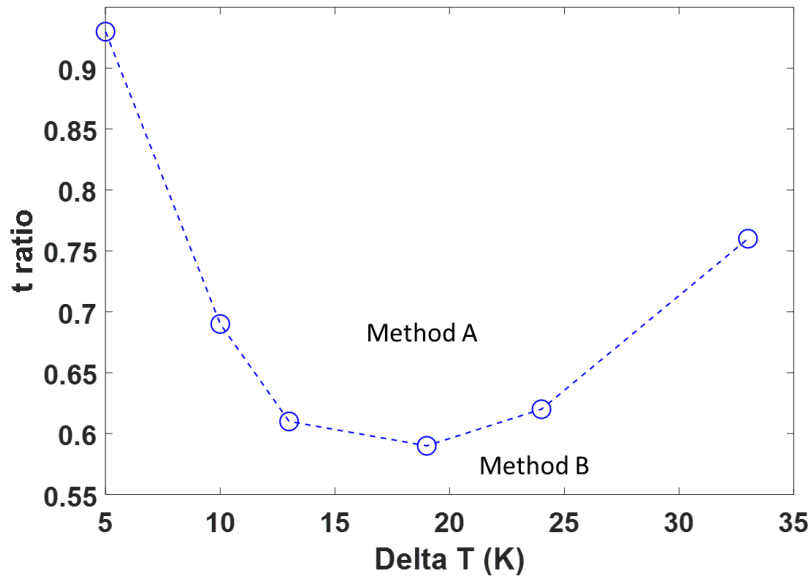


Figure 76: t_{ratio} as a function of temperature delta

For a given temperature delta, at t_{ratio} values greater than the corresponding point on this curve, Method A provides the best efficiency. When t_{ratio} is less than the corresponding point on this curve, Method B provides the best efficiency.

Currently, Figure 76 just has the temperature delta on the x axis. Recall, the parameter $d\lambda/dT$ determines how much the center wavelength of laser diode output shifts for a given temperature change. To make Figure 76 more general, consider t_{ratio} as a function of wavelength shift by

$$\lambda_{shift} = \Delta T * d\lambda/dT$$

Now, plot t_{ratio} as a function of the new variable λ_{shift} in Figure 77.

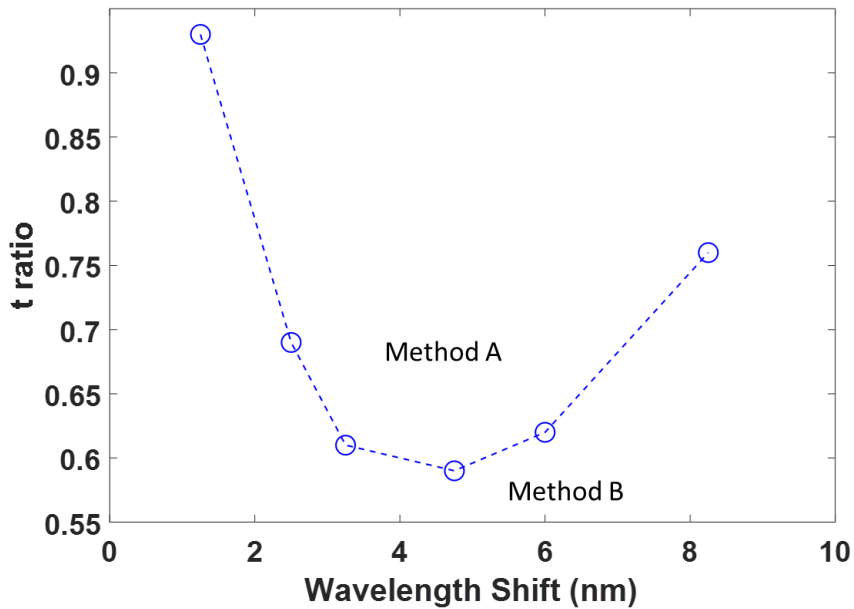


Figure 77: t_{ratio} as a function of λ_{shift}

Now, for any combination of temperature delta and $d\lambda/dT$, the cooling methodology to achieve the highest laser efficiency based on pulse length can be found. This is more general than just using the temperature delta. The process shown here can be used to compare any two cooling methodologies (not just single phase), and it provides a very clear metric for understanding the

various ways of getting the maximum efficiency possible out of a laser system for a given pulse time and thermal capability.

The laser diodes modeled throughout this research are continuous wave (CW) operation diodes. This means they are meant to be operated for pulse times on the order of 10s of seconds. This differentiates them from other class of lasers (QCW/ultrafast) where the pulse times can be as small as femtoseconds. For example, laser spectroscopy is an application of ultrafast lasers. CW lasers can operate with t_{ratio} values of 1 or greater, but that's not in the realm of normal applications. CW laser lifetimes are provided assuming the laser is operated at steady state conditions for the majority of its operating time. Laser diode manufacturers normally do not provide much information beyond this. Laser diode lifetime is a completely separate area of study far too specific to fully integrate into the current research. Hence, for simplicity, a "majority" is taken to mean a t_{ratio} of less than 0.5. With this metric and comparing back to Figure 76, the t_{ratio} values where efficiency lines cross is never less than 0.5. Thus, Method B is always going to be best for achieving the highest possible overall efficiency out of a typical CW laser system.

In situations when with t_{ratio} values are 1 or greater, Method A is best. There may be some laser applications where the laser system requires t_{ratio} values of 1 or greater, so the designer may have options of how best to approach thermal management. And even if the laser application is a situation where t_{ratio} value is less than 0.5, the designer may not have the option to use Method B for a number of reasons. Perhaps thermal control is inadequate and the cooling fluid simply cannot be provided at the required lower temperature. On the other side, perhaps a laser diode with a high enough reference temperature simply does not exist. All these considerations come together when designing the thermal management system for a high-

power fiber laser, and capturing the optical/thermal interactions as shown here allows for the designer to make the best decision with the laser technology and thermal capability available.

14. Research Outcomes Achieved:

The research outcomes initially set forth are revisited here and discussed. Responding to them demonstrates how the research has not only met its goals, but also how the research evolved and grew in unexpected directions throughout the process.

1. It is known electro-to-optical (E-O) efficiency degrades if excess heat builds up in laser diodes. The question is: How significant is the efficiency degradation? If so, what fidelity of modeling the laser physics is necessary to capture said degradation?
 - i. The research has shown when diode temperature is not adequately controlled, the overall laser system efficiency degradation is very significant. For a given diode temperature change, the loss seen in fiber optical power compared to the laser diode optical power is much larger. The significant decrease in efficiency means longer laser activation times to get the same amount of optical energy out. A lower level of optical power also means more heat generated, which means more thermal capability is required for temperature control.
 - ii. The fidelity of modeling required to capture the degradation seen in laser diode physics is considered reasonable. The equations governing optical power out of a laser diode are simple in that they are algebraic. Modeling the fiber gain media required a higher level of fidelity. A simplified fiber gain media model was not adequate to capture the necessary aspects of fiber operation. Hence, the higher fidelity rate equations were used instead, allowing for a more complete understanding of fiber optical power absorption/emission and heat generation within.

2. Virtually no previous research exists in modeling the output of multiple laser diodes, as it is all done experimentally. The proposed research presents a methodology for stringing multiple laser diodes together in an array formation along with a thermal model to estimate laser diode temperatures, all through modeling and simulation.
 - i. The research has provided a peer-reviewed methodology for representing multiple laser diodes together in an array formation, allowing for the simulation of laser systems with optical power levels on the order of 100 kW.
3. In the proposed research, models of both the laser diode and fiber gain media will be coupled in a transient sense. Doing so will show how a change in laser diode output affects fiber gain media absorption/emission. Previous research shows laser diodes and fiber being coupled in steady state operation, but not in transient operation.
 - i. The research has provided a multiphysics modeling method for coupling four essential subsystems, each an integral part of the entire laser system: Diode Optical, Fiber Optical, Diode Thermal, and Fiber Thermal Models. As per the literature review, coupling all the subsystems together and operating them in a transient manner has not been seriously considered. The research achieves the initial goal of providing a way to see how the performance of each subsystem affects the others. The dynamic coupling is successful in demonstrating what happens to fiber emission/absorption when laser diode output wavelength spectrum shifts from on-design to off-design. As per the literature review, this remained largely undemonstrated until now.
4. Fiber rate equations dictate how diode pump power is absorbed/emitted in the fiber, but they do not directly provide the heat generated inside the fiber. In the proposed research, a method

is provided to dig deeper into the rate equations and understand this heat. The goal is to use the heat generation data to perform worst-case scenario analysis concerning fiber temperature and determine the thermal requirements for acceptable fiber operation. Little attention has been given to this area in previous research.

- i. A deeper dive into the rate equations revealed how they account for heat generation inside a fiber, which had not been clearly explained in previous research. Using such insight, the thermal requirements for acceptable fiber operation were studied and presented. The research shows how different levels of thermal management (natural vs. forced convection) can bring fiber duty cycle to as high as 100%. Hence, it is possible to control fiber temperature well enough so the fiber never increases more than 100K from its initial temperature. Taking fiber duty cycle into account is integral when talking about laser system duty cycle.

5. Are there any particular parameters, either in laser diodes/fiber gain media/thermal management, which have a more significant effect on optical power output than others?

- i. The four most significant parameters from a system designer's perspective revealed by the research are Nusselt Number N_u , power flux P_{flux} , wavelength temperature coefficient $d\lambda/dT$, and fiber length L . Put together, these parameters provide the bridge to understanding how the various subsystems interact with each other and how they affect overall laser system performance. These four parameters encompass the most significant optical/thermal interactions between the various subsystems, given the type of fiber used is

held constant (meaning only fiber length L in the rate equations can be adjusted for a given laser system).

- ii. Determining optimal fiber parameters should take place once the diode performance is known. When diode output center wavelength and spectrum at steady state are known, a fiber can be chosen that provides the best emission/absorption capabilities for that diode light spectrum. All this can be done while taking into account things like keeping the LP_{01} mode the only propagating mode within the fiber. Such restrictions mean certain fiber parameters must fall within a certain range, leading to a better picture of what can be done to truly optimize for the best possible fiber performance. Although it is heavily a fiber physics-centered topic, learning which fiber parameters provide the best performance for a given pump spectrum is of significant importance for understanding the optical/thermal interactions of a high-power laser system.
6. These particular parameters could be used to understand laser performance response variables over a given parameter space and, in the process, eliminate the need constantly simulate the full physics laser models for every parameter combination. Such ability would greatly benefit laser system design decision making and optimization by providing insight into the effect of optical/thermal interactions on laser system performance and efficiency.
- i. For insight into the most significant optical/thermal interactions, the four parameters (Nusselt Number N_u , power flux P_{flux} , wavelength temperature coefficient $d\lambda/dT$, and fiber length L) were put into a statistical surrogate model. They were varied within certain ranges to give a four-dimensional

parameter space. The surrogate model provided values for each response variable of interest. Each response variable is represented by a single function with the most significant parameters as independent variables. How the response variables change over the parameter space directly shows the optical/thermal interactions.

- ii. When the combination of significant parameters changes, thermal capabilities change. When thermal capabilities change, laser optical power changes. In the simplest form, this is the optical/thermal interaction. Understanding the optical/thermal interactions from this novel perspective paves the way for a more clear and concise approach to future laser system design and optimization. Using the significant parameter space is integral for a less complex way of representing laser performance while retaining enough fidelity to make informed design decisions on both the optical side and the thermal side.

- 7. Are there cooling methodologies to achieve optimum laser performance? Perhaps fluid cooler than the laser diode reference temperature could be used so the diodes are on-design at steady state (moving to the reference temperature) instead of off-design (moving away from the reference temperature). Developing a metric to decide if one cooling methodology is better than another would be of great benefit.

- i. As an example of how such a comparison might work, two cooling methodologies were considered. Several simulations were run, varying the thermal control of the laser diode temperature through mass flow rate. In doing so, the time to steady state for the laser diodes changes. If multiple pulse lengths are considered, the average efficiency over a pulse can be calculated for

each pulse length. Using pulse length and time to steady state, a metric t_{ratio} was created to determine how much time the laser spent in transient versus steady state operation.

- ii. Ultimately, the average efficiency for each cooling methodology can be plotted as a function of t_{ratio} for value of mass flow rate. Mass flow rate determines the temperature delta seen in the diodes. The point where the curves cross is the t_{ratio} where one methodology becomes better than the other. The point of crossing can then be plotted against the temperature delta seen in the laser diodes. Based on temperature delta and t_{ratio} cross point, the cooling methodology providing the highest average efficiency can be directly determined.
- iii. To make the analysis more general, the delta temperature can be multiplied by the wavelength temperature coefficient $d\lambda/dT$. Now, the t_{ratio} cross point can be plotted against the wavelength shift seen in the laser diode, which is potentially very useful for system designers and high-level design decision making. It directly connects observed wavelength shift and t_{ratio} to which cooling methodology provides the best laser performance.

15. Conclusions and Discussion:

The research outcomes are high level summaries. It is worthwhile to discuss the main advancements from the research in more detail. A more in-depth discussion of the ramifications is also included.

The current state of the art, in terms of laser system literature, is very focused on the experimental side of things. There are many opportunities to look at such systems from a modeling/simulation point of view. Laser diodes and fiber are often studied separately and only rarely coupled together. When they are coupled together, the analysis only looks at steady state performance with diode center wavelength spectrum perfectly tuned for the given fiber. There is no mention of coupling the components from a transient perspective. The lack of transient modeling was a gap that now, thanks to research provided in this dissertation, has been initially bridged. Modeling all four subsystems (Diode Optical, Fiber Optical, Diode Thermal, Fiber Thermal) made it possible to go further in comprehending just exactly how the optical/thermal interactions of laser systems affect their performance. The research herein provides significant insight into why bridging the gap between the optical and thermal sides of laser performance is integral. The number of potential applications for laser continues to grow along with the optical power levels. More optical power means more heat, and this makes the optical/thermal interactions all the more important.

The four models created here required an extensive literature review. Additionally, the information on laser physics (both diodes and fibers) had to be gathered, sifted through, and understood to the appropriate level to apply with the required fidelity. The literature review provided little, if any, guidance on how to model the coupling of all four laser subsystems from a

simulation perspective. A major accomplishment of the research herein was to successfully bring together the four models. The fact that coupling the models lead to further optical/thermal interaction insight was hoped for, but not necessarily expected. The laser diode optical model was relatively straight-forward to create. The equations were well defined, and they simply had to be applied properly. The fiber gain media rate equations were more difficult. Although there were many references in literature to study, such references didn't talk much as to what the rate equations represented. They were simply applied as the authors needed them. The research herein required a much more detailed look at the rate equations to understand not just optical power, but heat generation as well. Another thing considered was not just the fiber internal heat generation, pump power remaining in the cladding at the fiber exit. This needs to be stripped away and is an additional heat load from the laser system that must be managed properly. Looking at the subsystems in a coupled manner is beneficial because it forced consideration of the system as a whole, not just specific areas of each individual component.

Duty cycle is a very common topic as it pertains to laser performance. A laser, as described here, has two separate duty cycles: Laser diode and fiber. The laser diode duty cycle is normally 100%, as laser diodes can still operate when their temperature is not adequately controlled. However, at some point, the output spectrum simply becomes undesirable and the diode lifetime is shortened because it is not operated at the nominal temperature conditions. This is not ideal. If the thermal system cannot keep up, continuing to operate the diode beyond nominal conditions may not have any benefit and more optical will be lost in the fiber, thereby generating even more heat to manage. Hence, the thermal system controlling laser diode temperature is the limiting factor for duty cycle. It needs to be good enough to control temperature and operate

for the required amount of time. If the thermal system has a duty cycle of 90%, for example, it gives the diode a duty cycle of 90%. Maybe the thermal system needs to time recharge in some fashion, and it requires 10% of the time to do so. The fiber duty cycle is fully dependent on fiber temperature control. If the change in fiber temperature can be kept to less than 100K for an indefinite amount of time, the duty cycle is 100%. However, that thermal capability may not be feasible. In general, a certain thermal capability provides a certain fiber duty cycle. The thermal capability needs to be decided upon for the given laser application and is a design requirement set forth in the beginning of the design process. The diode thermal system and fiber thermal system may be separate, or it might be one thermal system managing both components. Either way, the ability of the thermal systems to effectively manage component temperature and degradation will determine the overall laser system duty cycle.

Determining which four parameters (Nusselt Number N_u , power flux P_{flux} , wavelength temperature coefficient $d\lambda/dT$, and fiber length L) to use for surrogate modeling required some sensitivity analyses and consideration from a system designer perspective. On the thermal side, to see N_u and P_{flux} as the most significant, all laser parameters had to be held constant. Figures 51 through 63 show the variation of thermal parameters. The capacitance ratio, between the heat sink material and the fluid, was found to be significant only on the time response. It is reasonable to assume the other two parameters can change easily while capacitance ratio is kept the same. Of course, capacitance ratio has an effect. However, such an effect is minimal when compared to the other parameters that really drive the heat transfer and time response. The surface area of a heat exchanger or the mass flow rate provided can be changed with relative ease and will not necessarily significantly affect the capacitance ratio. In terms of the diode optical side, a sensitivity analysis was performed to show how the four major diode

parameters affected laser performance, while thermal and fiber parameters remained constant. The results give a clear indication that the major parameter on the diode side is the wavelength temperature coefficient $d\lambda/dT$. On the fiber optical side, and fiber length L was chosen for simple reason: It is the only parameter of a given fiber that a laser designer can easily change. The doping ion used, doping concentration, attenuation losses, and filling factors are inherent in a given fiber and cannot be changed unless a different fiber is used. Hence, the only parameter that can be changed once a fiber is chosen is fiber length L . In reality, any number of parameters could be used when creating the parameter space, depending on the level of detail desired.

Even though it wasn't the main focus in this research, fiber rate equation parameters like pump and signal filling factors are very important. A little change in them can drastically change fiber efficiency. It would be interesting to know if the filling factors are constant throughout a fiber, or if they vary with axial location. Such a phenomenon could be very significant in terms of fiber performance. Another thing to consider is the fiber core/cladding radii limits. Pump filling factor is determined from the core and cladding radii. If the core is too large, multiple modes of light will start to propagate in the fiber, not just the LP_{01} mode. The rate equations are not capable of accounting for light propagation beyond the LP_{01} mode. If core radius can only be so big, cladding radius must decrease to increase pump filling factor. However, a smaller cladding radius means less pump power can be launched into the fiber. Another thing to consider is heat generation. Changing filling factors can change the heat generation within a fiber. To make sure the fiber can still operate as desired, the fiber temperature profiles must be recalculated and the worst-case temperature scenarios must again be studied along with fiber duty cycle to determine what thermal capability is required for the desired fiber operation. From a more thermal perspective, studying fibers in this way should be done with a known laser diode and

accompanying diode thermal control system. The pump center wavelength and spectrum at steady state would then be known. At this point, the fiber parameters can be designed so the fiber is at its highest efficiency for this particular wavelength. Additionally, multiple doping ion types and concentrations could be simulated to optimize fiber performance. Different doping ions provided better absorption/emission at different pump/signal wavelengths. Depending on the pump wavelength into the fiber or the desired signal wavelength out, certain doping ions may be better than others due to their absorption/emission cross sections.

The statistical surrogate model provided a clever way to create a parameter space over which to calculate pertinent response variables (like overall efficiency, dimensionless diode and fluid temperatures, and time to steady state). Setting ranges on the four chosen parameters, along with the statistical surrogate approach, meant variables like overall efficiency could be defined by a single equation as a function of those four parameters. The equation for each response variable can be quite long with many coefficients, but the data can easily be put into something as simple as a Microsoft Excel spreadsheet. This allows for quick and easy determination of the important response variables with minimal error in a very timely fashion. Such a surrogate model is very effective in terms of saving computation time, given that the error level is acceptable and the parameters are kept within the prescribed ranges. A designer now has the ability to look at possibly thousands of parameter combinations and see which ones provide values for response variables that meet design requirements. The designer has the ability to change aspects of the laser, fiber, and thermal systems in order to find the combination best suited for the specific application, allowing for further optimization. For example, if the laser diode is less sensitive to temperature, perhaps the thermal system can be smaller in terms of volume and weight. The SWaP (size, weight, and power) savings could be beneficial for a design

where weight and volume are very important. Such considerations can be effectively weighed by the designer when the pertinent parameter space is appropriately represented.

The number of possible laser diode cooling methodologies is limited only by imagination. Being able to compare the effectiveness of cooling methodologies with a single metric is very powerful. Combining average laser efficiency over a pulse along with the system time response for varying levels of thermal control yielded this single metric, a value called t_{ratio} . Using t_{ratio} in the described manner, two cooling methodologies can be compared to see which one provides the highest average efficiency over a given pulse length, simply by knowing the corresponding t_{ratio} for the laser system and wavelength shift experienced by the laser diodes. Having a metric which provides such insight into how a laser system performs with various cooling methodologies would be invaluable to a designer. Now, they can make an informed decision on how to cool the laser diodes based on the performance requirements, allowing for further optimization of the system SWaP. The metric provides indispensable guidance for making high-level design decisions, the likes of which have not yet been seriously investigated in previous research.

16. Possible Relevant Future Research Areas:

Finally, it is appropriate to state some final thoughts in terms of possible future research. A solid foundation has been laid for better understanding the optical/thermal interactions of laser systems and how those interactions need to be considered when making high-level decisions for laser system design. Bringing together multiphysics models of the four subsystems and reducing/simplifying them using the most significant parameters to study laser performance across a bounded parameter space provides an invaluable step forward in showing the importance of considering the optical/thermal interactions as they pertain to overall laser system design and performance. There are several areas in which future research would be worthwhile.

Digging deeper into the optimization side of laser system design has significant potential. SWaP analysis is the next logical step in determining the feasibility of a laser system for a given application, as the research herein provides the basis for comprehending what happens when laser systems do not have adequate thermal control. Understanding the optical/thermal interactions and necessary for obtaining accurate weight and volume measurements of a potential laser system, both of which are very important in the integrated system design process. This is because very often, these laser systems are part of even bigger platforms, where various other engineering systems need to be integrated along with the laser system. System level optimization is becoming an ever more important topic in engineering circles and is especially relevant when it comes to high power laser systems.

The dimensionless laser diode/fiber rate equations are an interesting concept with no previous consideration or study, as per the literature review. The topic was seen as a potential area for

novel research. They were considered for a time, but ultimately were not completed in time for inclusion in this dissertation. Dimensionless equation forms have the potential to provide lots of information for better optimization of the system from a laser physics perspective, and understanding the physics to that level wasn't a focus of the research herein. It doesn't add significantly to the more thermal perspective sought here. And yet, further research of this on the fiber physics side has the potential to add greatly to the optimization of high-power laser system performance. If the pump spectrum out of the laser diodes can be kept constant by appropriate thermal control, the fiber physics can be further explored to specifically tune fiber parameters for the highest possible efficiency.

References:

- [1] Einstein, A. (1917). The Quantum Theory of Radiation. *Physikalische Zeitschrift*, 18(121), 1–15. <https://doi.org/10.1038/138483a0>
- [2] Maiman, T. (1960). Stimulated Optical Radiation in Ruby. *Nature*, 187(4736), 493–494.
- [3] Townes, C. H. (2007). Theodore H. Maiman (1927–2007). *Nature*, 447(7145), 654–654. <https://doi.org/10.1038/447654a>
- [4] Photonics Media, “A History of the Laser: 1960-2019” Available: https://www.photonics.com/Articles/A_History_of_the_Laser_1960_-_2019/a42279
- [5] Hopkins, F. (1998). Military laser applications. *Opt. Photonic News*, 9, 33–38.
- [6] Jalopnik, “The Airborne Laser May Rise Again But It Will Look Very Different,” Available: <https://foxtrotalpha.jalopnik.com/the-airborne-laser-may-rise-again-but-it-will-look-very-1724892313>
- [7] Global Security, “AN/SEQ-3 (XN-1) Laser Weapon System (LAWS),” Available: <https://www.globalsecurity.org/military/systems/ship/systems/laws.htm>
- [8] Defense News, “When it comes to missile-killing lasers, the US Navy is ready to burn its ships” Available: <https://www.defensenews.com/naval/2019/05/23/when-it-comes-to-missile-killing-lasers-the-us-navy-is-ready-to-burn-its-ships/>
- [9] Popular Mechanics, “The Navy Just Tested its Most Powerful Laser Yet,” Available: <https://www.popularmechanics.com/military/navy-ships/a32676643/navy-laser-weapon-system-demonstrator-test/>
- [10] Lockheed Martin, “Tactical Airborne Laser Pods are Coming,” Available: <https://www.lockheedmartin.com/en-us/news/features/2020/tactical-airborne-laser-pods-are-coming.html>
- [11] Li, P., Zhu, C., Zou, S., Zhao, H., Jiang, D., Li, G., & Chen, M. (2008). Theoretical and experimental investigation of thermal effects in a high power Yb³⁺-doped double-clad fiber laser. *Optics & Laser Technology*, 40(2), 360–364.
- [12] Chen, Y. F., Kao, C. F., Huang, T. M., Wang, C. L., & Wang, S. C. (1997). Influence of thermal effect on output power optimization in fiber-coupled laser-diode end-pumped lasers. *IEEE Journal on Selected Topics in Quantum Electronics*, 3(1), 29–34.
- [13] Wang, Y., Xu, C. Q., & Po, H. (2004). Thermal Effects in Kilowatt Fiber Lasers. *IEEE Photonics Technology Letters*, 16(1), 63–65. <https://doi.org/10.1109/LPT.2003.818913>

- [14] Kim, D. S., Holloway, C., Han, B., & Bar-Cohen, A. (2016). Method for predicting junction temperature distribution in a high-power laser diode bar. *Applied Optics*, 55(27), 7487–7496. <https://doi.org/10.1364/AO.55.007487>
- [15] Gapontsev, V.P., Platonov, N.S., Shkurihin, O., & Zaitsev, I., “400 W low-noise single-mode CW ytterbium fiber laser with an integrate,” in Proc. Conf. Lasers and Electro-Optics (CLEO) 2003, Baltimore, MD, postdeadline paper CThPDB9.
- [16] Limpert, J., Liem, A., Zellmer, H., & Tünnerman, A., “500 W continuous-wave fiber laser with excellent beam quality,” *Electron. Lett.*, vol. 39, pp. 645-647, 2003.
- [17] Beier, F., Hupel, C., Kuhn, S., Hein, S., Nold, J., Proske, F., ... Tünnermann, A. (2017). Single mode 4.3 kW output power from a diode-pumped Yb-doped fiber amplifier. *Optics Express*, 25(13), 14892.
- [18] Shen, H., Lou, Q., Quan, Z., Li, X., Yang, Y., Chen, X., ... Zhou, J. (2019). Narrow-linewidth all-fiber amplifier with up to 3.01 kW output power based on commercial 20/400 μm active fiber and counterpumped configuration. *Applied Optics*, 58(12), 3053.
- [19] Beier, F., Hupel, C., Nold, J., Kuhn, S., Hein, S., Ihring, J., ... Tünnermann, A. (2016). Narrow linewidth, single mode 3 kW average power from a directly diode pumped ytterbium-doped low NA fiber amplifier. *Optics Express*, 24(6), 6011.
- [20] Yu, C. X., Shatrovov, O., Fan, T. Y., & Taunay, T. F. (2016). Diode-pumped narrow linewidth multi-kilowatt metalized Yb fiber amplifier. *Optics Letters*, 41(22), 5202.
- [21] Lin, H., Tao, R., Li, C., Wang, B., Guo, C., Shu, Q., ... Chu, Q. (2019). 3.7 kW monolithic narrow linewidth single mode fiber laser through simultaneously suppressing nonlinear effects and mode instability. *Optics Express*, 27(7), 9716.
- [22] Wang, Y., Gao, C., Tang, X., Zhan, H., Peng, K., Ni, L., ... Lin, A. (2018). 30/900 Yb-doped Aluminophosphosilicate Fiber Presenting 6.85-kW Laser Output Pumped with Commercial 976-nm Laser Diodes. *Journal of Lightwave Technology*, 36(16), 3396–3402.
- [23] Tao, R., Wang, X., & Zhou, P. (2018). Comprehensive Theoretical Study of Mode Instability in High-Power Fiber Lasers by Employing a Universal Model and Its Implications. *IEEE Journal of Selected Topics in Quantum Electronics*, 24(3).
- [24] Fang, Q., Li, J., Shi, W., Qin, Y., Xu, Y., Meng, X., ... Peyghambarian, N. (2017). 5 kW near-Diffraction-limited and 8 kW High-Brightness Monolithic Continuous Wave Fiber lasers Directly Pumped by laser Diodes. *IEEE Photonics Journal*, 9(5).
- [25] Zenteno, L., “High-power double-clad fiber lasers,” *J. Lightwave Technol.*, vol. 11, pp.1435-1446, Sept, 1993.
- [26] Davis, M.K., Digonnet, M.J.F., and Pantell, R.H., “Thermal effects in doped fibers,” *J. Lightwave Technol.*, vol. 16, pp. 1013-1023. June 1998.

- [27] Brown, D.C., and Hoffman, H.J., "Thermal, stress, and thermal-optic effects in high average power double-clad silica fiber lasers," *IEEE J. Quantum Electronics*, vol. 37, pp. 207-217, Feb. 2001.
- [28] Li, T., Ke, W., Ma, Y., Sun, Y., & Gao, Q. (2019). Suppression of stimulated Raman scattering in a high-power fiber amplifier by inserting long transmission fibers in a seed laser. *Journal of the Optical Society of America B*, 36(6), 1457. <https://doi.org/10.1364/josab.36.001457>
- [29] Mobini, E., Peysokhan, M., Abaie, B., & Mafi, A. (2018). Thermal modeling, heat mitigation, and radiative cooling for double-clad fiber amplifiers. *Journal of the Optical Society of America B*, 35(10), 2484–2493. <https://doi.org/10.1364/JOSAB.35.002484>
- [30] Beier, F., Plötner, M., Sattler, B., Stutzki, F., Walbaum, T., Liem, A., ... Tünnermann, A. (2017). Measuring thermal load in fiber amplifiers in the presence of transversal mode instabilities. *Optics Letters*, 42(21), 4311. <https://doi.org/10.1364/ol.42.004311>
- [31] Jauregui, C., Stutzki, F., Tünnermann, A., & Limpert, J. (2018). Thermal analysis of Yb-doped high-power fiber amplifiers with Al:P co-doped cores. *Optics Express*, 26(6), 7614. <https://doi.org/10.1364/oe.26.007614>
- [32] Motes, R.A., Shakur, S.A., & Berdine, R.W. (2013). *Introduction to High-Power Fiber Lasers: Second Edition*.
- [33] Shao, H., Duan, K., Zhu, Y., Yan, H., Yang, H., & Zhao, W. (2013). Numerical analysis of Ytterbium-doped double-clad fiber lasers based on the temperature-dependent rate equation. *Optik*, 124, 4336–4340. <https://doi.org/10.1016/j.ijleo.2013.02.017>
- [34] Newell, T. C., Peterson, P., Gavrielides, A., & Sharma, M. P. (2007). Temperature effects on the emission properties of Yb-doped optical fibers. *Optics Communications*, 273(1), 256–259. <https://doi.org/10.1016/j.optcom.2007.01.027>
- [35] Lv, Y., Zheng, H., & Liu, S. (2018). Thermal cooling analysis and validation of the ytterbium doped double clad fiber laser by a general analytic method. *Optical Fiber Technology*, 45, 336–344. <https://doi.org/10.1016/j.yofte.2018.08.014>
- [36] Albalawi, A., Zhu, H., & Taccheo, S. (2016). Numerical modeling of the impact of pump wavelength on Yb-doped fiber amplifier performance. *Optical and Quantum Electronics*, 48, 1–7. <https://doi.org/10.1007/s11082-016-0771-z>
- [37] Butt, N., Roberts, R., & Patnaik, S. (2019). Transient Temperature Effects on the Optical Power Wavelength Shift of a High-Power Laser System. *Applied Thermal Engineering*. <https://doi.org/10.1016/j.applthermaleng.2019.04.060>
- [38] Butt, N.J., Roberts, R.A., and Patnaik, S.S. (2020). Laser diode optical output dependence on junction temperature for high-power laser systems. *Optics and Laser Technology*, 125(106019), 1-12. <https://doi.org/10.1016/j.optlastec.2019.106019>
- [39] Wetter, A., Faucher, M., & Sévigny, B. (2008). High power cladding light strippers. In *Fiber Lasers*

- V: Technology, Systems, and Applications* (Vol. 6873, p. 687327). San Jose: SPIE.
<https://doi.org/10.1117/12.763003>
- [40] Poozesh, R., Norouzy, A., Golshan, A. H., Roohforouz, A., Babazadeh, A., Nasirabad, R. R., ... Amidian, A. (2012). A novel method for stripping cladding lights in high power fiber lasers and amplifiers. *Journal of Lightwave Technology*, 30(20), 3199–3202.
<https://doi.org/10.1109/JLT.2012.2213295>
- [41] Guo, W., Chen, Z., Zhou, H., Li, J., & Hou, J. (2014). Cascaded Cladding Light Extracting Strippers for High Power Fiber Lasers and Amplifiers. *IEEE Photonics Journal*, 6(3), 1–6.
<https://doi.org/10.1109/JPHOT.2014.2320736>
- [42] Yan, P., Sun, J., Huang, Y., Li, D., Wang, X., Xiao, Q., & Gong, M. (2017). Kilowatt-level cladding light stripper for high-power fiber laser. *Applied Optics*, 56(7), 1935–1939.
<https://doi.org/10.1364/ao.56.001935>
- [43] Zou, S., Chen, H., Zhang, J., Yu, H., Zhang, Z., Sun, J., & Lin, X. (2018). Cladding Light Stripper of High Average Stripped Power Density with High Attenuation of 39 dB and Low Temperature Rise. *IEEE Photonics Journal*, 10(1). <https://doi.org/10.1109/JPHOT.2017.2785392>
- [44] Yan, M. J., Wang, Z., Meng, L. Q., Yin, L., Han, Z. G., Shen, H., ... Zhu, R. H. (2018). Heat suppression of the fiber coating on a cladding light stripper in high-power fiber laser. *Applied Optics*, 57(3), 485–491. <https://doi.org/10.1364/AO.57.000485>
- [45] Butt, N.J. (2018). "Development and Thermal Management of a Dynamically Efficient, Transient High Energy Pulse System Model," Master's Thesis, Department of Mechanical and Materials Engineering, Wright State University, Dayton, Ohio.
- [46] Liu, X., Zhao, W., Xiong, L., & Liu, H. (2015). Packaging of High Power Semiconductor Lasers.
- [47] Arai, M., Watanabe, T., Yuda, M., Kinoshita, K., Ogata, Y., Yoda, S., & Kondo, Y. (2006). 1.3 μm -band laser with a high characteristic temperature ($T_0 = 130\text{K}$) on an InGaAs ternary substrate grown by the traveling liquidus-zone method. In *IEEE 20th International Semiconductor Laser Conference* (pp.157-158).
- [48] OdicForce Lasers, "Laser Diode" Available: <http://odicforce.com/Background-and-Projects/Laser-Diodes>
- [49] Sun, H. (2015). *A Practical Guide to Handling Laser Diode Beams*.
- [50] Bacchin, G., Fily, A., Qiu, B., Fraser, D., Robertson, S., Loyo-Maldonado, V., ... Schmidt, B. (2010). High temperature and high peak-power 808nm QCW bars and stacks. In *SPIE 7583, High-Power Diode Laser Technology and Applications VIII* (p. 75830P (1-11)). San Francisco.
<https://doi.org/10.1117/12.843735>
- [51] Zhang, Y. (2014). *Self-heating control of edge emitting and vertical cavity surface emitting lasers*. Doctoral Dissertation, College of Optics and Photonics, University of Central Florida, Orlando, Florida.

- [52] Saini, S. S., Cho, S. H., & Dagenais, M. (2007). Thermal considerations in High Power Semiconductor Lasers and Semiconductor Optical Amplifiers. In *SPIE 6478, Photonics Packaging, Integration, and Interconnects VII* (p. 647805). <https://doi.org/10.1117/12.714295>
- [53] Asryan, L. V., & Suris, R. A. (2002). Theory of Threshold Characteristics of Quantum Dot Lasers : Effect of Quantum Dot Parameter Dispersion. *International Journal of High Speed Electronics and Systems*, 12(1), 111–176. <https://doi.org/10.1142/S0129156402001149>
- [54] Cooke, M. (2011). Stepping up EBL in laser diode internal quantum efficiency. *Semiconductor Today*, 6(4), 106–107. <https://doi.org/10.1063/1.3581080>
- [55] Akahane, K., Yamamoto, N., & Kawanishi, T. (2010). High Characteristic Temperature of Highly Stacked Quantum-Dot Laser for 1.55- μm Band. *IEEE PHOTONICS TECHNOLOGY LETTERS*, 22(2), 103–105.
- [56] Akahane, K., Matsumoto, A., Umezawa, T., & Yamamoto, N. (2016). High Characteristic Temperature for Ridge-waveguide Laser with a Highly Stacked InAs Quantum Dot Structure. In *2016 International Semiconductor Laser Conference (ISLC)* (pp. 1–2).
- [57] Akahane, K., Yamamoto, N., & Kawanishi, T. (2012). The dependence of the characteristic temperature of highly stacked InAs quantum dot laser diodes fabricated using a strain-compensation technique on stacking layer number. In *ISLC 2012 International Semiconductor Laser Conference* (pp. 82–83).
- [58] Arsenijević, D., Liu, C., Payusov, A., Stubenrauch, M., & Bimberg, D. (2012). Temperature-Dependent Characteristics of Single-Mode InAs Submonolayer Quantum-Dot Lasers. *IEEE PHOTONICS TECHNOLOGY LETTERS*, 24(11), 906–908.
- [59] Li, Y., Rotter, T. J., Xin, Y. C., Stinz, A., Martinez, A., Malloy, K. J., ... Lester, L. F. (2006). High Characteristic Temperature of p-doped InAs Quantum Dots-in-a-Well Lasers on InP Substrate. In *Conference on Lasers and Electro-Optics* (pp. 1–2).
- [60] Fathpour, S., Mi, Z., Bhattacharya, P., Kovsh, A. R., Mikhurin, S. S., Krestnikov, I. L., ... Ledentsov, N. N. (2004). The role of Auger recombination in the temperature-dependent output characteristics ($T_0 = \infty$) of p-doped 1.3 μm quantum dot lasers. *Applied Physics Letters*, 85(22), 5164–5166. <https://doi.org/10.1063/1.1829158>
- [61] Chen, W., Li, L., Zhao, J., Wang, Y., Li, T., Lu, P., ... Liu, G. (2012). 1.47 μm High Characteristic Temperature InGaAsP/InP MQW Laser. In *International Conference on Optoelectronics and Microelectronics (ICOM)* (pp. 115–118).
- [62] Arai, M., Watanabe, T., Yuda, M., Kinoshita, K., Ogata, Y., Yoda, S., & Kondo, Y. (2006). 1.3 μm -band laser with a high characteristic temperature ($T_0 = 130\text{K}$) on an InGaAs ternary substrate grown by the traveling liquidus-zone method. In *IEEE 20th International Semiconductor Laser Conference* (pp.157-158).

- [63] Zubov, F. I., Semenova, E. S., Kulkova, I. V., Yvind, K., Kryzhanovskaya, N. V., Maximov, M. V., & Zhukov, A. E. (2017). On the high characteristic temperature of an InAs/GaAs/InGaAsP QD laser with an emission wavelength of $\sim 1.5 \mu\text{m}$ on an InP substrate. *Semiconductors*, 51(10), 1332–1336. <https://doi.org/10.1134/S1063782617100207>
- [64] Chackrabarti, S., Sharma, D., Joseph, S., Zaker, T. A., Hafiz, A. K., & Kafle, R. (2016). Experimental study on the mechanism governing spectral shifts in low power 670 nm AlGaInP multiple quantum well (MQW) laser diodes over temperature range 5 – 45 °C. *Canadian Journal of Physics*, 94, 640–644.
- [65] Ryu, H. (2017). Negative characteristic temperature of GaN-based blue laser diode investigated by numerical simulation. *Optical and Quantum Electronics*, 49(30), 1–6. <https://doi.org/10.1007/s11082-016-0861-y>
- [66] Kim, D. S., Holloway, C., Han, B., & Bar-Cohen, A. (2016). Method for predicting junction temperature distribution in a high-power laser diode bar. *Applied Optics*, 55(27), 7487–7496. <https://doi.org/10.1364/AO.55.007487>
- [67] Fan, L., Cao, C., Thaler, G., Nonnemacher, D., Lapinski, F., Ai, I., ... Thiagarajan, P. (2011). Reliable high-power long-pulse 8XX-nm diode laser bars and arrays operating at high temperature. In SPIE 7918, *High-Power Diode Laser Technology and Applications IX* (Vol. 7918, p. 791805 (1-7)). San Francisco. <https://doi.org/10.1117/12.871184>
- [68] Hu, M., Liu, X., & Zah, C. (2002). Transient and static thermal behavior of high-power single-mode semiconductor lasers. In SPIE 4905, *Materials and Devices for Optical Wireless Communications* (Vol. 4905, p. 32–36).
- [69] Kondow, M., Kitatani, T., Nakahara, K., & Tanaka, T. (2000). Temperature dependence of lasing wavelength in GaInNAs laser diode. *IEEE Photonics Technology Letters*, 12(7), 777–779. <https://doi.org/10.1109/68.853497>
- [70] Schlenker, E. (2018). “Modeling and Characterization of High-Power Electronic Devices: System Analysis of Laser Diodes with Flash Boiling and GaN Hemt Reliability Modeling,” Master’s Thesis, Department of Electrical and Computer Engineering, Purdue University, West Lafayette, Indiana.
- [71] Liu, X., Wang, J., & Wei, P. (2008). Study of the mechanisms of spectral broadening in high power semiconductor laser arrays. In *Electronic Components and Technology Conference* (pp. 1005–1010). <https://doi.org/10.1109/ECTC.2008.4550099>
- [72] Yuan, Z., Wang, J., Wu, D., Chen, X., & Liu, X. (2009). Study of steady and transient thermal behavior of high power semiconductor lasers. In *Electronic Components and Technology Conference* (pp. 831–836). <https://doi.org/10.1109/ECTC.2009.5074108>

- [73] FIBERCORE, “Double-clad fiber” Available: <https://www.fibercore.com/expertise/fiberpaedia/double-clad-fiber> , accessed 2019-06-12.
- [74] Wikipedia Commons, “File: Schematic diagram of high power fiber laser using a double-clad fiber.png” Available: https://commons.wikipedia.org/wiki/File:Schematic_diagram_of_high_power_fiber_laser_using_a_double-clad_fiber.png , accessed 2019-06-12.
- [75] Richardson, D. J., Nilsson, J., & Clarkson, W. A. (2010). High power fiber lasers: current status and future perspectives [Invited]. *Journal of the Optical Society of America B*, 27(11), B63–B92. <https://doi.org/10.1364/josab.27.000b63>
- [76] Paschotta, R., Nilsson, J., Tropper, A. C., & Hanna, D. C. (1997). Ytterbium-Doped Fiber Amplifiers. *IEEE JOURNAL OF QUANTUM ELECTRONICS* (Vol. 33).
- [77] El-Sherif, A. F., & El-Tahlawy, M. K. (2010). Design and performance analysis of a tunable and self-pulsation diode pumped double-clad D-shaped Yb³⁺-doped silica fiber laser. In *Laser Beam Shaping XI* (Vol. 7789, pp. 778911–778916). SPIE. <https://doi.org/10.1117/12.860462>
- [78] Zervas, M. N., & Codemard, C. A. (2014). High power fiber lasers: A review. *IEEE Journal on Selected Topics in Quantum Electronics*, 20(5). <https://doi.org/10.1109/JSTQE.2014.2321279>
- [79] Paschotta, R, “LP Modes” in the RP Photonics Encyclopedia, https://www.rp-photonics.com/lp_modes.html , accessed 2019-06-12.
- [80] Paschotta, R, “Seed Lasers” in the RP Photonics Encyclopedia, https://www.rp-photonics.com/seed_lasers.html , accessed 2019-06-21.
- [81] Stachowiak, D., Kaczmarek, P., & Abramski, K. M. (2017). (5 + 1) × 1 Pump and Signal Power Combiner With 9/80 Mm Feed-Through Signal Fiber. *Optics and Laser Technology*, 93, 33–40. <https://doi.org/10.1016/j.optlastec.2017.01.035>
- [82] Lei, C., Wu, W., Chen, Z., Wang, Z., & Chen, J. (2018). Incoherent beam combining of fiber lasers by an all-fiber 7 × 1 signal combiner at a power level of 14 kW. *Optical Fiber Technology*, 26(7), 10421–10427. <https://doi.org/10.1016/j.yofte.2019.102109>
- [83] Yang, G., Liu, L., Jiang, Z., Guo, J., & Wang, T. (2018). Incoherent beam combining based on the momentum SPGD algorithm. *Optics and Laser Technology*, 101, 372–378. <https://doi.org/10.1016/j.optlastec.2017.11.039>
- [84] Lei, C., Li, Z., Zhang, H., & Chen, Z. (2020). Taper-fused side pump combiner for all-fiber lasers and amplifiers : A review. *Optics and Laser Technology*, 130(May), 106353. <https://doi.org/10.1016/j.optlastec.2020.106353>
- [85] Sprangle, P., Ting, a, Fischer, R., & Hafizi, B. (2008). High-Power Fiber Lasers for Directed-Energy Applications. *NRL Review*, 89–99.

- [86] Bai, G., Shen, H., Yang, Y., Zhao, X., Zhang, J., Zhang, H., ... Zhou, J. (2018). Theoretical analysis of beam quality degradation in spectral beam combining of fiber laser array with beam deviation. *Optics and Laser Technology*, 105, 281–287. <https://doi.org/10.1016/j.optlastec.2018.03.010>
- [87] Chen, F., Ma, J., Zhu, R., Yuan, Q., Zhou, W., Su, J., ... Pan, S. (2017). Coupling efficiency model for spectral beam combining of high-power fiber lasers calculated from spectrum. *Applied Optics*, 56(10), 2574. <https://doi.org/10.1364/ao.56.002574>
- [88] Kelson, I., & Hardy, A. (1999). Optimization of strongly pumped fiber lasers. *Journal of Lightwave Technology*, 17(5), 891–897. <https://doi.org/10.1109/50.762908>
- [89] Kelson, I., & Hardy, A. (1998). Strongly pumped fiber lasers. *IEEE Journal of Quantum Electronics*, 34(9), 1570–1577. <https://doi.org/10.1109/3.709573>
- [90] Hardy, A., & Oron, R. (1997). Signal amplification in strongly pumped fiber amplifiers. *IEEE Journal of Quantum Electronics*, 33(3), 307–313. <https://doi.org/10.1109/3.555997>
- [91] Digonnet, M. J. F. (1990). Closed-Form Expressions for the Gain in Three- and Four-Level Laser Fibers. *IEEE Journal of Quantum Electronics*, 26(10), 1788–1796. <https://doi.org/10.1109/3.60903>
- [92] Tao, R., Ma, P., Wang, X., Zhou, P., & Liu, Z. (2016). Study of dopant concentrations in high power fiber lasers. *Laser Physics*, 26(6).
- [93] Northrop Grumman, “Golden Bullet Laser Diode Submodule 200W QCW,” Available: http://www.optoscience.com/maker/ceo/pdf/200W_QCW_golden_bull.pdf
- [94] Butt, N.J., Roberts, R.A., Wolff, M., & Patnaik, S. (2018). Transient Temperature Effects on a High Energy Pulse System Model. In *AIAA Propulsion and Energy Forum 2018* (pp. 1-11). Cincinnati, OH.
- [95] Cengel, Y.A. & Ghajar, A.J., *Heat and Mass Transfer: Fundamentals and Applications* 4th Edition, New York: 2011.
- [96] Eastbourn, S.M. (2012). *Modeling and Simulation of a Dynamic Turbofan Engine Using Simulink* (Master thesis), Wright State University, Dayton, OH.
- [97] Roberts, R. & Doty, J. (2012). Implementation of a Non-Equilibrium Exergy Analysis for an Aircraft Thermal Management System. In *AIAA: Aerospace Sciences Meeting*, Nashville, TN.
- [98] Roberts, R. & Doty, J. (2015). Implementation of a transient exergy analysis for a plate–fin heat exchanger. *International Journal of Exergy*, 16(1).

- [99] Roberts, R & Eastbourn, S. (2014). Vehicle Level Tip-to-Tail Modeling of an Aircraft. *International Journal of Thermodynamics*, 17(2).
- [100] Yu, H., Zhang, H., Wang, X., Leng, J., Xiao, H., Guo, S., ... Chen, J. (2015). 3.15 kW direct diode-pumped near diffraction-limited all-fiber-integrated fiber laser. *Applied Optics*, 54(14), 56–60. <https://doi.org/10.2184/laj.21.78>
- [101] AFRL RD, Kirtland AFB (2019). Private conversation.
- [102] Abouricha, M., Boulezhar, A., & Habiballah, N. (2013). The Comparative Study of the Temperature Distribution of Fiber Laser with Different Pump Schemes. *Open Journal of Metal*, 03(04), 64–71. <https://doi.org/10.4236/ojmetal.2013.34010>
- [103] J. Li, K. Duan, Y. Wang, X. Cao, W. Zhao, Y. Guo, and X. Lin. (2008). Theoretical analysis of the heat dissipation mechanism in Yb³⁺-doped double-clad fiber lasers. *Journal of Modern Optics*, 55(3), 459–471.

Appendix A: Simplified Fiber Model Parameters and Equations

Parameter – Definition	Value
$T_{ref LD}$ – Reference Temperature for Laser Diode Characteristics (K)	298
$\lambda_{center LD nom}$ – Nominal Center Wavelength of Laser Diode Output at $T_{ref LD}$ (m)	8.08e-07
$\lambda_{fwhm LD nom}$ – Nominal Full Width Half Maximum of Laser Diode Output (m)	2.5e-09
$d\lambda/dT$ – Wavelength Temperature Coefficient for Laser Diode (m/K)	2.5e-10
$d\beta/dT$ – Spectral Width Temperature Coefficient for Laser Diode (m/K)	8.84e-11
$I_{th,ref}$ - Threshold Current Reference (A)	15
I_{max} – Max Current per Laser Diode (A)	180
V_{max} – Max voltage per Laser Diode (V)	2
$Power_{per LD,ref}$ – Reference optical power out per laser diode (W)	200
T_0 – Threshold Current Characteristic Temperature (K)	180
T_1 – Slope Efficiency Characteristic Temperature (K)	680
$NUM_{LD/bar}$ – Number of Laser Diodes per Bar (diodes thermally in parallel)	5
$NUM_{LD bars}$ – Number of Laser Diode Bars (diodes thermally in series)	5
$\eta_{max GM}$ – Peak Efficiency of Gain Medium at Center Wavelength	0.80
$\lambda_{center GM}$ – Center Wavelength of Gain Medium Absorption Spectrum (m)	8.08e-07
$\lambda_{fwhm GM}$ – Full Width Half Maximum of Gain Medium Absorption Peak (m)	2e-08
η_{BD} – Beam Director Thermal Efficiency	0.95
η_{MR} – Optical Training Mirror Lumped Reflectivity	0.92
η_{ASE} – Aperture Sharing Element Thermal Efficiency	0.97
$Power_{optical}$ – HPLS Design Optical Power from Laser Diodes (W)	75000
$Power_{wall plug}$ – HPLS Wall Plug Power (W)	135000

From these defined input parameters, all other needed values can be calculated. The equations that follow will define the process by which the model does calculations to find the laser system efficiency. There are more input variables that must be determined before the calculations start, and the parameters from Table 1 are used to find these other input variables, shown below.

$\eta_{LD slope,ref}$ – Laser diode slope efficiency reference value (W/A)

$$\eta_{LD slope,ref} = \frac{Power_{per LD,ref}}{(I_{max} - I_{th,ref})} \quad (42)$$

I_{HPLS} – Current to Laser Diodes (Amps)

$$I_{HPLS} = I_{max} * NUM_{LD/bar} \quad (43)$$

V_{HPLS} – Voltage to Laser Diodes (Volts)

$$V_{HPLS} = \frac{Power_{wall\ plug}}{I_{HPLS}} \quad (44)$$

$V_{per\ LD}$ – Voltage per Laser Diode (Volts)

$$V_{per\ LD} = \frac{V_{HPLS}}{NUM_{LD\ bars}} \quad (45)$$

$Power_{per\ LD,elec}$ – Electrical Power per Laser Diode (W)

$$Power_{per\ LD,elec} = V_{per\ LD} * I_{max} \quad (46)$$

$\eta_{LD,max}$ – Max Laser Diode Efficiency

$$\eta_{LD,max} = \frac{Power_{per\ LD,ref}}{Power_{per\ LD,elec}} \quad (47)$$

$NUM_{Modules}$ – Number of laser diode modules in system

$$NUM_{Modules} = \frac{Power_{optical}}{Power_{per\ LD,ref} * NUM_{LD\ bars} * NUM_{LD/bar}} \quad (48)$$

NUM_{Diodes} – Total number of laser diodes in system

$$NUM_{Diodes} = NUM_{LD\ bars} * NUM_{LD/bar} * NUM_{Modules} \quad (49)$$

With all these variables defined and preliminary calculations solved, the model can now use these values to do the actual optical power production calculations. There is no power conditioning model here. The optical power out of each laser diode bar is first calculated. From this, the amount of heat generated from the laser diodes can be found. Next, the center wavelength and spectral width of each bar is calculated. Following this, the Gaussian Curve mathematics are used to represent the laser beams and find the Gaussian Curve spectrum profiles for one diode bar over a range of wavelength values. The Gaussian Curve profiles for each bar are then added together. The total optical power out of the laser diodes is the area under the curve of all the bar profiles added together. The equations below outline this process. The equations are presented in order so the process of calculations can be easily followed.

The junction temperature dependent parameters for optical power are first calculated.

$I_{th}(T_j(x))$ – Threshold current based on junction temperature. The variable $T_j(x)$ is the laser diode junction temperatures. The variable x in all equations goes from 1 to $NUM_{LD\ bars}$ to represent all the bars.

$$I_{th}(T_j(x)) = I_{th,ref} e^{\left(\frac{T_j(x) - T_{ref}}{T_0}\right)} \quad (50)$$

$\eta_{slope}(T_j(x))$ – Slope efficiency based on junction temperature

$$\eta_{slope}(T_j(x)) = \eta_{LD\ slope,ref} e^{-\left(\frac{T_j(x) - T_{ref}}{T_1}\right)} \quad (51)$$

Now the optical power out of a single diode bar can be found.

$Power_{LD\ bar}(x)$ – Optical Output Power of the Laser Diode bars. Each value x is the power of $NUM_{LD/bar}$ diodes for each diode bar.

$$Power_{LD\ bar}(x) = \left[\eta_{slope}(T_j(x)) \left(I_{max} - I_{th}(T_j(x)) \right) \right] * NUM_{LD/bar} \quad (52)$$

$\lambda_{center\ LD}(x)$ – Center Wavelength of each bar. The variable $T_j(x)$ is the laser diode junction temperatures. The variable x goes from 1 to $NUM_{LD\ bars}$ to represent all the bars.

$$\lambda_{center\ LD}(x) = \lambda_{center\ LD\ nom} + \left((T_j(x) - T_{ref\ LD}) * d\lambda/dT \right) \quad (53)$$

$\lambda_{FWHM\ LD}(x)$ – Spectral width (FWHM) of each bar. $T_j(x)$ is the laser diode junction temperatures. The variable x goes from 1 to $NUM_{LD\ bars}$ to represent all the bars.

$$\lambda_{FWHM\ LD}(x) = \lambda_{FWHM\ LD\ nom} + \left((T_j(x) - T_{ref}) * d\beta/dT \right) \quad (54)$$

$C_{value\ LD}(x)$ – C Value for Laser Diode Gaussian Profile (spectral width).

$$C_{value\ LD}(x) = \frac{\lambda_{FWHM\ LD}(x)}{2\sqrt{2\ln(2)}} \quad (55)$$

$A_{value\ LD}(x)$ – A Value for laser diode bar Gaussian profile (peak at center wavelength). The integral is the area under the Gaussian curve with a peak equal to 1. The area required under a curve with peak $A_{value\ LD}$ divided by the area under a curve with a peak of 1 yields the peak $A_{value\ LD}$ required to achieve the area required.

$$A_{value\ LD}(x) = \frac{Power_{LDbar}(x)}{\int_{\lambda_{center\ LD} - \lambda_{fwhm\ LD} * 10}^{\lambda_{center\ LD} + \lambda_{fwhm\ LD} * 10} \exp\left(\frac{-(\lambda - \lambda_{center\ LD}(x))^2}{2(C_{value\ LD}(x))^2}\right) d\lambda} \quad (56)$$

$Gaussian_{LD\ bar}(x)$ – Actual Gaussian Curve profiles for each diode on a single bar.

$$Gaussian_{LD\ bar}(x) = A_{value\ LD}(x) * \exp\left(\frac{-(\lambda - \lambda_{center\ LD}(x))^2}{2(C_{value\ LD}(x))^2}\right) \quad (57)$$

Here, λ ranges from 0 to 900 nm (or whatever range is required) for each x. A Gaussian curve for each bar can be obtained and graphed. Each bar contains $NUM_{LD/bar}$ diodes. The Gaussian curve for one bar is this number of diode Gaussian curves added together, as the power used to find the Gaussian curve peak ($A_{value\ LD}$) for each bar is the combined power of all diodes on that one bar, again assuming the bar/junction is uniform in temperature.

$Gaussian_{all\ bars}$ – Gaussian Curve for all Bar Profiles added together to form one curve. It is the output curves of all laser diodes added together to make a single curve.

$$Gaussian_{all\ bars} = \sum_{x=1}^{NUM_{LD\ bars}} Gaussian_{LD\ bar}(x) \quad (58)$$

$Power_{optical\ LD}$ – Total optical power out of all laser diodes, area under $Gaussian_{all\ bars}$.

The main value of concern from the laser diode calculations is $Power_{optical\ LD}$. This is the value that cascades into the next set of computations for the gain medium. All electrical power not converted to optical power by the laser diodes is considered lost as heat. The optical power out of the laser diodes is the input optical power to the gain medium. The gain medium has its own specific center wavelength and wavelength fwhm, set to

be the same as the laser diode output. When the laser diode output shifts due to temperature change, this effects the gain medium absorption. Equations 59 through 61 below show and explain this process.

$C_{value\ GM}$ – C value for Gain Medium Gaussian Profile

$$C_{value\ GM} = \frac{\lambda_{fwhm\ GM}}{2\sqrt{2\ln(2)}} \quad (59)$$

$Absorption\ Curve_{GM}$ – Gain Medium Efficiency Absorption Profile (Gaussian Curve)

$$Absorption\ Curve_{GM} = \eta_{max\ GM} * \exp\left(\frac{-(\lambda - \lambda_{center\ GM})^2}{2(C_{value\ GM})^2}\right) \quad (60)$$

λ goes from 0 to 900 nm or whatever range is required. The A value is $\eta_{max\ GM}$ because the gain medium efficiency is to be set. The next step creates a gain medium power absorption curve of the same magnitude as the single Gaussian curve of the output of all laser diodes added together, only now the gain medium efficiency can be set using the value $\eta_{max\ GM}$. This is how the simplified model differs form the full fiber model. The rate equations are not used here, and the maximum fiber efficiency is an input parameter instead of actually being calculated.

$Absorption\ Power_{GM}$ – Multiply input laser diode power across all wavelengths by the Gain Medium Absorption Curve, this yields the actual gain medium absorption power curve that is close to the same magnitude as the laser diode $Gaussian_{all\ bars}$ curve.

$$Absorption\ Power_{GM} = Gaussian_{all\ bars} * Absorption\ Curve_{GM} \quad (61)$$

$Power_{optical\ GM}$ – Total area under the curve $Absorption\ Power_{GM}$. This is the amount of optical power out of the Gain Medium.

Any optical power that is not transferred to the gain medium is considered lost as heat. Notice how the temperature of the gain medium is not taken into account. The optical power out of the gain medium then cascades onward into the combiner. The combiner consists of three subcomponents, and each one of these subcomponents has a constant efficiency value. The beam director, mirrors, and particularly the aperture sharing element in fiber lasers are the controls that help guide the output of all the gain medium fibers and help to coalesce all the individual laser beams into a single coherent, very high-power beam that is then directed out of the high-power laser system. The equations for calculating the optical power out of the combiner components are shown below by equations 62 through 64.

For the beam director,

$$Power_{optical\ BD} = Power_{optical\ GM} * \eta_{BD} \quad (62)$$

For the mirrors,

$$Power_{optical\ MR} = Power_{optical\ BD} * \eta_{MR} \quad (63)$$

For the aperture sharing element,

$$Power_{optical\ ASE} = Power_{optical\ MR} * \eta_{ASE} \quad (64)$$

This is the entire process of modeling the optical power out of the high-power laser system model. The equations were built into Simulink for model simulation. From these equations, a changing laser diode bar temperature does not yield a significant decrease in laser diode optical output power. The optical power loss occurs in the gain medium when diode output center wavelength no longer lines up with the gain medium absorption center wavelength.

Appendix B: Full Fiber Model Parameter Values

Parameter – Definition	Value
$T_{ref LD}$ – Reference Temperature for Laser Diode Characteristics (K)	298
$\lambda_{center LD nom}$ – Nominal Center Wavelength of Laser Diode Output at $T_{ref LD}$ (m)	9.76e-07
$\lambda_{fwhm LD nom}$ – Nominal Full Width Half Maximum of Laser Diode Output (m)	2.5e-09
$d\lambda/dT$ – Wavelength Temperature Coefficient for Laser Diode (m/K)	2.5e-10
$d\beta/dT$ – Spectral Width Temperature Coefficient for Laser Diode (m/K)	8.84e-11
$I_{th,ref}$ – Threshold Current Reference (A)	15
I_{max} – Max Current per Laser Diode (A)	180
V_{max} – Max voltage per Laser Diode (V)	2
$Power_{per LD,ref}$ – Reference optical power out per laser diode (W)	200
T_0 – Threshold Current Characteristic Temperature (K)	180
T_1 – Slope Efficiency Characteristic Temperature (K)	680
$NUM_{LD/bar}$ – Number of Laser Diodes per Bar (diodes thermally in parallel)	5
$NUM_{LD bars}$ – Number of Laser Diode Bars (diodes thermally in series)	5
L – Fiber Length (m)	10.8
R_{core} – Fiber Core Radius (m)	0.00002
R_{clad} – Fiber Cladding Radius (m)	0.0004
λ_s – Center Wavelength of Fiber Output Signal (Same for Seed Laser) (m)	1.064e-6
λ_1 – Starting Value for Laser Signal Wavelength Vector (m)	1e-6
λ_2 – Ending Value for Laser Signal Wavelength Vector (m)	1.1e-6
$\Delta\lambda$ – Step Size for Discretization of Laser Signal Wavelength Vector (m)	1e-9
$Seed_{pwr}$ – Seed Laser Optical Power into Fiber Core (W)	15
$Seed_{FWHM}$ – Seed Laser Full Width Half Maximum (m)	1e-9
$Seed_{Eff}$ – Seed Laser Electrical/Optical Efficiency (%)	55
N_{tot} – Total Population Density of Doping Ions in Fiber Core (m ⁻³)	7.9e25
Γ_p – Pump Power Filling Factor (0 to 1)	0.0025
Γ_s – Signal Power Filling Factor (0 to 1)	1

α_p – Fiber Attenuation Coefficient for Pump (cladding) (cm^{-1})	0.002
α_s – Fiber Attenuation Coefficient for Signal (core) (cm^{-1})	0.0004
τ – Spontaneous Lifetime of Doping Ions at the Upper Level (sec)	0.001
$Max Pwr_{fiber}$ – Maximum Allowable Optical Power into a Single Fiber (W)	5000
η_{BD} – Beam Director Thermal Efficiency	0.95
η_{MR} – Optical Training Mirror Lumped Reflectivity	0.92
η_{ASE} – Aperture Sharing Element Thermal Efficiency	0.97
$Power_{optical}$ – HPLS Design Optical Power from Laser Diodes (W)	75000
$Power_{electrical}$ – HPLS Electrical Power (W)	135000

Appendix C: Statistical Surrogate Model Data

Functions, plots, and coefficient data for the T_m^* equation 37.

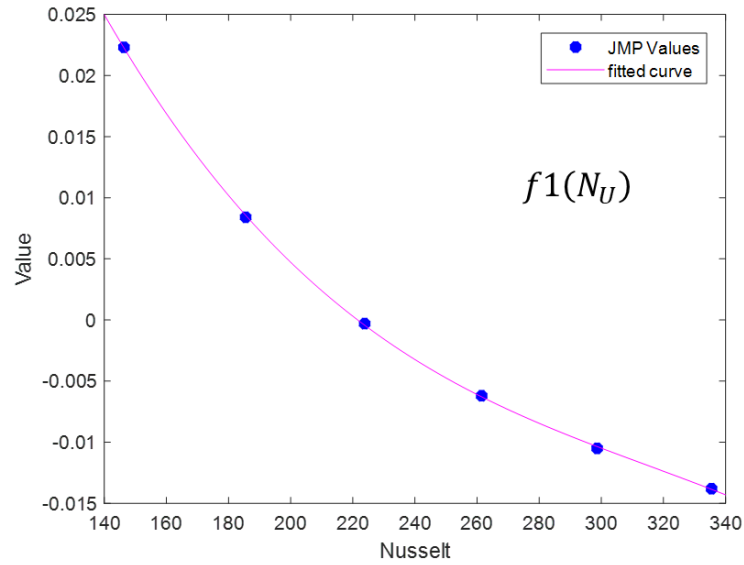


Figure 78: Data plot for f_1 curve of T_m^* equation

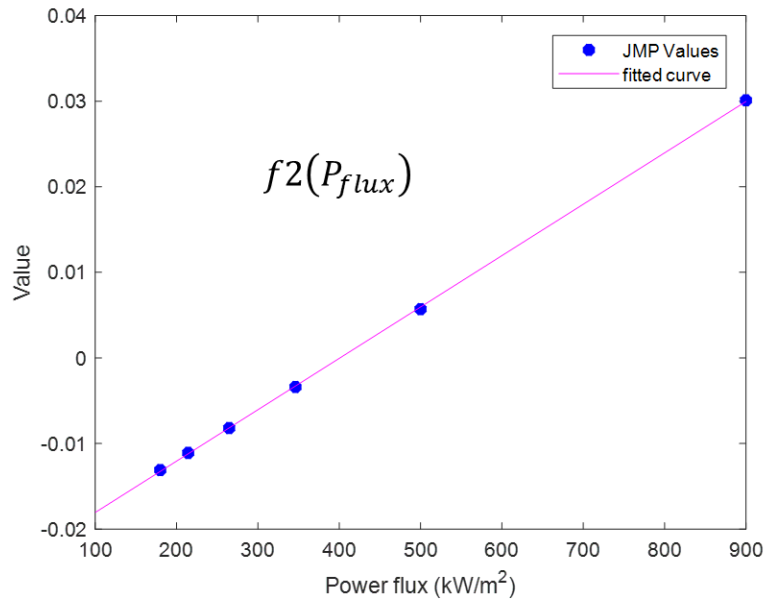


Figure 79: Data plot for f_2 curve of T_m^* equation

Table 19: Coefficients of fitted curves for T_m^* equation

Function	f1 (Nu)	f2 (Pflux)
p1	-3.77873660267427E-09	6.00290163459493E-05
p2	3.57816198745859E-06	-2.40630914247324E-02
p3	-1.22317111829595E-03	
p4	1.36462544571765E-01	

Functions, plots, and coefficient data for the T_f^* equation 38.

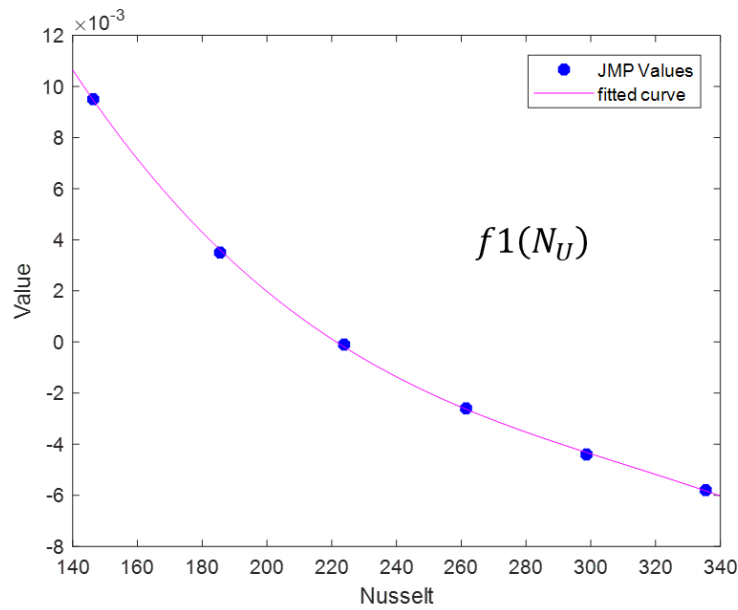


Figure 80: Data plot for f1 curve of T_f^* equation

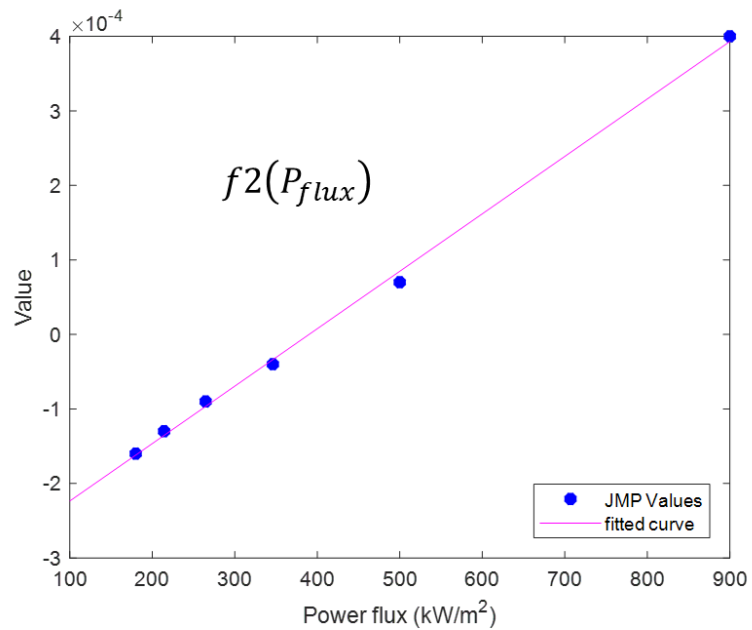


Figure 81: Data plot for f2 curve of T_f^* equation

Table 20: Coefficients of fitted curves for T_f^* equation

Function	f1 (Nu)	f2 (Pflux)
p1	-1.73531795313486E-09	7.70773445718801E-07
p2	1.61687450911918E-06	-3.00637111646132E-04
p3	-5.42255307371842E-04	
p4	5.96346129002552E-02	

Functions, plots, and coefficient data for the t_{ss} equation 39.

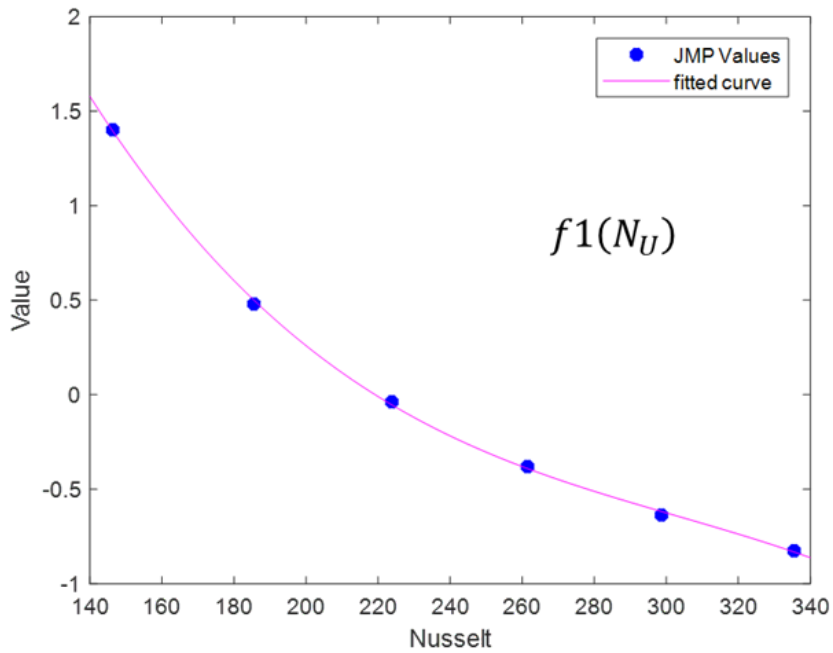


Figure 82: Data plot for f1 curve of t_{ss} equation

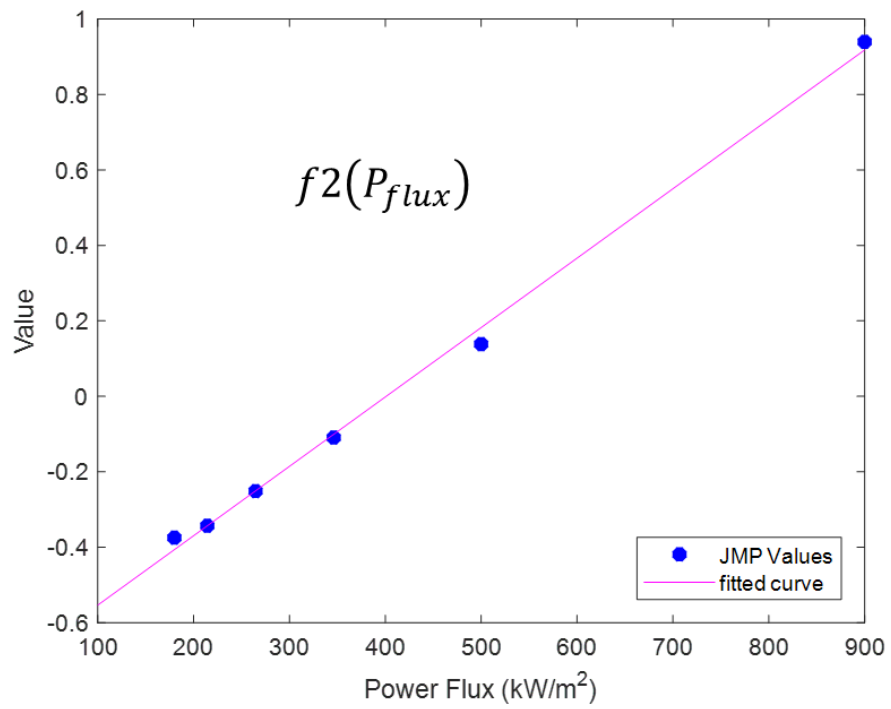


Figure 83: Data plot for f2 curve of t_{ss} equation

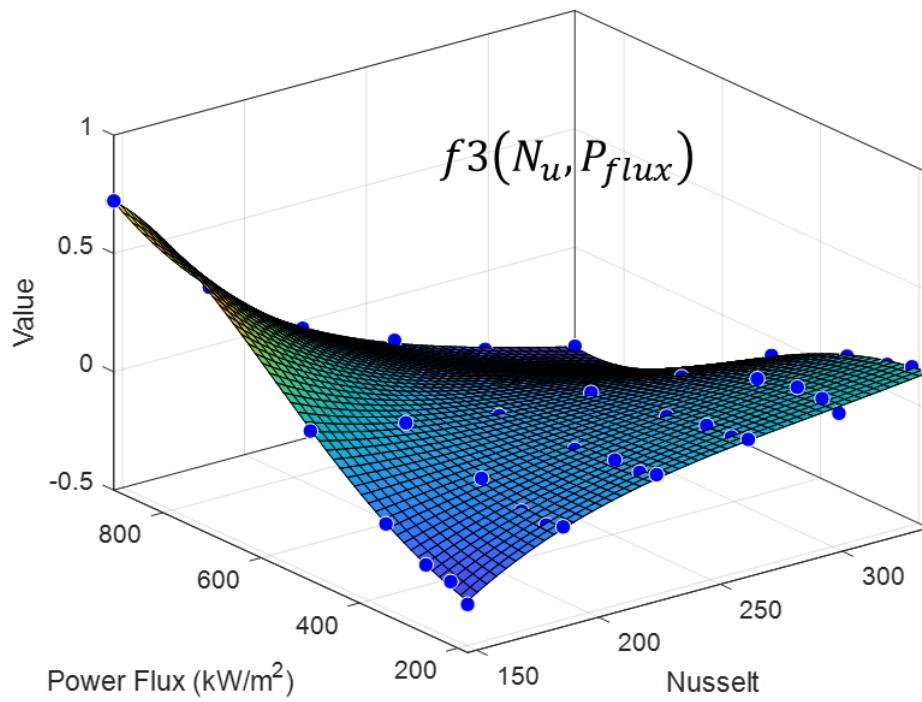


Figure 84: Data plot for f3 surface of t_{ss} equation

Table 21: Coefficients of fitted curves/surfaces for t_{ss} equation

Function	f1 (Nu)	f2 (Pflux)	f3 (Nu,Pflux)
p1	-3.06107865249336E-07	1.83888387197248E-03	-5.05539036409674E+00
p2	2.77967824544384E-04	-7.37130698189854E-01	6.35399833683526E-02
p3	-8.96670843367290E-02		1.16129858713599E-02
p4	9.52279905005918E+00		-2.89183341446856E-04
p5			-1.64845472180991E-04
p6			1.23287020533396E-06
p7			5.67674171654216E-07
p8			7.97247910561889E-07
p9			7.23641459477804E-09
p10			8.03909233441452E-09
p11			-4.05021198488718E-10
p12			-1.52210679479174E-09
p13			-1.25599276374740E-10
p14			-2.09553130567314E-11
p15			-9.24629166455322E-12
p16			3.64397532035604E-14
p17			9.01466360248055E-13
p18			2.84626269060602E-13
p19			-4.73049124036042E-14
p20			3.82113447434521E-14

Functions, plots, and coefficient data for the $overall_{eff}$ equation 40.

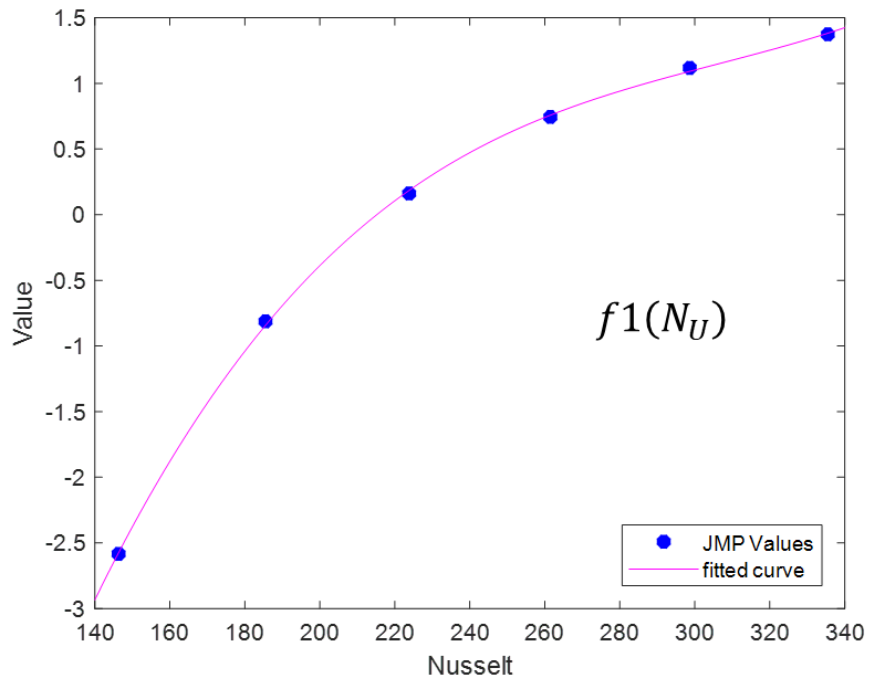


Figure 85: Data plot for f1 curve of $overall_{eff}$ equation

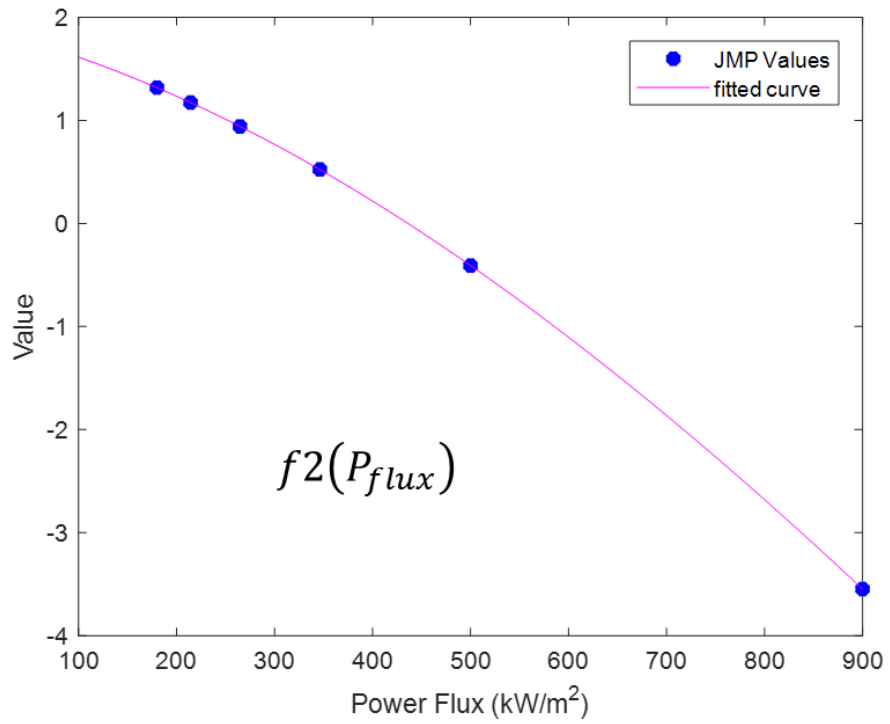


Figure 86: Data plot for f2 curve of $overall_{eff}$ equation

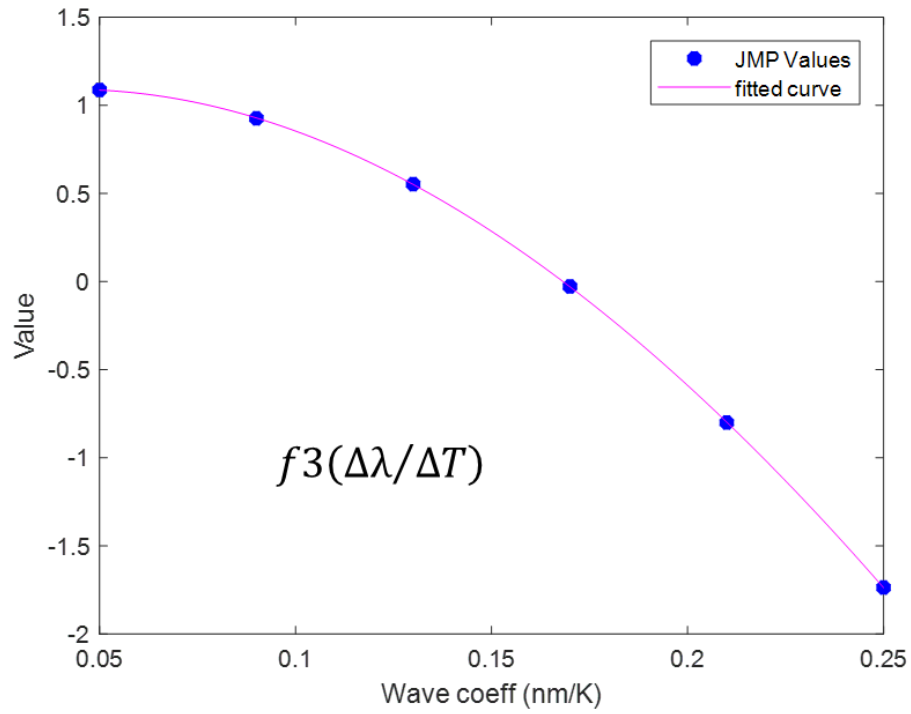


Figure 87: Data plot for f3 curve of $overall_{eff}$ equation

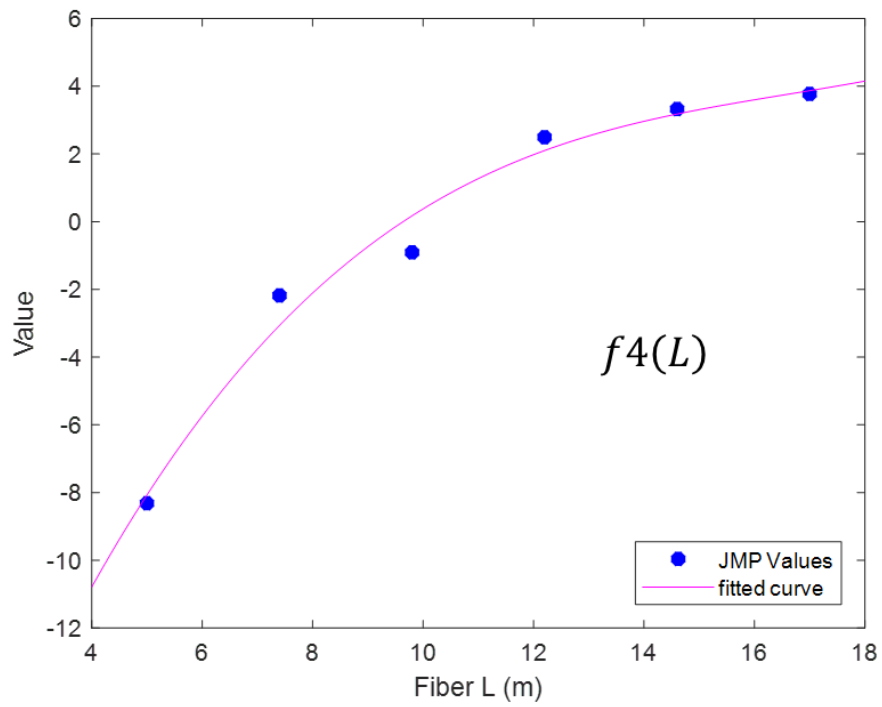


Figure 88: Data plot for f4 curve of $overall_{eff}$ equation

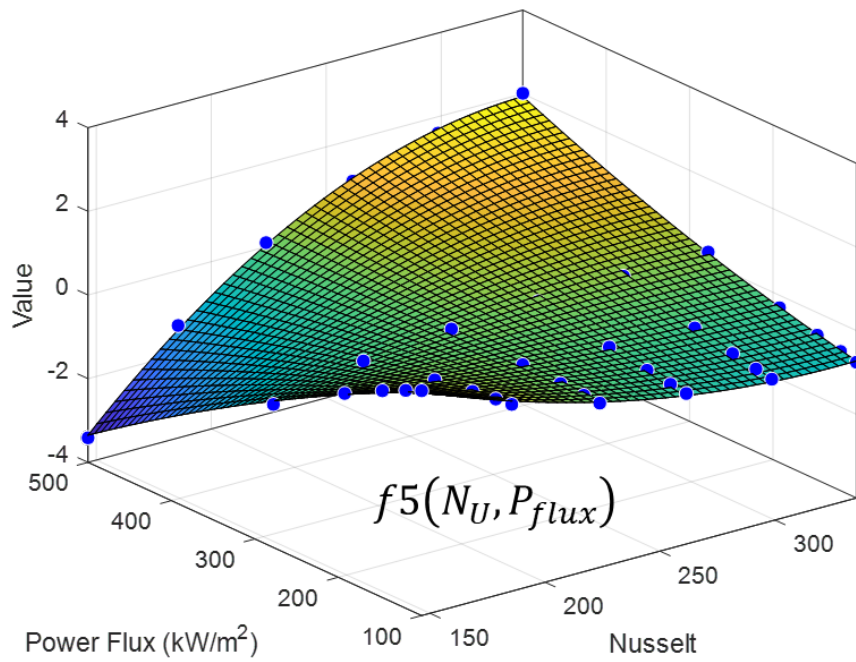


Figure 89: Data plot for f5 surface of $overall_{eff}$ equation

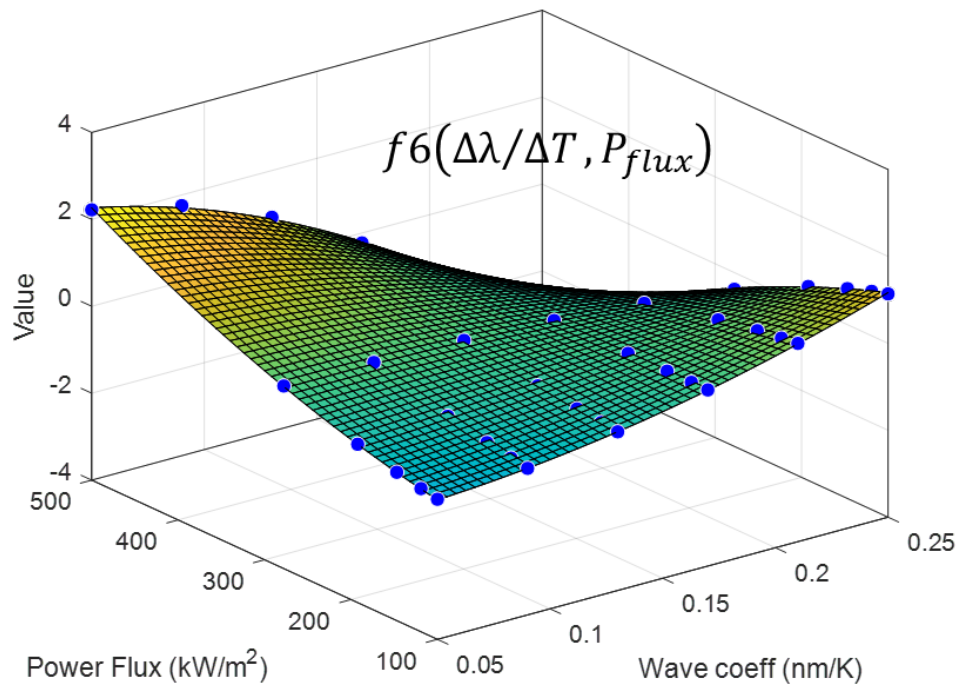


Figure 90: Data plot for f6 surface of $overall_{eff}$ equation

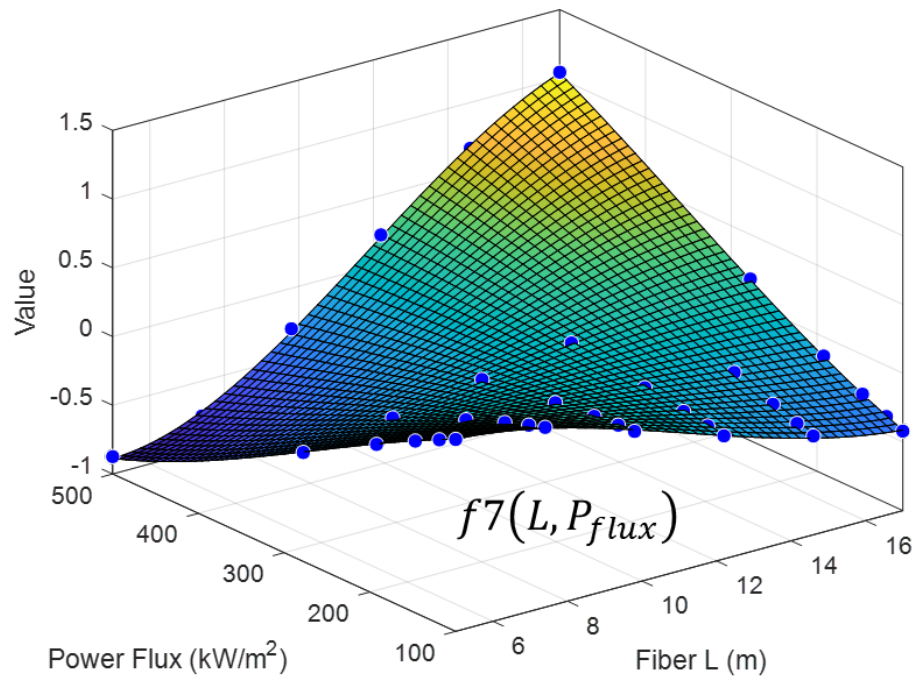


Figure 91: Data plot for f7 surface of $overall_{eff}$ equation

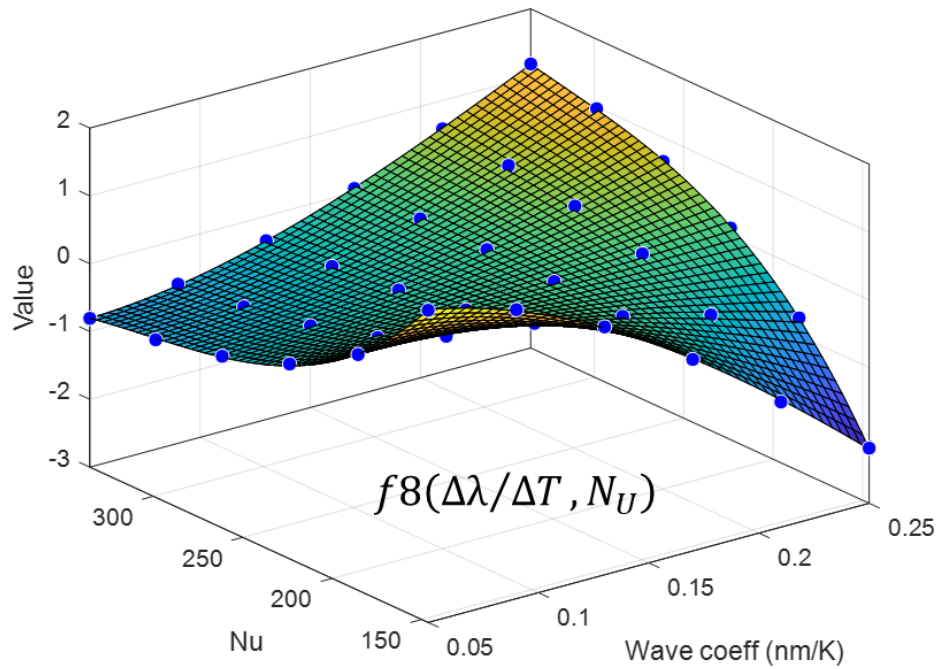


Figure 92: Data plot for f8 surface of $overall_{eff}$ equation

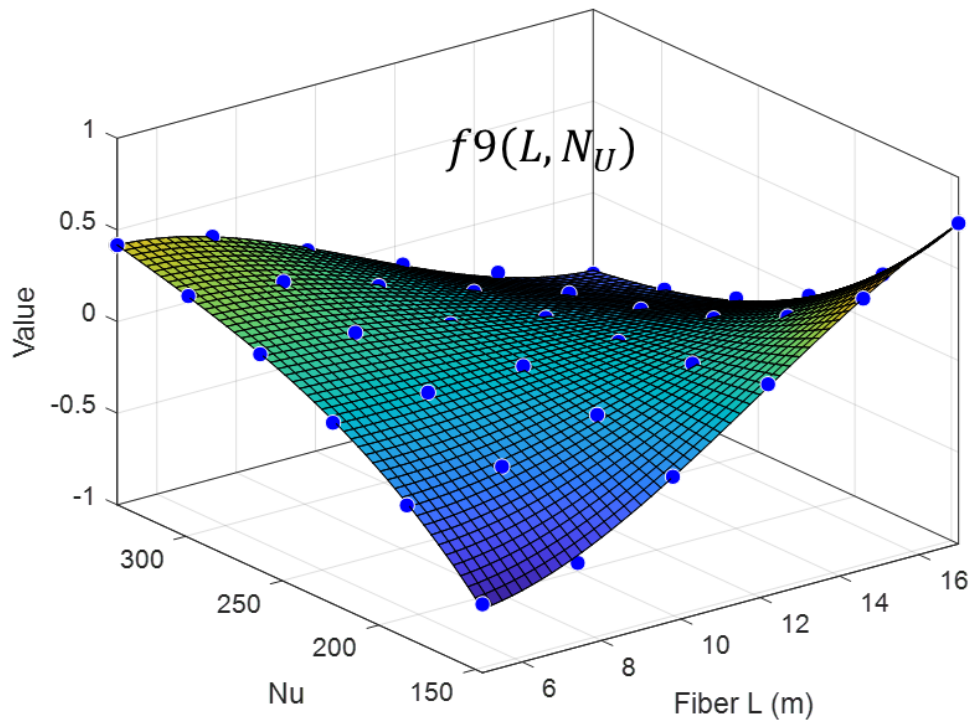


Figure 93: Data plot for f9 surface of $overall_{eff}$ equation

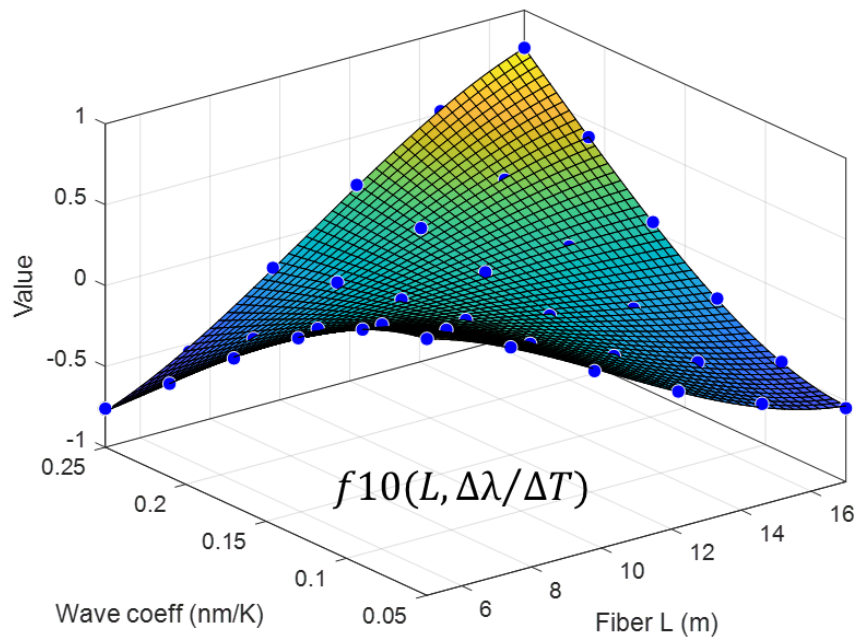


Figure 94: Data plot for f10 surface of $overall_{eff}$ equation

Table 22: Coefficients of fitted curves/surfaces for $overall_{eff}$ equation

Function	f1 (Nu)	f2 (Pflux)	f3 (dλ/dT)	f4 (L)
p1	6.16191186523192E-07	1.05026149826873E-09	4.17390046296308E+01	5.54905853480801E-03
p2	-5.66390433794560E-04	-5.06567851660419E-06	-7.98238467261911E+01	-2.76804757541522E-01
p3	1.81018973361318E-01	-2.34000383820787E-03	6.59430576223555E+00	4.87062468883196E+00
p4	-1.88660849817659E+01	1.89665217378109E+00	9.50830921378964E-01	-2.61982209494569E+01

Function	f5 (Nu,Pflux)	f6 (dλ/dT,Pflux)	f7 (L,Pflux)	f8 (dλ/dT,Nu)
p1	1.04043813695041E+01	-9.75309060491483E-01	1.30509984066419E-01	1.64168440052540E+01
p2	-7.27044029681556E-02	-5.15812490082400E+00	2.65959206184769E-01	-5.79273038836542E+01
p3	-2.33272001745350E-02	-2.79392689824564E-05	1.19975773128442E-05	-1.71403469943298E-01
p4	1.14586021367242E-04	6.43777117500446E+01	-3.89249255099058E-02	-3.35745898563692E+02
p5	1.70507904663548E-04	2.92780428694594E-02	-5.66965423216819E-04	8.37896603037433E-01
p6	-4.75919567259682E-06	4.45549840818530E-06	-2.44097589688872E-06	5.79764364779234E-04
p7	3.38889167805021E-12	-4.82253086412089E-03	1.22345345937894E-03	2.55061709759735E+02
p8	-2.85858814740350E-07	-1.60592656487889E-01	8.69759457486868E-05	1.89360732515086E+00
p9	1.96762035580661E-08	-2.97179626233093E-05	-7.93336386633803E-09	-3.50980840799159E-03
p10	-8.21902743600950E-14	1.40165300824719E-12	2.60090257898652E-09	-6.58024372556552E-07
p11			6.27933706281887E-08	-6.78168403006467E-01
p12			-3.05903764898686E-06	-1.05285686903611E+00
p13			1.85356238783949E-08	-1.95242934357616E-03
p14			-2.40098462423498E-10	4.38234881516620E-06
p15			2.10575359220685E-14	6.48128978924294E-13

Function	f9 (L,Nu)	f10 (L,dλ/dT)
p1	-3.58013469890083E+00	2.06471725091936E-01
p2	-3.98269945872954E-01	2.01938577155951E-01
p3	4.01484326918791E-02	1.03326687413602E+01
p4	8.70358035176602E-02	-3.23533661895934E-02
p5	1.27454452140930E-04	-2.17117802581835E+00
p6	-1.41338696996616E-04	-9.63474006220359E+01
p7	-2.13757662853922E-03	1.07704624577455E-03
p8	-4.22743755186455E-04	1.96512582807289E-01
p9	9.83275593905389E-06	7.44191307708002E+00
p10	1.58611960714218E-07	1.57115644290133E+02
p11	1.04655617707594E-08	4.48627498596103E-19
p12	8.83516216524050E-06	-7.17896871325701E-03
p13	2.42951433613264E-07	1.05638568904118E-01
p14	-1.44961360238130E-08	-1.43132716049385E+01
p15	8.66529419328246E-13	5.42534722209378E-01

Appendix D: Parameter values for Statistical Surrogate Model

Parameter – Definition	Value
$T_{ref LD}$ – Reference Temperature for Laser Diode Characteristics (K)	298
$\lambda_{center LD nom}$ – Nominal Center Wavelength of Laser Diode Output at $T_{ref LD}$ (m)	9.76e-07
$\lambda_{fwhm LD nom}$ – Nominal Full Width Half Maximum of Laser Diode Output (m)	2.5e-09
$d\lambda/dT$ – Wavelength Temperature Coefficient for Laser Diode (m/K)	“Varied”
$d\beta/dT$ – Spectral Width Temperature Coefficient for Laser Diode (m/K)	8.84e-11
$I_{th,ref}$ - Threshold Current Reference (A)	15
I_{max} – Max Current per Laser Diode (A)	180
V_{max} – Max voltage per Laser Diode (V)	2
$Power_{per LD,ref}$ – Reference optical power out per laser diode (W)	200
T_0 – Threshold Current Characteristic Temperature (K)	180
T_1 – Slope Efficiency Characteristic Temperature (K)	680
$NUM_{LD/bar}$ – Number of Laser Diodes per Bar (diodes thermally in parallel)	1
$NUM_{LD bars}$ – Number of Laser Diode Bars (diodes thermally in series)	1
L – Fiber Length (m)	“Varied”
R_{core} – Fiber Core Radius (m)	0.00001
R_{clad} – Fiber Cladding Radius (m)	0.0002
λ_s – Center Wavelength of Fiber Output Signal (Same for Seed Laser) (m)	1.064e-6
λ_1 – Starting Value for Laser Signal Wavelength Vector (m)	1e-6
λ_2 – Ending Value for Laser Signal Wavelength Vector (m)	1.1e-6
$\Delta\lambda$ – Step Size for Discretization of Laser Signal Wavelength Vector (m)	1e-9
$Seed_{pwr}$ – Seed Laser Optical Power into Fiber Core (W)	15
$Seed_{FWHM}$ – Seed Laser Full Width Half Maximum (m)	1e-9
$Seed_{Eff}$ – Seed Laser Electrical/Optical Efficiency (%)	55
N_{tot} – Total Population Density of Doping Ions in Fiber Core (m ⁻³)	7.9e25
Γ_p – Pump Power Filling Factor (0 to 1)	0.0025
Γ_s – Signal Power Filling Factor (0 to 1)	1

α_p – Fiber Attenuation Coefficient for Pump (cladding) (cm^{-1})	0.002
A_s – Surface area through which heat transfer occurs (m^2)	“Varied”
A_c – Flow cross sectional area in HX (m^2)	2.2e-5
D_h – hydraulic diameter of flow passages in HX (m)	1.34e-3
ε – equivalent roughness for friction factor calculation (m)	5e-6
$c_{p,m}$ – Heat sink material specific heat (J/kg K)	385
ρ_m – Heat sink material density (kg/m^3)	8954
V_m – Heat sink material volume (m^3)	1e-5
k_m – Heat sink thermal conductivity (W/m K)	401
$c_{p,f}$ – Fluid specific heat (J/kg K)	4184
ρ_f – Fluid density (kg/m^3)	1000
V_f – Fluid volume inside HX (m^3)	2.5e-5
T_{in} – Fluid temperature into HX (K)	298
\dot{m} – Mass flow rate (kg/sec)	“Varied”
P_{Elec} – Electrical power to diodes on a single bar (W)	1800W

Appendix E: Relevant Laser Physics/Component Overview

An HPLS, such as is modeled in this work, has three main components: Laser diodes, fiber gain media, and combining optics⁴⁵. The laser physics section is devoted to compiling the necessary laser physics for understanding basic laser operation. Each components produces heat, and all the heat together factors into the thermal management system (TMS) architecture required to achieve the desire laser system operation.

Laser Diodes – Structure and Operating Basics:

A laser diode, at its simplest, is the component where laser light is produced. First, consider the structure and individual components of a typical semiconductor laser diode. High power semiconductor laser diodes are of a double heterojunction design, meaning the active region (where laser light is actually emitted) is sandwiched between two layers of waveguide-type material. This waveguide contains the current carrier and optical gain in the active region with the p-waveguide on one side and the n-waveguide on the other side⁴⁶. For this reason, the active region is sometimes referred to as the p-n junction, or just junction. The temperature of this junction plays a large role in the electro-optical efficiency of a laser diode. The material used in laser diode can vary, but typically elements like Ga, As, N, In, P, Sb, Si, and Al or combinations thereof are used. The lasing output wavelength of the laser diode is determined by what semiconductor materials are particularly used in the active region, shown in Figure 95.

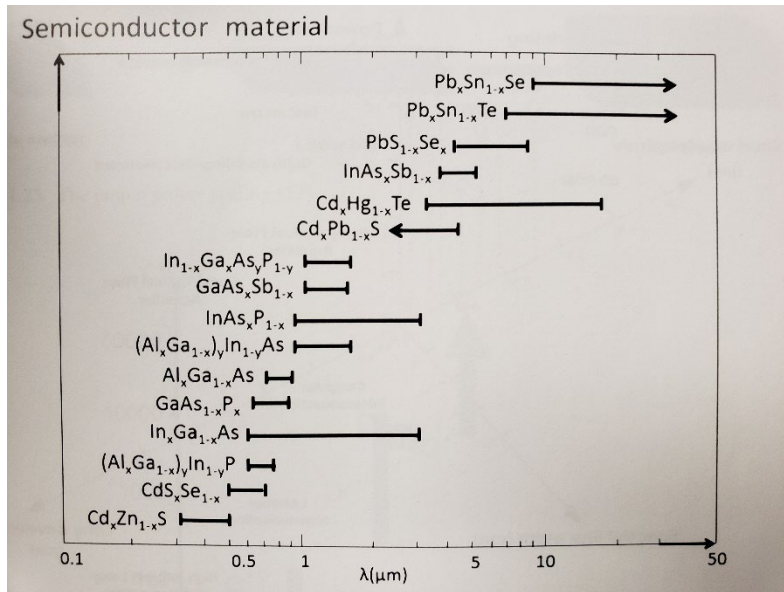


Figure 95: Lasing wavelength for certain semiconductor materials in the active region⁴⁶

Certain lasing wavelength are used for certain applications. The structure of the laser diode and the materials used in its creation are very important for proper operation. It is important to know exactly the materials used because the material properties play directly into the diode optical performance. The active region, waveguide, cladding substrate, and other parts of the laser diode all use some combination of the typical semiconductor materials listed above. Figure 96 below shows a typical laser diode and the different layers/materials used in its construction.

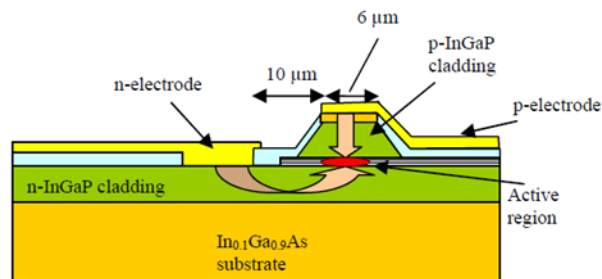


Figure 96: Typical laser diode diagram showing materials/components for operation⁴⁷

The p-side and n-side contacts are the electrical contacts where wires are attached to deliver electricity from a power source. P is the positive contact, and n is the negative contact. Any material labeled p is simply on the p contact side of the quantum well, and any material labeled n is simply on the n contact side of the quantum well. Starting from the quantum well and moving out, the next layer met is the doped waveguide, followed by the cladding, substrate, and electrical contact in that order. Notice the Dielectric material on the p contact side of the quantum well. Laser output comes from the quantum well, which is a type of active region. There are other representations of the active region used in laser diode manufacturing, and these will be discussed later. When a semiconductor is doped, this means impurities have been intentionally added in a way that changes the electrical, optical, structural properties in a performance-enhancing manner⁴⁶. When doped to high enough levels, semiconductors behave more like full-on conductors.

The laser light does not just come straight out of the laser diode as soon as it is created. Figure 97 helps to visualize the process laser light goes through after its creation but before it leaves the diode.

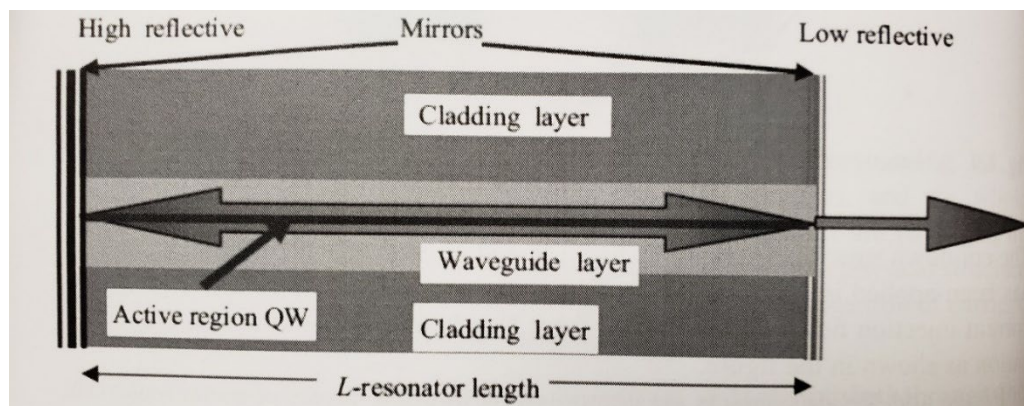


Figure 97: Explanation of laser diode operation using the Fabry-Perot Resonator⁴⁶

Laser light is first created inside the active region. This active region can be thought of as having a certain length L . The mirrors are placed at either end of the active region. One mirror has a high reflectivity and one has a low reflectivity. There is a certain gain threshold that needs to be achieved before laser light can actually escape from just bouncing back and forth between the two mirrors. When the optical gain reaches this threshold gain, the inner losses (like that of absorption into the optical medium, optical scattering, and output loss. When optical gain is greater than the gain threshold, positive optical gain is obtained and the laser operates. This process is complex, but it is better understood with the concept of threshold current. Laser diodes will not produce laser light until the forward current applied through them is greater than the threshold current. Any amount of current below the threshold current is not enough to push the laser into stimulated emission operation. The electrical power put in is all lost as heat until the threshold current value is reached and surpassed, as seen in Figure 98.

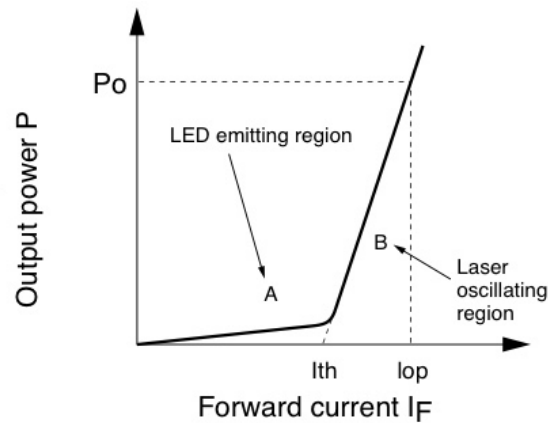


Figure 98: Laser diode threshold current diagram⁴⁸

Notice how the optical power is very low until the forward current supplied to the diode is greater than the threshold current. This is a unique characteristic of laser diodes, as they do not just begin stimulated emission right when electrical power is applied.

Another important concept of laser diode output to understand is the fast axis and slow axis. Laser light does not come out of the active region in a beam that has a constant area. As the beam moves further from the active region, it spreads out as shown in Figure 99.

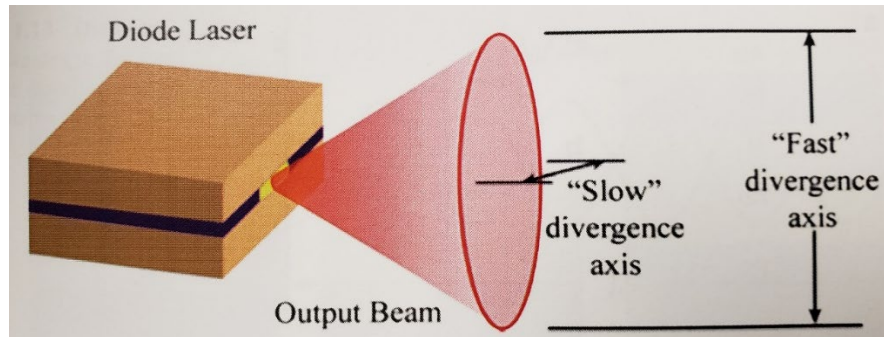


Figure 99: Diagram Denoting the "Fast" and "Slow" Axis of Laser Diode Output⁴⁶

The slow divergence axis is called so because along this axis, the laser light spreads out slower (less spread per unit of distance away from the exit of the active region). The fast divergence axis is called so because along this axis, the laser light spreads out faster (more spread per unit of distance away from the exit of the active region). Power content is higher along the fast axis than lower along the slow axis. This gets into the complex optics that go along with fully understanding laser diode operation, and this work will not go into that much detail. Laser diode output can be accurately represented with negligible error by using a single Gaussian curve^{37,38,45,49} to represent the combined output of both the slow and fast axes in terms of a power per unit wavelength as seen in Figure 100.

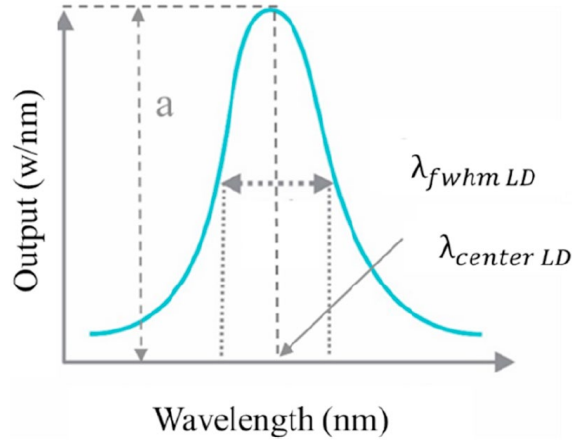


Figure 100: Diagram of Gaussian Curve representing laser diode optical power output³⁷

A Gaussian Curve can be modeled mathematically for the specific application of laser diodes in equations 65-67 shown below⁴⁵.

$$f(\lambda) = A_{value\ LD} * e^{\frac{(\lambda - \lambda_{center\ LD})^2}{2 * C_{value\ LD}^2}} \Bigg|_m^n \quad (65)$$

$$C_{value\ LD} = \frac{\lambda_{fwhm\ LD}}{2\sqrt{2 \ln(2)}} \quad (66)$$

$$A_{value\ LD} = \frac{Power_{LDbar}}{\int_{\lambda_{center\ LD} - \lambda_{fwhm\ LD} * 10}^{\lambda_{center\ LD} + \lambda_{fwhm\ LD} * 10} \exp\left(\frac{-(\lambda - \lambda_{center\ LD})^2}{2(C_{value\ LD})^2}\right) d\lambda} \quad (67)$$

Using Gaussian curve methodology, the optical power out of a laser diode can be defined by a center wavelength $\lambda_{center\ LD}$, full width half maximum (FWHM, meaning spectral width) $\lambda_{fwhm\ LD}$, peak intensity output value a ($A_{value\ LD}$), and optical power value P_{opt} . The area under this curve is equal to the total optical power out of a laser diode along both its fast and slow axes. This assumption allows for neglecting the optics knowledge necessary to carry out the complex math for finding the optical power from the fast and slow axes. The area of the

output beam at a certain distance away from the exit of the active region is an important value, but optical lenses and other components help to properly direct and collimate the laser light as soon as it comes out of the laser diode. Hence, from a mechanical-thermal engineering perspective, the optical power contained in the laser beam is the most important value. Laser diodes do generate significant heat, and the effects of this heat will be looked at and defined next.

Laser Diodes – Optical Power Temperature Dependence:

Laser diode optical power is temperature dependent. When diode temperature increases due to self-heating from normal operation, the electro-optical efficiency decreases. The temperature of interest in a laser diode is called the junction temperature, defined as the active region of the laser diode (where the laser light is actually being produced, called the p-n junction).

For CW (continuous wave) operation, the steady state junction temperature is given by equation 68.

$$T_j = T_{hs} + \Delta T \quad (68)$$

Here, T_j is junction temperature, T_{hs} is heat sink temperature, and ΔT is the difference between the heat sink and junction temperature. The next question to ask is how to find ΔT . This temperature difference is caused by the waste heat generated in the laser diode. If the laser diode is said to have a certain total thermal resistance R_{th} from the junction through the varying diode materials to the heat sink, ΔT can be represented by equation 69.

$$\Delta T = R_{th} Q_{Diode} \quad (69)$$

Here, Q_{Diode} is the waste heat generated in the laser diode that must be removed. This value Q_{Diode} can be further defined as shown in equation 70.

$$Q_{Diode} = P_{Elec} - P_{Opt} \quad (70)$$

Here, P_{Opt} is the optical power out of the laser diode and P_{Elec} is the electrical power into the laser diode. It makes sense that the waste heat is the electrical power in minus the optical power out. The value P_{Elec} can be further defined as shown in equation 71.

$$P_{Elec} = I_{op}V_{op} \quad (71)$$

Here, I_{op} is the operating current sent to the diode and V_{op} is the operating voltage for the diode. The equations 68-71 are taken from Liu et al.⁴⁶.

The optical power P_{Opt} is more complicated to define. The optical power out of a laser diode decreases as its junction temperature increases. Two laser characteristics, threshold current I_{th} and slope efficiency η_{slope} (normally units of W/A), determine the optical power out a laser diode. The value I_{th} is defined as the current required before coherent emission takes place from the laser. When a current value lower than I_{th} is sent to the laser, that electrical power is all turned into heat. Refer back to Figure 98 and see how slope efficiency is the slope of the curve from I_{th} to I_{op} , hence the units of W/A.

The effect of junction temperature on both laser characteristics is generalized in Figure 101.

Notice how as junction temperature increases, threshold current increases and slope efficiency decreases.

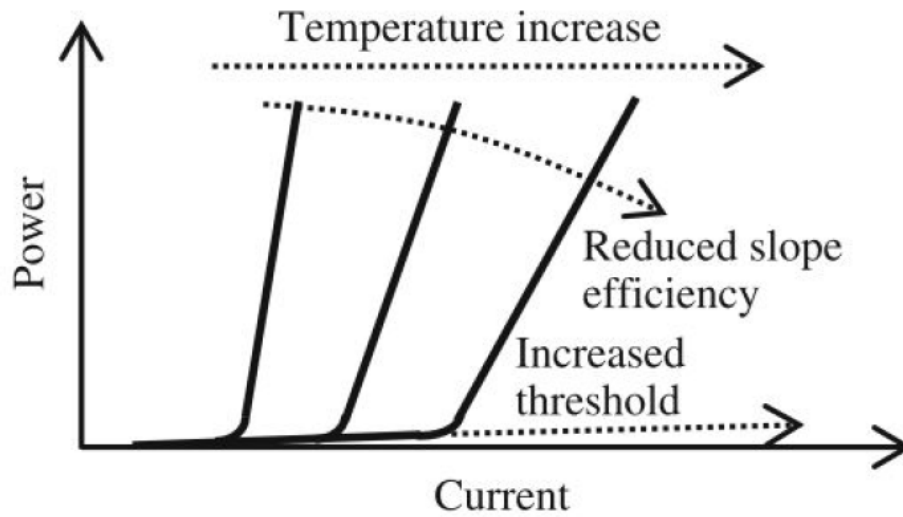


Figure 101: Generalized graph of optical output power vs. forward current showing the effects of junction temperature on threshold current and slope efficiency⁴⁹

Research by Bacchin et al.⁵⁰ verifies the trends described above, shown in Figure 102. Again, notice how the threshold current increases and slope efficiency decreases as junction temperature increases. The trends are still the same whether the optical power out is on the order of mW or W. Bacchin et al.⁵⁰ do several other tests with laser diode stacks yielding output powers on the order of kW that show threshold current and slope efficiency respond to junction temperature change in the same manner.

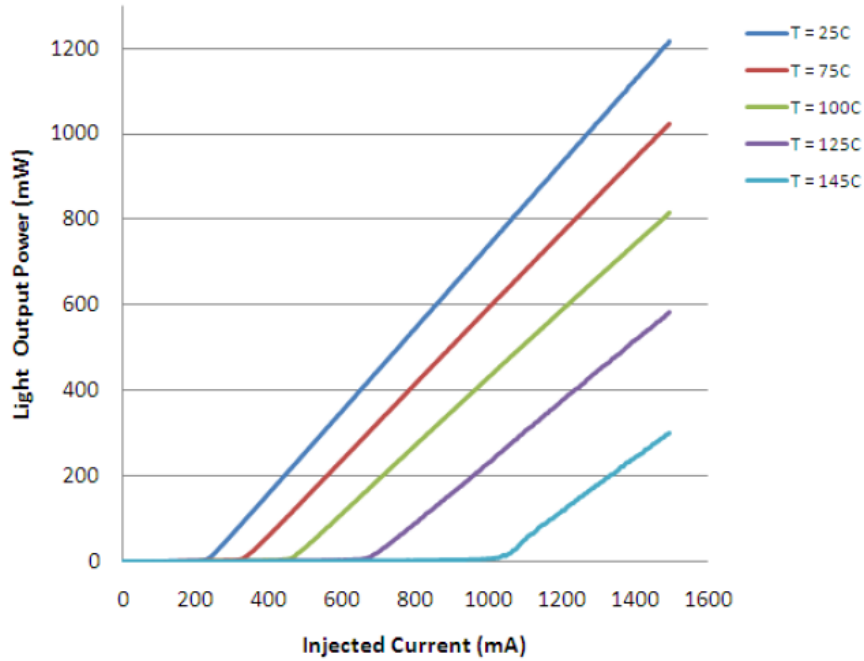


Figure 102: Experimental research showing the trend of increasing threshold current and decreasing slope efficiency due to increasing junction temperature (mW of optical power)⁵⁰

Another reference by Zhang⁵¹ considering research on laser diode threshold current and slope efficiency explains how the placement of the heat sink on the p side of the diode versus the n side of the diode can have a significant impact on the observed junction temperature. This means there is an optimal way to orient/mount the laser diode on a given heat sink to achieve the best performance. The values of I_{th} and η_{slope} characteristics are both junction temperature dependent as shown in their respective equations 72 and 73 below⁴⁶.

$$I_{th}(T_j) = I_{ref} e^{\left(\frac{T_j - T_{ref}}{T_0}\right)} \quad (72)$$

$$\eta_{slope}(T_j) = \eta_{ref} e^{-\left(\frac{T_j - T_{ref}}{T_1}\right)} \quad (73)$$

Here, I_{ref} is the threshold current at some laser diode operating reference temperature T_{ref} and η_{ref} is the slope efficiency at that same reference temperature. They are normally specified by the laser diode manufacturer on a specification sheet. The value T_0 is called the threshold characteristic temperature, and T_1 is called the slope characteristic temperature. These values are found through experiments and are particular to a specific laser diode. They are not normally found on the specification sheets. A more in-depth explanation of laser characteristic temperatures is given at a later point. Equations 72 and 73 are empirical equations and come from Liu et al.⁴⁶. They are further defined and explained by Saini et al.⁵². This source supplements Liu et al.⁴⁶ and dives deeper into the actual development of the equations shown here that determine laser diode optical power efficiency.

The P_{Opt} value for a laser diode is given in equation 74 below⁴⁶.

$$P_{Opt} = \eta_{slope}(I_{op} - I_{th}) \quad (74)$$

By observation, it is seen that either a decrease in η_{slope} or an increase in I_{th} yields an overall decrease in the P_{Opt} value, as I_{op} is kept constant. By equations 72 and 73, it is clear that when T_j increases, η_{slope} decreases and I_{th} increases. Hence, the P_{Opt} value is affected by two variables when T_j increases, not just by one variable. Plugging equations 72 and 73 into equation 74 yields equation 75 below⁴⁶.

$$P_{Opt} = \eta_{ref} e^{-\left(\frac{T_j - T_{ref}}{T_1}\right)} \left(I_{op} - I_{ref} e^{\left(\frac{T_j - T_{ref}}{T_0}\right)} \right) \quad (75)$$

By combining equations 69, 70, 71, and 75 into equation 68 yields the final form of the steady state T_j relation, equation 76 below⁴⁶.

$$T_j = T_{hs} + R_{th} \left[I_{op} V_{op} - \eta_{ref} e^{-\left(\frac{T_j - T_{ref}}{T_1}\right)} \left(I_{op} - I_{ref} e^{\left(\frac{T_j - T_{ref}}{T_0}\right)} \right) \right] \quad (76)$$

For steady state operating conditions, T_j must be known in order to find T_j . This simply means solve for T_j iteratively. However, the transient conditions are more useful. It is interesting to see what happens to the optical power output in the time from initial laser activation until it reaches steady state operation. What is the time constant for junction temperature to settle out? This requires a deeper look at the laser diode, carrier, sub mount, and heat sink, possibly as complex as a transient 3D heat conduction problem where the energy into and out of the junction control volume can be used to estimate the junction temperature.

Laser Diodes – Characteristic Temperatures:

The following is a discussion on the concept of laser diode characteristic temperature. There are two characteristic temperatures, T_0 for threshold current, and T_1 for slope efficiency. The relations for T_0 and T_1 are shown in equations 77 and 78.

$$T_0 = \frac{\partial T}{\partial \ln(I_{th})} \quad (77)$$

$$T_1 = - \left(\frac{\partial T}{\partial \ln(\eta_{slope})} \right) \quad (78)$$

Equations 77 and 78 are created from the following relationship (equation 79) provided by Asryan et al.⁵³. The basic equation given is

$$T_0 = \left(\frac{\partial \ln(j_{th})}{\partial T} \right)^{-1} \quad (79)$$

Here, j_{th} is the current density. This is a rather difficult value to use without diving deep into laser diode theory. Hence, for experimental purposes, j_{th} is replaced with the threshold current

I_{th} , yielding equation 77. The concept can be applied to slope efficiency as well, yielding equation 78. Changing equation 79 in this manner has been utilized successfully in experimental research by Bacchin et al.⁵⁰.

The characteristic temperatures can be found experimentally by plotting the threshold current and slope efficiency points as a function of temperature on a logarithmic scale and then measuring the slope of the linear fit line. With this technique, Bacchin et al.⁵⁰ utilized the data in Figure 103 to find T_0 and T_1 for a specific laser diode with a nominal center wavelength of 808 nm.

<u>T (°C)</u>	BSRL results		<u>Slope efficiency (W/A)</u>
	<u>I_{th} (mA)</u>		
23	222		1.05
45	247		1.02
70	290		0.98

Figure 103: Laser diode threshold current and slope efficiency experimental values⁵⁰

For T_0 ,

$$T_0 = \frac{\partial T}{\partial \ln(I_{th})} = \frac{70 - 23}{\ln(290) - \ln(222)} \cong 176K$$

For T_1 ,

$$T_1 = - \left(\frac{\partial T}{\partial \ln(\eta_{slope})} \right) = - \left(\frac{70 - 23}{\ln(0.98) - \ln(1.05)} \right) \cong 681K$$

These are the same values Bacchin et al.⁵⁰ provide in their research. Several other sources discuss finding these T_0 and T_1 values. Liu et al.⁴⁶ gives values for T_0 based on the laser diode nominal center wavelength. T_0 is $\sim 200\text{K}$ for wavelength at 980 nm, $\sim 140\text{K}$ for wavelength at 800 nm, and below 100K for shorter wavelengths (630-760 nm). Cooke et al.⁵⁴ describes work done by researchers at Georgia Tech who found the T_0 value experimentally for several different structures of an InGaN-based violet-blue laser diode. Their value of 180K was comparable to typical values reported for other InGaN-based violet-blue laser diodes (range 140-190K). Cooke et al.⁵⁴ goes on to say how a high value of T_0 indicates less shift in the threshold current with a given change in temperature.

Akahane et al.⁵⁵ discuss how a conventional 1550 nm center wavelength laser has a T_0 value of around 100K. Through experimentation, they were able to fabricate a 1529 nm centerwavelength quantum dot laser diode to operate with $T_0 = 113\text{K}$ within an operating temperature range of 293K to 353K. Figure 104 shows data from their experiments.

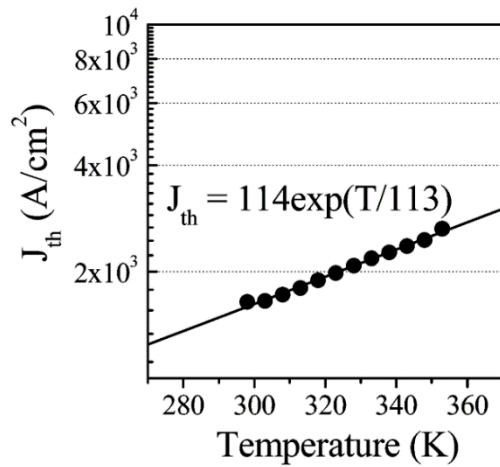
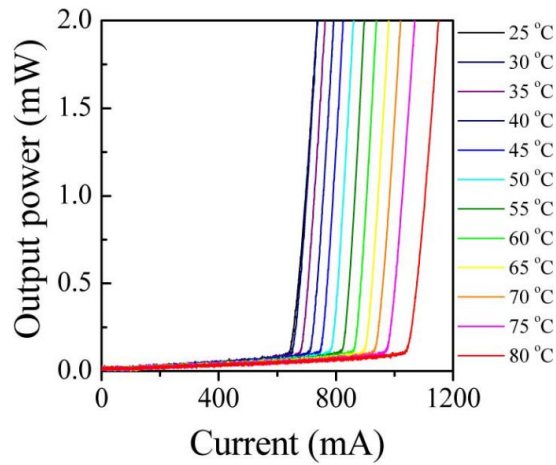


Figure 104: Temperature dependence of L-I characteristic curves and relationship between threshold current density and operating temperature with $T_0 = 113\text{K}$ ⁵⁵

Akahane et al.⁵⁶ also fabricated another laser in the 1550 nm range. This one had a wavelength of 1520 nm with a $T_0 = 102\text{K}$. It was of similar quantum dot design as in Akahane et al.⁵⁵ and had lower threshold current values with similar optical power output values. The data is shown in Figure 105.

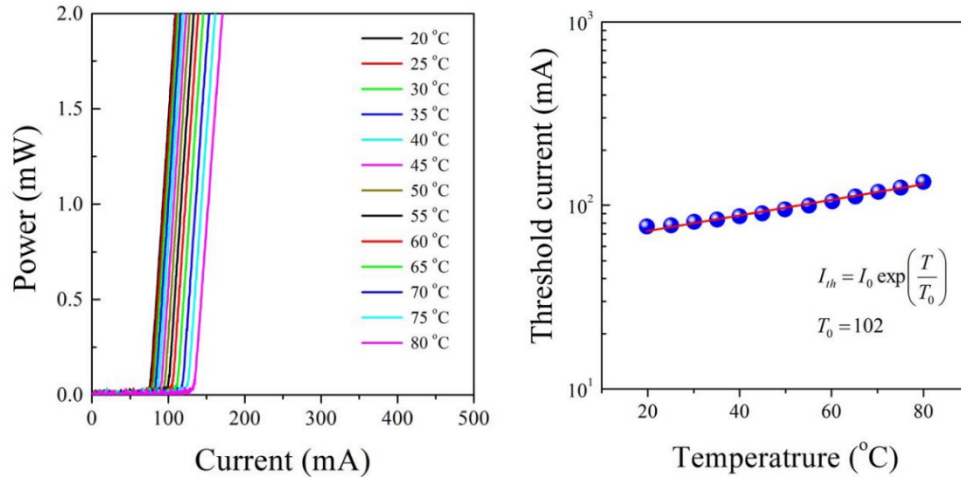


Figure 105: Temperature dependence of L-I characteristic curves and relationship between threshold current and operating temperature with $T_0 = 102\text{K}$ ⁵⁶

Another area of research by Akahane et al.⁵⁷ experimented on the threshold current for a quantum dot laser diode with a varying number of quantum-dot layers in the active region (junction). They experimented with number of layers N equal to 5, 10, 15, and 20. The highly stacked InAs quantum dot structure was fabricated using a strain compensation technique on a InP(311)B substrate. Strain compensation is a technique used in the manufacturing of semiconductor structures that allows for the fabrication of a high number of stacked quantum dot layers (larger N value). Figure 106 shows the pertinent results from the work.

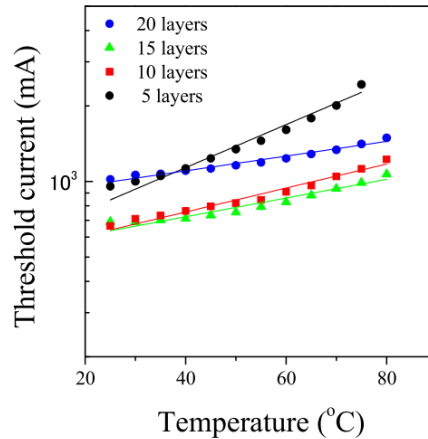


Figure 106: Relationship between threshold current and operating temperature with a varying number of quantum dot layers. The T_0 values for each sample were 51K for $N = 5$, 91K for $N = 10$, 116K for $N = 15$, and 148K for $N = 20$ dot layers⁵⁷

It is interesting to note how the T_0 values found in the experiment were different with the number of quantum dot layers. Specifically, T_0 increased with an increasing number of quantum dot layers. The strain compensation technique which allowed the adding of 10 or more quantum dot layers to a laser diode was found to yield both significant gain and better temperature stability (higher T_0) in the semiconductor device.

Arsenijević et al.⁵⁸ investigated the temperature dependent characteristics of a transverse single-mode GaAs-based InAs submonolayer (SML) quantum dot laser with a nominal center wavelength of 980 nm. While operating the laser in continuous wave (cw) conditions from operating temperatures of 15°C to 60°C, they found a T_0 value of 101K. The pertinent results of their work are shown in Figure 107.

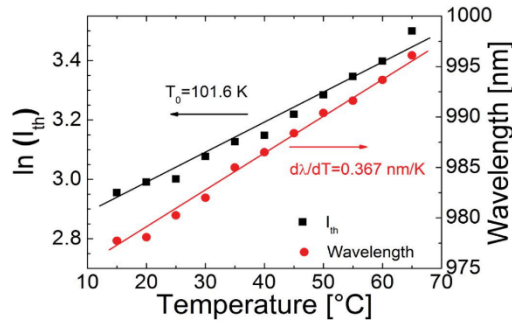


Figure 107: Operating temperature versus the natural log of threshold current and lasing wavelength showing $T_0 = 101K$ and wavelength temperature coefficient $d\lambda/dT = 0.367 \text{ nm/K}$ ⁵⁸

The T_0 value found by Arsenijević et al. can be confirmed using equation 77 and estimations from the figure above as shown here.

$$T_0 = \frac{\partial T}{\partial \ln(I_{th})} = \frac{60 - 20}{3.4 - 3.0} = 100K \cong 101K$$

This is yet more research where the T_0 value is found experimentally and shows equation 77 is commonly used among researchers to determine T_0 .

Li et al.⁵⁹ conducted research on creating an InAs quantum dot laser on GaAs-based materials to push emission wavelength towards the $1.55 \mu\text{m}$ range. They said this is difficult because the dots must be significantly larger and may suffer strain relaxation. The goal was to study the thermal stability of a laser using these materials with p-doped quantum dots and undoped quantum dots. The results are shown in Figure 108.

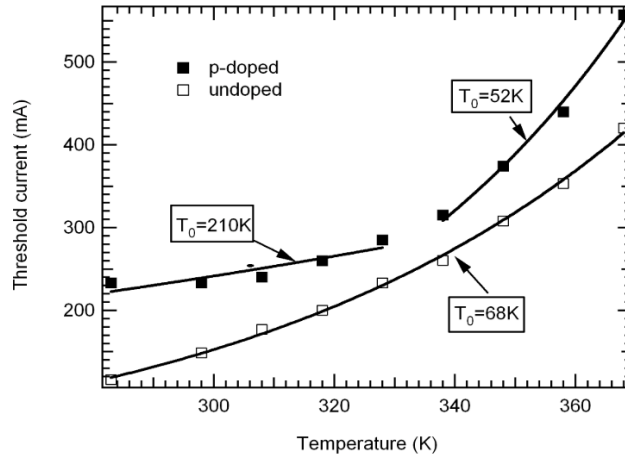


Figure 108: Characteristic temperature T_0 for P-doped and undoped quantum dot lasers emitting in the 1.55 μm regime⁵⁹

For the undoped laser, the T_0 is 68K in the range from 290K to 370K, which is a typical value for QD lasers grown on an InP (001) substrate. For the p-doped laser, T_0 is greatly improved in the temperature region from 280K to 330K, the T_0 reaches a high value of 210K. But, the T_0 drops to 52K from 330K to 370K.

Fathpour et al.⁶⁰ conducted research with a 1.3 μm quantum dot laser and were able to achieve operation in the 278 to 348K temperature range with a temperature invariant threshold current. This means T_0 approaches infinity. The observation of an invariant threshold current in their experiments can only be explained by a process called Auger recombination and they explain it further in the complete journal article. The results are shown in Figure 109.

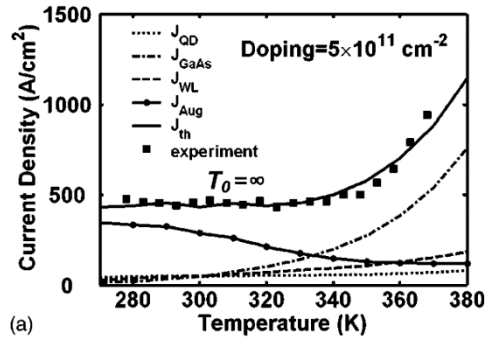


Figure 109: Graph showing invariant threshold current ($T_0 = \infty$) in the range of 278 to 348K⁶⁰

A T_0 of infinity indicates a very high laser thermal stability, which is ideal from a thermal management perspective. Fathpour et al.⁶⁰ report an abrupt drop in T_0 at around 340K, and this is similar to the laser performance observed in the research done by Li et al.⁵⁹.

Chen et al.⁶¹ studied a InGaAsP/InP multi-quantum-well (MQW) laser diode emitting at about 1.47 μm . Their goal was to obtain a laser with high temperature characteristics. To achieve this, they created a laser diode as seen in Figure 110.

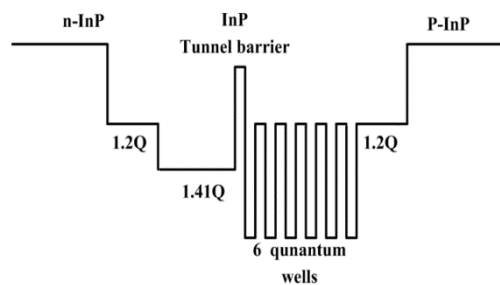


Figure 110: Schematic of InGaAsP/InP MQW laser with tunnel layer⁶¹

The goal was to see if they could take the typical characteristic temperature of $T_0 = 80\text{K}$ at room temperatures for InGaAsP lasers, which are normally plagued by Auger recombination issues, and increase T_0 through the use of a tunnel layer. This layer would function as a barrier and help

with Auger recombination and current leakage, as both affect the value of T_0 . Their results are shown in Figure 111.

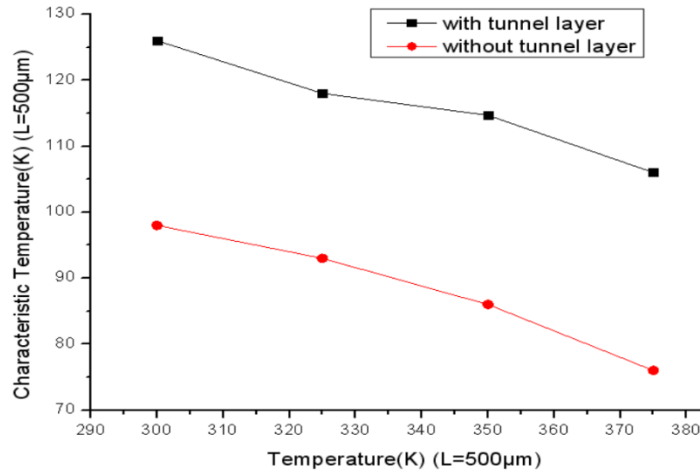


Figure 111: Laser characteristic temperature T_0 as a function of junction temperature comparing the performance of an InGaAsP laser diode with and without a tunnel barrier⁶¹

Notice the significant increase in characteristic temperature with the use of a tunnel barrier. Instead of $T_0 = 98\text{K}$ at room temperature, it is now $T_0 = 126\text{K}$.

Arai et al.⁶² created and operated a $1.3\ \mu\text{m}$ InGaAs laser diode with low Indium composition under pulsed conditions for research into whether or not a certain substrate growing method (traveling liquidus-zone) along with the lower composition of Indium in the substrate could be used to increase the characteristic temperature T_0 when compared to laser diodes with conventional InGaAs substrate (In:0.2-0.3). They achieved a T_0 of 130K for the temperature range of 25 to 90°C and a T_0 of 95K from 95 to 155°C. The lasing wavelengths at 25 and 85°C were $1.28\ \mu\text{m}$ and $1.31\ \mu\text{m}$ respectively. Their results are shown in Figure 112.

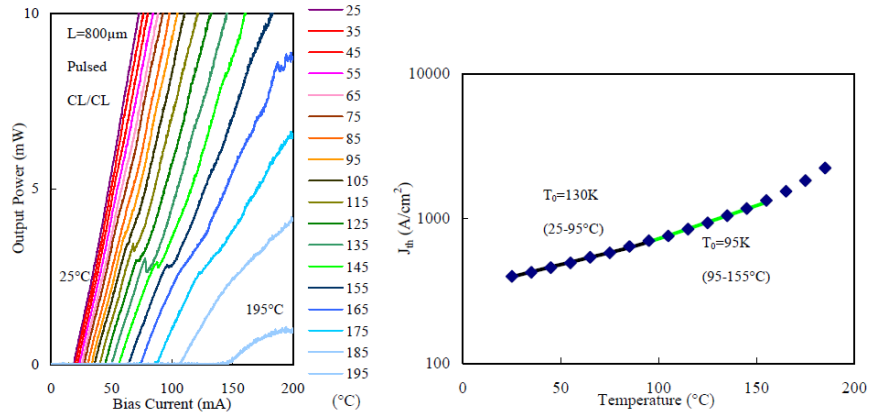


Figure 112: L-I curves at various operating temperatures and operating temperature vs. threshold current density plots⁶²

Zubov et al.⁶³ reported on an InAs/GaAs/InGaAsP laser with an emitting wavelength of 1.5 μm. They found values for $T_0 = 235K$ and $T_1 = 205K$ with in an operating temperature range of 20 – 70°C. This is significant because much less literature exists on finding T_1 (slope efficiency characteristic temperature). They also looked at the laser diode cavity length L of the laser diode and the effects it has on characteristic temperature T_0 . It shows the physical geometry of the laser diode plays a role in determining this parameter. Figure 113 below shows their results.

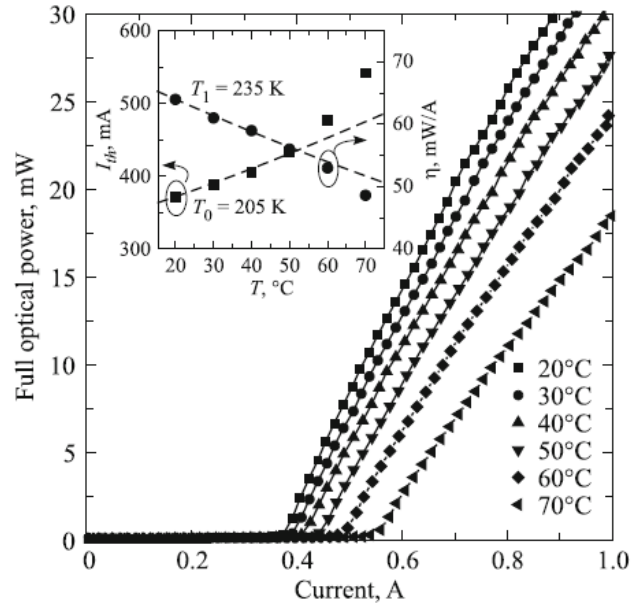


Figure 113: L-I curve at various operating temperatures, both characteristic temperature graphs, and T_0 variation with cavity length L ⁶³

Chackrabarti et al.⁶⁴ studied the temperature dependent aspects of a 670 nm laser diode's operation to a very in-depth level. Part of this research was finding the characteristic temperature T_0 . For this particular laser, they found a value for T_0 of 114K. Their results are shown in Figure 114.

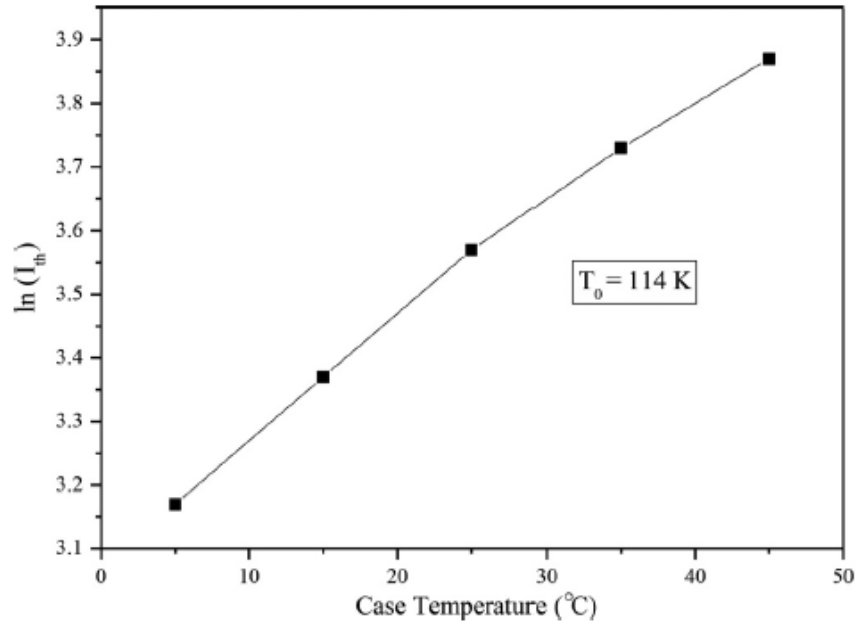


Figure 114: Threshold current vs. operating temperature, slope of curve is $T_0 = 114\text{K}^{64}$

Ryu⁶⁵ studied the temperature performance characteristics of a blue GaN laser emitting at around 400 nm with two different levels of doping. The results in Figure 115 actually predict a negative $T_0 = -360\text{K}$ for the more heavily doped region of $1.5 \cdot 10^{18} \text{ cm}^{-3}$. For the lower doping level of $1 \cdot 10^{17} \text{ cm}^{-3}$, $T_0 = 129\text{K}$.

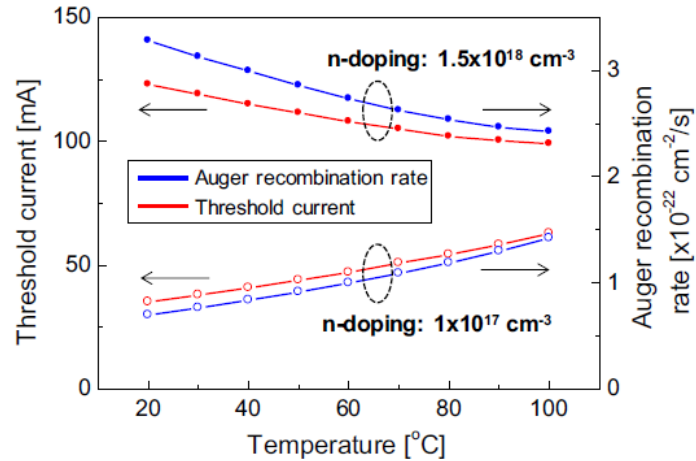


Figure 115: Threshold current vs. operating temperature for 2 n-doping levels⁶⁵

Clearly, the laser characteristic temperatures can vary widely based on aspects of a laser diode's physical design. Since they are diode specific, it is difficult to decide what values of them to use in a generic laser system model analysis. These characteristic temperatures are essentially a measure of a laser diode's thermal stability. Larger characteristic temperatures mean a certain ΔT from junction temperature to reference temperature will have a smaller effect on the optical power. This is clearly seen in equation 76. If given e^x and x gets closer to 0, e^x trends towards a value of 1. This is why laser diodes operating at cryogenic temperatures are more thermally stable than laser diodes operating at room temperature, as their characteristic temperatures are naturally larger. This increase in characteristic temperature with a decrease in diode junction temperature is shown in Figure 116 from research by Asryan et al.⁵³.

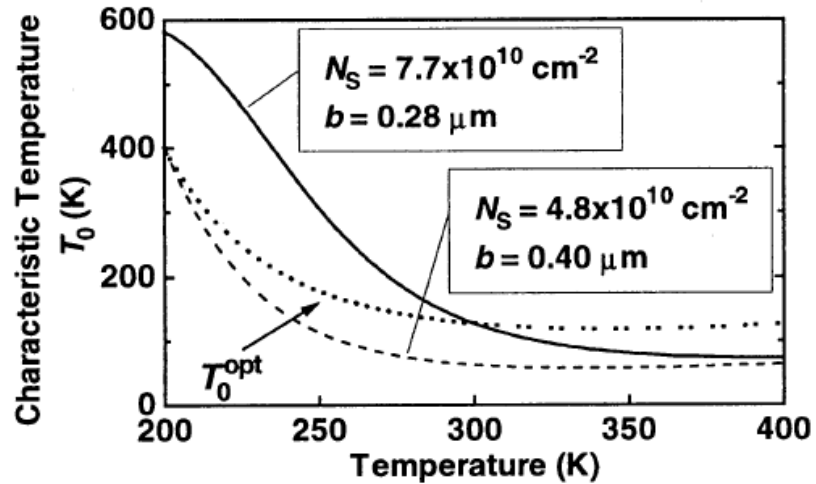


Figure 116: Experimental results of characteristic temperature T_0 as a function of laser diode operating temperature⁵³

The research by Asryan et al.⁵³ is very complicated to read and comprehend, as it is written at a very high technical level. The values N_s and b in Figure 5 are design parameters of the diodes being tested. The main thing to take away from this graph is that the characteristic temperature of a laser depends strongly on the operating temperature T , as T_0 drops profoundly with increasing T . This is because T_0 is found from the slope of this curve, and the T_0 for any operating temperature T is found by calculating the derivative of the T_0 curve at the point T . Although it is difficult reading, Asryan et al.⁵³ is a very good source for understanding the absolute fundamentals of laser diode physics.

Laser Diodes – Wavelength Shift Temperature Dependence:

The spectrum wavelength of laser diode output is also temperature dependent. Wavelength shift in laser diode optical power is an important phenomenon to capture. Laser diode output can be modeled with reasonable accuracy as a Gaussian curve^{37,38,45,49} (see Figure 100).

Manufacturers will specify a diode’s nominal center wavelength and full width half maximum (fwhm). A wavelength shift simply refers to the center wavelength increasing/decreasing by a certain amount. If junction temperature increases, diode output experiences a red shift in its spectrum. If junction temperature decreases, diode output experiences a blue shift in its spectrum. The junction temperature actually changes the semiconductor band gap distance. This phenomenon is well approximated in a linear manner (see equation 32), and manufacturers give this wavelength shift value on spec sheets in units of nm/K.

Research by Kim et al.¹⁴ showed how to predict the junction temperature of a high-power laser diode bar and that a change in this junction temperature corresponds to a wavelength shift in the laser diode optical power output, relative to the nominal center wavelength value. They made serious exploration into the area of estimating junction temperature in order to find the relationship of how laser diode output center wavelength changes with junction temperature. They found an approximate $d\lambda/dT$ of ~ 0.3 nm/K. This value agrees with the $d\lambda/dT$ value of ~ 0.28 nm/K for 808 nm laser diodes from research by Fan et al.⁶⁷ and ~ 0.32 nm/K for 980 nm laser diodes from research by Hu et al.⁶⁸. Research by Kondow et al.⁶⁹ showed a $d\lambda/dT$ of ~ 0.42 nm/K for a 1.3 μm GaInNAs laser diode. Some results from Kim et al.¹⁴ are provided in Figure 117.

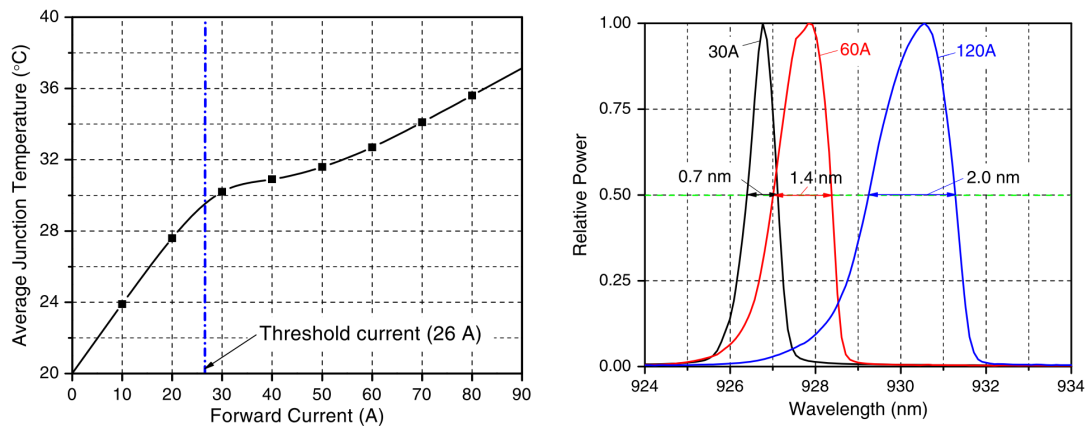


Figure 117: Results showing average junction temperature as a function of forward current and the wavelength shift/spectral broadening due to higher junction temperatures from increased forward current levels¹⁴

The research by Fan et al.⁶⁷ also displayed the wavelength shift using an 808 nm laser diode, as provided in Figure 118.

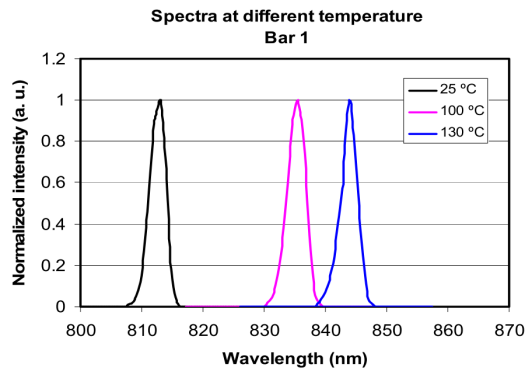


Figure 118: Wavelength shift due to higher junction temperatures from increased forward current in an 808 nm laser diode⁶⁷

Notice how not only is the center wavelength changing with junction temperature, but the width of the power curve is changing as well. This is a value called spectral width, and it is given on laser diode spec sheets with the units of nm. It is described as the full width half maximum (FWHM) value of the power curve (Figure 18). An increasing spectral width (called spectral broadening) means the laser diode output is now more spread out over a larger range of wavelength. Both phenomena described here contribute to optical power absorption problems in the gain media because the gain media are set to absorb optical power at a specific center wavelength and spectral width.

Chackrabarti et al.⁶⁴ studied the temperature dependent aspects of a 670 nm laser diode's operation to a very in-depth level. Their research agreed with that of Kim et al.¹⁴ in that both the center wavelength and spectral width of laser diode output are functions of junction temperature. However, because junction temperature is difficult to measure, Chackrabarti et al.⁶⁴ based it on the heat sink temperature. A change in heat sink temperature is representative of the same corresponding change in junction temperature. Therefore, the equations can be modified to use a change in heat sink temperature from reference temperature in order to predict the change in junction temperature. They also explain how the intensity of laser diode output changes with junction temperature, and this is directly tied to the laser's optical power output. This intensity change with wavelength shift is shown in Figure 119.

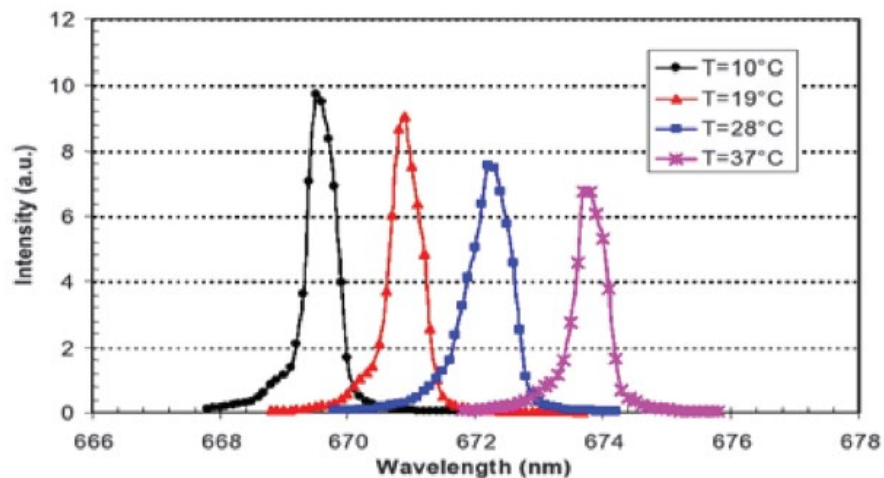


Figure 119: Laser diode output intensity changing with wavelength shift due to shifting heat sink temperature⁶⁴

The peak shifted from 669.4 nm at 10 °C to 673.6 nm at 37 °C, yielding a $d\lambda/dT = 0.155$ nm/K. In addition, the emission intensity decreased to 8.7, 7.6, and 6.7 at a heat sink temperature of 19,

28, and 37 °C, respectively, from 9.7 at 10 °C. This is expected because it is known that as the junction temperature strays from the reference temperature, optical power out decreases (see equation 75) . Optical power can be thought of as the area under the curves in the figure above. Since an increase in heat sink temperature yields a decrease in emission intensity, the area under the curve also decreases. Clearly the area under each curve is decreasing as heat sink temperature changes. Another aspect of temperature dependent operation observed by Chackrabarti et al.⁶⁴ is the FWHM spectral broadening, seen in Figure 120.

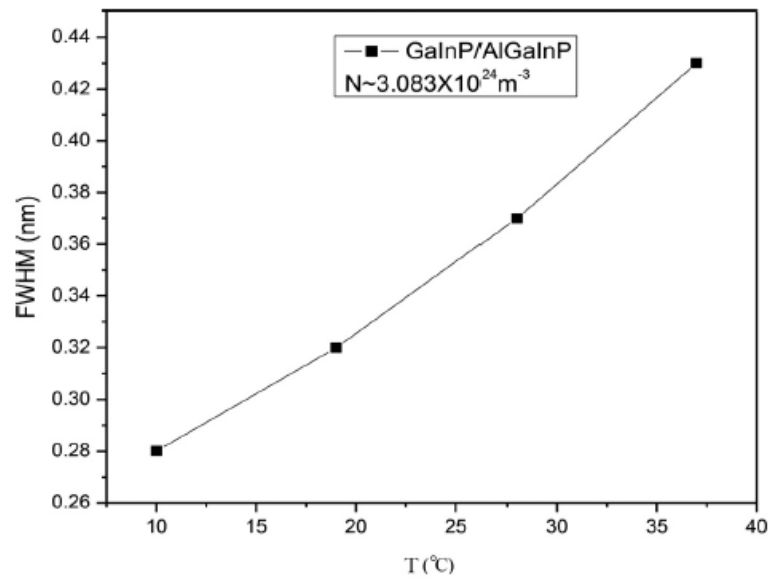


Figure 120: Spectral width changing with heat sink temperature, 0.28, 0.32, 0.37, and 0.43 nm for 10, 19, 28, and 37 °C, respectively⁶⁴. If FWHM is represented by β , then the slope of the line

$$\text{is } d\beta/dT = 0.0056 \text{ nm/K}^{64}$$

The spectral broadening equation is shown below. It is very similar in form to the wavelength shift equation. Both are considered linear and use a nominal value plus the quantity of a temperature coefficient multiplied by a change in temperature yielding a change in distance based on temperature.

$$FWHM_{LD}(t) = FWHM_{LD} + \left((T_j(t) - T_{ref}) * d\beta/dT \right) \quad (80)$$

Schlenker⁷⁰ studied and observed a wavelength shift during pulse operation using the Golden Bullet Laser Diode Submodule by Northrop Grumman (center wavelength of 808 nm). The laser diodes were cooled with a flash boiling technique using methanol. The goal was to see if the laser diode temperature was properly controlled by judging the diode's optical power profile and center wavelength. The results show a shift in operating wavelength from 808 nm as the current is increased from 20 to 100 amps. See Figure 13. Note that the different curves in each plot are taken at varying instances in time during the pulse. Notice how the center wavelength is different at 60A case versus the 100 A case. However, due to the thermal management techniques, there is not much change in the center wavelength from initial pulse activation to 5 seconds into pulse activation.

The research by Schlenker⁷⁰ makes reference to research in laser diode wavelength shift and spectral broadening by Liu et al.⁷¹. The research explains how in high power semiconductor lasers, a laser array (laser bar) is made up of several emitters. In Figure 121 below, these emitters are placed on a bar with a certain fill factor (how close the emitters are located to each other), which is attached to a heat sink.

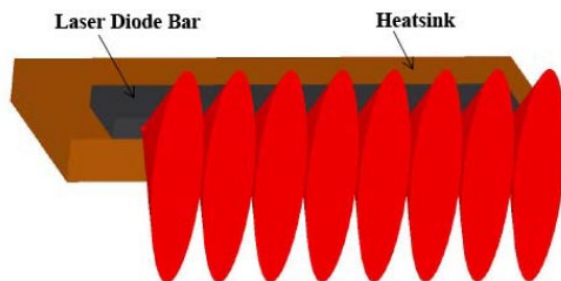


Figure 121: Packaging of a high power semiconductor laser array showing laser output (“fast” divergence axis in vertical direction and “slow” divergence axis in the horizontal direction)⁷¹

The phenomenon of spectral broadening shown by Kim et al.¹⁴ occurs because of the orientation in which high power semiconductor lasers are arranged. Liu et al.⁷¹ talks about the “smile” of a laser array. This is simply the spectral mapping of the output of each individual emitter on the laser bar, as seen in Figure 122.

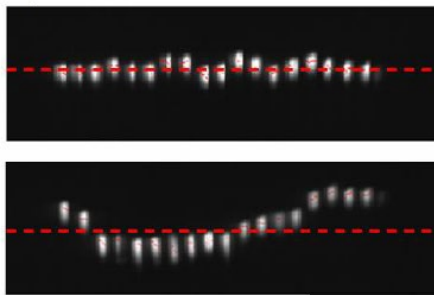


Figure 122: Laser bar “smile” showing a good spectrum vs. a bad spectrum⁷¹. A laser bar is operating optimally when the spectrums of all emitters are the same⁷¹

Smile occurs because of uneven heating in the emitters. If they are not cooled properly, emitters in the center can become hotter than emitters on the edges. This means the junction temperatures of the emitters are not the same. Hence, the wavelengths of the emitters are not the same. If all the laser output is not at the same center wavelength, the laser bar is not operating at its best possible conditions (the electro-optical efficiency is not as good as it could be).

Yuan et al.⁷² (also referenced by Schlenker⁷⁰) look into the spectral broadening of laser array output as well as the simulated versus actual thermal resistance of the heat path from the junction to the heat sink in a 19 emitter CW laser bar (reference Figure 19). They accomplished

this using a combination of experimentation and finite element methods. For the finite element method (simulation) approach, the semiconductor laser package used was mounted to a thermo-electric cooler (TEC) where the bottom surface of the TEC was kept at 25°C. Figure 123 below shows the temperature profile of the quantum wells (junction) as steady state operation.

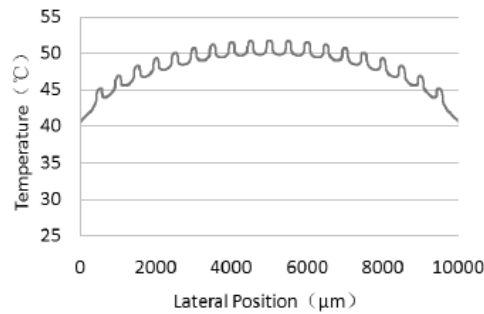


Figure 123: Transverse temperature profile of quantum wells at steady state⁷²

In this 808 nm semiconductor laser, they supplied 120 W of electrical power and got 60 W of optical power. This means the waste heat produced was 60 W. In the finite element analysis of the semiconductor laser bar, they found a ΔT between the bottom TEC surface and the active region (junction) of 26.8°C. This gave them an overall simulated thermal resistance for the laser of 0.472 K/W. Yuan et al.⁷² go on to state how the temperature rise in a semiconductor laser cannot be easily measured. Hence, measuring the wavelength shift is used as a more practical way to approximate the temperature in the active region. One semiconductor laser sample was subjected to wavelength shift testing, and this was done using a spectrum and PIV test system yielding the results seen in the Figure 124.

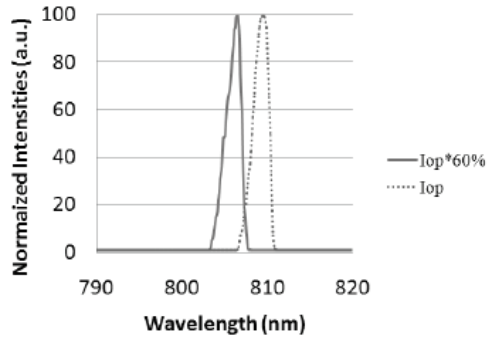


Figure 124: Wavelength of steady state laser bar output for a particular operating current value and 60% of that value⁷²

They found a shift of 4.6 nm, which when used with the fact that a typical 808 nm laser shifts at a rate of 0.27 nm/K yields a device thermal resistance of 0.656 K/W (found by using equations in the paper). This is larger than the resistance of 0.472 K/W found in the simulation. They expected this discrepancy and explain by the fact that the simulation finite element analysis assumed the solder layers in the laser materials are perfect. The simulation also neglects the effect of nonlinear material molecular makeup, material defects, and contact thermal resistance for these varying laser bar materials.

Fiber Gain Media – Basics/Background:

Fiber lasers use optical fibers as the gain media component. Optical fibers do not act as a typical gain media because the amount of signal power out of the fiber can never be more than the pump power into the fiber. There is no power “gain”. The benefit of using a fiber is it takes high power, low beam quality pump light from diode lasers and creates slightly lower power, but much higher beam quality laser light. The geometry of a typical dual-clad fiber consists of an

active core, an inner cladding layer, and an outer cladding layer to trap and keep light inside the fiber (see Figure 125).

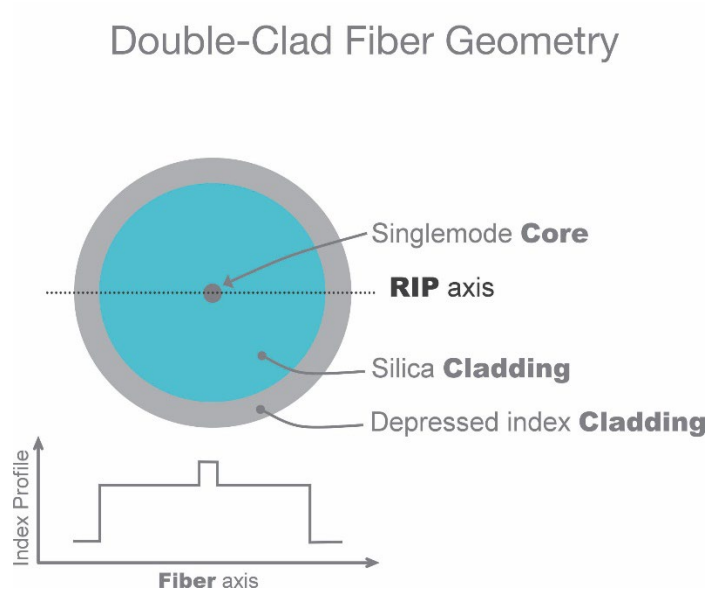


Figure 125: Diagram of fiber geometry with core, inner cladding, and outer cladding. The refractive index profile (RIP) of each layer is given to show how its magnitude changes⁷³

Pump light from diode lasers is highly divergent and difficult to couple directly into a single mode active fiber core, as the numerical aperture (NA) of the single mode active core is too small. The equation for NA is shown in equation 81 along with a diagram in Figure 126.

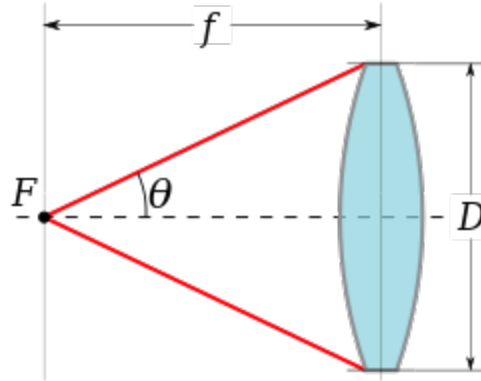


Figure 126: Illustration of relationship between focal length (f) and aperture diameter of lens (D), where F is the focal point (reprinted from Figure 2.4 in Motes et al. ³²).

The derivation of the expression for NA is as follows. NA is defined initially according to principles of Snell's Law and using the concept of total internal reflection (TIR)³², as per

$$n \sin \theta_{ic} = \sqrt{n_1^2 - n_2^2} = NA$$

Here, n is the refractive index of air, n_1 is the refractive index of the core, n_2 is the refractive index of the inner cladding, and θ_{ic} is the internal critical angle for TIR. The F-number ($F\#$) parameter from optics is defined as f/D in Figure 126. If the angle θ in Figure 126 is less than θ_{ic} and significantly small, then

$$n \sin \theta \approx n \tan \theta = nD/2f = n/(2F\#)$$

Taking $n=1$ for air,

$$NA \approx 1/(2F\#) \tag{81}$$

To collect all pump light, the fiber NA needs to be equal to or greater than the NA of the component used to couple light to the fiber. If not, light will be lost when inserted into the fiber.

This is simply a fiber design issue, and the NA problem is overcome through the use of dual-clad fibers. Figure 127 shows a fiber with pump input (Large NA) and signal output (small NA), with the pump rays having TIR in the inner cladding.

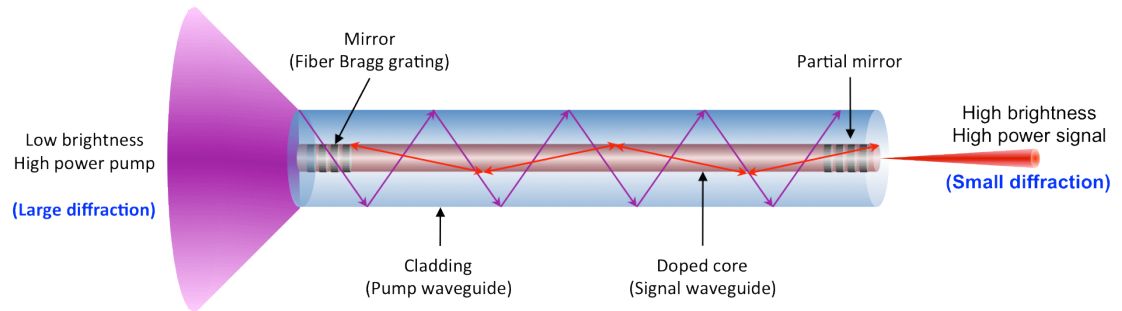


Figure 127: Pump power is converted to signal power through an optical fiber by doping ions in the core, turns large NA pump light into small NA signal light⁷⁴

The inner cladding is designed to have an index of refraction slightly lower than the core, providing a low core NA. The outer cladding, however, normally has a much lower index of refraction than the inner cladding, resulting in a large NA for the inner cladding. Hence, the inner cladding has a much larger NA relative to the active core, allowing highly divergent pump light to be more easily injected into the inner cladding³². Designers use equation 81 to be sure the pump light is launched properly into the inner cladding. A typical index of refraction for a dual clad fiber is shown describing how the index of refraction changes at each intersection in Figure 125. Pump light absorbed in the inner cladding is then eventually converted to signal power along the fiber length in the active core through the use of rare-earth doping ions. The dual-clad fiber design is beneficial because it forces total internal reflection (TIR) of all pump light absorbed in the inner cladding. Hence, the pump light is eventually reflected into the active core, creating the signal power output of the fiber laser. The ease of launching pump light into

the inner cladding, coupled with the natural creation of laser light within the active core, are the main reasons for use of fiber gain media.

To maintain a high pump light absorption, all pump rays must eventually intersect the signal core (see Figure 127) where pump light is absorbed, exciting the rare-earth doping ions to higher energy levels. If the fibers are perfectly symmetrical, helical or spherical pump modes will not be absorbed. To avoid the problem of only typical transverse wave-type modes being absorbed, the inner cladding can be manufactured in a non-circular geometry. Yet another method is to simply place the active core off-center relative to the inner cladding.

Signal power out is the laser output of the fiber. Pump light enters the cladding at a certain wavelength, but the signal power out is at a longer wavelength due to the process of photon conversion. The ratio of pump wavelength over signal wavelength is the quantum defect. The incoming pump light excites doping ions in the fiber core. The ions move from their ground energy level state to an excited upper energy level state. The ions exist at the upper energy level state for a very short time (the spontaneous lifetime) and then drop to a lower energy level state, emitting a photon of a very precise wavelength and phase in the process. The photon emission is happening all along the fiber length as long as adequate pump light is present. Every photon emitted is of the same wavelength and phase, so they are all monochromatic, coherent, and highly collimated. Therefore, the signal out of the active core is laser light. Each doping element has its own particular absorption and emission cross section. A common element used for doping optical fibers is Ytterbium Yb^{3+} ions. Absorption and emission cross-sections for Ytterbium are well documented^{36,75-78}. A plot of the energy level diagram and emission/absorption cross-sections for Ytterbium is given in Figure 128.

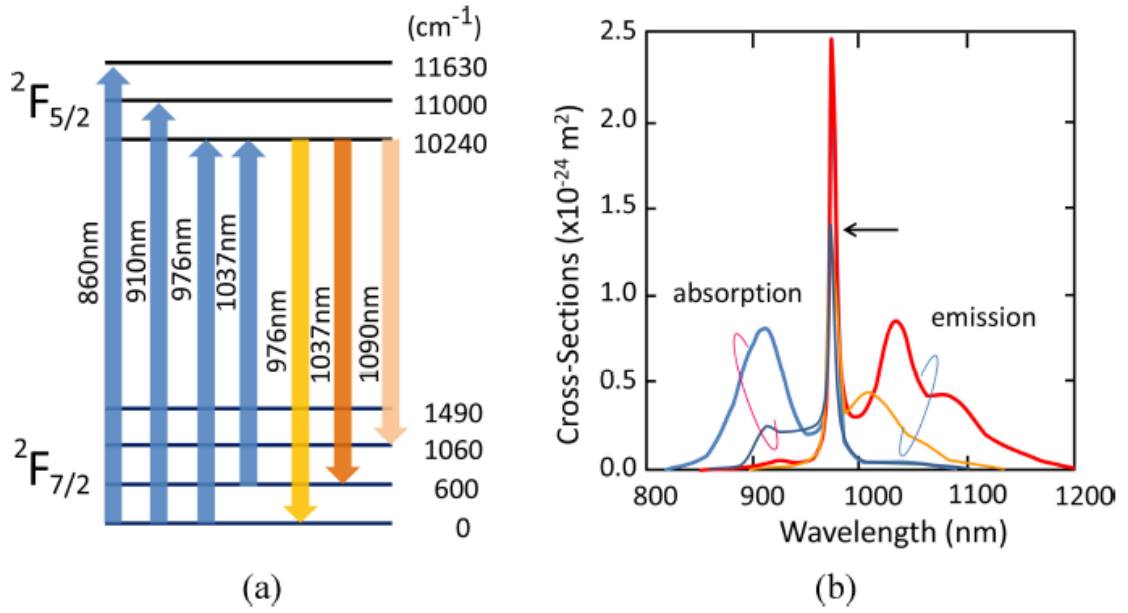


Figure 128: Typical energy level diagram of Yb^{3+} ions in silica glass (a) and typical emission and absorption cross-sections in aluminosilicate (thicker lines) and phosphosilicate (thinner lines) fibers. The arrow represents the peak of the phosphosilicate emission/absorption⁷⁸

Yb^{3+} has a wide absorption spectrum spanning from $\sim 850 \text{ nm}$ to $\sim 1080 \text{ nm}$, allowing for multi-wavelength pumping schemes for power scaling to the kilowatt level⁷⁸. It is common to pump ytterbium with 976 nm pump light and generate 1064 nm signal light³².

Fiber Gain Media – LP Modes of Fibers:

The refractive index profile of many optical fibers is radially symmetric and only varies with the radial coordinate⁷⁹. Since most index profiles exhibit small incident contrast, where the difference between the refractive indexes of the core and cladding are very small (1% or less), the fiber is assumed to be weakly guiding³². This assumption means the linearly polarized (LP) modes can more simply be obtained. The LP mode/modes actually propagating within a fiber

are based on the planar waveguide dispersion equation shown in equation 82, derived using ray optics³².

$$\sqrt{\left(\frac{1}{X^2} - 1\right)} = \tan\left(VX - \frac{m\pi}{2}\right) \quad (82)$$

With

$$X = \frac{n_1 \sin \theta}{NA}$$

$$V = \frac{2\pi}{\lambda} r_{core} NA \quad (83)$$

Here, m is an integer with the number of modes in the waveguide equal to $m+1$, λ is the pump light wavelength ($2\pi/\lambda$ is the free-space wavenumber), and r_{core} is the core radius. Plotting X versus V yields the dispersion curves shown in Figure 2-7 in Motes et al.³². Single mode (SM) ($m=0$) operation for all values of X in an optical planar waveguide can only occur when V is less than or equal to $\pi/2$. Therefore, as per inspection of equation 83, SM operation can only be maintained if the core radius or core NA is kept small, or the free-space wavelength λ is made large. In reality, fibers are cylindrical, not planar. Hence, Maxwell's equations are used to derive the cylindrical waveguide LP modes. In doing so, the cutoff V value for SM operation changes to 2.405³². Any V value lower than 2.405 will produce SM operation with only the lowest order (fundamental) mode LP_{01} , as per Figure 129. The curves of $V=2.405$ and $V=4$ are quarter circles in Figure 129. Any modes contained inside those curves will propagate for the given V value. If $V \leq 4$, the LP_{01} , LP_{11} , LP_{21} , and LP_{02} modes will all propagate as the various cutoff points are 0, 2.405, 3.823, and 3.823

respectively (Table 2-1 in Motes et al.³²). Say, for example, $V=2$. Then, the only propagating mode would be LP_{01} . High order modes appear faster as the value of V increases.

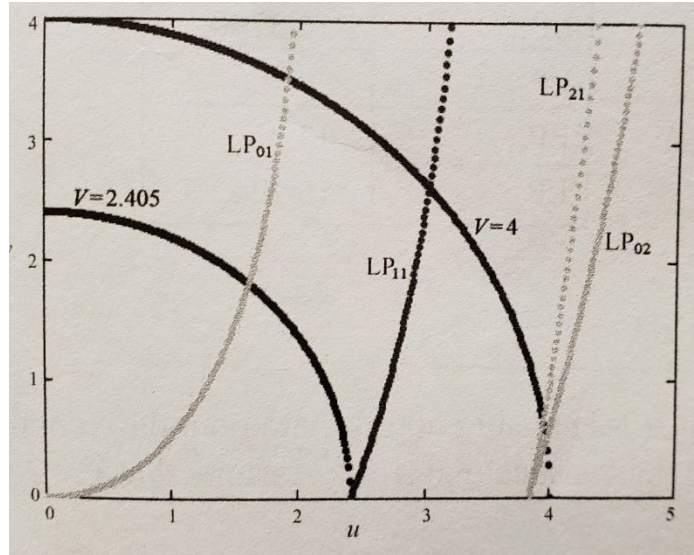


Figure 129: Graphical solution showing V cutoff points for various LP modes. Parameters w and u come from the planar waveguide mode derivation of Maxwell's equations and are defined such that

$$V^2 = u^2 + w^2 \text{ (reprinted from Figure 2-14 in Motes et al.}^{32}\text{).}$$

Larger values of V will result in additional higher order mode propagation within the fiber.

Propagation of higher order modes degrades the beam quality at the fiber output. Hence, SM operation with the fundamental mode LP_{01} is desirable because it yields the best beam quality.

The LP_{01} mode has an intensity profile similar to a Gaussian beam, which is desirable because the spectrum of a Gaussian beam is focused and gives a high value of irradiance (power per unit area). The intensity profiles of the first several $LP_{l,m}$ modes for $V=11.4$ are shown in Figure 130.

Note the respective mode indices l and m .

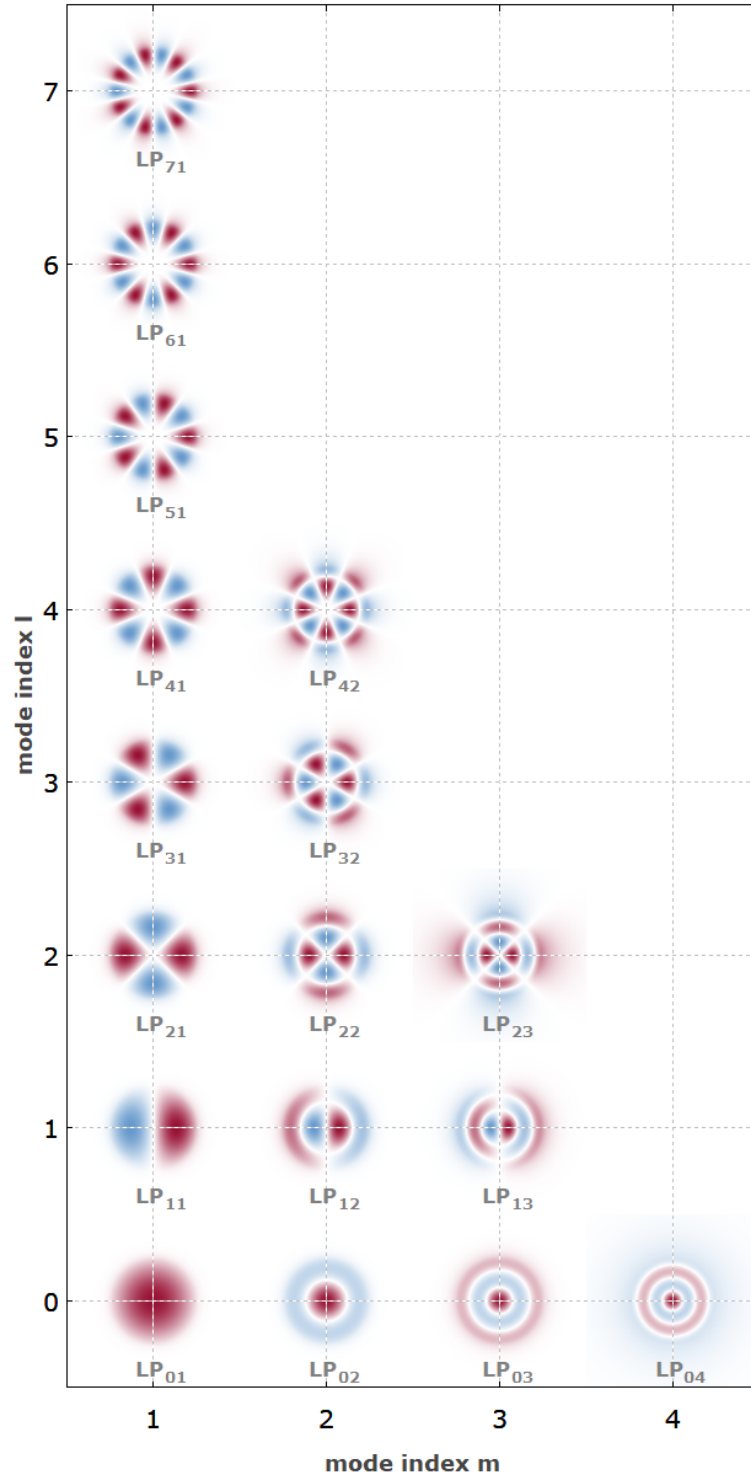


Figure 130: Generic intensity profiles for guided $LP_{l,m}$ modes of a fiber with $V=11.4$. The two colors indicate positive (red) and negative (blue) signs of the electric field⁷⁹

By Figure 130, high order modes propagating in addition to the fundamental LP_{01} mode reduce the beam quality by creating several peaks in the curve having less intensity than a typical single gaussian beam (just the LP_{01}). Having the intensity spread out over more area gives a smaller irradiance, dramatically decreasing the beam quality. A beam with smaller irradiance is simply less effective.

Sizing the fiber core becomes a question of design application and optimization. A larger fiber core means the core can handle higher levels of overall optical power. However, along with a large core comes the potential for multimodal operation due to the definition of V (equation 83). A multimodal (MM) fiber's beam quality is degraded significantly compared to that of a SM fiber. The MM fiber may have more optical power, but the SM could give better irradiance even with its lower optical power. The SM fiber output would be more effective. To maintain SM operation with larger fiber cores, NA must be reduced. Indeed, there is a limit to how small the difference between n_1 and n_2 can be physically manufactured. SM operation fiber core maximum diameters are around $30 \mu\text{m}^{32}$. It is also possible to have SM operation with a large fiber core if a longer pump wavelength is used. The longer wavelength can allow for higher levels of optical power while still maintaining the good beam quality of SM operation.

So far, the section here on LP modes has considered the launching of pump light directly into an SM fiber core. This is very challenging due to the restrictions of equation 83. A double clad fiber, as defined earlier, is therefore beneficial because now the pump light just has to be launched into the inner cladding, not directly into the single mode core. The laser power now being generated in the fiber core as pump light interacts with the doping ions is still of the fundamental LP_{01} mode (due to the radius and NA of the fiber core), but it can reach much higher power levels due to the fiber's ability to accept high power pump light with higher order

propagating modes into the inner cladding. Hence, another reason why double clad fiber lasers are the first choice for high power laser system applications where good beam quality is paramount.

Fiber Gain Media – Seeding a Fiber:

Due to the nature of fibers, it is sometimes difficult to force fiber output to a desired wavelength or particular narrow linewidth. Both are important for obtaining high quality fiber output. If necessary, a fiber can be seeded to help obtain the desired signal properties. A seed laser is a lower power, high quality laser injected directly into the fiber core⁸⁰. It is of the desired signal wavelength and sufficiently narrow linewidth, normally with a power level on the order of 10 W¹⁷.